UNIVERSITY OF CALIFORNIA, SAN DIEGO

Investigation of Torsional Effects on Thirteen-Story Reinforced Concrete Frame-Wall Structure Modeled in ETABS and SAP2000 Using Linear and Nonlinear Static and Dynamic Analyses

A Thesis submitted in partial satisfaction of the requirements for the degree Master of Science

in

Structural Engineering

by

Julie Christine Bolander

Committee in charge:

Professor José I. Restrepo, Chair
Professor Joel P. Conte
Professor Gilberto Mosqueda

2014

The Thesis of Julie Christine Bolander is approved and it is acceptable in quality and form for publication on microfilm and electronically:

Chair

University of California, San Diego

2014

DEDICATION

I dedicate this thesis to my family, who has provided the support to get me to where I am today.

I would also like to dedicate this thesis to the Katsuyama family, particularly Brent, who has provided advice and emotional support throughout the duration of completing the thesis.

TABLE OF CONTENTS

LIST OF FIGURES

LIST OF TABLES

ACKNOWLEDGEMENTS

I would like to acknowledge Professor José Restrepo for his guidance each week as my advisor and the chair of my committee, Professor Joel P. Conte for obtaining the appropriate software needed to complete the research and participating on my committee, and Professor Gilberto Mosqueda for participating on my committee. I would also like to thank Arpit Nema for providing some of the references and OpenSees data used, in addition to finding errors in a couple of my codes, which saved me several days of pointless work and endless searching.

ABSTRACT OF THE THESIS

Investigation of Torsional Effects on Thirteen-Story Reinforced Concrete Frame-Wall Structure Modeled in ETABS and SAP2000 Using Linear and Nonlinear Static and Dynamic Analyses

by

Julie Christine Bolander

Master of Science in Structural Engineering

University of California, San Diego, 2014

Professor José I. Restrepo, Chair

The primary objective of this thesis is to evaluate the effects of torsion on the nonlinear seismic response of a thirteen-story reinforced concrete frame-wall structure with an asymmetric stiffness in plan. The NEHRP building structure, located in Berkeley, CA and previously designed by André Barbosa, was modeled in ETABS and SAP2000 to

perform several analyses. The models accounted for realistic cracked concrete section stiffnesses, expected material properties, and nonlinear plastic hinges. Due to limitations of ETABS in performing nonlinear dynamic time history analysis, the model was exported to SAP2000. An asymmetric lateral stiffness model was created by moving one of the shear walls from the center of the building toward the outside of the building. OpenSees was used to find the nonlinear hinge moment-rotation relationships.

Using a suite of seven ground motion record pairs, an essentially linear dynamic time history analysis was performed on the symmetric and asymmetric ETABS models. The SAP2000 models were used to perform a series of nonlinear static (pushover) analyses. Fully nonlinear, including material and geometric nonlinearity, time history analyses were performed on the SAP2000 models using the seven ground motion pairs, appropriately cut to shorter lengths to reduce the analysis run-time. In each analysis case, the results of the symmetric and asymmetric models were compared. Overall, the asymmetric model typically experienced torsional effects and larger displacement responses than the symmetric model. The more nonlinear the structure behaved, the more influence torsion had on the response of the model with asymmetrically-placed shear walls.

1 INTRODUCTION

The purpose of this thesis is to investigate the effects of moving a shear wall, and therefore inducing torsional response, in a thirteen-story reinforced concrete frame-wall building structure subjected to seismic loading. To achieve this objective, a computational model was created using the Computers and Structures, Inc. software ETABS v9.7.4 Nonlinear and SAP2000 Ultimate v15. ETABS and SAP2000, as opposed to more advanced nonlinear modeling tools, were used to perform linear and nonlinear analyses in order to gain experience with programs that are used more commonly in practice. The structural models are based on the design of an office building, with some retail shops on the ground floor, located in Berkeley, California. Originally a design example provided in the FEMA 451 NEHRP (National Earthquake Hazards Reduction Program) Recommended Provisions [1] by Charney based on the 2000 Provisions [2], André Barbosa redesigned the structure [3] to a more recent standard – the 2003 Provisions [4]. Since the building is located in a region of high seismic hazard, the structure was designed for large lateral forces based on the building code's equivalent lateral force procedure. Since it is common for shear walls to be placed asymmetrically in buildings to provide greater architectural flexibility, the ETABS and SAP2000 symmetric models based on Barbosa's design were altered such that one of the interior shear walls was moved toward the exterior of the structure.

In Section 2 of this thesis, a full description of the original building and design is presented, followed by the details and parameters of the preliminary ETABS symmetric models created. In Section 3, the final material properties, cracked concrete section

stiffnesses, and addition of discrete nonlinear plastic hinges are described for the ETABS and SAP2000 symmetric and asymmetric models, along with the differences in dynamic characteristics found using modal analysis. The properties and implementation of the nonlinear plastic hinges are also fully discussed with these final model descriptions. Section 4 presents the code-based response spectra for the Berkeley site and the response spectra for the suite of seven ground motion record pairs used for the time history analyses. The analyses performed, including a dynamic time history analysis for the ETABS model and nonlinear static and nonlinear dynamic time history analyses for the SAP2000 model are presented and the results discussed in Section 5. A summary of the results and the relevant limitations of the research performed are presented in Section 6, along with a few recommendations for future research. Finally, the appendix provides supplemental data and figures, in addition to a comparison of the nonlinear time history analysis results of the symmetric SAP2000 model to the time history analysis results of a nonlinear finite-element fiber section model of the same structure created by Barbosa and analyzed by UCSD student Arpit Nema.

2 ORIGINAL DESIGN AND PRELIMINARY MODELS

2.1 Original Building Description and Design

The original thirteen-story reinforced concrete (RC) building that was designed by Barbosa is rectangular and symmetric in plan (Figure 2.1). There are twelve stories above grade and one basement level below grade. In the twelve stories above grade, typical spans are 30 feet in the North-South (N-S) direction. The East-West (E-W) direction consists of 40-ft long exterior bays and a 20-ft long interior bay for Gridlines 2 through 7, where Gridlines 1 and 8 each have five 20-ft long bays. At the basement level 12-inch thick walls are assumed to surround the entire perimeter, shown in the exterior elevation views (Figure 2.2 and Figure 2.3).

The gravity system consists of beams along the major gridlines as shown in Figure 2.1, which support the two-way 8 inch thick post-tensioned slab. Beams along Gridlines A through D, Gridlines 1 and 8, and the interior bay of Gridlines 2 through 7 are 32 inches deep by 22.5 inches wide. As shown in Figure 2.4, the exterior bays of Gridlines 2 through 7 consist of "haunched" girders that are 22.5 inches wide with depth varying from 32 to 20 inches to provide clearance for mechanical and electrical systems. All columns are 30 inches by 30 inches. A dual system of frame-walls along Gridlines 3 through 6 (Figure 2.4, left) and special moment frames along Gridlines 1, 2, 7 and 8 (Figure 2.2 and Figure 2.4, right) provide lateral force resistance in the E-W direction. The lateral force-resisting system in the N-S direction consists of special moment-resisting frames, along Gridlines A, B, C, and D (Figure 2.5).

The entire structure is constructed with normal weight concrete. The assumed material properties of the original structure are a nominal concrete compressive strength (f'_c) of 6 ksi and the yield strength of reinforcing steel (f_y) is 60 ksi.

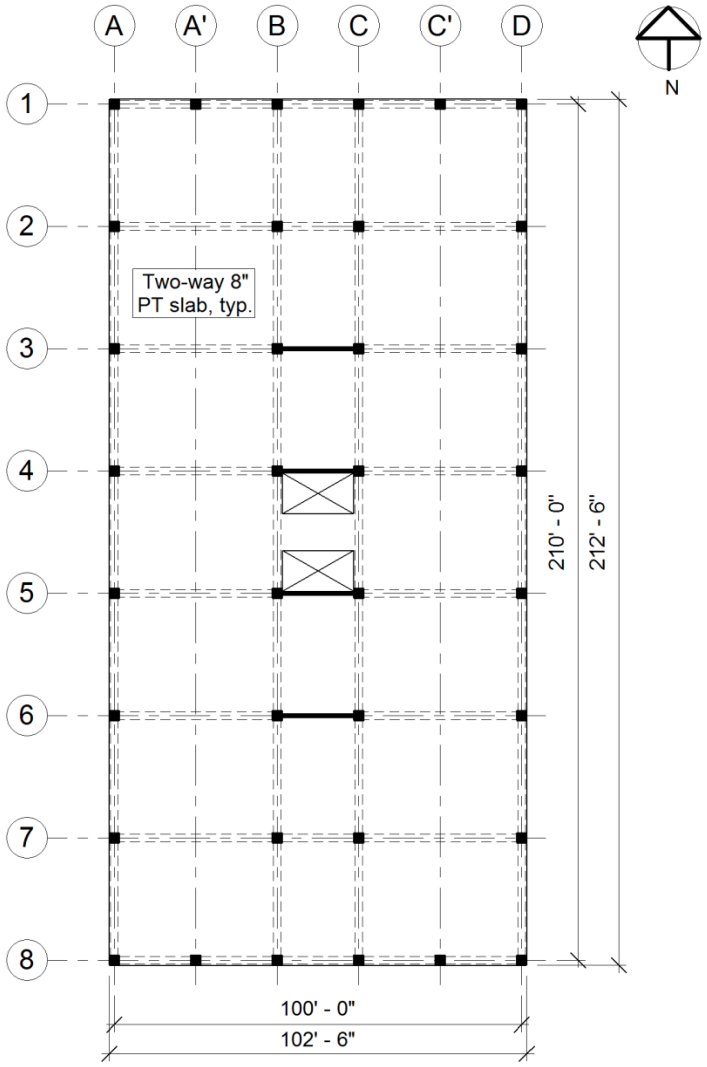

Figure 2.1: Typical floor plan

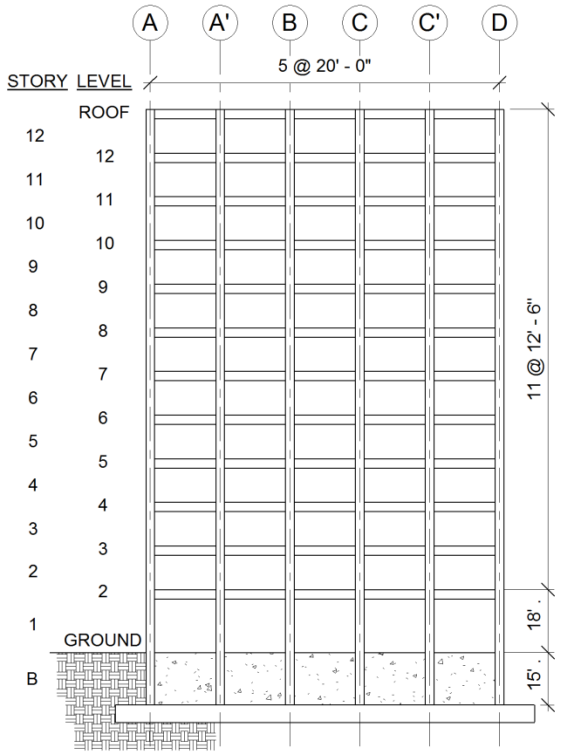

Figure 2.2: Typical N-S elevation (Gridlines 1 and 8)

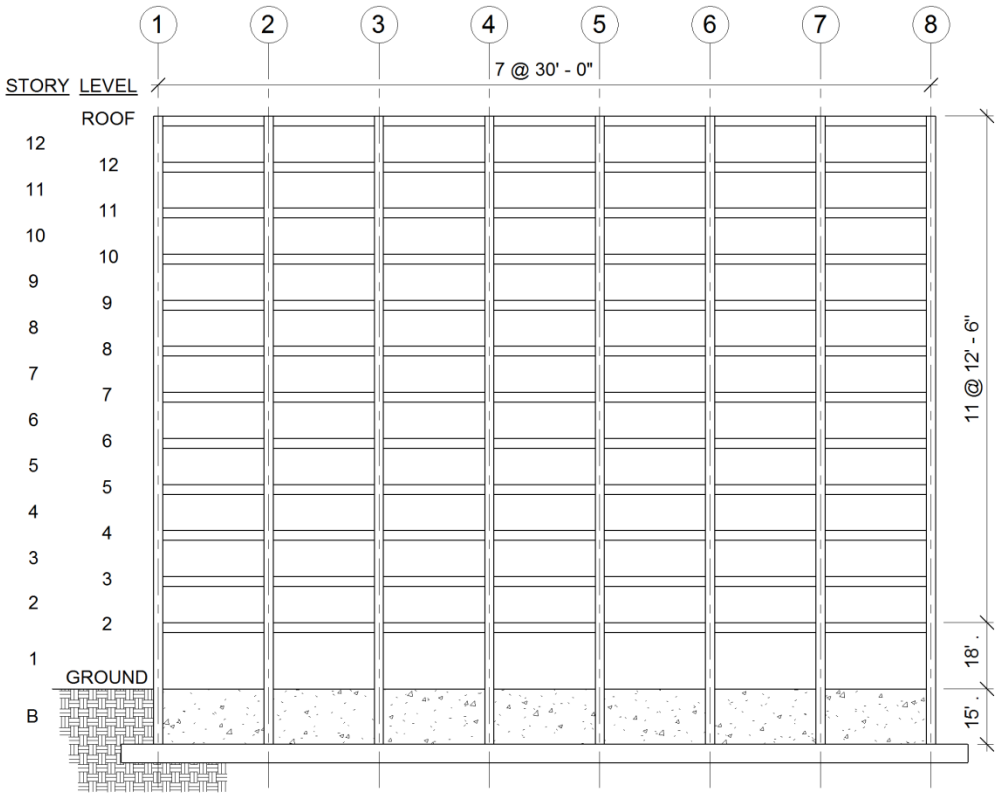

Figure 2.3: Typical E-W elevation (Gridlines A and D)

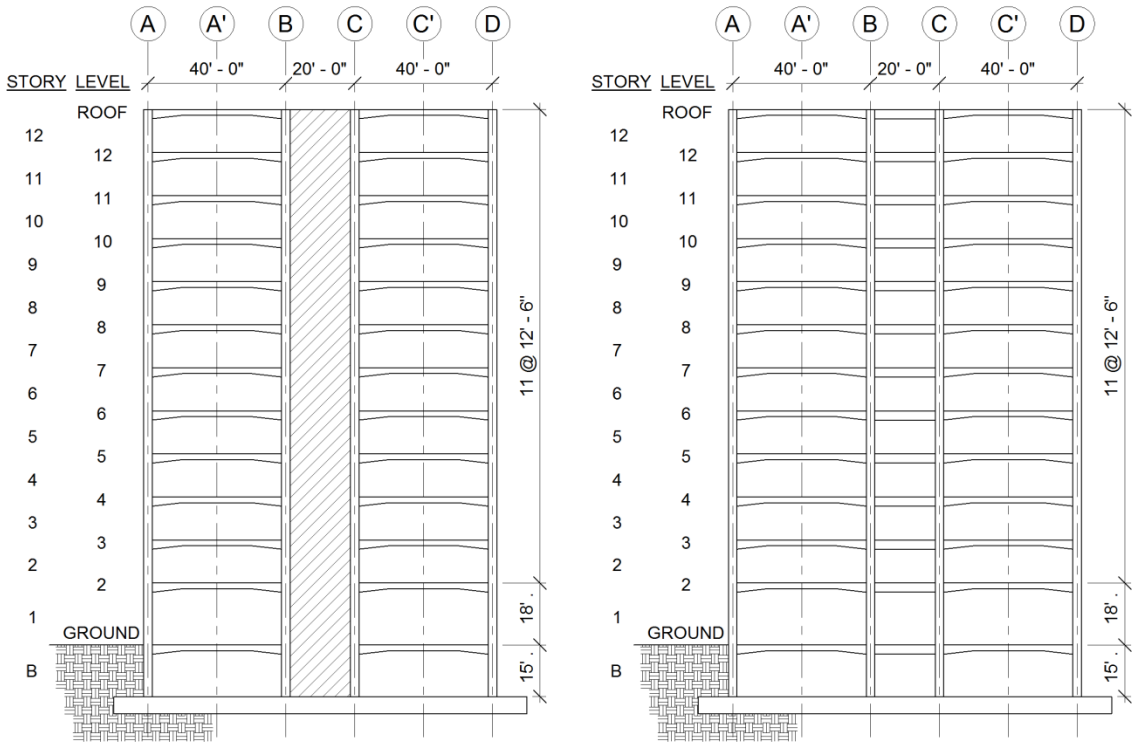

Figure 2.4: Typical N-S sections: at wall - Gridlines 3 through 6 (left) and at frame - Gridlines 2 and 7 (right)

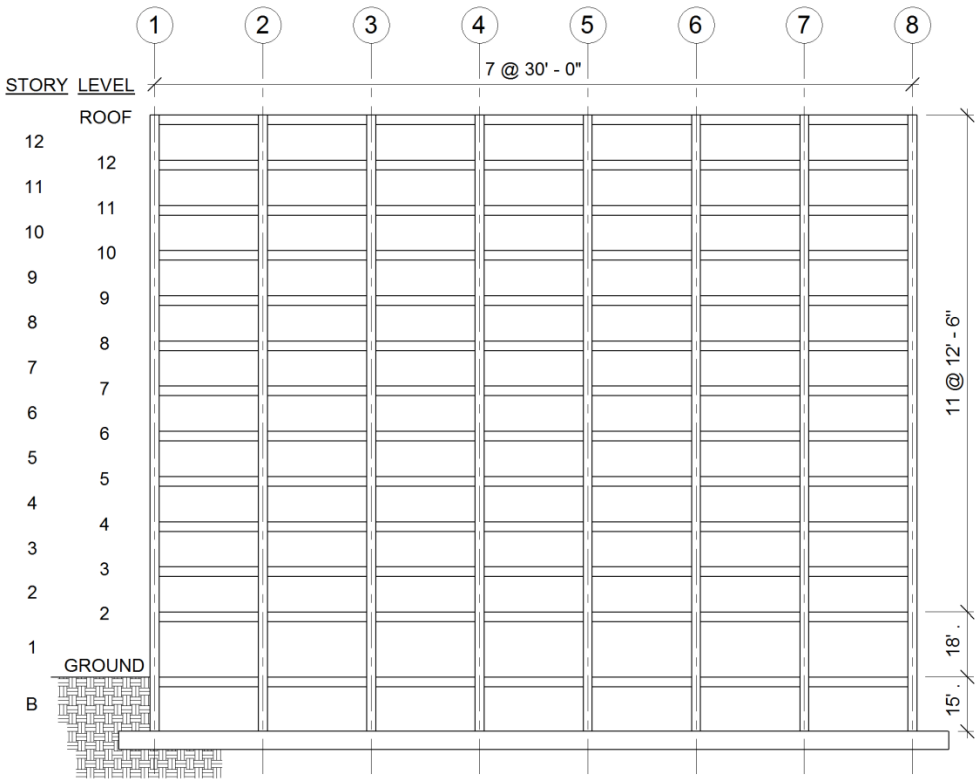

Figure 2.5: Typical E-W section at frame (major Gridlines A through D)

Barbosa used the 2003 NEHRP Recommended Provisions alongside the ASCE 7-05 [5] and ACI 318-08 [6] codes to design the structure. Since the building is located in Berkeley, a high seismic hazard area, the structure is designed to resist large seismic forces defined by the orthogonal combination and equivalent lateral force procedures (ASCE 7, Ch. 12) for Seismic Design Category D with an importance factor, I, of 1. Demands from the appropriate code-based combinations of dead, live, and earthquake loads are applied to design the beam flexural steel reinforcement. The column longitudinal reinforcement is also based on the demands of basic load combinations and verified by axial force - bending moment interaction diagrams. As shown in Figure 2.1, each of the shear walls on Gridlines 3 through 6 consist of a 17.5-ft long, 12” thick wall panel and two 30-in square columns that are considered as boundary elements for the

wall. The panel shear reinforcing is designed to resist the shear demands resulting from basic load combinations. Axial-moment interaction diagrams are again used to verify that load combination demands are less than the capacity of boundary elements with the longitudinal reinforcing design.

To determine the required beam and column transverse shear reinforcing (hoops) and beam-column joint designs for the special moment frame and frame-wall systems, capacity-based design is used. For the capacity-based design approach, the desired mechanism for the frames and frame portion of the frame-walls is the first-mode mechanism of strong-column/ weak-beam, where flexural plastic hinges form at the ends of beams. As shown in Figure 2.6, the columns and shear walls exhibit flexural yielding at the base, which in this case is assumed to be ground level due to rigid diaphragm-basement wall action. This first-mode mechanism is utilized to encourage predictable ductile response and avoid dangerous and unpredictable brittle failures. The hoop size and spacing in the plastic hinge regions are determined based on maximum probable moment demands that can occur in the beams resulting from expected material properties. This method of hoop design is intended to provide effective confinement of the concrete core to ensure the desired ductile response. The boundary elements of the shear wall are designed with transverse reinforcement satisfying the special boundary element conditions of ACI 318, Chapter 21 in the region where plastic deformation is expected: from the base up to level 3.

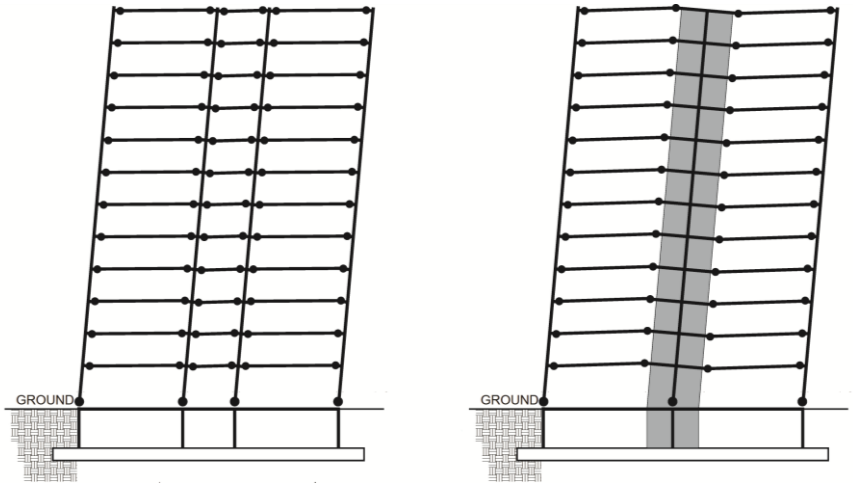

Figure 2.6: First-mode mechanism for frames (left) and frame-walls (right)

2.2 ETABS Model Creation and Verification

2.2.1 Barbosa's SAP2000 Model Description

To aid in the estimation of modal properties, determination of axial, shear, and moment demands, and prediction of story drifts for his design, Barbosa created a 3-D elastic finite element model of the building structure in SAP2000. As in the plans, elevations, and sections presented in Section 2.1, the model has twelve levels above grade and one level below. The basement walls are modeled as 12" thick shear panels with pinned connections at their base. At ground level, horizontal displacements perpendicular to the basement walls are restrained. All columns and shear walls are pinned at the base. The shear walls are modeled with columns as boundary elements and 12" thick shear panels. To model beam-column joints as halfway between fully rigid (fixed) and fully flexible (pinned) joints, beam rigid-end offsets are applied and assigned as 50% rigid. The haunches provided for mechanical and electrical systems are not modeled, so beams with a constant depth of 24 inches are used in place of all "haunched" beams. The beams without haunches are modeled as 32 inches deep, as specified earlier. All beams are

modeled as flanged, or T-beams, to account for the effective width of the concrete slab. The slab itself is not modeled, so rigid diaphragms are assumed and appropriate point constraints are created to get the desired rigid floors. The story masses are concentrated at the center of mass of each diaphragm. Additionally, P-Delta effects are not included in the model.

The concrete material properties are defined such that f'_c = 6 ksi. Steel reinforcing is not modeled because in the elastic dynamic analysis, concrete sections are uncracked and the steel reinforcing is not activated and thus does not contribute to modal properties. To account for cracked section properties, as required by the 2003 Provisions Section 5.3.1, a second model was created such that bending stiffness modifiers are applied to the gross cross-sections properties. The bending property modifiers defined in the cracked model are 0.35 for beams, 0.50 for walls, and 0.70 for columns and wall boundary element. Since minimal tension and shear demands well below the elastic limit are expected, full axial and shear stiffnesses are assumed and the corresponding section properties are not modified.

2.2.2 Preliminary ETABS Model Description

A preliminary elastic 3-dimensional computational model that is based on Barbosa's final design was created by the author of this thesis in ETABS Nonlinear v9.7.4 and compared to the SAP2000 model described in Section 2.2.1 to verify that the modeling details are adequate and the model behaves as expected. This preliminary model serves as the basis of all future models described in the thesis. The specific modeling parameters and techniques used are presented in this section.

To start building the structural model in ETABS, the member cross-sections were identified from Barbosa's final design. For simplicity, the number of cross-sections used in the model was reduced to include only representative members. Table 2.1 summarizes the longitudinal reinforcement and dimensions for the cross-sections chosen to be modeled in ETABS; per the design, the clear cover for all reinforcing is taken as 1.5 inches. For a graphical representation of the locations of each beam and column member, see the model elevations in Figure 2.7 to Figure 2.10. Since the primary objective of the software is code-based design, this version of ETABS does not allow the user to specify the spacing or size of hoop reinforcing in beams and columns for analysis. Additionally, vertical and horizontal reinforcing cannot be specified for wall elements. Thus, these parameters are not summarized in Table 2.1 but will be discussed in Section 3. The purpose of modeling longitudinal steel reinforcement is to allow for future models to be modeled with nonlinearity.

Table 2.1: Summary of cross-sections specified in preliminary ETABS model

Member Dimensions	**Tag in ETABS**	**Longitudinal Reinforcement**		**Levels**	**Gridline Locations**
Walls 12" thick (typ.)	WALLB	Not Specified in Design		Base - Ground	Entire Building Perimeter
	WALL1	Not Included in Model		Base - Roof	Lines 3 - 6 Between B and C
Boundary Elements 30" x 30" (typ.)	BE1	24 #11		Base - Lv. 2	Lines 3 - 6 at B and C
	BE2	12 #11		Lv. 2 - Lv. 6	
	BE3	12 #9		Lv. 6 - Roof	
Columns 30" x 30" (typ.)	COL1	12 #9		All	A-1, D-1, A-8, D-8 (Corners)
	COL2	12 #10		All	Lines A, D, 1, and 8 (Except Corners)
	COL3	12 #11		All	B-2, C-2, B-7, C-7 (Interior)
Beams		**Top**	**Bottom**		
32" x 22.5"	BM1	3 #8 + 2 #9	3 #8 + 2 #7	All	Frames 1 and 8; Interior Bay of Lines 2 and 7
24" x 22.5"	BM2	7 #11	5 #9	All	Exterior Bays of Frames 2 - 7
32" x 22.5" (typ.)	BM3	3 #8 + 2 #8	3 #8 + 2 #7	Ground - Lv. 2	Frames A - D
	BM4	3 #8 + 2 #7	3 #8 + 2 #7	Lv. 3 - Lv. 9	
	BM5	3 #8	3 #8	Lv. 10 - Roof	
Slab 8" thick	SLAB1	Not Specified in Design		Ground - Roof	All

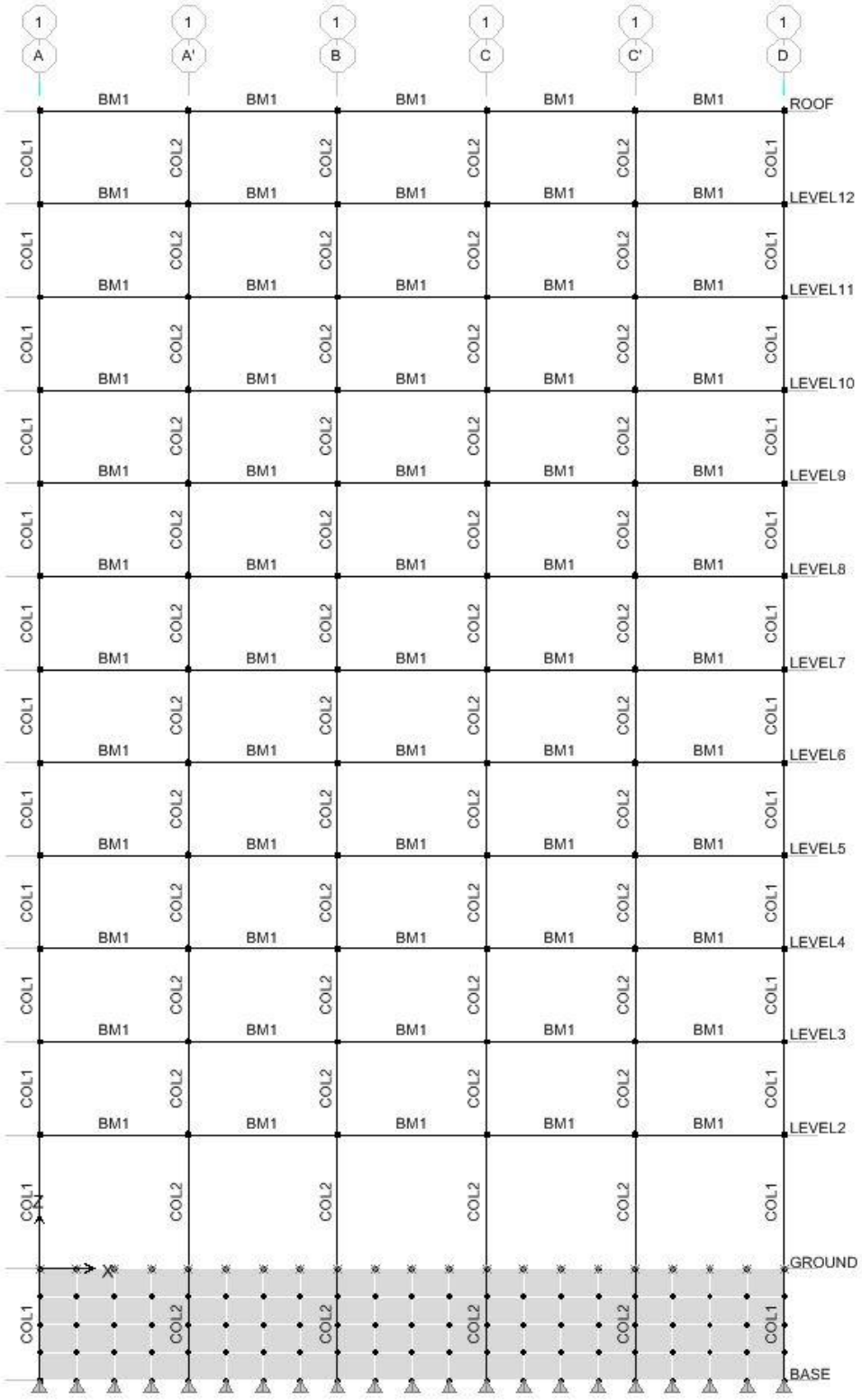

Figure 2.7: ETABS elevation of Gridlines 1 and 8

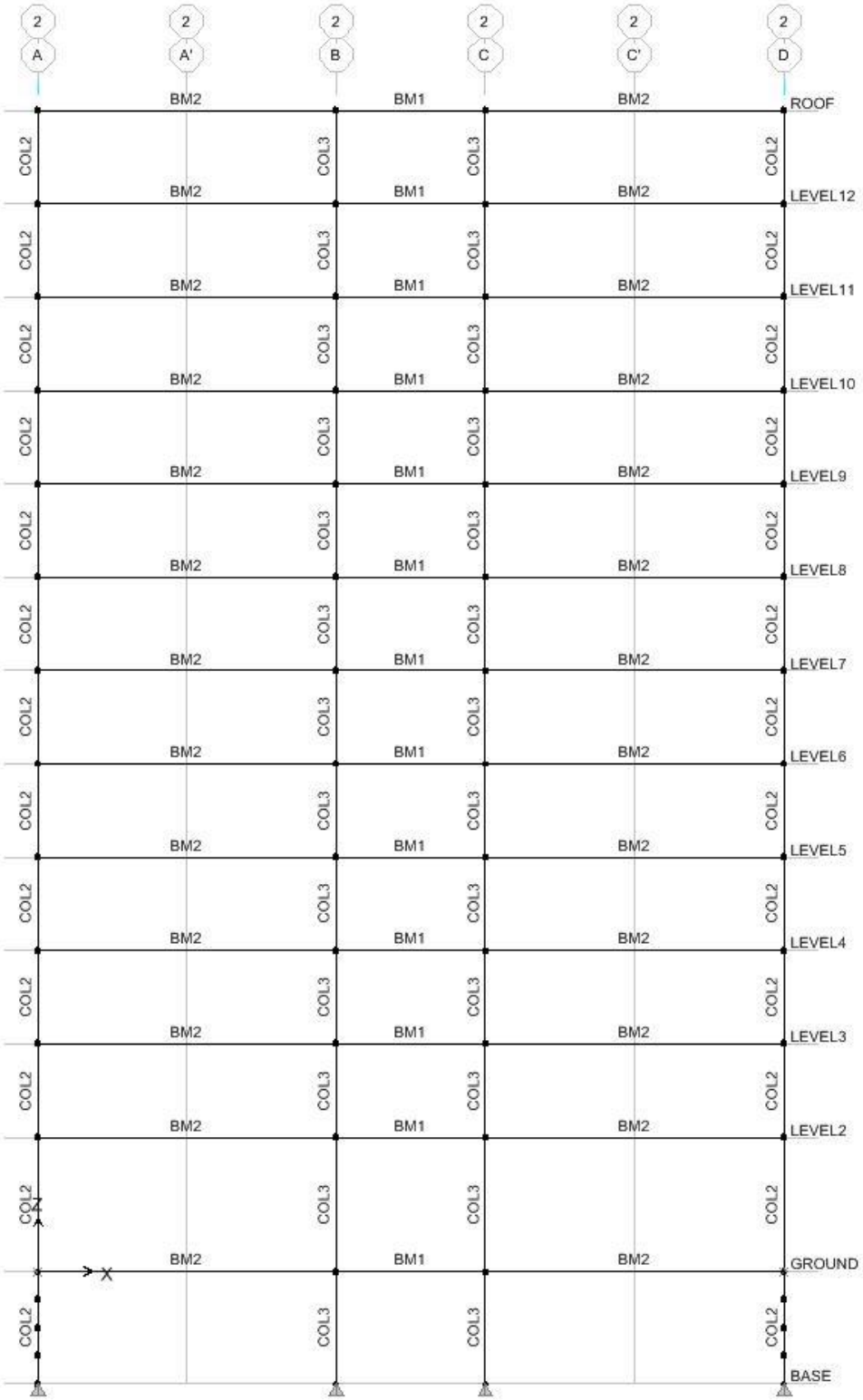

Figure 2.8: ETABS elevation of Gridlines 2 and 7

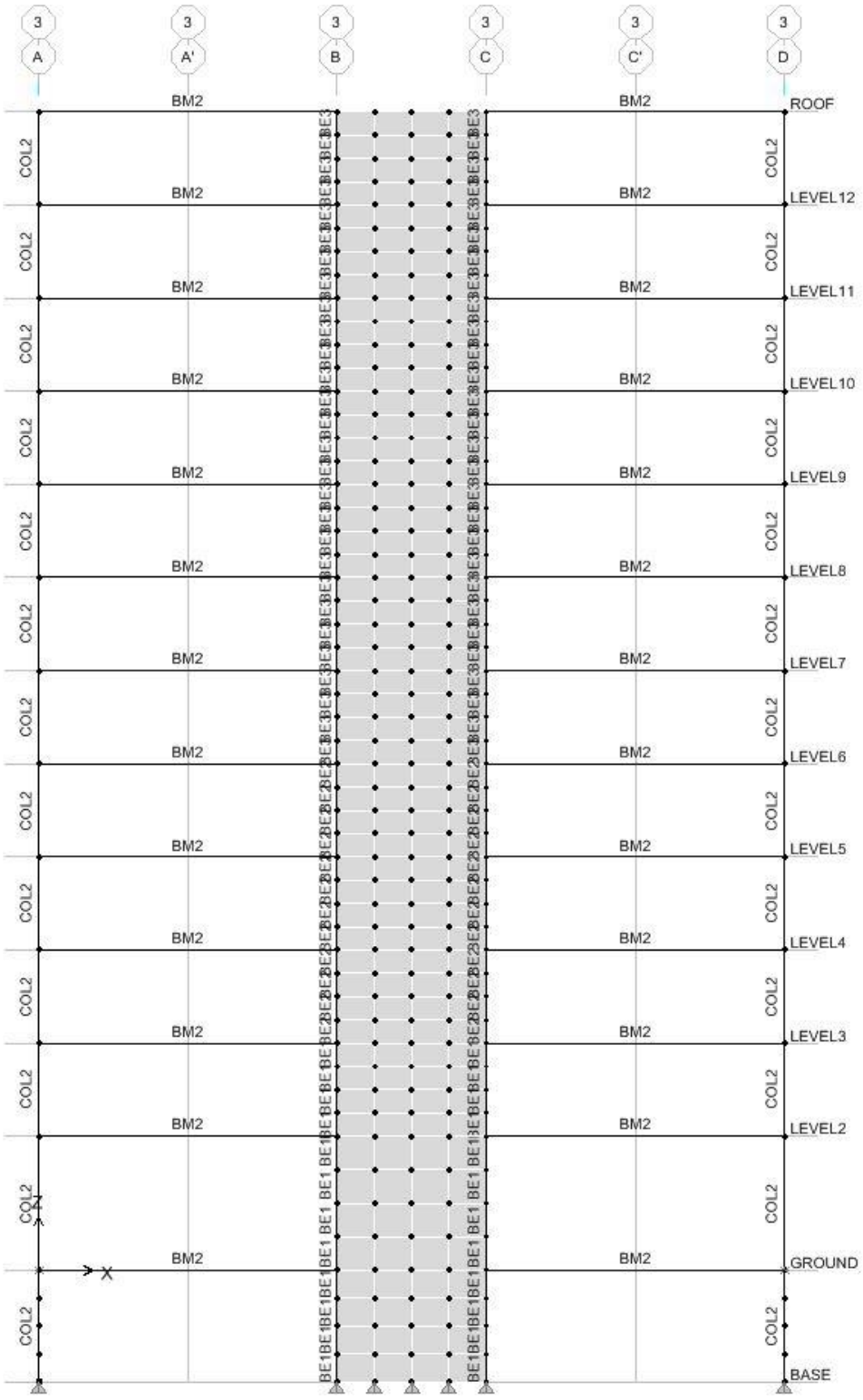

Figure 2.9: ETABS elevation of Gridlines 3 through 6

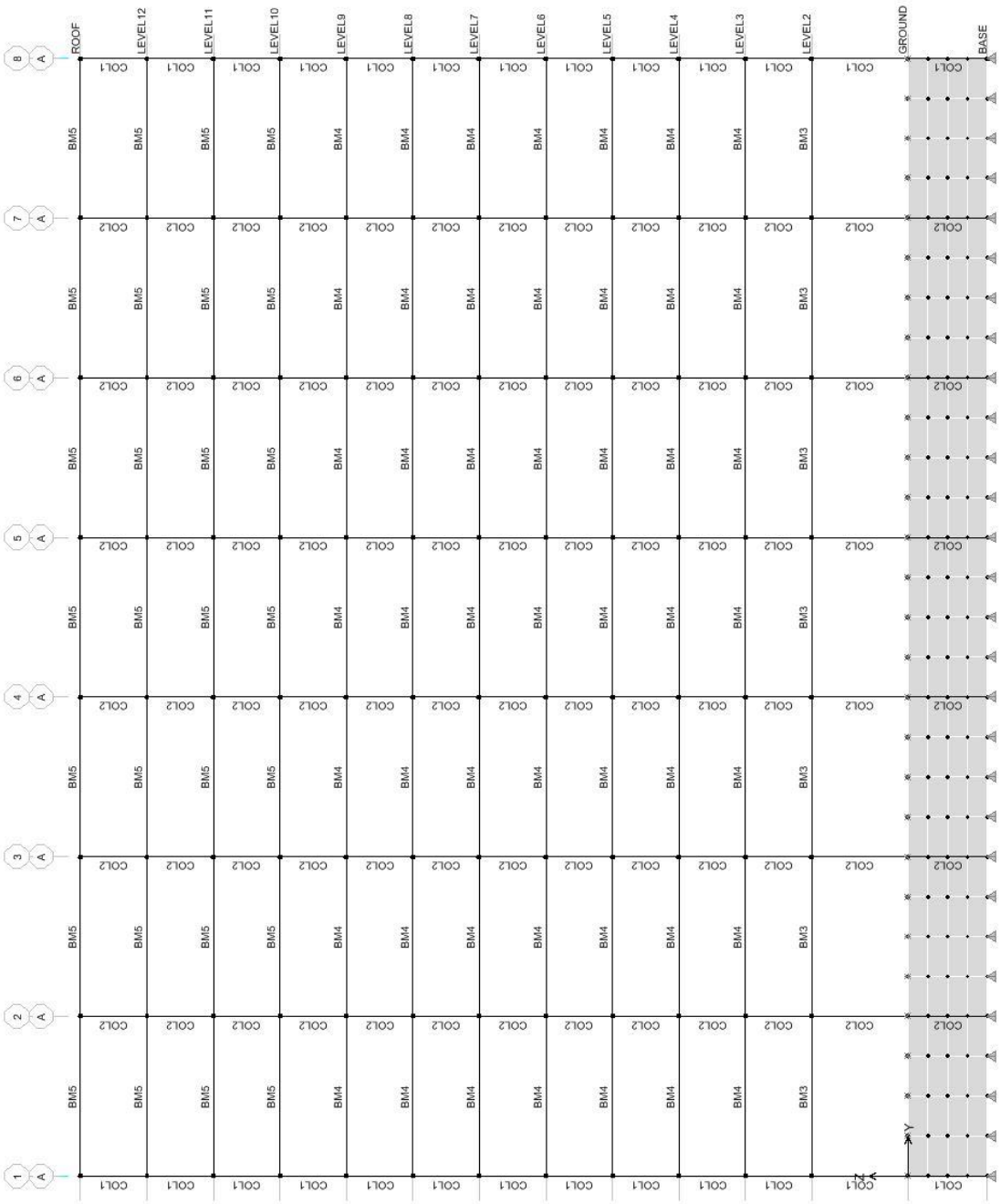

Figure 2.10: ETABS elevation of Gridlines A and D; Gridlines B and C are similar

In order to assign the cross-section parameters to members, the type of finite modeling element must be chosen. In ETABS there are two main categories of member types: frame sections and wall/slab/deck sections. Frame sections are line objects and wall/slab/deck sections are area objects that can be modeled as shell-, membrane-, or plate-type elements, chosen depending on the intended element behavior.

To model the basement walls and shear wall panels, wall sections are defined using the shell-type element with 12 inches of membrane thickness and 12 inches of bending thickness. This allows the full wall thickness to be considered in both in-plane and out-of-plane stiffness, as opposed to a membrane element which only accounts for the in-plane stiffness or a plate element with only out-of-plane stiffness [7]. All wall members were drawn separately for each story and in each bay using wall sections. A wall section is used instead of a frame section so that a mesh of size 4 x 4 can be applied to each area and a direct comparison can be made with Barbosa's SAP model, which also used shell elements with 4 x 4 meshes. A disadvantage of using the wall section in ETABS is that, as noted earlier, the reinforcing steel cannot be specified. Additionally, the shear wall panels cannot be modeled directly with the boundary elements when using a wall section. Thus, the wall boundary elements are modeled as frame sections and drawn as separate members for each story. To be consistent with the meshes of the wall panels, the boundary element objects are divided into 4 lines per story. This meshing and division of lines, shown in Figure 2.9, provides more accurate results by helping to realistically redistribute loads. As is done in the SAP2000 model by Barbosa, all walls and boundary elements are pinned at their base and horizontal displacements perpendicular to the basement walls at ground level are restrained.

The columns and beams are modeled as frame sections and were again drawn in segments for each story/ bay. The columns are pinned at the base and the longitudinal reinforcing is specified as previously described. The beams were assigned rigid-end offsets of half the column width (15”) at each end with a rigid zone factor of 0.5 to achieve a 50% rigid joint fixity. To create the correct beam longitudinal reinforcing layout, custom sections were created with the Section Designer tool in ETABS. A main advantage of the Section Designer is its ability to analyze the custom section properties, including moment-curvature relationships and axial-moment interaction diagrams [8], which can then be verified by the user. For simplicity and because it is a tedious and time-consuming process, the column sections were not created with the Section Designer. This is acceptable because the proper reinforcing layout is achieved with the regular section definition options. However, certain properties, such as moment-curvature relationships and axial-moment interaction diagrams, for frame objects not defined using the Section Designer cannot be seen and thus cannot be user-verified prior to performing analyses.

To model the floor slabs a wall/slab/deck section was defined using a shell element with 8 inches of both membrane thickness and bending thickness. The elevator openings shown in Figure 2.1 are also included in the model. An automatic mesh is applied to the floors by the program, but the user specifies where the mesh occurs. The options chosen are to include an Auto Mesh at: beams and meshing lines, wall and ramp edges, and visible grids. Rigid diaphragms are assigned at each level and the centers of mass and rigidity are automatically calculated by the program. The diaphragm extents created by the program are shown in Figure 2.11.

As Barbosa had done, a second model was created in ETABS with cracked section properties. For direct comparison purposes, the gross cross-section property modifiers Barbosa applied were assigned to each main member of the model, with full axial and shear stiffnesses maintained. Thus, the moment of inertia modifier for both local axes - bending about the strong axis and the weak axis of the member - is assigned as 0.50 for walls, 0.70 for boundary elements and columns, and 0.35 for beams. The slabs and basement walls are considered to be uncracked and no modifiers are applied, since the slabs are considered to be post-tensioned and rigid and the basement walls are expected to remain elastic.

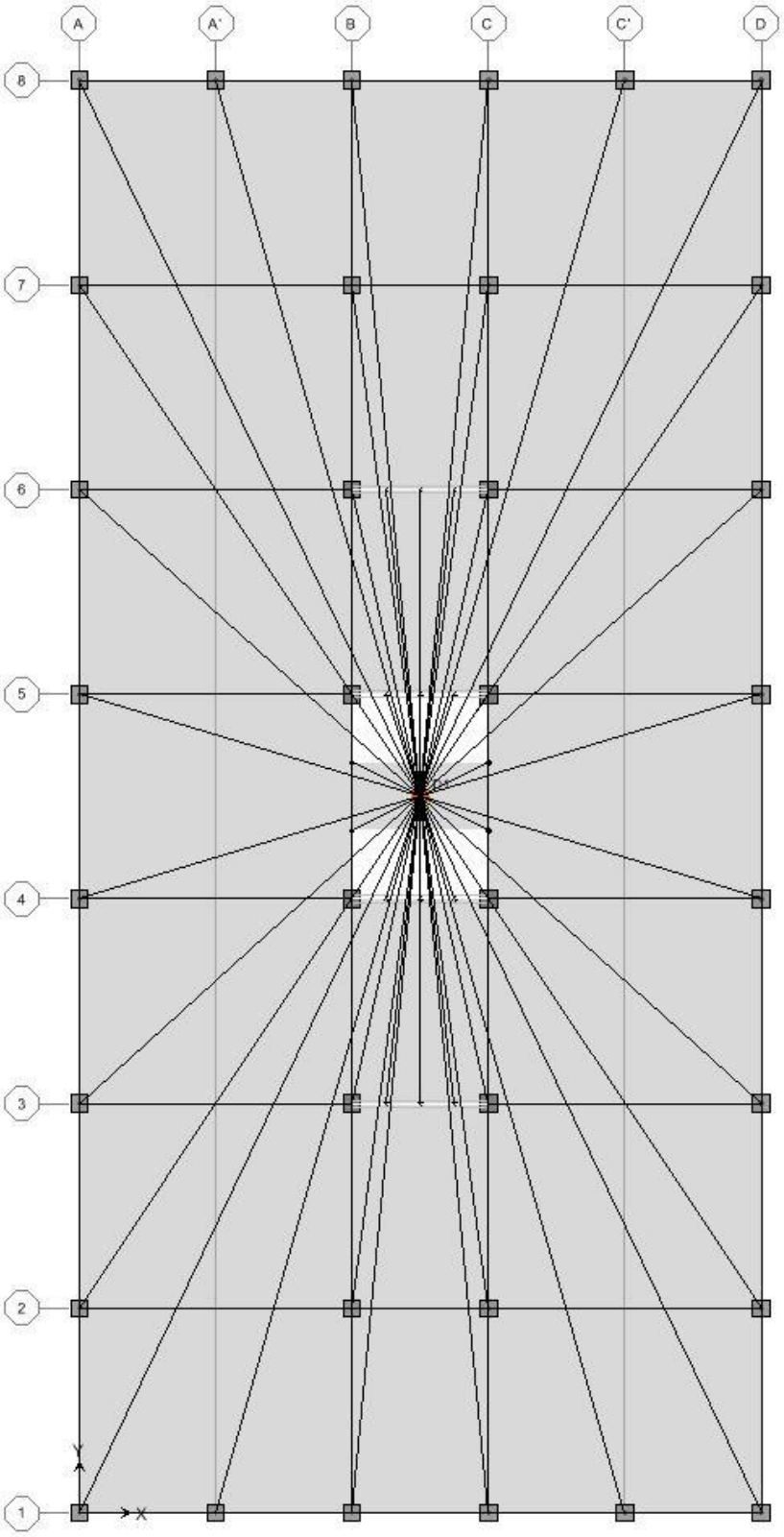

Figure 2.11: ETABS rigid diaphragm extents

2.2.3 Comparison of Preliminary ETABS Model to Barbosa's Model

Eigenvector analysis is performed to calculate the modal properties for the ETABS and SAP2000 uncracked and cracked models. Table 2.2 and Table 2.3 provide natural period comparisons of the uncracked and cracked models, respectively.

Table 2.2: Comparison of first 9 natural periods of uncracked models

Mode	Description	Period, T (sec)		T_{ETABS}/T_{SAP}	
		Barbosa's SAP2000	ETABS	Ratio	Ratio^2
1	1st mode N-S	1.49	**1.63**	1.09	1.20
2	1st mode E-W	1.25	**1.26**	1.01	1.01
3	1st mode Torsion	1.10	**1.24**	1.13	1.27
4	2nd mode N-S	0.49	**0.53**	1.10	1.20
5	2nd mode Torsion	0.34	**0.38**	1.11	1.22
6	2nd mode E-W	0.33	**0.31**	0.96	0.92
7	3rd mode N-S	0.28	**0.31**	1.10	1.21
8	4th mode N-S	0.19	**0.21**	1.10	1.21
9	3rd mode Torsion	0.18	**0.20**	1.09	1.18

Table 2.3: Comparison of first 9 natural periods of cracked models

Mode	Description	Period, T (sec)		T_{ETABS}/T_{SAP}	
		Barbosa's SAP2000	ETABS	Ratio	Ratio^2
1	1st mode N-S	2.20	**2.25**	1.02	1.05
2	1st mode Torsion*	1.57	**1.62**	1.03	1.07
3	1st mode E-W*	1.69	**1.54**	0.91	0.83
4	2nd mode N-S	0.71	**0.73**	1.02	1.05
5	2nd mode Torsion	0.48	**0.48**	1.00	1.01
6	3rd mode N-S	0.41	**0.42**	1.01	1.03
7	2nd mode E-W	0.41	**0.36**	0.88	0.77
8	4th mode N-S	0.27	**0.28**	1.02	1.05
9	3rd mode Torsion	0.25	**0.24**	0.96	0.93
* Order shown is for ETABS model					

Although the structure has 12 dominant natural modes, the higher modes are not shown in the tables above because the higher mode shapes for the SAP2000 and ETABS models are different and the periods cannot be compared. While there are many similarities between the ETABS model and Barbosa's SAP2000 model, there are also a few key differences that affect the modal properties.

One difference is that Barbosa modeled T-beams instead of slabs, which are used in the ETABS model. Explicitly modeling the slab increases the stiffness of each floor, and thus increases the stiffness of the entire structure. In addition, rigid diaphragms are assigned directly to the slab in ETABS where SAP2000 defines diaphragms based on constraints assigned to user-selected points. The modeling of the slabs may contribute to the difference in the order of mode shapes due to how the programs determine the load path and thus mass distribution. This effect becomes amplified when comparing the cracked models, where the second mode is the first mode in the E-W direction for the SAP2000 model but the first torsional mode has the second longest period in the ETABS model.

The way that mass is defined and distributed throughout the structure is another source of difference between the dynamic characteristics. For Barbosa's SAP2000 model, the materials were assigned such that all elements had zero mass. The total mass and mass moments of inertia for the structure were calculated by hand and input directly at the diaphragm's center of mass for each level so that the slab weight could be accounted for. To determine if the total weights of the models were similar, the default concrete weight per unit volume and mass per unit volume was used in ETABS to automatically calculate the mass based solely on the elements modeled. When the dynamic eigenvector

analysis is performed, the program determines and lumps the masses and mass moments of inertia at the diaphragm centers of mass for each floor. Using the elements' weights to determine the mass resulted in a total mass that was about 2% larger than the mass defined in SAP2000.

Since the periods for both the uncracked and cracked models are typically greater for the ETABS model than the SAP2000 model, the difference in mass has a greater affect than the difference in stiffness due to modeling of the slab versus modeling the effective slab width with T-beams. Additionally, the two different programs use slightly different algorithms and assumptions when computing the modal properties, so even a model that is exactly the same would have slightly different natural periods calculated by each program. Thus, despite the differences in modeling methods and analysis techniques the programs use, the dynamic characteristics of the preliminary ETABS model agree well with Barbosa's SAP2000 model and the preliminary model is deemed sufficient to serve as a basis for future models used in this thesis.

2.3 Second Preliminary ETABS Model

In order to model nonlinearity, ETABS Nonlinear only allows discrete plastic hinges to be modeled in frame elements only. Thus, the first preliminary model discussed in Section 2.2 does not allow for nonlinearity to be modeled in the shear walls because they are area shell elements. Since the discrepancy would be very large to not include nonlinearity in the walls, the first preliminary model was modified to use frame elements for the shear walls. Basement walls were still modeled as area objects/ shells since they are expected to remain elastic and the nonlinear properties are not needed. In this section,

the second preliminary ETABS model details are discussed followed by a comparison of the dynamic characteristics to the first preliminary model.

2.3.1 Modeling of Shear Walls as Frame Elements

To adequately model the shear walls, one vertical frame element was drawn down the centerline of the wall and is connected to the rest of the structure with “rigid” frame elements at each floor, shown in Figure 2.12. The vertical frame element must include both the wall panel and the boundary elements, so the ETABS Section Designer tool was utilized to create the custom cross-section as shown in Figure 2.13. For simplicity, the steel reinforcing bars are not included in this model.

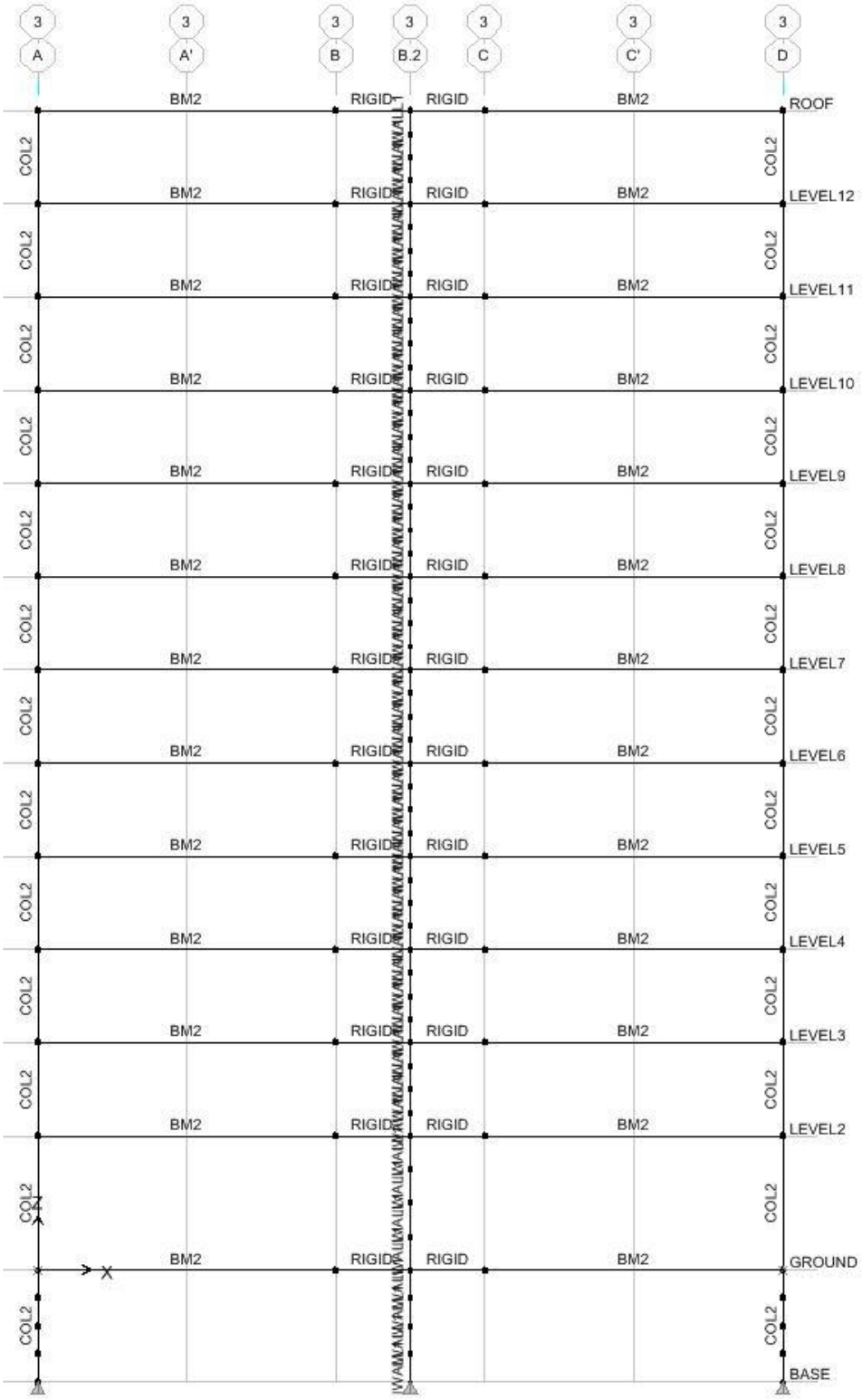

Figure 2.12: ETABS elevation of Gridlines 3 through 6 with walls modeled by frame elements

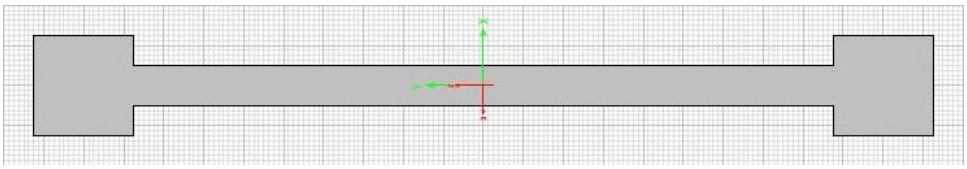

Figure 2.13: Cross-section of shear wall using Section Designer tool

To model the “rigid” frame element, a 12-inch wide concrete beam frame element was defined with the same 24-inch depth as the adjacent beams (BM2). The section properties were modified with a multiplier of 1,000,000 to make the member effectively rigid. Since the “rigid” beam overlaps the wall frame section, the mass and weight of the “rigid” element were set to zero so that they would not be counted twice. Rigid end offsets of 15 inches were applied to the ends that intersect the boundary elements of the walls. Unlike the beam-column connections of the rest of the structure, these end offsets were assigned a rigid zone factor of 1.0 to make the connection to the boundary elements completely fixed. Figure 2.14 shows the extrusions of these defined members to display their actual dimensions and geometry.

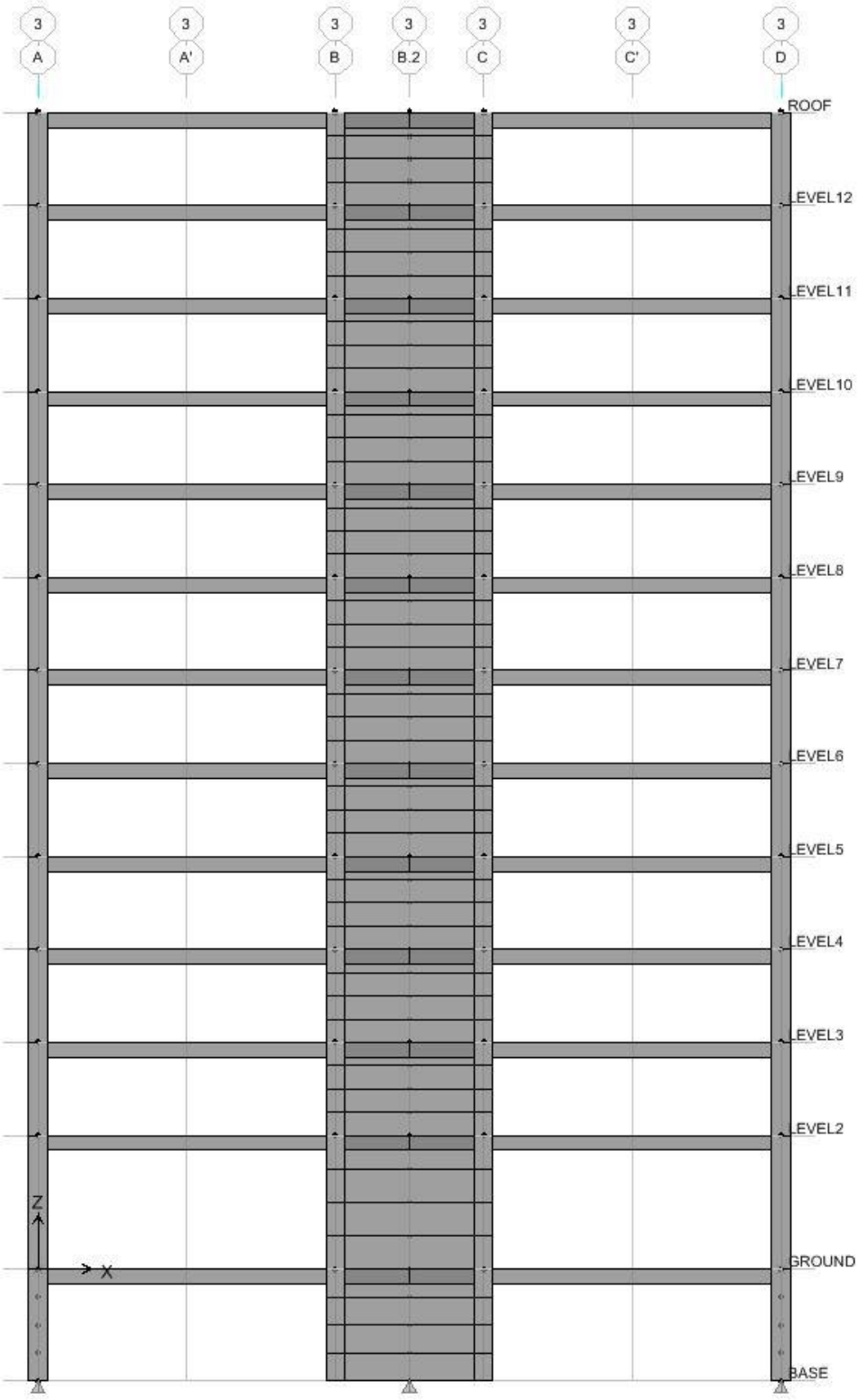

Figure 2.14: ETABS elevation of Gridlines 3 through 6, extruded members

2.3.2 Dynamic Characteristics Comparison

A comparison of the elastic dynamic characteristics was again made to verify that the second preliminary model is sufficiently close to Barbosa's model. Other than how the interior shear walls were modeled, the rest of the model parameters remained exactly the same as in the first preliminary model. Eigenvector analysis was done on the second preliminary model using uncracked section properties and the same cracked section properties as previously discussed. The resulting natural periods are summarized in Table 2.4 and Table 2.5.

Table 2.4: Comparison of first 9 natural periods of uncracked models: shell v. frame

Mode	Description	Period, T (sec)			$T_{ETABS\text{-}shell}/T_{SAP}$		$T_{ETABS\text{-}frame}/T_{SAP}$	
		Barbosa's SAP2000	ETABS - shell	ETABS - frame	Ratio	$Ratio^2$	Ratio	$Ratio^2$
1	1st mode N-S	1.49	1.63	**1.62**	1.09	1.20	1.09	1.20
2	1st mode E-W	1.25	1.26	**1.32**	1.01	1.01	1.05	1.11
3	1st mode Torsion	1.10	1.24	**1.26**	1.13	1.27	1.15	1.32
4	2nd mode N-S	0.49	0.53	**0.53**	1.10	1.20	1.09	1.20
5	2nd mode Torsion	0.34	0.38	**0.39**	1.11	1.22	1.13	1.28
6	2nd mode E-W	0.33	0.31	**0.33**	0.96	0.92	1.01	1.02
7	3rd mode N-S	0.28	0.31	**0.31**	1.10	1.21	1.10	1.21
8	4th mode N-S	0.19	0.21	**0.21**	1.10	1.21	1.10	1.20
9	3rd mode Torsion	0.18	0.20	**0.20**	1.09	1.18	1.11	1.24

Table 2.5: Comparison of first 9 natural periods of cracked models: shell v. frame

Mode	Description	Period, T (sec)			$T_{ETABS-shell}/T_{SAP}$		$T_{ETABS-frame}/T_{SAP}$	
		Barbosa's SAP2000	ETABS - shell	ETABS - frame	Ratio	$Ratio^2$	Ratio	$Ratio^2$
1	1st mode N-S	2.20	2.25	**2.29**	1.02	1.05	1.04	1.09
2	1st mode Torsion*	1.57	1.62	**1.72**	1.03	1.07	1.09	1.19
3	1st mode E-W*	1.69	1.54	**1.70**	0.91	0.83	1.00	1.01
4	2nd mode N-S	0.71	0.73	**0.75**	1.02	1.05	1.04	1.09
5	2nd mode Torsion	0.48	0.48	**0.52**	1.00	1.01	1.08	1.16
6	3rd mode N-S	0.41	0.42	**0.43**	1.01	1.03	1.04	1.09
7	2nd mode E-W	0.41	0.36	**0.43**	0.88	0.77	1.05	1.10
8	4th mode N-S	0.27	0.28	**0.29**	1.02	1.05	1.05	1.10
9	3rd mode Torsion	0.25	0.24	**0.27**	0.96	0.93	1.07	1.14
* Order shown is for ETABS models								

For both the uncracked and cracked models, modeling the walls as frame elements instead of shell elements resulted in very similar or slightly longer periods for all modes. While some natural periods, such as that of the first North-South mode, got further from those of Barbosa's SAP2000 model, others were closer to Barbosa's model. The first East-West mode period, in the direction of the shear walls, deviated further from the SAP2000 model for uncracked section properties, but was almost identical for the cracked section properties. In general, the cracked section model tended to be more accurate than the uncracked model. Since the results of modeling the shear walls with frame elements are all within 10% of Barbosa's model for the cracked section properties, this second preliminary model is deemed to be sufficient as the new basis for a model that must account for cracked section properties and material nonlinearity in the structure.

3 FINAL MODELS WITH NONLINEARITY

Now that an appropriate model which is able to include material nonlinearity has been created, a new and final ETABS model was made with expected material properties and revised cracked stiffnesses. In addition to the change in material and cracked section parameters, nonlinear plastic hinges were added to the model. Another model with these final properties was then created such that one of the shear walls is moved to induce torsional response. Due to limitations in the ETABS Nonlinear software with performing nonlinear dynamic analyses, the final ETABS model was exported to SAP2000. This chapter describes the updated modeling parameters and nonlinear hinge details that are implemented in the final ETABS and SAP2000 models created by the author of this thesis.

3.1 Final ETABS Model

3.1.1 Revised Material and Section Parameters

The ETABS model described in Section 2.3 was updated to reflect the material properties that are expected to be achieved during seismic loading. The nominal compressive strength of unconfined concrete is assumed to be 6 ksi, and the expected compressive strength is taken as 6.8 ksi. The corresponding modulus of elasticity assigned to the concrete elements modeled in ETABS is E_c = 4700.34 ksi. The yield strength of all reinforcing steel is 60 ksi, so 69 ksi is taken as the expected yield strength. These expected material properties are used to calculate nonlinear properties of the reinforced concrete sections, which will be discussed in more complete detail later.

The stiffness modifiers used to model cracked properties in the preliminary models were based on the values presented in tables from ACI 318/ FEMA 356. For this final model, revised cracked section properties, chosen based on experience by Professor José Restrepo, are used in an attempt to better capture the response of an actual reinforced concrete building. The cracked stiffness modifier for all beams is taken to be 0.30. For the shear walls, including boundary elements, 0.25 of the gross section properties is adopted. The cracked stiffness modifiers for the columns are determined based on gravity analysis: 0.50, 0.40, and 0.25 for axial loads greater than 30%, between 20% and 30%, and less than 20% of $A_g f'_c$, respectively. The axial load at ground level due to full, unscaled dead loads is determined for each type of column (COL1, COL2, and COL3). Based on the gravity analysis, the columns are further classified based on the total axial load they carry. For the COL2 sections, three significantly different axial loads resulted: columns on Gridlines A and D (COL2AD), columns on Gridlines 1 and 8 at lines B and C (COL2in18), and columns on Gridlines 1 and 8 at lines B' and C' (COL2out18). A summary of the axial load and corresponding cracked section stiffness modifiers adopted is presented in Table 3.1.

Table 3.1: Column gravity analysis results and adopted stiffness modifiers

Column	Axial Load, P (kips)	$P/(A_g f'_c)$	Stiffness Modifier
COL1	-604	11%	0.25
COL2AD	-1237	23%	0.40
COL2in18	-879	16%	0.25
COL2out18	-718	13%	0.25
COL3	-1691	31%	0.50

3.1.2 Creation of Asymmetric Model

With the new material and cracked section properties determined, another final model was created such that the shear wall on Gridline 3 was moved to Gridline 7 to investigate the effects of torsion due to an asymmetric lateral force-resisting system. Additionally, the column (COL3) and beam (BM1) sections originally assigned between Gridlines B and C on Gridline 7 were added to gridline 3 in place of the wall. Since the tributary areas for these beam and column sections is the same for Gridlines 3 and 7, the gravity load demand is very similar and the same beam and column sections were used. As a check, another gravity load analysis was performed and indeed the axial loads on the columns were almost the same as the symmetric model, so the cracked section properties did not change.

In order to ensure that the steel reinforcing of the shear walls was still adequate, the equivalent lateral force procedure from ASCE 7-10 was used to check the base shear forces in the walls. After applying the equivalent lateral loads with 5% eccentricity to account for accidental torsion, the resulting drifts were checked to see if the asymmetric placement of the walls created a Torsional Irregularity. Upon determining that the torsional moments did not need amplification because there was in fact no torsional irregularity per code (Table 12.3-1 in ASCE 7), the shear force demands found at the base of the wall on Gridline 4 were still greater than the demand on the walls of the symmetric model. However, the increase in demand was verified to be less than the capacity of the wall, so the reinforcement did not need to be redesigned. For illustrative purposes, Figure 3.1 shows the difference between a typical floor plan of the symmetric and asymmetric ETABS models.

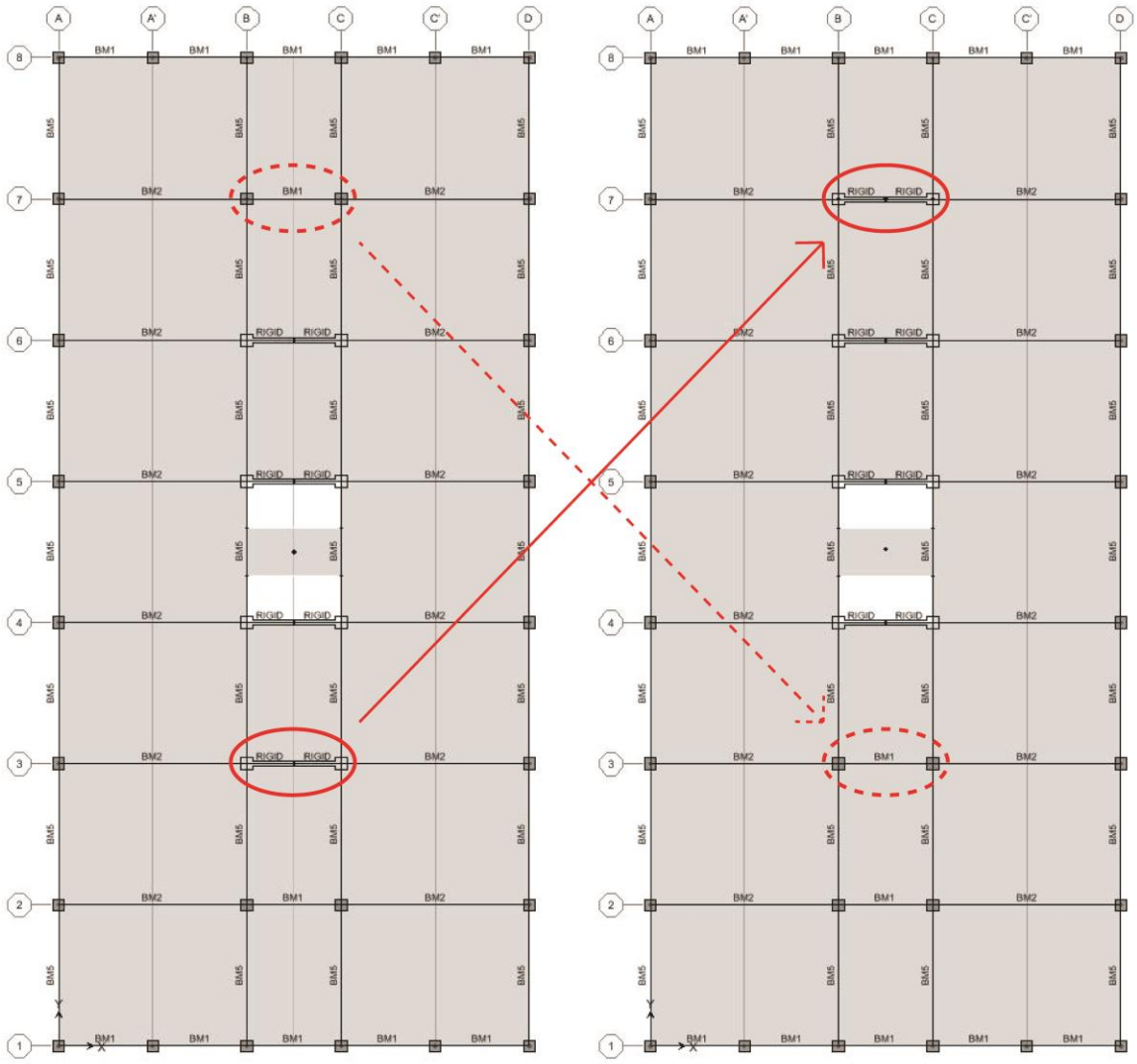

(a) **(b)**

Figure 3.1: Typical floor plans for (a) symmetric model and (b) asymmetric model

In the symmetric model, both the center of mass (CM) and center of rigidity (CR) of each diaphragm were located at the geometrical center of the floor plan, such that the coordinated in the global model axes were $X_{CM} = X_{CR} = 600$ inches and $Y_{CM} = Y_{CR} = 1260$ inches. However, after creating the asymmetric wall placement, the center of mass and center of rigidity moved away from the geometrical center of the floor plan and towards the walls in the global Y-direction. Both centers remained in the same X-

direction location of 600 inches. The center of mass and center of rigidity Y-coordinates, along with the resulting eccentricity, determined at each floor above grade are provided in Table 3.2. While the center of mass of each diaphragm only moved less than 0.5% closer to the southern end (Gridline 8) of the structure, the resulting eccentricities of the center of rigidity for each diaphragm ranged from about 3% at the roof to about 12% at the second floor.

Table 3.2: Center of mass, center of rigidity, and eccentricity for asymmetric model

Story	Y_{CM} (in.)	Y_{CR} (in.)	Eccentricity (%)
Roof	1261.4	1339.0	3.14
Floor 12	1267.9	1356.6	3.83
Floor 11	1267.9	1374.8	4.55
Floor 10	1267.9	1392.2	5.24
Floor 9	1267.9	1409.2	5.92
Floor 8	1267.9	1426.6	6.61
Floor 7	1267.9	1445.2	7.35
Floor 6	1267.9	1465.6	8.16
Floor 5	1267.9	1487.9	9.04
Floor 4	1267.9	1512.4	10.01
Floor 3	1267.9	1538.7	11.06
Floor 2	1270.4	1565.8	12.13

3.1.3 Dynamic Characteristics

The twelve dominant natural periods and the associated modal mass participation ratios based on elastic eigenvalue analysis of the final ETABS symmetric and asymmetric models are summarized in Table 3.3 and Table 3.4, respectively. For both models, the first mode is described by the first North-South mode. The natural period remains unchanged, since moving the walls only affects the stiffness in the East-West direction. The rest of the asymmetric model modes are combinations of significant torsional

response with North-South, East-West, or both orthogonal direction modes, as shown by the mass participation ratios.

Table 3.3: Dynamic characteristics of final ETABS symmetric model

Mode	Description	Period, T (sec)	Mass Participation Ratios (%)			
			N-S	Cumulative N-S	E-W	Cumulative E-W
1	1st mode N-S	2.62	86.98	86.98	0.00	0.00
2	1st mode Torsion	2.01	0.00	86.98	0.00	0.00
3	1st mode E-W	1.99	0.00	86.98	76.42	76.42
4	2nd mode N-S	0.84	8.57	95.55	0.00	76.42
5	2nd mode Torsion	0.61	0.00	95.55	0.00	76.42
6	2nd mode E-W	0.52	0.00	95.55	13.99	90.41
7	3rd mode E-W	0.23	0.00	95.55	5.23	95.64
8	4th mode E-W	0.13	0.00	95.55	2.32	97.96
9	5th mode E-W	0.08	0.00	95.55	1.08	99.04
10	6th mode E-W	0.06	0.00	95.55	0.51	99.55
11	7th mode E-W	0.05	0.00	95.55	0.29	99.85
12	8th mode E-W	0.03	0.00	95.55	0.15	100.00

Table 3.4: Dynamic characteristics of final ETABS asymmetric model

Mode	Description	Period, T (sec)	Mass Participation Ratios (%)			
			N-S	Cumulative N-S	E-W	Cumulative E-W
1	1st mode N-S	2.62	86.98	86.98	0.00	0.00
2	Torsional mode	2.13	0.00	86.98	46.11	46.11
3	" "	1.85	0.00	86.98	30.83	76.93
4	" "	0.64	0.00	86.98	3.85	80.79
5	" "	0.49	0.00	86.98	9.84	90.62
6	" "	0.40	6.79	93.77	0.00	90.62
7	" "	0.34	0.00	93.77	1.09	91.71
8	" "	0.21	0.00	93.77	4.48	96.19
9	" "	0.16	0.21	93.98	0.06	96.25
10	" "	0.12	0.17	94.15	1.52	97.78
11	" "	0.10	0.54	94.69	0.98	98.75
12	" "	0.06	0.22	94.91	1.16	99.91

The last change made to both the symmetric and asymmetric models is the modeling of material nonlinearity using nonlinear plastic hinges. Discrete plastic hinges are assigned at the ends of all beams at column faces, at the ground level of all columns, and at ground level for the four shear walls. The properties of the hinges modeled are discussed in detail in Section 3.3. It should be noted that the assigned plastic hinges do not affect the natural periods of the structure, since they are not activated during elastic analyses.

3.2 Final Model Exported to SAP2000

As referred to earlier, the version of ETABS Nonlinear used to model the structure does not account for material nonlinearity modeled by plastic hinges when performing nonlinear dynamic time-history analyses; the only nonlinearity that can be accounted for is geometric nonlinearity (e.g. P-delta effects or large displacements). Thus, the final model was exported from ETABS and imported into SAP2000 Ultimate version 15.1.0 to perform all nonlinear analyses for this thesis. The adjustments made to the model after it is imported into SAP2000 are described in this section along with the corresponding dynamic characteristics.

3.2.1 Adjustments Made to SAP2000 Model

When a model is exported from ETABS and imported into SAP2000, the assigned properties, such as rigid end offsets, assigned stiffness property modifiers, and hinge locations, must be manually defined again in the SAP2000 model. In addition to re-assigning the properties that did not get carried over during the export, the slab was removed from the model and the beams were re-modeled as T-beams using the effective slab widths defined in Section 8.12 of ACI 318-08. The dimensions used for the T-beam

flanges are summarized in Table 3.5. The reason for removing the slab in the SAP2000 model is because the geometry of the slab inhibits the beam plastic hinges from behaving as intended during nonlinear analyses. As a result, the slab stiffness is accounted for by the T-beams and the weight is accounted for by scaling the dead load of all members such that the total weight of the building matched that of ETABS. The total mass from all elements assembled at the centers of the diaphragms by ETABS remained unchanged when exported to SAP2000, so the masses assigned did not need to be altered and were used as the mass source for all dynamic analyses.

Table 3.5: Flange widths of T-beams to account for effective slab

Beam Type	Gridlines	b_{eff} (in)
BM1	1 and 8	42.5
	2 and 7	60
BM2	2 to 7	120
BM3, BM4,	A and D	52.5
BM5	B and C	70.5

With the slabs removed, a 12-inch wide by 24-inch deep frame element was added at each floor from the centerline of the walls on Gridlines 4 and 5 to the rigid diaphragm centers where the mass was defined, as shown in Figure 3.2. Since the mass was not physically connected to the rest of the structure without the slab, adding this "link" beam element prevented the model from being ill-conditioned and removed any potential source of numerical instability. The properties of this frame element were not modified other than making the weight and mass zero. The "rigid" element used in modeling the shear walls was assigned a modifier of 100 for all properties, with mass and weight still set to zero. These two beam properties were adjusted as described so that the

natural periods of the SAP model without slabs were as close as possible to those of the ETABS model with slabs.

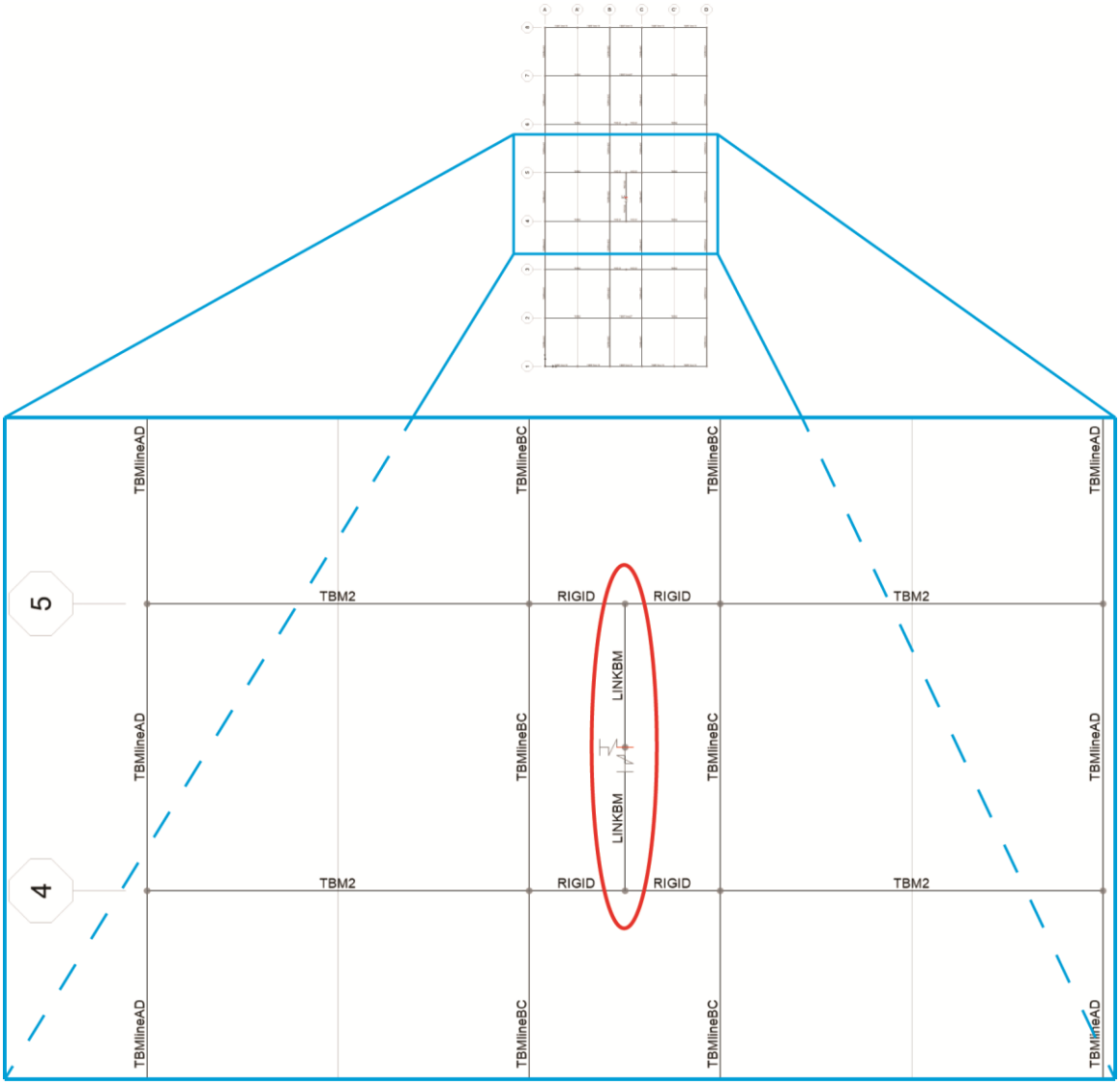

Figure 3.2: Illustration of "link" beam added to typical floor plan of SAP2000 model

Since the model was redone in SAP2000 with different member sections, the asymmetric ETABS model was not exported. Instead, a new SAP2000 model was created based on the T-beam model without slabs that accounted for the asymmetric wall locations. Thus, the shear wall on Gridline 3 was moved to Gridline 7 and the beam and column elements from Gridline 7 were moved to Gridline 3, as discussed in Section

3.1.2. For both the symmetric and asymmetric SAP2000 models, the same material properties and cracked stiffness modifiers for walls, beams, and columns are used as the final ETABS model.

3.2.2 Dynamic Characteristics and Mode Shapes

To verify that the SAP2000 models without slabs were close to those of the ETABS models with slabs, modal analysis was performed. The resulting natural periods and mass participation ratios for the SAP2000 models are presented in Table 3.6 and Table 3.7. Despite modeling T-beams instead of slabs, the mode shapes and the associate periods are very similar to the ETABS model with slabs for both the symmetric and asymmetric SAP2000 models.

The major difference between the symmetric models is that in the ETABS model the second mode was the first torsional mode shape, but in the SAP2000 model the second mode is the first East-West mode shape. In the ETABS model, the 2^{nd} and 3^{rd} mode periods were very close, around 2 seconds each. However, in the SAP2000 model, the 2^{nd} and 3^{rd} mode periods were further apart, but the torsional mode was still about 2 seconds. As with the ETABS model, the East-West modes dominated the higher modes of the symmetric model, but a noticeable difference for the SAP2000 model is that there are even more E-W dominant modes and there is more mass participation in the North-South direction due to torsional effects in the highest three modes. These changes in mode shapes is most likely a result of how the slab is represented in each model in addition to the different parameters that SAP2000 and ETABS use to calculate modal properties. For the asymmetric models, the main difference is that in the higher modes of

the SAP2000 model the North-South direction mass participation is negligible, where it contributed more significantly in the ETABS model.

Table 3.6: Dynamic characteristics of final SAP2000 symmetric model

Mode	Description	Period, T (sec)	Mass Participation Ratios (%)			
			N-S	Cumulative N-S	E-W	Cumulative E-W
1	1st mode N-S	2.62	87.20	87.20	0.00	0.00
2	1st mode E-W	2.11	0.00	87.20	75.76	75.76
3	1st mode Torsion	2.02	0.00	87.20	0.00	75.76
4	2nd mode N-S + T	0.80	7.39	94.59	0.00	75.76
5	2nd mode E-W	0.54	0.00	94.59	14.49	90.25
6	3rd mode E-W	0.23	0.00	94.59	5.34	95.60
7	4th mode E-W	0.13	0.00	94.59	2.35	97.95
8	5th mode E-W	0.08	0.00	94.59	1.09	99.03
9	6th mode E-W	0.06	0.00	94.59	0.51	99.54
10	7th mode E-W + T	0.05	0.17	94.76	0.14	99.68
11	8th mode E-W + T	0.04	0.19	94.95	0.21	99.89
12	9th mode E-W + T	0.03	0.06	95.01	0.11	100.00

Table 3.7: Dynamic characteristics of final SAP2000 asymmetric model

Mode	Description	Period, T (sec)	Mass Participation Ratios (%)			
			N-S	Cumulative N-S	E-W	Cumulative E-W
1	1st mode N-S	2.62	87.21	87.21	0.00	0.00
2	Torsional mode	2.22	0.00	87.21	57.79	57.79
3	" "	1.90	0.00	87.21	18.51	76.30
4	" "	0.66	0.00	87.21	4.83	81.13
5	" "	0.50	0.00	87.21	9.31	90.43
6	" "	0.35	0.00	87.21	1.28	91.71
7	" "	0.22	0.00	87.21	0.03	91.74
8	" "	0.21	0.00	87.21	4.45	96.19
9	" "	0.15	0.00	87.21	0.16	96.35
10	" "	0.12	0.00	87.21	1.95	98.30
11	" "	0.08	0.00	87.21	1.02	99.33
12	" "	0.05	0.00	87.21	0.64	99.97

The first mode shapes of the SAP2000 symmetric and asymmetric models are provided in Figure 3.3 and Figure 3.4, showing the extruded member 3-dimensional view and the wireframe East-West elevation. Figure 3.5 and Figure 3.6 show the second mode shapes. The second mode for the symmetric model is the first East-West mode, so the North-south elevation is shown. For the asymmetric model, the second mode is a combination of the first East-West mode and torsion, so the roof plan view is provided with the 3-dimensional view. The third modes are torsional modes for both symmetric and asymmetric models, which are best shown by the 3-D view and roof plans given in Figure 3.7 and Figure 3.8.

The first three mode shapes are what would be expected for the symmetric structure. Since there are moment frames in the North-South direction, the first mode shape in that direction shows a sway-like displaced shape where the interstory drifts are larger toward the base and gradually decrease up the structure, typical of moment frame lateral systems. The second mode is the first East-West mode, which is also expected for the symmetric structure. This mode shows the influence of shear walls in addition to moment frames, yielding a displaced shape that mostly resembles a cantilever but almost has the appearance of a column in double-bending since the curvature shows signs of reversal towards the roof. The third mode shape is purely the first torsional mode, where the axis of rotation is the center of rigidity/mass and thus the center of the building plan.

The first three mode shapes of the asymmetric building are also what would be expected. The first mode is the same as the symmetric building, since moving the walls does not affect the North-South direction stiffness, as observed with the ETABS model. The second mode is largely influenced by the first East-West mode but the larger

stiffness at the southern end of the building causes smaller displacements, allowing the structure to rotate and exhibit torsional response. The third mode is a torsional mode, but not purely torsional like the third mode of the symmetric building because there is some translation in the E-W direction.

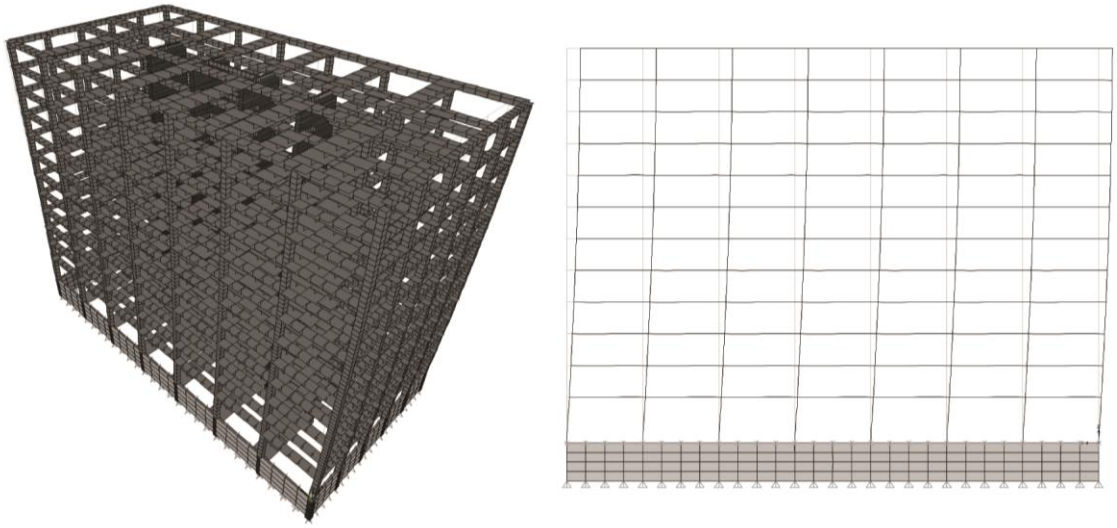

(a) **(b)**

Figure 3.3: (a) 3D view and (b) E-W elevation of first N-S mode ($T_{1,N-S}$ = 2.62 sec); symmetric SAP2000 model

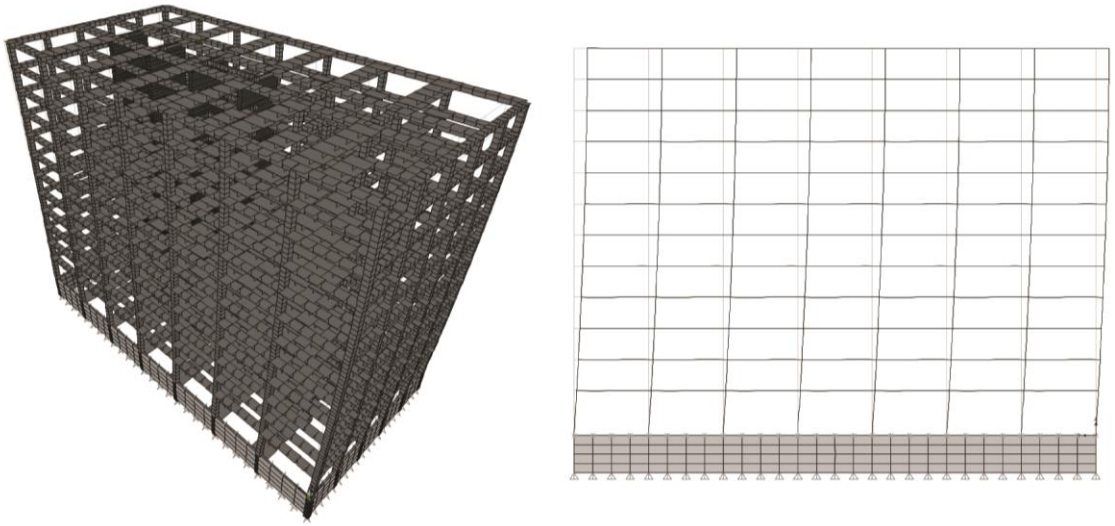

(a) **(b)**

Figure 3.4: (a) 3D view and (b) E-W elevation of first N-S mode ($T_{1,N-S}$ = 2.62 sec); asymmetric SAP2000 model

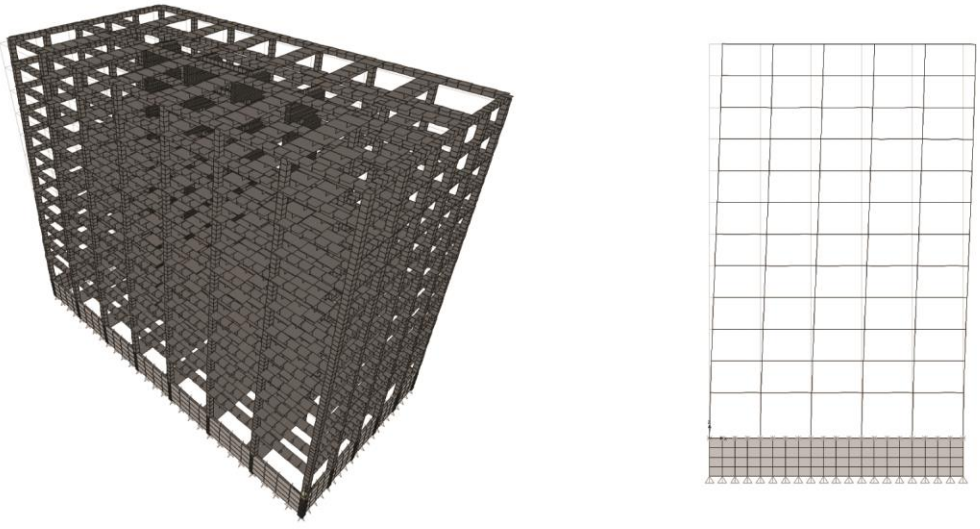

(a) **(b)**

Figure 3.5: (a) 3D view and (b) N-S elevation of first E-W mode ($T_{1,E-W}$ = 2.11 sec); symmetric SAP2000 model

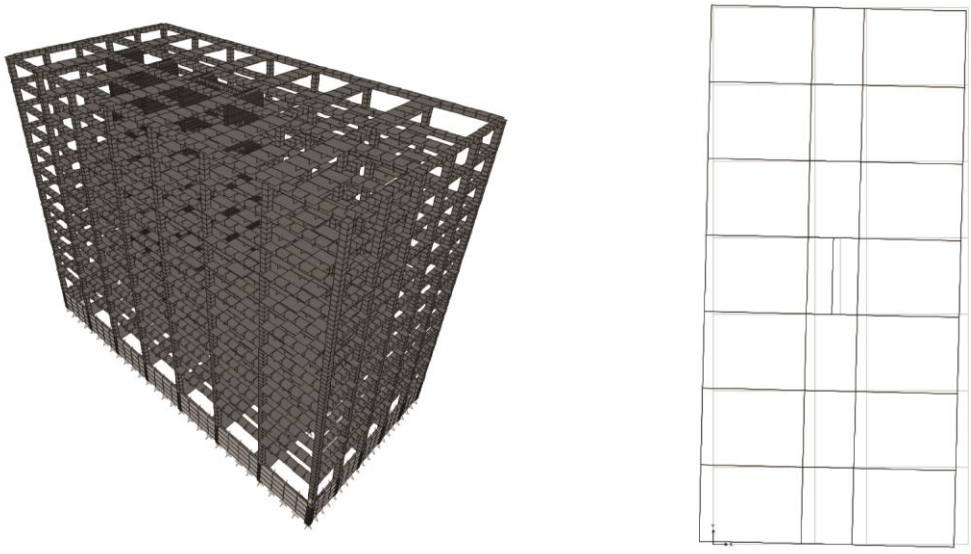

(a) **(b)**

Figure 3.6: (a) 3D view and (b) roof plan view of second mode (T_2 = 2.22 sec); asymmetric SAP2000 model

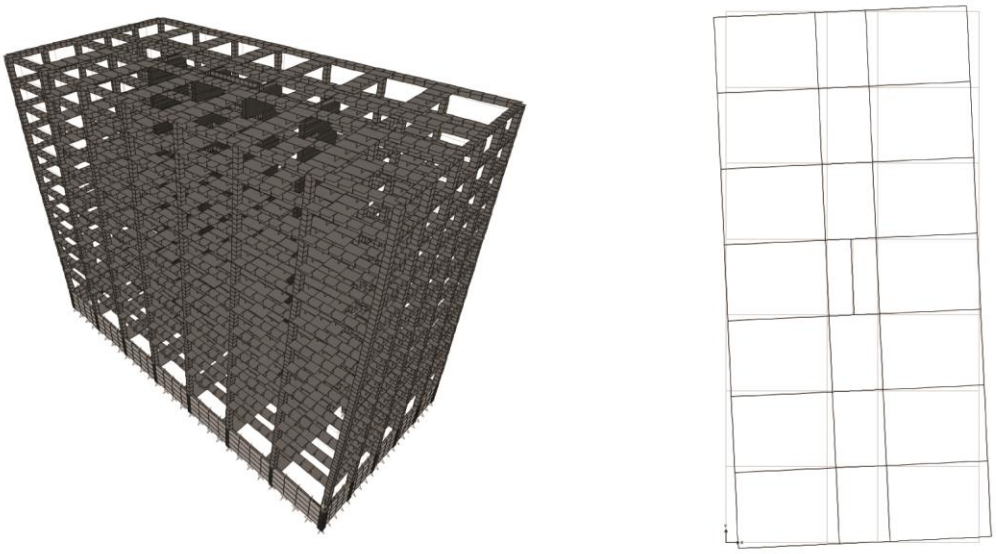

(a) **(b)**

Figure 3.7: (a) 3D view and (b) roof plan view of third mode (T_3 = 2.02 sec); symmetric SAP2000 model

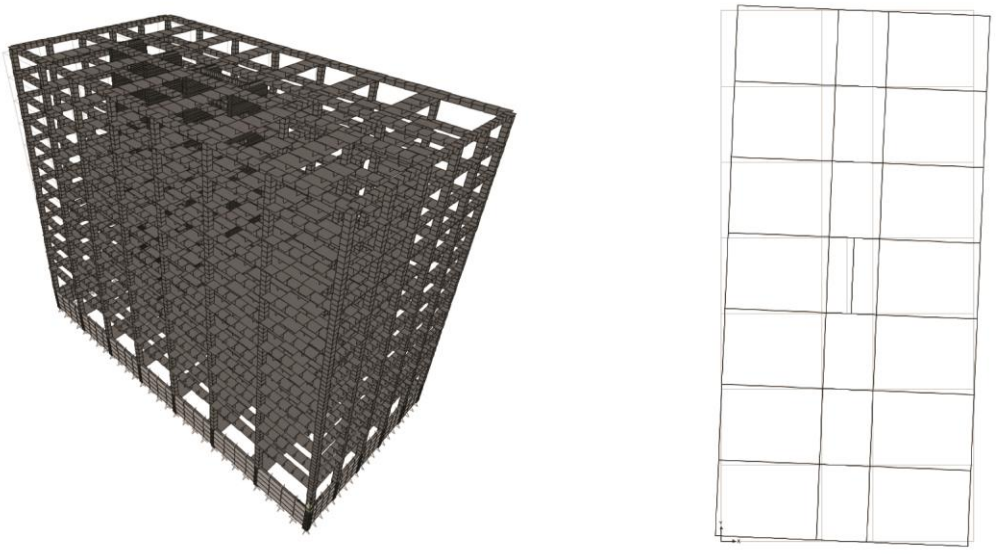

(a) **(b)**

Figure 3.8: (a) 3D view and (b) roof plan view of third mode (T_3 = 1.90 sec); asymmetric SAP2000 model

3.3 Modeling of Nonlinear Plastic Hinges

In this section, the details of how material nonlinearity was accounted for in the ETABS and SAP2000 models are presented. First, the options of modeling nonlinearity and the reason for the chosen method implemented in the final models are discussed. The models used to create nonlinear moment-curvature relationships for the members that were expected to be in the plastic range are presented next. Structural damage limit states typically defined in performance-based design for reinforced concrete structures built in areas of high seismic hazard are described and used to create idealized moment-curvature curves. Finally, the actual properties of the nonlinear plastic hinges used in the structural models are summarized.

3.3.1 Background of Modeling Material Nonlinearity in ETABS

The background of how the version of ETABS Nonlinear used for this thesis allows modeling of material nonlinearity is described in this section, including the relevant limitations and requirements. In SAP2000 and ETABS, material nonlinearity can be modeled by link elements or discrete, lumped plasticity hinges [9]. Link elements are additional members added to the structure that must be independently defined from the structure's frame and area elements. They are suitable for modeling base isolation and supplemental damping, but also have a larger variety of hysteresis models than discrete hinges that make them advantageous for nonlinear time history analyses. In addition, links can provide nonlinearity in multiple degrees of freedom using just a single element. Hinges, on the other hand, are better suited for static nonlinear (pushover) analysis because the hinges can be modeled with strength loss and hinge state at each step of analysis can be observed graphically. Link elements should be modeled with

monotonically increasing force-deformation response, which cannot be graphically observed. Additionally, the distribution of plasticity can be easily modeled through the application of multiple hinges along the member's length.

For this thesis, the chosen method to model nonlinearity is through discrete flexural plastic hinges because it is commonly used in academia and practical design. The modeling of link elements would take a substantial amount of additional time, and for the purposes of the analyses performed, it was determined that hinges were adequate and more efficient to model. In addition, because the hinge state can be plotted and viewed graphically, which the latter cannot be done for link elements, modeling hinges provides an advantage with valuable insight into the structure's response to loading. Since the model was originally created in ETABS and there are fewer hinge options in ETABS than in SAP2000, the following discussion will focus on the ETABS requirements. However, discrete plastic hinges were also modeled in SAP2000 and additional parameters had to be defined, which will be discussed when appropriate.

One of the first limitations that resulted in the way the final structure was modeled is that material nonlinearity modeled by discrete plastic hinges is only applicable to frame elements. Thus, all members that are expected to behave nonlinearly during the analysis must be modeled using frame elements, which is why the shear walls were constructed as previously described (Section 2.3.1). The types of hinges that can be applied to frame members include uncoupled moment, torsion, axial, shear and coupled axial with moment interaction (PMM) hinges. The degrees of freedom that are not assigned as a hinge remain elastic. Any combination of the different types of hinges can be applied at the same location, and any number of discrete hinges can be used to distribute plasticity

along a member, if desired. However, modeling several hinges greatly increases the computational cost and thus increases analysis run-time, so it is not always appropriate to use several hinges on each member if the structural model is large. In the case of the structure under investigation in this thesis, it is very large with many elements and several nonlinear analyses were performed, so the minimum number of hinges was used to model plasticity.

The location of a hinge is specified as a relative distance along the member, chosen by the user. It is important to ensure that the location of the hinges is representative of where the moment demands are greatest so that the hinges will be activated appropriately and the structure will perform as expected and realistically. To be consistent with the intended first-mode, strong-column weak-beam hinge mechanism described in Section 2.1, plastic hinges were assigned at the ground level for columns and shear walls, and at each end (i.e. beam-column faces) of all beams. Since everything below grade is expected to remain elastic, hinges are not modeled beneath the ground level.

Hinge properties can be determined using the default ETABS hinges, or they can be completely user-defined. The default hinge properties in ETABS and SAP2000 are based on FEMA 356 guidelines, which are material-dependent. Since the hinges are also dependent on the cross-section properties of the element it is assigned to, the properties cannot be viewed until after the hinge is applied to an element and becomes a "generated" hinge. Also, once generated, the hinge properties cannot be modified. Thus, in order for the program to automatically define the hinge properties, the user must make sure the section is correctly modeled, including all steel reinforcing and material

properties. If a member is modeled using the Section Designer, the stress-strain curve can be modified to accommodate different material behavior. However, the version of ETABS used does not have the ability to account for the difference between confined and unconfined concrete regions because hoop/ tie transverse reinforcing cannot be modeled analytically. Thus, the generated hinge properties based on the default FEMA guidelines are not accurate for reinforced concrete sections that are designed to provide ductility through adequate confinement.

User-defined hinge properties can also be used and are based on plastic force-displacement (F-D), for axial and shear degrees of freedom, or moment-rotation (M-θ), for bending and torsion moment degrees of freedom, relationships. User-defined properties can be based on the default FEMA properties and modified, or they can be fully user-defined. Fully user-defined properties allow for symmetric F-D/ M-θ backbone curves, or the curves can be different in the negative and positive directions. To define the plastic deformation curve, several points must be input into ETABS/ SAP2000. Figure 3.9 (a) shows the points on the plastic deformation curve and while the shape shown is typically used for pushover analysis, any shape can be defined as long as they comply with the following point definitions. Point A is always the origin and cannot be changed. From Point A to Point B, all deformation is linear and occurs inside the frame element. Point B represents yielding, but in the ETABS version used, the hinges are rigid-plastic, so the deformation at B is always defined as zero, as shown in Figure 3.9 (b). Thus, no deformation occurs in the hinge up to Point B and only plastic deformation beyond B will be exhibited by the hinge. For a typical pushover analysis, Point C should be defined as ultimate capacity and Point D represents residual strength. For other

purposes, a positive slope can be defined from C to D and/ or D to E. For any shape of backbone curve, Point E represents total failure. Beyond E, the hinge will drop the load to zero force/ moment as shown in the figures.

In addition to the five points required for defining the plastic deformation backbone curve, the user has the option of specifying the deformation values at the Immediate Occupancy (IO), Life Safety (LS), and Collapse Prevention (CP) levels used for performance-based design. These measures are used only as recorders for obtaining analysis results at the defined points, and do not affect the structure's behavior. As such, they can be used to measure other points of interest and are not required to be specified.

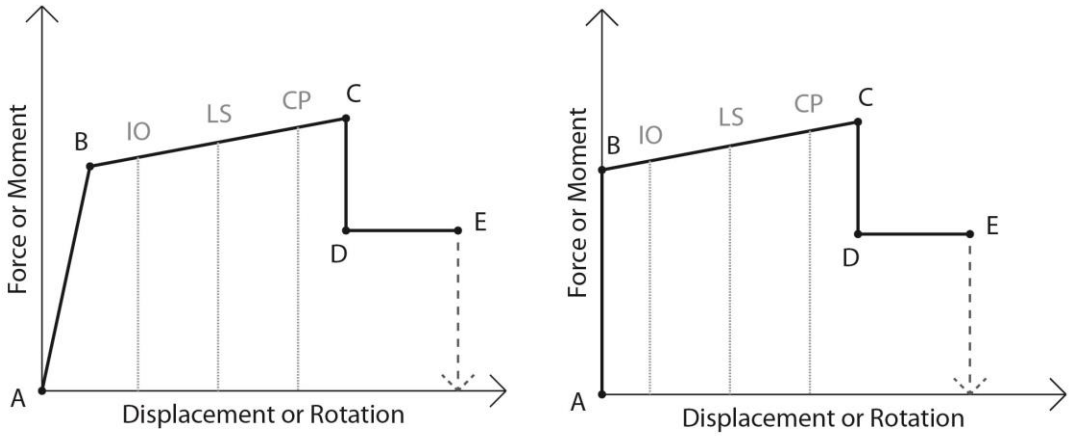

(a) **(b)**

Figure 3.9: (a) Plastic deformation backbone curve and (b) Actual rigid-plastic deformation curve used for hinges

Fully user-defined hinges were used to model material nonlinearity for the structure under investigation because the default hinges were not able to accurately account for confinement without the transverse steel modeled. Since all hinges intended for use in this thesis are purely flexural hinges, the bending moment-rotation relationships were obtained for each element. Thus, moment-curvature relationships

needed to be computed and plastic hinge lengths assumed to obtain the moment-rotation curves.

3.3.2 Moment-Curvature Analysis Models

To compute the moment-curvature relationships for the beams, columns, and shear walls, the open source, object-oriented finite element earthquake engineering software OpenSees (Open System for Earthquake Engineering Simulation) is used. When modeling a given cross-section, the material properties were first defined based on expected properties. There are several different hysteretic models available in OpenSees for concrete and steel. In this thesis, the Concrete02, linear tension softening concrete, and Steel01, bilinear with kinematic hardening steel, uniaxial materials are utilized. To account for the effects of transverse reinforcing, unconfined (cover) and confined (core) concrete regions and materials were assigned. For the confined concrete, the following equations were used to obtain the properties:

$$e_{c0,confined} = \frac{2f'_{c,confined}}{E_{c0}}, where\ E_{c0}\ (ksi) = 57\sqrt{f'_{c,unconfined}}$$

$$f'_{cu,confined} = 0.2f'_{c,confined}$$

$$e_{cu,confined} = 20e_{c0,confined}$$

For both confined and unconfined concrete:

$$f_t\ (ksi) = \frac{4}{1000}\sqrt{f'_{c,unconfined}}$$

$$E_{ts,unconfined} = E_{c0}/20$$

$$E_{ts,confined} = E_{c0}/40$$

It should be noted that whenever the square root of f'_c is computed, f'_c is in units of pounds per square inch (psi). A summary of the concrete and steel reinforcing material properties specified are provided in Table 3.8 and Table 3.9, respectively.

Table 3.8: Concrete material properties used in OpenSees

Concrete Property		Unconfined (cover)	Confined (core)
28-day compressive strength:	f'_c (ksi)	-6.8	-9.0
strain at max. compressive strength:	e_{c0}	-0.0025	-0.0038
crushing strength (ultimate strength):	f'_{cu} (ksi)	0.0	-1.8
crushing strain at ultimate strength:	e_{cu}	-0.005	-0.0766
ratio between unloading slope at e_{cu} and initial slope, E_{c0}:	λ	0.1	0.1
tensile strength:	f_t (ksi)	0.33	0.33
linear tension softening stiffness:	E_{ts} (ksi)	235.0	117.5

Table 3.9: Steel reinforcing properties used in OpenSees

Steel Reinforcing Property		Grade 60
yield strength (expected):	F_y (ksi)	69.0
modulus of elasticity:	E_s (ksi)	29000
strain hardening ratio:	b	0.01

A monotonic displacement-controlled moment-curvature analysis about the strong axis of bending is performed on each of the twelve different sections described by Figure 3.10 - Figure 3.12 and Table 3.10 - Table 3.12 below, with constant axial load applied at the center of columns and shear walls. The axial load due to full dead loads at the ground level was determined for each column, as discussed in Section 3.1.1, and the same was done for the shear walls. Unconfined properties are used for all cover regions and the web

of shear walls while confined concrete properties are used for the core regions. Clear cover is assumed to be 1.5 inches for all sections and the core is considered to be bounded by the center of the outer-most longitudinal reinforcement, as shown. To get the final number of fibers used in each discretization region, several analyses were performed until the moment-curvature results of a given cross-section no longer changed.

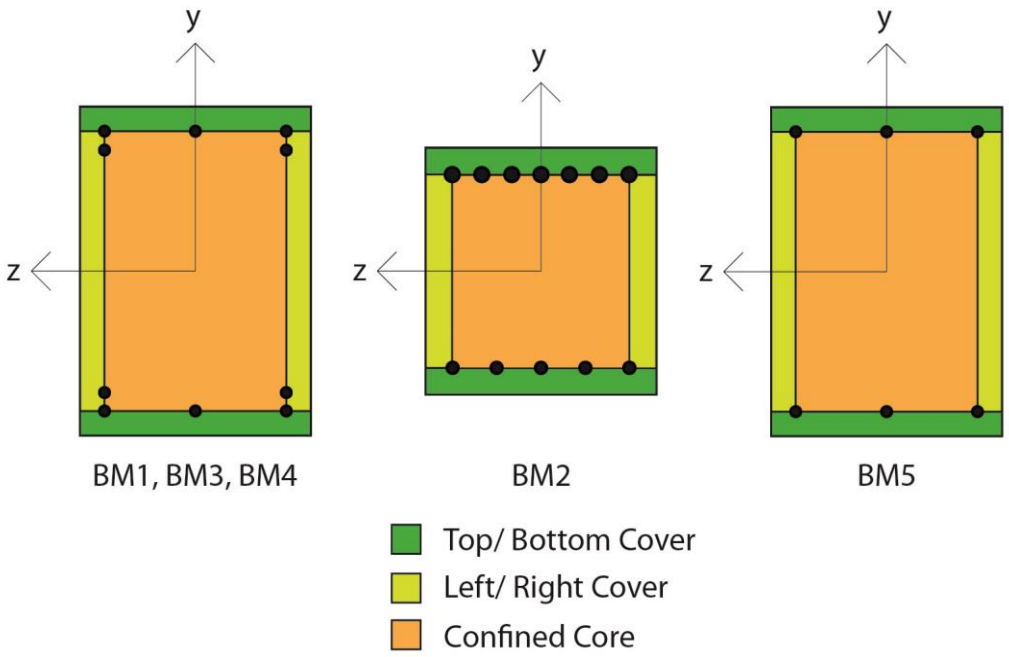

Figure 3.10: Illustration of beam cross-sections with regions of discretization

Table 3.10: Beam cross-section properties and fiber discretization

Tag	Steel Reinforcing			Beam Dimensions	Fibers (#, location)	
	Longitudinal		Hoops		T/ B Cover	R/L Cover and Core
	Top	Bottom				
BM1	3 #8 + 2 #9	3 #8 + 2 #7	#3 @ 5.5"	32" x 22.5"	50, parallel to z-axis	150, parallel to z-axis
BM3	3 #8 + 2 #8	3 #8 + 2 #7				
BM4	3 #8 + 2 #7	3 #8 + 2 #7				
BM2	7 #11	5 #9	#3 @ 5"	24" x 22.5"		
BM5	3 #8	3 #8	#3 @ 5.5"	32" x 22.5"		

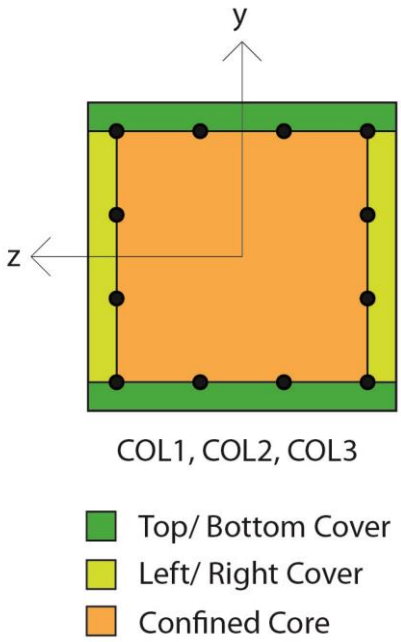

Figure 3.11: Illustration of column cross-section with regions of discretization

Table 3.11: Column cross-section properties and fiber discretization

Tag	Axial Load, P (kips)	Steel Reinforcing		Column Dimensions	Fibers (#, location)	
		Long.	Hoops		T/ B Cover	R/L Cover and Core
COL1	-604	12 #9	#5 @ 5"	30" x 30"	10, parallel to z-axis	30, parallel to z-axis
COL2AD	-1237	12 #10				
COL2in18	-879					
COL2out18	-718					
COL3	-1691	12 #11				

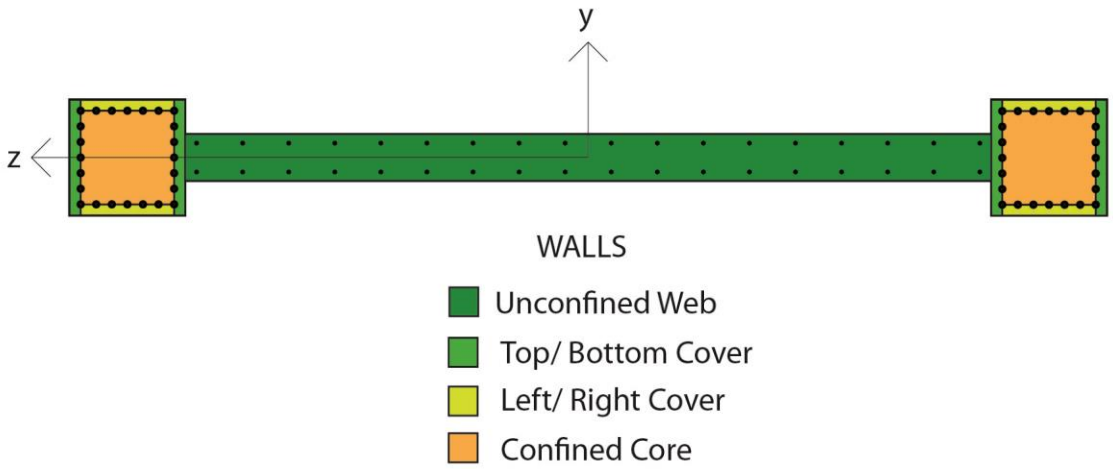

Figure 3.12: Illustration of shear wall cross-section with regions of discretization

Table 3.12: Shear wall cross-section properties and fiber discretization

Tag	Axial Load, P (kips)	Boundary Elements					Web			
		Steel Reinf.		Dim.	Fibers (#, location)		Steel Reinf.		Dim.	Fibers (#, location)
		Long.	Hoops		T/ B Cover	R/L Cover and Core	Vert.	Horiz.		
WALL36	-4190	24 #11	#5 @ 4"	30" x 30"	10, parallel to y-axis	30, parallel to y-axis	#4 @ 12" E.F.	#4 @ 6" E.F.	12" x 210"	420, parallel to y-axis
WALL45	-3783									

For the beam and column sections, the moment about the z-axis was monitored as curvature about the z-axis was monotonically increased. For the wall sections, the moment about the y-axis was monitored as curvature about the y-axis monotonically increased. Since the moment-curvature relationships were nonlinear, the Newton-Raphson algorithm was used at each step of computation. The energy unbalance convergence test with a tolerance of $1x10^{-6}$ and a maximum of 50 iterations was employed. If the analysis had problems converging, the displacement (curvature) increment per step was decreased. Furthermore, if the analysis still had issues

converging, the algorithm was changed to the Modified Newton-Raphson method. However, convergence was easily achieved for all of the cross-sections analyzed, with each step of curvature increment converging within 2 iterations.

3.3.3 Moment-Curvature Results and Idealizations

The results of the moment-curvature analyses performed in OpenSees are presented in this section. Since only five points can be defined in the ETABS/ SAP2000 plastic deformation curve, the moment-curvature relationships were linearly idealized. Material strain measurements have been found to be the best measurement of assessing the amount of damage in, or health state of, a flexural plastic hinge. Thus, typical material strain-limit states for reinforcing steel and concrete used in performance-based design are utilized in this thesis to identify significant points on the moment-curvature curve and to create idealized curves. In addition to recording the moment-curvature response, the stress and strain was measured in the unconfined concrete at the extreme fiber of cover in compression and tension, in the confined concrete at the extreme fiber of core in compression and tension, and in the reinforcing steel at the extreme fiber of compression and tension. These stress-strain measurements are required to identify when the strain-limit states occur.

For concrete, there are four strain-limit states typically observed for performance-based design. The first is the onset of concrete cracking (Ci), which occurs when the strain in the extreme fiber of cover concrete in tension, ε_{ct}, reaches the cracking strain of concrete, ε_{cr}, where $\varepsilon_{cr} = f_t/E_{c0}$. The second strain-limit state of concrete is the onset of concrete cover spalling (Cii). This corresponds to a strain of 0.4% on the extreme fiber of cover concrete in compression, ε_c. Both Ci and Cii states do not cause any structural

damage and little to no action is required to fix the issue and the building can remain operational. Deep concrete cover spalling (Ciii) represents the situation when the entire cover concrete has detached and the reinforcing steel is exposed. Ciii typically occurs when the strain in the extreme fiber of the core in compression, ε_{cc}, reaches 0.4%. The damage is mostly cosmetic, but it is necessary to protect the steel from corrosion and fire, so repair work may disrupt the building occupants. The final strain-limit state for concrete is crushing of the confined concrete core (Civ), which occurs when the strain in the extreme fiber in the core in compression, reaches a value of $\varepsilon_{ccu} = -\left(0.004 + 2\sqrt{\rho_{sx}\rho_{sy}}\right)$, where $\rho_{sx} = A_{shx}/(h_y s_h)$ and $\rho_{sy} = A_{shy}/(h_x s_h)$ are the geometrical reinforcement ratios in the short (x) and long (y) directions of a rectangular cross-section, respectively. The distance between the centers of the outermost transverse ties of a rectangular cross-section is h_x in the short dimension and h_y in the long dimension. A_{shx} is the total area of all ties parallel to the short dimension and A_{shy} is the total area of ties parallel to the long dimension. The hoop spacing is given by s_h. Civ occurs after longitudinal bar buckling or hoop fracture, so the concrete is no longer confined and crushes, and represents the start of rapid loss in flexural capacity and the end of displacement capacity. Such loss in capacity is clearly a mark of heavy, unsafe structural damage and extensive repairs, such as placing a steel jacket around the section and pouring new concrete, or demolition may be required. The four typical strain-limit states for concrete are summarized in Table 3.13.

Table 3.13: Typical strain-limit states for concrete

Label	Description	Strain Limit	Location of Interest
Ci	Onset of Concrete Cracking	$\varepsilon_{ct} = \varepsilon_{cr}$	extreme cover, tension
Cii	Onset of Concrete Cover Spalling	$\varepsilon_c = -0.004$	extreme cover, compression
Ciii	Deep Concrete Cover Spalling	$\varepsilon_{cc} = -0.004$	extreme core, compression
Civ	Crushing of Confined Concrete Core	$\varepsilon_{cc} = \varepsilon_{ccu} = -(0.004+2\sqrt{(\rho_{sx}\rho_{sy})})$	extreme core, compression

For longitudinal reinforcing steel, there are also four strain-limit states typically used in performance-based design. When the outermost steel reinforcing bar in tension yields, the first strain-limit state is achieved: first yield (Si). Residual cracks are likely to be small and cannot be seen upon inspection. The second steel limit state (Sii) occurs when the tensile strain in the outermost longitudinal bar, ε_s, reaches 1%. Sii is typically a useful quantity that benchmarks yielding of a reinforced concrete column, where residual cracks are likely to be large (around 1 mm). For Si and Sii, no action is required unless the structure is exposed to marine or other aggressive environments, in which case epoxy can used to fill in cracks that may expose the rebar to corrosive air, but the building can remain fully operational. Onset of longitudinal bar buckling (Siii) cannot be seen, but occurs when the longitudinal bar cycles from tension to compression and buckles in the compression domain. A somewhat conservative measure of Siii is when the difference between the tensile strain on the extreme steel fiber, ε_s (positive), and the strain of the extreme compressive fiber of the concrete core, ε_{cc} (negative), is $\varepsilon_s - \varepsilon_{cc} \geq (10 - s_h/d_b)/100$, where $s_h$is the hoop spacing and d_b is the longitudinal bar diameter.

The final strain-limit state for reinforcing steel is when the outermost longitudinal bar fractures (Siv), which occurs when $\varepsilon_s - \varepsilon_{cc} = (14 - 4s_h/3d_b)/100$ and $\varepsilon_{cc} \leq -0.004$. The latter condition corresponds to the state when the entire cover has spalled off, which must be true for the longitudinal bars to fracture. When Siv is achieved, there is a significant decrease in flexural capacity and no more displacement capacity of the member, and as with Civ, extensive repairs or demolition may be necessary. The four strain-limit states for reinforcing steel are summarized in Table 3.14.

Table 3.14: Typical strain-limit states for reinforcing steel

Label	Description	Strain Limit	Location of Interest
Si	First Yield	$\varepsilon_s = \varepsilon_y$	extreme steel, tension
Sii	Tensile Strain in Outermost Longitudinal Bar = 1%	$\varepsilon_s = 0.01$	extreme steel, tension
Siii	Onset of Longitudinal Bar Buckling	$\varepsilon_s - \varepsilon_{cc} \geq (10\text{-}s_h/d_b)/100$	extreme steel, compression
Siv	Longitudinal Bar Fracture	$\varepsilon_s - \varepsilon_{cc} = (14\text{-}4s_h/3d_b)/100$	extreme steel, compression

With the concrete and reinforcing steel strain-limit states defined as above, each can be categorized into one of three structural damage limit states: DS1, DS2, or DS3 based on the amount of damage done and the extent of repairs needed for the structural element under inspection. DS1 corresponds to the fully operational performance level, which requires no action to repair the issue, so the Ci, Cii, Si, and Sii stain-limit states fit the category. DS2 means that the structural element is operational, but repairs are needed that requires little to no downtime. Strain-limit states Ciii and Siii typically fall under DS2. DS3 marks the life safety performance level since extensive repairs, or even

demolition, may be necessary. Achieving either Civ or Siv labels the element as DS3, and as soon as one of the two strain-limit states is reached, the other cannot be attained and the element is considered to have reached its ultimate curvature. In the strain-limit state summary tables above and the moment-curvature plots that follow, DS1 is represented by the color green, DS2 by yellow, and DS3 by red.

As mentioned at the beginning of this section, the moment-curvature relationships obtained using OpenSees needed to be linearly idealized before implemented in ETABS or SAP2000. A standard way to idealize moment-curvature is with a tri-linear approximation. The tri-linear curve is constructed by connecting four points: the origin, the Ci strain-limit state, reference yield, and the maximum moment developed (flexural overstrength), as shown in Figure 3.13. If the flexural overstrength curvature is less than the ultimate curvature corresponding to either Siv or Civ strain-limit states, the third branch of the tri-linear idealization is extended to the ultimate curvature value. Reference yield is a point defined as the intersection of the line that connects the origin to first yield and a line drawn horizontally at the value of expected moment. First yield is defined as the point on the moment-curvature relationship when the smallest curvature corresponding to: a strain on the extreme unconfined (cover) fiber of concrete in compression of $\varepsilon_c = -\varepsilon_{c0} = -[0.0017 + (f'_c/8702.3ksi)]$, the strain-limit state Si where $\varepsilon_{s,tens} = \varepsilon_y$ on the extreme tensile longitudinal bar, or when $\varepsilon_{s,comp} = -\varepsilon_y$ on the extreme compressive longitudinal bar, is reached using expected properties. Expected moment is defined as either the Cii or Sii strain-limit state, whichever occurs first (i.e. corresponds to the smallest curvature).

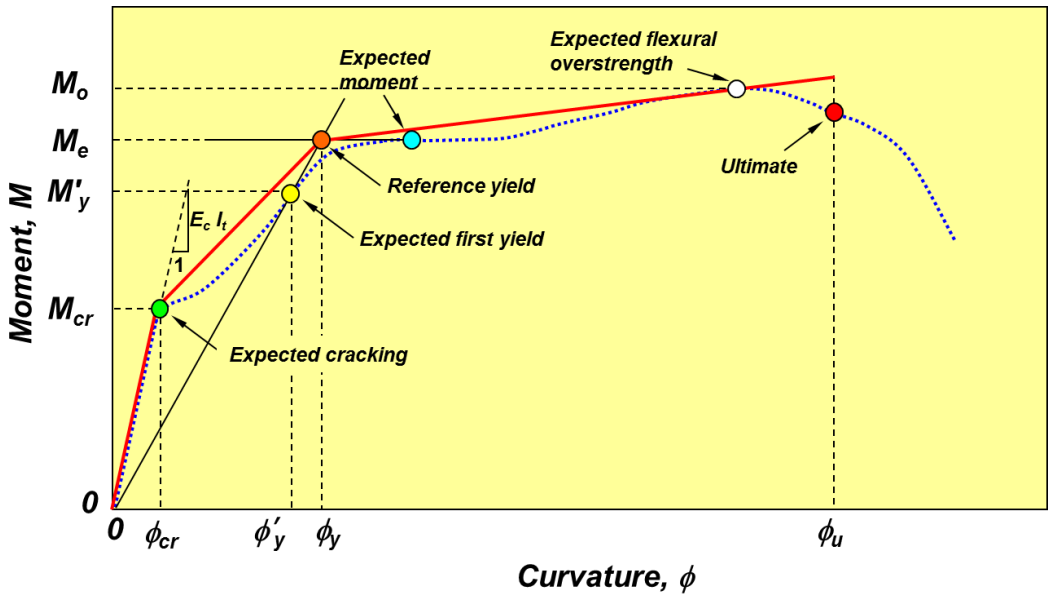

Figure 3.13: Points defined for constructing tri-linear idealization of moment-curvature relationship (Figure courtesy of Professor J. Restrepo, UCSD Seismic Design lecture notes, 2013)

The method of tri-linear idealization discussed above was used for the beam and shear wall sections of the structure analyzed in this thesis. However, the tri-linear idealization did not adequately represent the moment-curvature relationships for the column sections, since the flexural overstrength occurred at a very low curvature as compared to the ultimate curvature. As a result, the slope of the third branch of the idealization was too large. Thus, a multi-linear idealization was used for the columns, which was constructed by connecting the origin, the strain-limit state Ci, first yield, and flexural overstrength. The fourth and final branch of the multi-linear idealization was defined as a horizontal line extending from the point of flexural overstrength to the ultimate curvature. First yield is considered to be the "reference" yield in this case, and the expected moment value is not used in the linearization.

For each section, the resulting analytical and linearized moment-curvature relationships were normalized such that the moment was divided by the product of the building weight, W, and the height of the structure from ground to roof, h_r, and the curvature was multiplied by the depth of the section divided by the yield strain of reinforcing steel, ε_y. To check that the analytical moment-curvature relationships and idealizations were acceptable, the normalized reference yield curvature was identified and compared to the values suggested by Priestley [9], presented in Table 3.15. Figure 3.14 - Figure 3.16 show the normalized moment-curvature analytical and idealized relationships with the strain-limit states and the reference yield check for a representative beam, column, and shear wall section, respectively. The rest of the moment-curvature relationship figures are located in Section 7.1 of the appendix.

Table 3.15: Reference yield curvature values suggested by Priestley

Section	Reference Yield Curvature, ϕ_y
T-section beams	$1.70*\varepsilon_y/H_b$
Rectangular columns	$2.10*\varepsilon_y/H_c$
Rectangular walls	$2.00*\varepsilon_y/L_w$
Flanged walls	$1.50*\varepsilon_y/L_w$

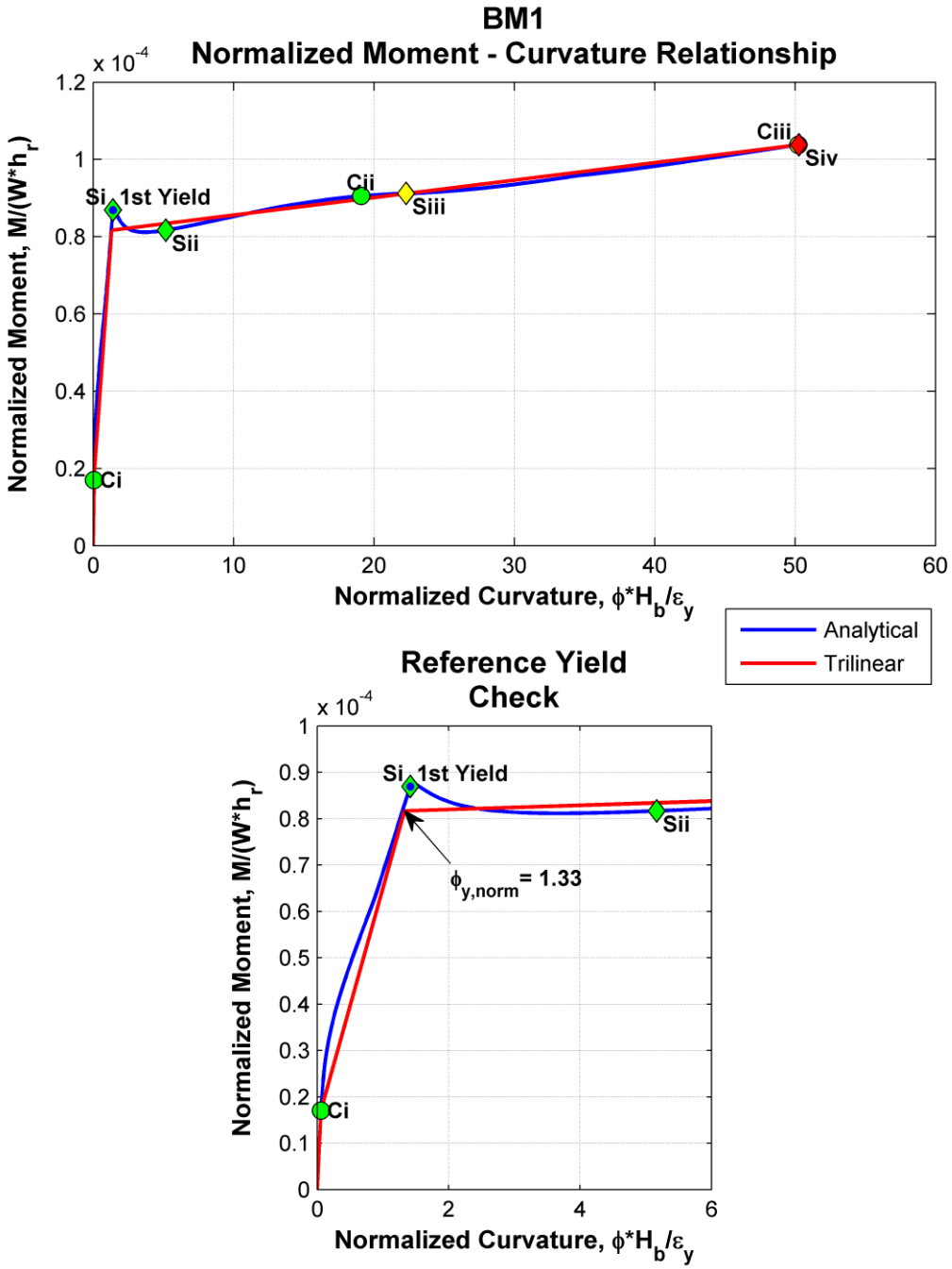

Figure 3.14: Normalized moment-curvature relationship, tri-linear idealization, and reference yield check for BM1

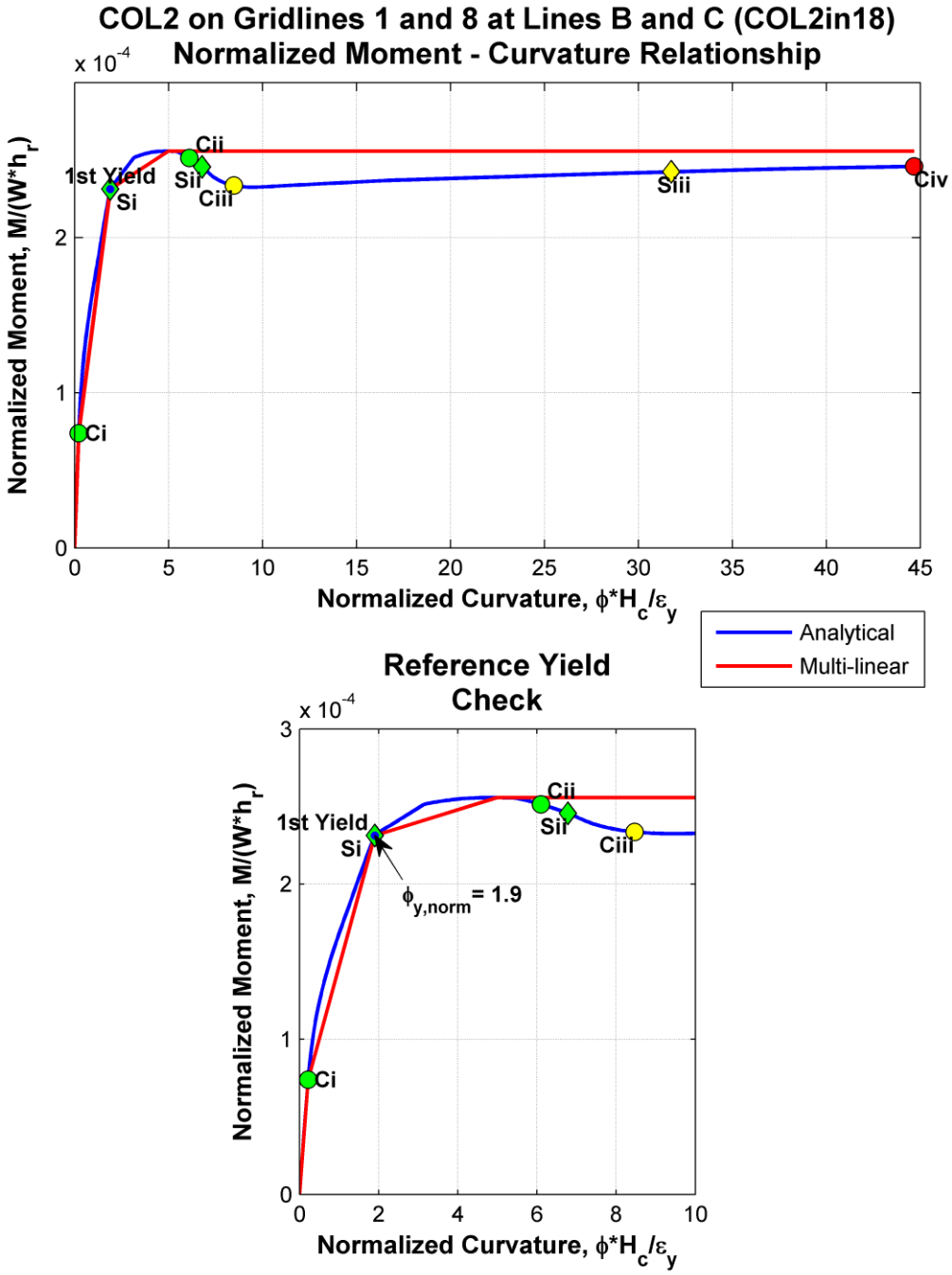

Figure 3.15: Normalized moment-curvature relationship, multi-linear idealization, and reference yield check for COL2in18

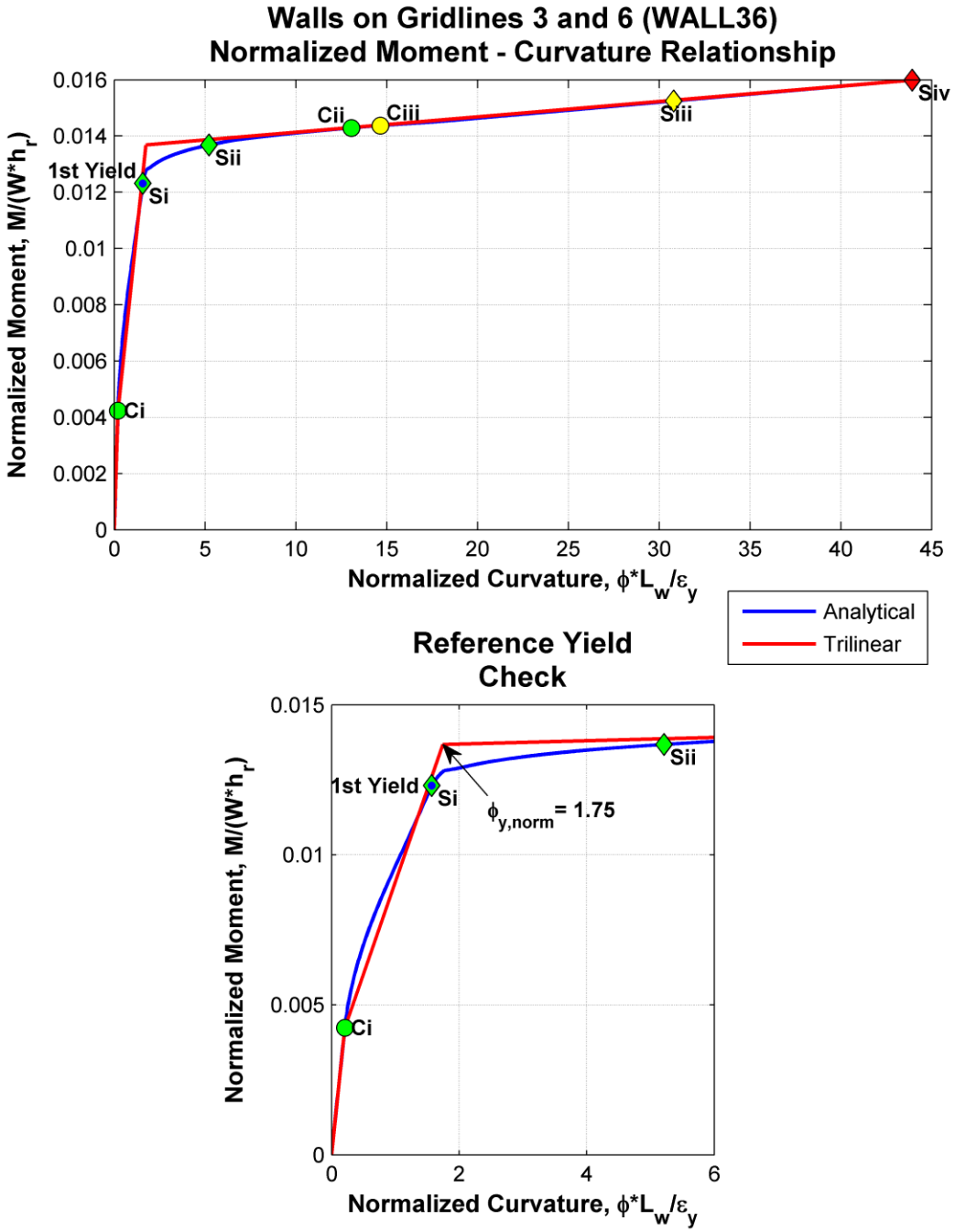

Figure 3.16: Normalized moment-curvature relationship, tri-linear idealization, and reference yield check for WALL36

A summary of the normalized reference yield curvature and curvature ductility for all sections is provided in Table 3.16. The normalized yield curvatures for the beams, averaging around 1.33, was quite a bit lower than the 1.70 benchmark value for T-beams. Since rectangular cross-sections were used for the moment-curvature analyses, a difference in the values was expected. For the column sections, the normalized yield curvature values were typically less than Priestley's 2.10 because the columns are square and not rectangular. For the walls, the normalized reference yield values were about halfway between the values determined for rectangular walls and flanged walls. Since the amount and layout of reinforcing steel, applied axial load, and section geometry all have an impact on the reference yield curvature value, the normalized values were within acceptable range of those recommended by Priestley. The curvature ductility capacity was computed as the ultimate curvature divided by the reference yield, or first yield for the columns, curvature. All sections were determined to be adequately ductile and thus deemed sufficient for seismic loading.

Table 3.16: Summary of normalized reference yield curvature and curvature ductility values for all sections

Reference Yield Curvature, $\phi_{y,norm}$, and Curvature Ductility, μ_ϕ								
Beams			Columns			Walls		
Tag	$\phi_{y,norm}$	μ_ϕ	Tag	$\phi_{y,norm}$	μ_ϕ	Tag	$\phi_{y,norm}$	μ_ϕ
BM1	1.33	37.8	COL1	1.76	24.0	WALL36	1.75	25.2
BM2	1.51	114.7	COL2AD	2.05	18.7	WALL45	1.71	25.6
BM3	1.33	38.4	COL2in18	1.90	23.5			
BM4	1.33	38.6	COL2out18	1.84	25.0			
BM5	1.20	66.7	COL3	2.26	14.7			

It was observed that increasing the amount of steel reinforcing for a given section caused the normalized reference yield curvature to increase, which results from an increase in the initial stiffness and the section's ability to reach higher moment capacities. Additionally, with increased axial load on the columns and walls, the yield curvature increased but ductility decreased. Yield curvature increases because increasing axial load on a section increases the initial tangent stiffness since the section is compressed and closes cracks in the concrete, which results in a larger moment of inertia. For the columns, the peak moment achieved occurred at lower curvature values but increased in magnitude as axial load increased. Ductility decreases as increased axial load is applied because the distance between ultimate and yield curvatures decreases, since the ultimate curvature the section can achieve occurs at a lower curvature. This occurs because, assuming plane sections remain plane, the maximum compressive strain is achieved sooner with the addition of axial load since the larger axial strain and adds to the compressive bending strain, causing the slope in the strain diagram to decrease, and thus curvature decreases (see Figure 3.17).

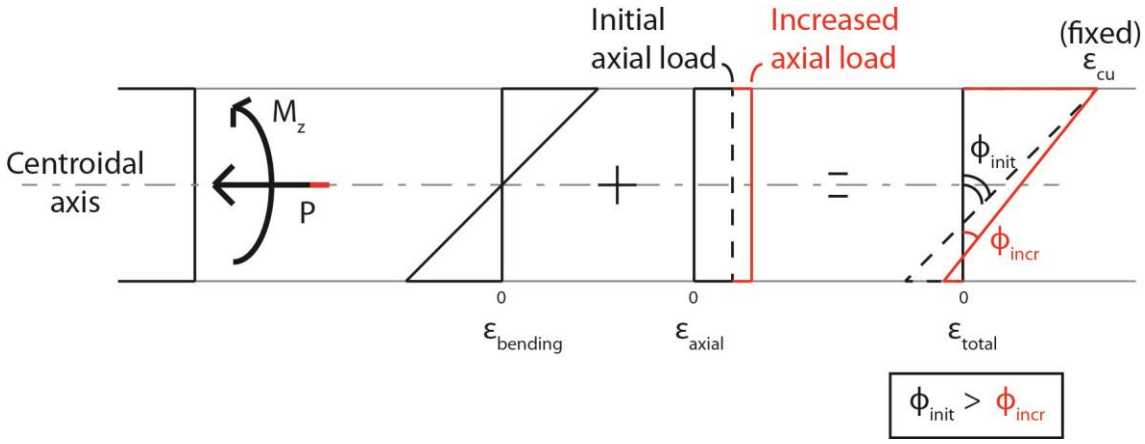

Figure 3.17: Illustration of mechanics of decrease in curvature with an increase in axial load

3.3.4 Moment-Rotation Relationships and Implementation in Models

To implement the plastic deformation curve for hinges, ETABS requires points A, B, C, D, and E as discussed in Section 3.3.1 to be points on a moment-rotation, as opposed to moment-curvature, relationship. Thus, the curvature must be considered to act over a chosen plastic hinge length, L_p, where plasticity is expected to occur in the element. In this case, the plastic hinge length was assumed to be half the member depth for all section types, which is typically used for reinforced concrete sections. Table 3.17 summarizes the depths of each member and the corresponding plastic hinge lengths used.

Table 3.17: Summary of member depths and assumed plastic hinge lengths

Section	Depth (in)	Plastic Hinge Length, L_p (in)
Beams	H_b	$0.5H_b$
BM1, BM3, BM4, BM5	32	16
BM2	24	12
Columns	H_c	$0.5H_c$
COL1, COL2 (all), COL3	30	15
Walls	L_w	$0.5L_w$
WALL36, WALL45	270	135

The rotation of each member was computed by multiplying the curvature by the plastic hinge length. Thus, the moment-rotation relationships were plotted along with the strain-limit states and linear idealizations. Figure 3.18 - Figure 3.20 show the analytical and idealized moment-rotation relationships for the representative beam, column, and shear wall, with the rest of the curves presented in Section 7.2 of the appendix. It should be noted that in this design and analysis, all beams were well-detailed for ductile seismic

response because every longitudinal bar was tied to prevent pre-mature buckling. As a result, the ultimate beam rotations found here were significantly, or about three times, larger than what would be expected of concrete beams with transverse reinforcing designed according to the ACI 318 provisions.

The type of analysis that will be performed on a structure and the desired results impact the way the plastic deformation curve of hinges should be defined in ETABS. Since several different types of linear and nonlinear analyses were performed on the structural models, only one shape of plastic deformation curve was used per member cross-section and was directly defined from points on each section's linear idealization of moment-rotation. Thus, there was no assumed residual strength value to which the moment capacity drops after the ultimate moment is achieved, as is typically done for pushover analyses.

The moment and rotation values put into the ETABS and SAP2000 models were normalized by the reference yield point for beams and shear walls, and by the first yield point for columns, so the actual yield point moment and rotation values were assigned as scale factors. Specifically, Point A was always the origin and Point B was always unity for the moment and zero for the rotation. For beams and shear walls, Point B represented the point on the moment-rotation curve at which reference yield occurred, and for the column sections, Point B represented the point of first yield. Points C and D were assigned as two intermediate points on the positive slope between reference yield and failure (Civ or Siv) for beam and shear wall sections. However, Point C was defined as the point of maximum moment/ flexural overstrength and Point D was an intermediate point on the horizontal branch of the multi-linear idealization for columns. For all

sections, the failure point of the moment-rotation idealization was assigned to Point E in ETABS. Additionally, the moment-rotation backbone curves were chosen to be symmetric, such that the absolute value of each point coordinate in the negative direction was the same as the positive direction coordinate. Table 3.18 - Table 3.20 summarize the normalized points, in the positive direction, and scale factors used for all beam, column, and shear wall sections.

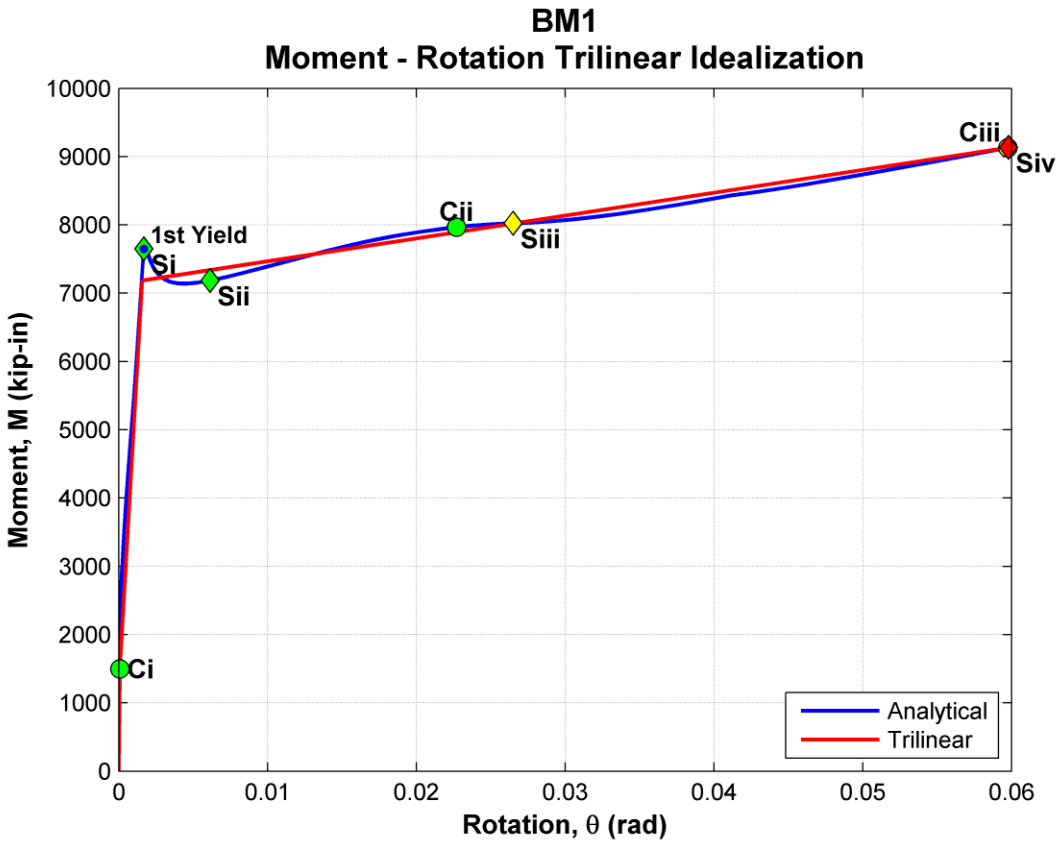

Figure 3.18: Moment-rotation relationship with tri-linear idealization for BM1

Table 3.18: Normalized points and scale factors (SF, units of kip-inches and radians) for ETABS moment-rotation relationship of beam plastic hinges

Point	BM1		BM2		BM3		BM4		BM5	
	M	θ	M	θ	M	θ	M	θ	M	θ
A	0	0	0	0	0	0	0	0	0	0
B	1	0	1	0	1	0	1	0	1	0
C	1.085	12.609	1.540	55.791	1.086	12.637	1.086	12.560	1.201	27.980
D	1.179	25.306	1.814	83.408	1.180	25.256	1.180	25.195	1.360	49.180
E	1.271	37.776	2.123	114.699	1.277	38.372	1.280	38.632	1.490	66.746
SF	7187	0.00158	7123	0.00180	7187	0.00159	7187	0.00159	4889	0.00143

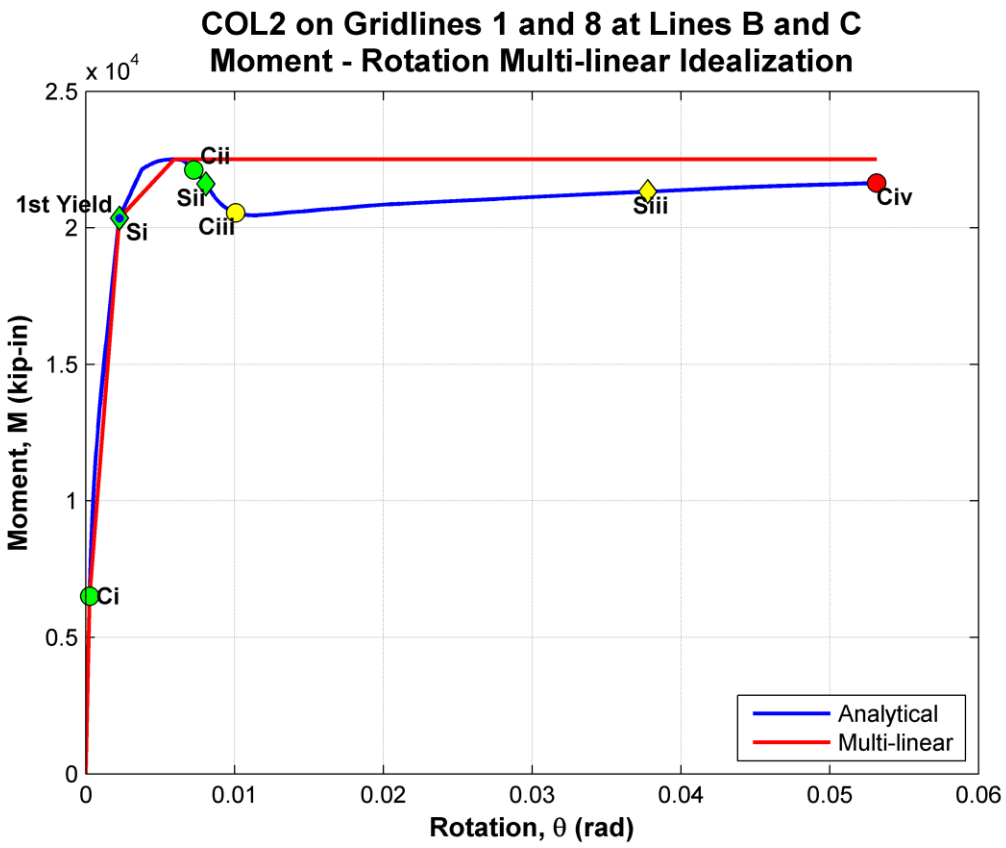

Figure 3.19: Moment-rotation relationship with multi-linear idealization for COL2in18

Table 3.19: Normalized points and scale factors (SF, units of kip-inches and radians) for ETABS moment-rotation relationship of column plastic hinges

Point	COL1		COL2AD		COL2in18		COL2out18		COL3	
	M	θ	M	θ	M	θ	M	θ	M	θ
A	0	0	0	0	0	0	0	0	0	0
B	1	0	1	0	1	0	1	0	1	0
C	1.123	3.875	1.079	1.842	1.106	2.625	1.121	3.138	1.032	1.333
D	1.123	14.347	1.079	12.285	1.106	13.257	1.121	13.730	1.032	11.136
E	1.123	23.979	1.079	18.669	1.106	23.482	1.121	24.966	1.032	14.707
SF	15930	0.00209	23410	0.00244	20350	0.00226	18920	0.00219	28850	0.00269

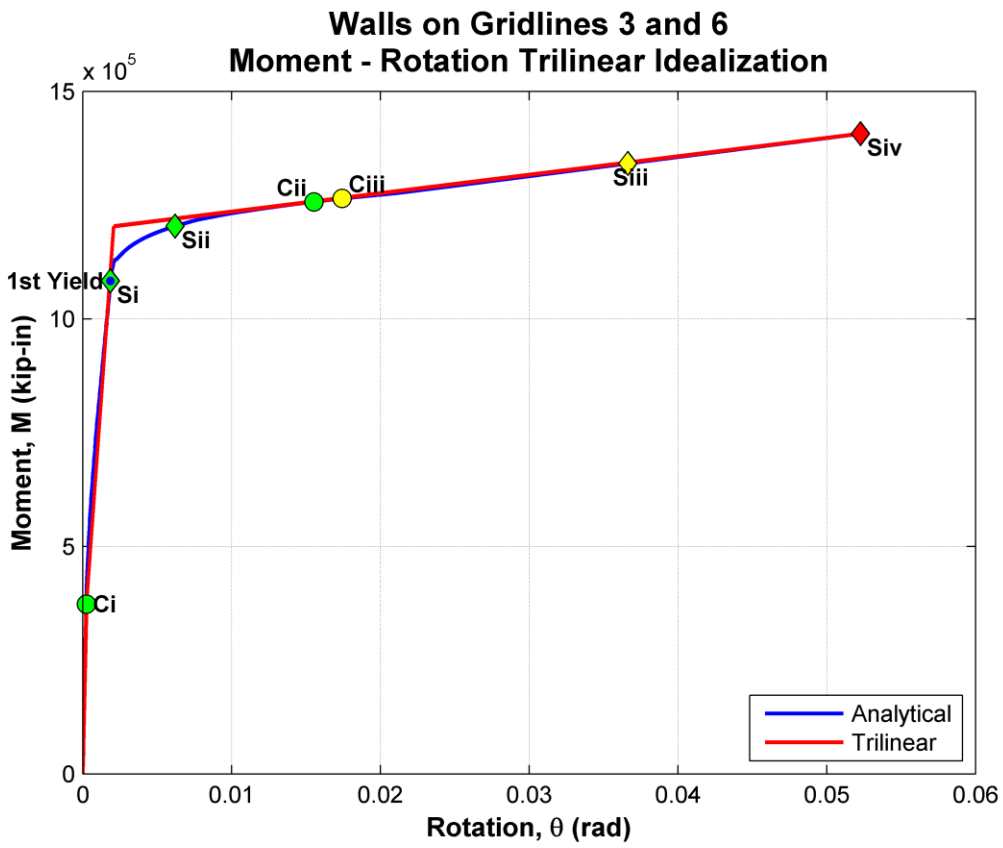

Figure 3.20: Moment-rotation relationship with tri-linear idealization for WALL36

Table 3.20: Normalized points and scale factors (SF, units of kip-inches and radians) for ETABS moment-rotation relationship of wall plastic hinges

Point	WALL36		WALL45	
	M	θ	M	θ
A	0	0	0	0
B	1	0	1	0
C	1.061	9.677	1.064	9.812
D	1.128	19.229	1.136	19.623
E	1.170	25.173	1.180	25.640
SF	1203000	0.00208	1157004	0.00204

While the hinge moment-rotation relationships described above were derived from the axial loads found by a gravity analysis of the final symmetric ETABS model, the same values were used in the asymmetric ETABS model and both symmetric and asymmetric SAP2000 models. Since only some of the sections' axial loads changed slightly between the symmetric and asymmetric case, the moment-rotation relationships that did change were all within 3% of the symmetric model and it was not necessary to update the new moment-rotation points in the asymmetric ETABS/ SAP2000 models. Thus, the WALL36 section properties were used for the shear walls on Gridlines 6 and 7 and WALL45 properties were still used for the walls on Gridlines 4 and 5.

3.3.5 Hysteretic Hinge Behavior in SAP2000

SAP2000 has an additional parameter to define for single degree of freedom hinges: the choice of hysteretic behavior the hinges will experience, using the moment-rotation points inputted by the user as a backbone curve. The four hysteretic options available are isotropic, kinematic, Takeda, and pivot. The default option is isotropic hysteresis, which is the only hysteretic behavior that ETABS uses. The following descriptions of the hysteresis types are based on information from the CSI Analysis Reference Manual [7].

When isotropic hysteresis is chosen, hinge unloading is elastic. Thus, the unloading follows a path parallel to the initial stiffness, the slope between points A and B on the backbone curve. Kinematic hysteresis is typically observed in steel and other metals and thus will not be further discussed in this thesis. As shown in Figure 3.21, the Takeda hysteretic loop degrades by following a secant path to the backbone curve after crossing the horizontal axis upon unloading. The pivot hysteresis model is based on the

degrading hysteretic loop, shown in Figure 3.22 and described by Dowell, Seible, and Wilson (1998), which uses pivot points as targets for the secant path upon unloading and reverse loading. The Takeda and pivot hysteresis models are commonly used to represent the behavior of reinforced concrete.

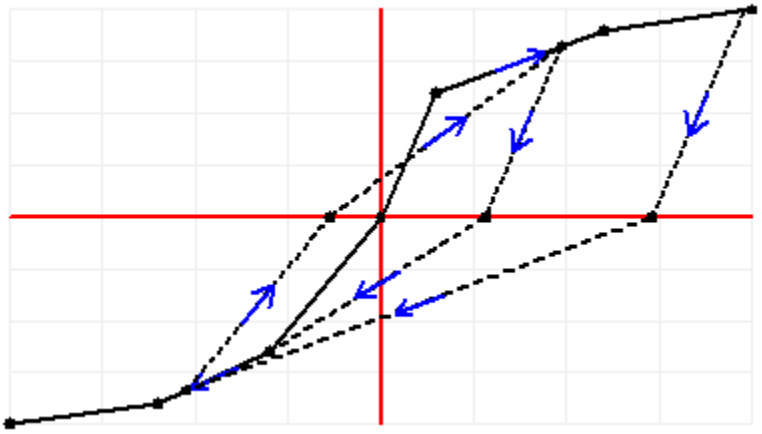

Figure 3.21: Screenshot of SAP2000 Takeda hysteresis for link elements

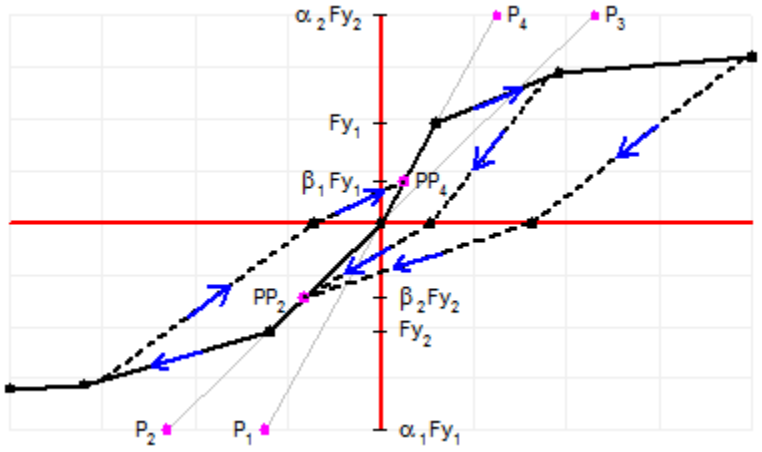

Figure 3.22: Screenshot of SAP2000 pivot hysteresis for link elements

It should be noted that although the screenshots above are from the link element definition window in SAP2000, it is assumed that the program uses the same behavioral rules for hinges. When the isotropic, kinematic, or Takeda hysteresis types are chosen for hinges, no additional parameters are required to be defined by the user. However, for the pivot option the factors α_1, α_2, β_1, β_2, and η can be modified. The factors α_1 and α_2 locate the pivot point for unloading to zero from positive and negative force, respectively, while β_1 and β_2 locate the pivot point for reserve loading from zero toward positive and negative force, respectively. The η factor is used to control the amount of elastic slope degradation after plastic deformation has occurred. The default values for these factors are $\alpha_1 = \alpha_2 = 10$, $\beta_1 = \beta_2 = 0.7$, and $\eta = 0$. Based on the intent of analyses performed, it may be appropriate to use different hysteretic relationships for different types of analyses.

4 RESPONSE SPECTRA AND GROUND MOTIONS

The building under investigation in this thesis is located in Berkeley, CA, a region of high seismic hazard. Response spectra for a site are typically used to predict the acceleration or displacement values over a range of natural periods for single degree of freedom oscillators located at that site. The response spectra can then be used to determine approximate seismic forces or displacements that a structure with a particular period will be designed for. The code-based response spectra are associated with the design basis earthquake (DBE), that has a return period of about 475 years corresponding to a 10% probability of exceedance in 50 years, and the maximum considered earthquake (MCE) of 2% probability of exceedance in 50 years, or 2475-year return period. These code-based response spectra are also used in the determination of which ground motion records and the appropriate corresponding scale factors to use in dynamic time-history analyses of a structure. Since the structure has already been designed, the purpose of determining the code-based response spectra in this thesis was to use it as a "target" for checking the chosen ground motion records used for analysis, which will be presented in this section.

4.1 Site Classification and Target Seismic Response Spectra

The seismic ground motion values used to find the site's target design response spectrum and MCE response spectrum were determined based on ASCE 7-05. The mapped MCE spectral response acceleration parameters for the site were taken as S_s = 1.766 g for short periods and S_1 = 0.654 g for a 1-second period, previously found by André Barbosa using the USGS Java Ground Motion Parameter Calculator. The soil

properties were assumed to be classified as Site Class D. Thus, the corresponding site coefficients for short and 1-second periods were found to be F_a = 1.0 and F_v = 1.5 from ASCE 7 Tables 11.4-1 and 11.4-2, respectively. Thus, the MCE spectral response acceleration adjusted for site effects for short periods (SMS) and at 1 second (SM1) are based respectively on Eq. 11.4-1 and 11.4-2 of ASCE:

$$S_{MS} = F_a S_s = 1.766\ g$$

$$S_{M1} = F_v S_1 = 0.981\ g$$

The target design (DBE) response spectrum for the site was computed for fundamental periods, T, varying between 0 and 4 seconds at intervals of 0.01 seconds using the following equations from ASCE 7 Section 11.4.5.

From Eq. 11.4-5, for $T < T_0$, the design spectral response acceleration, S_a, is:

$$S_a = S_{DS}\left(0.4 + 0.6\frac{T}{T_0}\right)$$

For $T_0 \leq T \leq T_s$:

$$S_a = S_{DS}$$

For $T_s < T \leq T_L$, from Eq. 11.4-6:

$$S_a = \frac{S_{D1}}{T}$$

For $T > T_L$, from Eq. 11.4-7:

$$S_a = \frac{S_{D1}T_L}{T^2}$$

Where the design spectral response acceleration parameters at short and 1-second periods are based on ASCE 7 Equations 11.4-3 and 11.3-4, respectively:

$$S_{DS} = \frac{2}{3}S_{MS} = 1.177g \ \ and \ \ S_{D1} = \frac{2}{3}S_{M1} = \ 0.654\ g$$

And where:

$$T_0 = 0.2\frac{S_{D1}}{S_{DS}} = 0.111\ sec$$

$$T_S = \frac{S_{D1}}{S_{DS}} = 0.555\ sec$$

The long-period transition period, T_L, for the site is 8 seconds, found from Figure 22-15 of ASCE 7.

To obtain the target MCE response spectrum, the design spectral accelerations, S_a, found as above were multiplied by 1.5. It should be noted that the spectral accelerations found correspond to 5% of critical damping. In addition to the target DBE and MCE acceleration response spectra, the spectral accelerations were converted to spectral displacements to create the target DBE and MCE displacement response spectra. For each period, T, the spectral acceleration value was multiplied by the acceleration due to gravity, g = 386.4 in/sec^2, and divided by the square of circular frequency (units of radians/sec), ω, to get spectral displacement values in inches. In equation form, $S_d = (S_a/\omega^2)g$, where $\omega = 2\pi/T$. The resulting target DBE and MCE acceleration and displacement response spectra for 5% damping are presented in Figure 4.1. The first North-South and first East-West periods for the symmetric SAP2000 model are also shown on the spectral plots for reference.

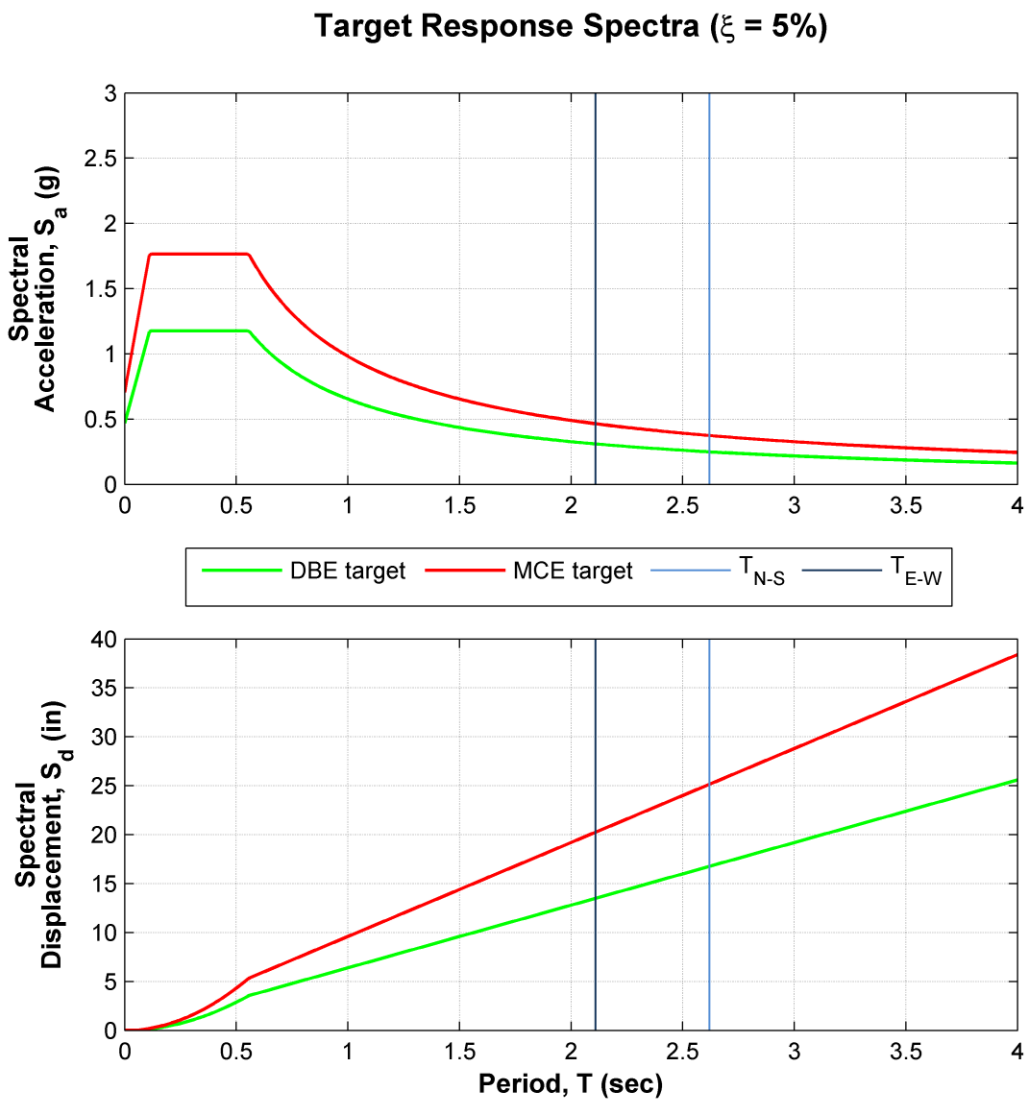

Figure 4.1: Target acceleration and displacement response spectra (5% of critical damping)

4.2 Suite of Ground Motion Pairs

A suite of seven ground motion pairs, each consisting of a fault normal (FN) and a fault parallel (FP) record, was selected for the time-history analyses. Scale factors, previously determined by UCSD student Arpit Nema for his Ph.D. work, were used to bring the records to the DBE and MCE levels of the site. Table 4.1 summarizes the earthquake data and scale factors for the seven ground motion records. The unscaled and

uncut ground acceleration time histories from both fault normal and fault parallel records are shown in Figure 4.2.

Table 4.1: Summary of seven ground motion records and their scale factors

Record ID	Earthquake	Date	Mag.	Station	Scale Factor	
					DBE	MCE
NZ002	Christchurch, New Zealand	2/22/2011	6.3	PRPC	0.8	1.2
P0179	Imperial Valley	10/15/1979	6.5	El Centro Array #7	1.0	1.5
P0082	San Fernando	2/9/1971	6.6	Pacoima Dam	0.8	1.2
P0990	Northridge	1/17/1994	6.7	Newhall - W. Pico Canyon Rd.	0.667	1.0
P1024	Northridge	1/17/1994	6.7	Sylmar - Converter Sta East	0.8	1.2
P0144	Tabas, Iran	9/16/1978	7.4	Tabas	0.667	1.0
C4816	Wenchuan, China	5/12/2008	7.9	Mianzuqingping	0.667	1.0

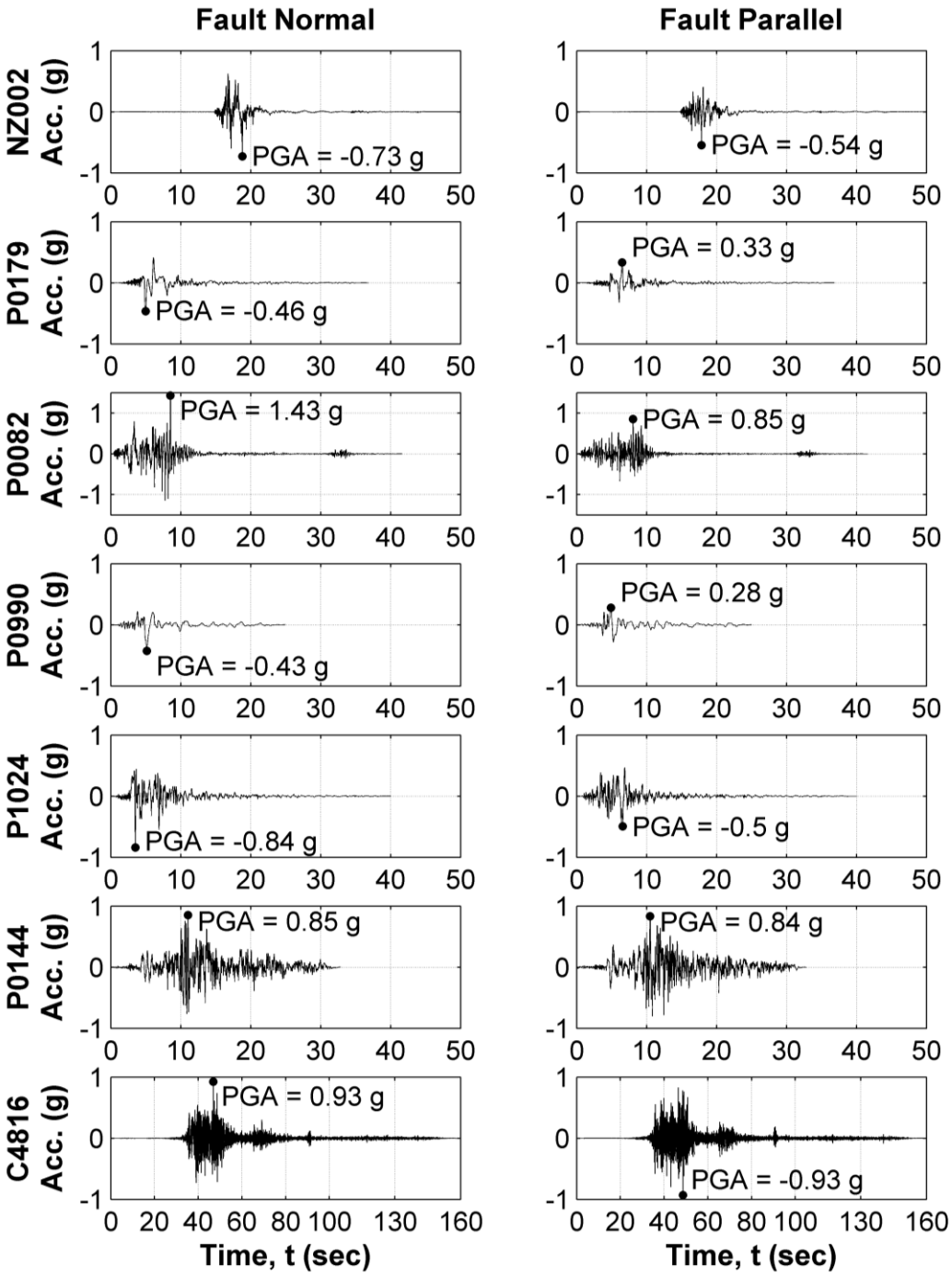

Figure 4.2: Acceleration time histories for all ground motion records (unscaled and uncut)

To verify that the suite of ground motions was adequate for the building site, SeismoSignal was used to get the 5% damped acceleration response spectra for the fault normal and fault parallel records of each ground motion. The acceleration records were scaled to the appropriate DBE and MCE levels using the scale factors previously defined. In SeismoSignal, a period range of 0.01 to 4 seconds with a step size of 0.01 seconds was used for computing the 5% damped elastic pseudo-acceleration response spectra. As was done with the target acceleration response spectra, the spectral acceleration values were converted to spectral displacements using $S_d = (S_a/\omega^2)g$.

Once all of the ground motion response spectra values were found, the geometric mean of the seven ground motions was computed for all cases individually: fault normal record spectral accelerations and displacements at DBE and MCE levels and fault parallel records spectral accelerations and displacements at DBE and MCE levels. Additionally, the square root sum of the squares (SRSS) combination rule was used on the fault normal and fault parallel spectra for both levels of earthquake to obtain the SRSS spectra, i.e. $SRSS = \sqrt{FN^2 + FP^2}$. Figure 4.3 and Figure 4.4 show the resulting spectral acceleration and spectral displacement plots for DBE level and MCE level, respectively.

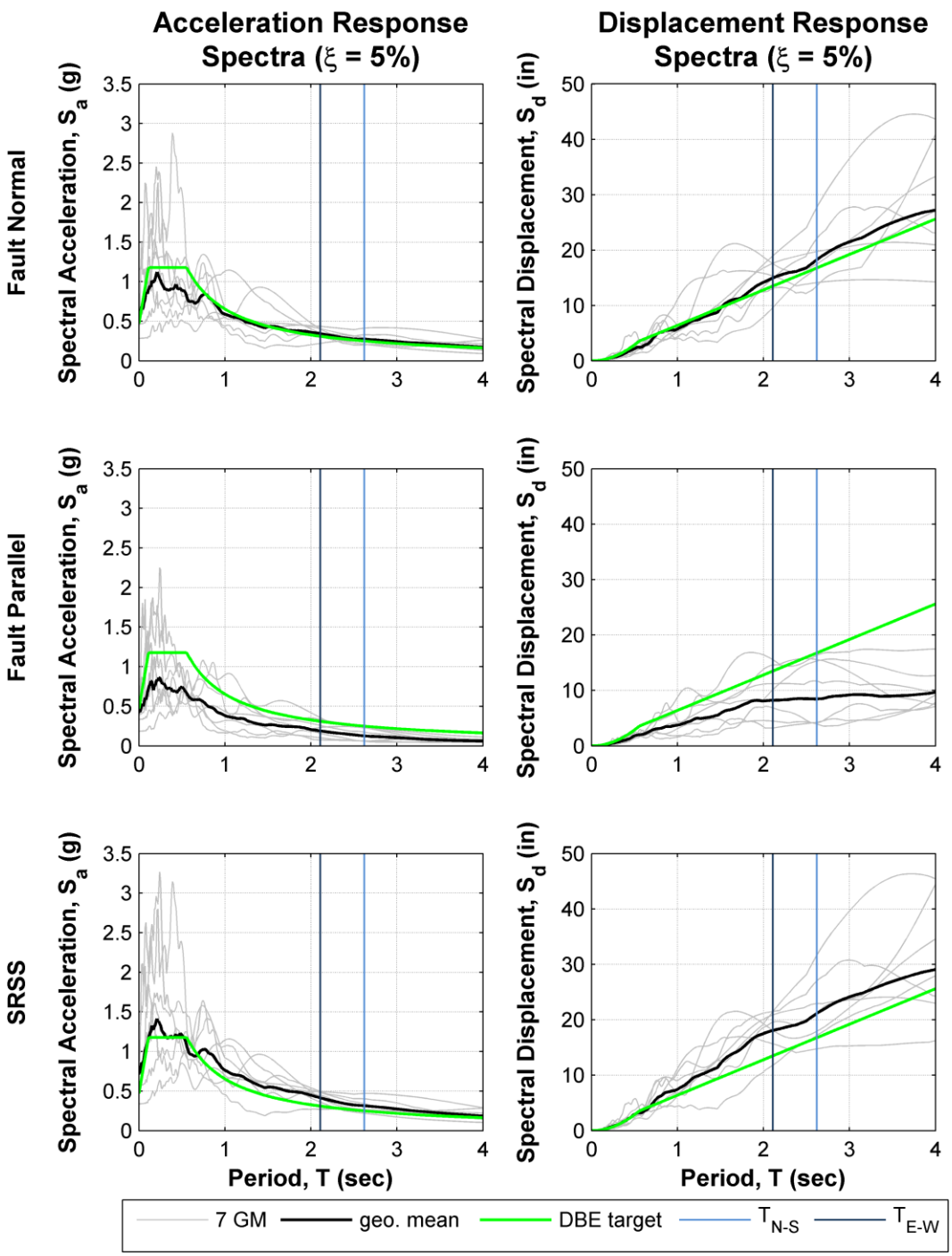

Figure 4.3: Acceleration and displacement response spectra (5% of critical damping) for ground motions at DBE level

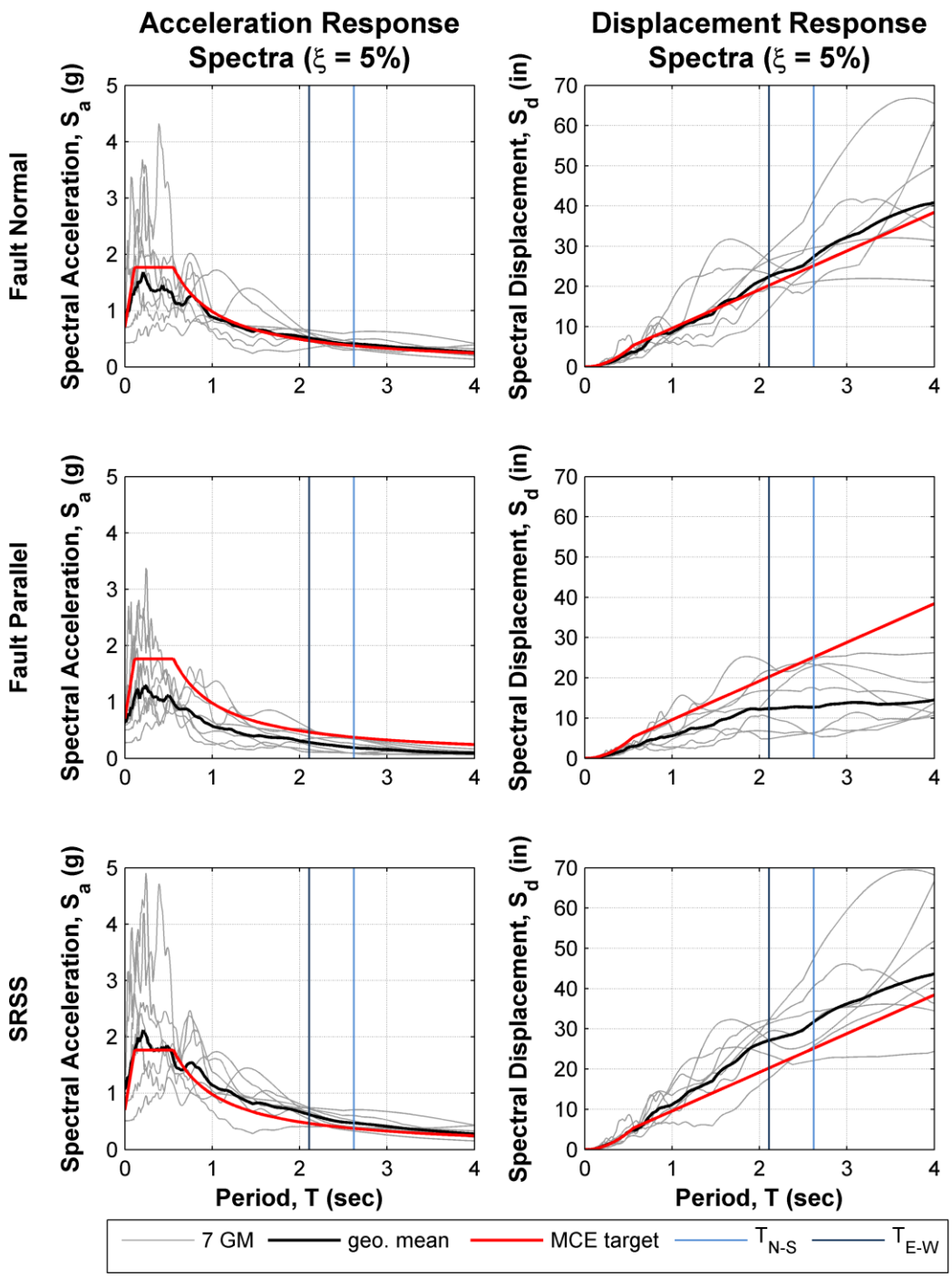

Figure 4.4: Acceleration and displacement response spectra (5% of critical damping) for ground motions at MCE level

For 3-dimensional response history analysis, it is required by ASCE 7 Section 16.1.3.2 that the average of the SRSS spectra from all horizontal component pairs of ground motions must not fall below 1.3 times the design response spectrum by more than 10% between 0.2T and 1.5T for each fundamental mode period, T, in the direction analyzed. Thus, for $T_{N\text{-}S}$ = 2.62 sec and $T_{E\text{-}W}$ = 2.11 sec, the effective range over which the SRSS geometric mean must exceed the design response spectrum limit is 0.42 sec – 3.93 sec. As shown in Figure 4.5, this requirement is typically satisfied, other than a small portion of the required period range: from 0.42 sec – about 0.75 sec. Thus, the suite of ground motions was determined to be acceptable for performing time history analyses.

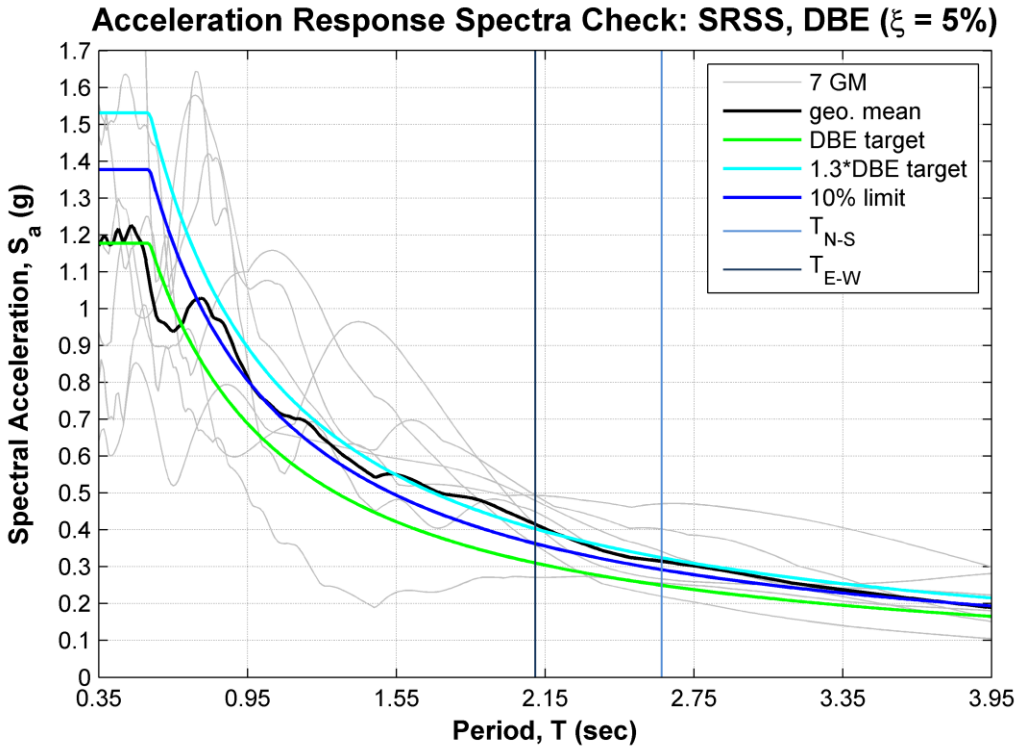

Figure 4.5: Check that geometric mean of SRSS response spectra is above the 10% limit for ASCE 7 Ch. 16 check

5 NONLINEAR ANALYSES AND RESULTS

To evaluate and compare the performance of the symmetric and asymmetric structures, various nonlinear analyses were performed. One of the major disadvantages of using discrete plastic hinges to model material nonlinearity is that they are not activated when performing Fast Nonlinear Analysis (FNA), which is an analysis method based on mode-superposition that ETABS uses to compute nonlinear response. FNA is intended for systems with only a few nonlinear link elements but the rest of the system is mainly linear-elastic, such as a base isolated structure with supplemental dampers. However, since SAP2000 has both FNA and direct-integration time-history analysis options for dynamic nonlinear analysis, hinges can be modeled, but the more time-consuming direct-integration time-history analysis method must be used to account for the nonlinear response of hinges. Although ETABS accounts for hinges in pushover analyses, SAP2000 was ultimately used for performing all inelastic nonlinear analyses, as discussed in the next paragraph.

An elastic dynamic time history analysis that included nonlinear geometric (P-Delta) effects was performed in ETABS with the full-length ground motion records. Using the SAP2000 models, a series of nonlinear static analysis procedures (pushovers) were completed. SAP2000 was also used to get the nonlinear dynamic time history response of the structure. For the nonlinear time history analysis, the ground motions had to appropriately cut to reduce analysis run time. The full details of each elastic and inelastic nonlinear analysis, along with the results, are presented in this section.

5.1 ETABS Time History Analysis and Results

As described above, the FNA method that ETABS uses does not account for material nonlinearity through plastic hinges. Thus, the time history analyses (THA) performed in ETABS were based on elastic material properties and nonlinear geometry, or P-Delta effects. In this section, the parameters used for analysis and the results of both the symmetric and asymmetric ETABS models are discussed.

5.1.1 Analysis Parameters

To define a time history analysis case in ETABS, several parameters must be chosen. The first option is the analysis type: linear, periodic, or nonlinear. When the nonlinear analysis option is chosen, there are advanced parameters available that allow the user to choose the tolerance, substep size, iteration limits, and convergence factor. These options can be changed to control the convergence, accuracy, and analysis run time. The load assignments allow the user to choose what direction the time history function is applied and input the scale factor. There is also an option to start the time history immediately after a previous time history has been analyzed, which applies the load to the structure with the stiffness matrix calculated at the end of the previous time history case. Additionally, the modal damping can be assigned as a constant value for all modes, or modal damping overrides can be specified. Thus, if the user elected to apply Rayleigh proportional damping, they would need to specify modal damping overrides for each mode. The output time step size must also be chosen, which controls the number of analysis steps that are actually stored and recorded for viewing when the analysis is complete.

Two different nonlinear analysis cases were assigned for each of the seven ground motion pairs to apply the DBE and MCE scale factors. Thus, 14 independent time history cases were defined. The time history cases were analyzed as separate events, so the "start from previous history" option was not used. In each case, the fault normal acceleration history was applied in the direction of the walls (global X-direction of the models) and the fault parallel acceleration history was applied in the direction of the frames (global Y-direction). The default advanced nonlinear parameters of relative force and energy tolerances, iteration limits, and convergence factors were used. The maximum substep size was chosen to be 0.01 seconds after a few trials of decreasing substep sizes were performed. Since the frame elements remained elastic and the nonlinear P-Delta effects were not significant, decreasing the substep sizes did not change the results. For simplicity, 2% of critical damping, constant for all modes, was assigned. The output time step size was chosen to be large enough to reduce analysis run time and file sized, but at least the same size as the input step size of the actual records to prevent the program from interpolating between data points. The input step size of each record and the chosen output time step sizes are presented in Table 5.1.

Table 5.1: Input and output step sizes for each record

Record ID	Input Step Size (sec)	Output Step Size (sec)
NZ002	0.02	0.02
P0179	0.005	0.01
P0082	0.01	0.01
P0990	0.01	0.01
P1024	0.005	0.01
P0144	0.02	0.02
C4816	0.005	0.01

5.1.2 Results and Discussion

To compare the results of the symmetric and asymmetric models, the lateral displacement, relative to the ground, time history results of each ground motion analysis case were obtained for every floor at the structure's Southeast corner where Gridlines 1 and D intersect. From the history results, the peak displacements in the positive and negative directions were found at the i^{th} floor and normalized by the height from ground to roof, h_r, and plotted as the peak relative displacement envelopes over the height of the structure. For each time step, the interstory drift ratio (IDR) was computed by taking the difference in displacements between consecutive floors and dividing that difference by the corresponding story height. The geometric mean of the seven ground motion pairs was computed for the peak relative displacement and IDR envelopes. These results were found in both the direction of the walls and the frames for the symmetric and asymmetric models. Figure 5.1 shows the comparison of the calculated response envelopes for the symmetric and asymmetric models with the ground motion acceleration records scaled to the DBE level. Figure 5.2 shows the same comparisons for the analysis cases where the ground motions were scaled to the MCE level.

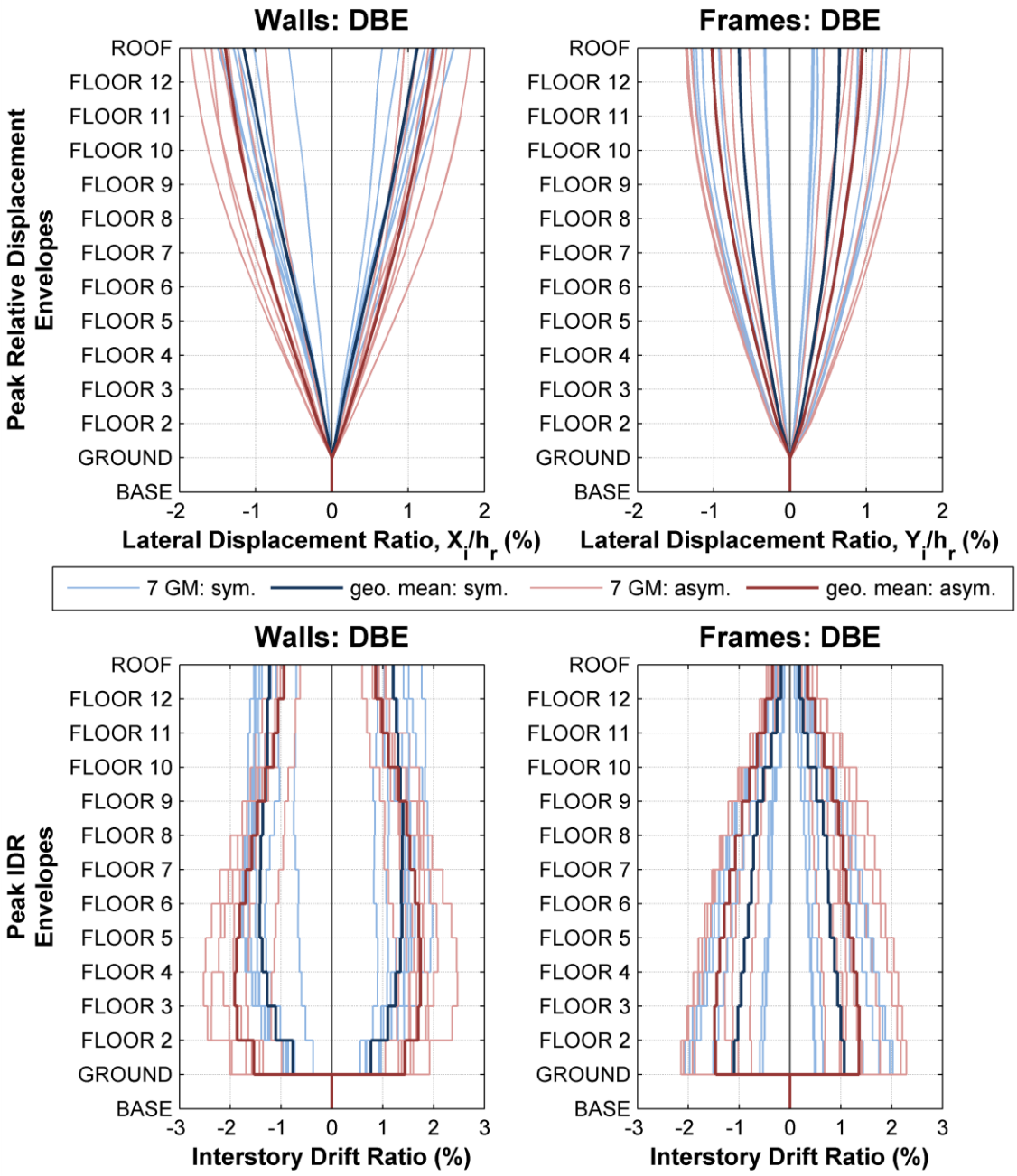

Figure 5.1: Response envelopes for symmetric and asymmetric ETABS models at DBE level

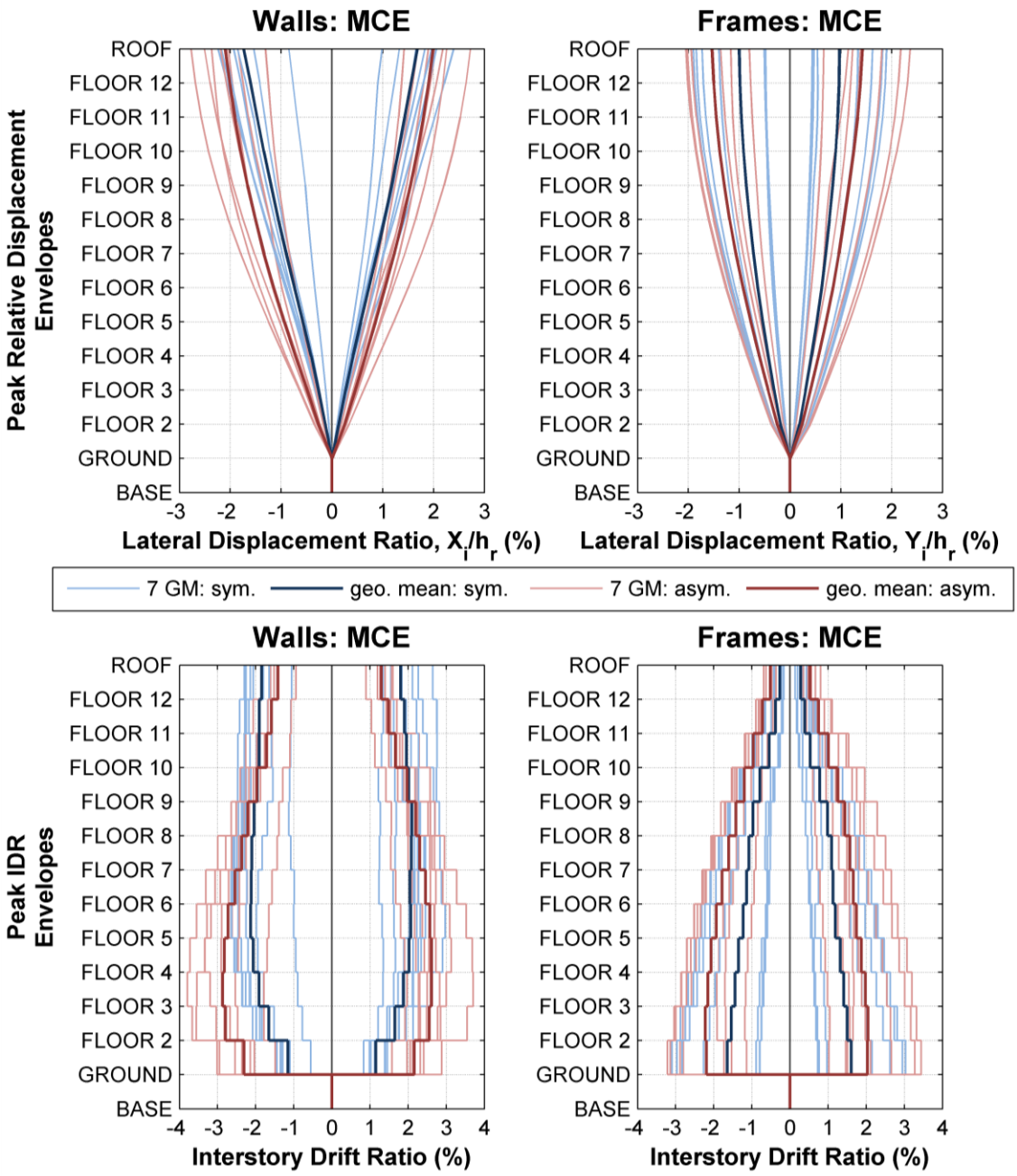

Figure 5.2: Response envelopes for symmetric and asymmetric ETABS models at MCE level

Since the time history analysis was essentially linear, with P-Delta effects being minimal, all of the response envelopes were nearly symmetric. Also a consequence of the essentially linear behavior, other than the magnitudes attained, there is no noticeable difference in the shape of a given DBE level envelope and the same MCE level envelope. Thus, the following trends observed describe the behavior of both levels of ground motion.

In both the frame and wall directions, the asymmetric model has consistently larger peak relative displacement (PRD) responses than the symmetric model. The shape of the PRD envelopes in the direction of the walls is fairly linear for the symmetric model, which is typical for symmetric shear wall structures. For the asymmetric model, the PRD envelopes have a slight inward curve that approaches the shape of a displacement envelope for frames. This curve arises because the corner where the displacements were measured is further away from the shear walls than it was for the symmetric model, so the effect of the frames along Gridlines 1, 2 and 3 is more pronounced. The shape of the PRD envelopes in the direction of the frames is reminiscent of the first North-South mode shape. Thus, the influence of higher modes is minimal and the response is typical of frame structures. The effect of asymmetric shear wall placement on the frames' PRD envelope shape is also minimal other than the increased magnitude.

For the peak IDR envelopes in the direction of the walls, the torsional effect of moving a shear wall is apparent. While the shape of the symmetric model IDR envelope is again typical of shear wall structures, with interstory drift ratios being smaller at the ground and increasing at smaller and smaller increments up the building height, the asymmetric envelope shows a pronounced "belly" of largest IDRs in the lower half of the

structure and the smallest IDRs occur at the roof. As discussed with the PRD envelopes, the fact that the displacements were measured at the corner furthest away from the walls, the frame influence is clear. In the direction of the frames, the IDR is smallest at the roof and increases towards the ground, as is typical of frame structures and consistent with the shape of the PRD envelope. Again, the difference between the shape of the symmetric and asymmetric models is mostly the magnitude, with a slight difference between the ground and the 2nd floor. At this story, the asymmetric IDRs do not increase much from the IDR between the 2nd and 3rd floors, showing that torsion has a very small impact on the frame direction response.

To compare the symmetric and asymmetric results more generally, Figure 5.3 presents the absolute maximum roof drift ratios (RDR) and maximum interstory drift ratios using the geometric mean in the wall and frame directions for both DBE and MCE levels. The maximum roof drift ratio was calculated as the absolute maximum of the positive and negative peak relative displacements measured at the roof and divided by the roof height. Since fault normal accelerations are typically much larger than fault parallel accelerations, the demand of the earthquakes on the structure was larger in the direction of the walls than the direction of the frames. This can be observed by both maximum RDR and maximum IDR, which are larger for the walls than the frames. The maximum RDR has a bigger change in magnitude, of about 53%, for the frame direction when comparing the symmetric and asymmetric models. In contrast, the asymmetric model maximum RDR magnitude increased by about 21% in the wall direction for both DBE and MCE levels. Similar to what was observed from the shapes of the envelopes, the

effect of asymmetry on maximum IDR is slightly larger in the direction of the walls (34.7% increase) than in the direction of the frames (34.5% increase).

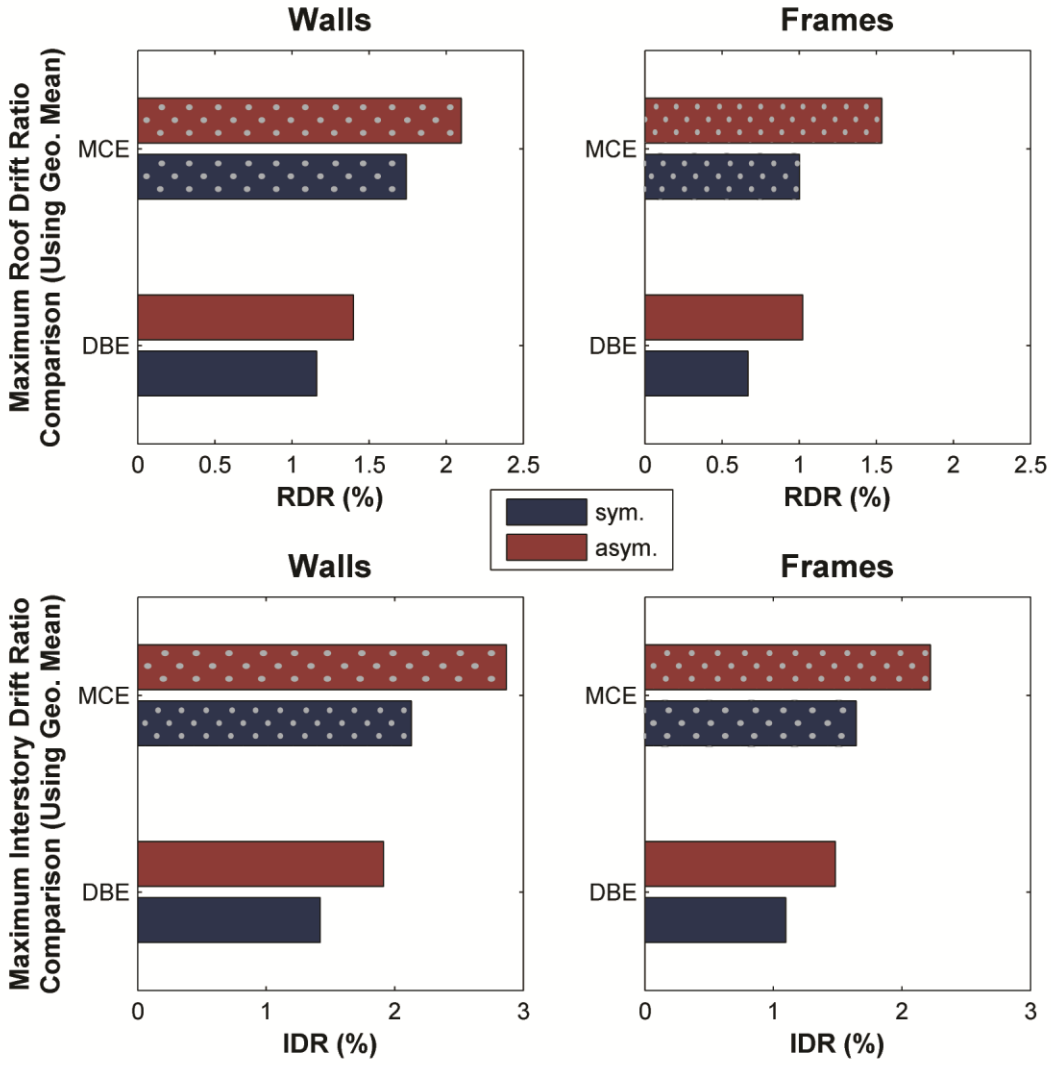

Figure 5.3: Comparison of symmetric and asymmetric ETABS THA results

5.2 SAP2000 Pushover Analysis and Results

A nonlinear static analysis, more commonly referred to as a pushover analysis, is typically used as a fast way to predict nonlinear performance of a structure subjected to seismic loading. In a pushover analysis, a monotonically increasing lateral load is statically applied to the structure until a target displacement is reached or a mechanism forms. At each step of analysis, the total base shear is plotted against roof lateral displacement, which provides information about the ductility capacity of the lateral system. While they have the advantage of being computationally less time-consuming than dynamic time history analyses, static pushovers are inherently not able to provide acceleration response and other valuable information that nonlinear dynamic analyses provide because inertia of mass is not effective.

For this thesis, pushover analyses were performed only in the direction of the shear walls for both the symmetric and asymmetric SAP2000 models. As previously discussed, the floor slabs were removed from the model in order to allow for proper hinging to occur in the beams. When the first trials of pushover analyses were performed on the models that included the slabs, it was discovered that the shape of the resulting base shear-roof displacement curves had excessive hardening behavior that was not expected or typical of reinforced concrete shear wall systems. This is a beneficial example of how a pushover analysis can be used to check that an analytical model is behaving as desired before performing time history analyses. The lateral load profiles and parameters used to perform the pushover analyses on the symmetric and asymmetric SAP2000 models (without the slabs) are discussed in this section, followed by the results.

5.2.1 Pushover Profile Descriptions and Analysis Parameters

Three different lateral load profiles were chosen to be independently applied to the structure for the pushover analyses. The first profile selected for analysis was the first mode in the direction of the walls, or the first East-West mode, determined from modal analysis of the symmetric building. The first mode shape is a commonly used profile for pushovers because it can be used to evaluate the pure first mode response of the structure, which is typically the most prominent mode participating in structural response. Figure 5.4 shows the first mode profile shape and vertical distribution factors applied in the analysis. The second profile was the code-based pattern defined by the vertical distribution factor (C_{vx}) of Equation 3-12 in FEMA 356, provided below.

$$C_{vx} = \frac{w_x h_x^k}{\sum_{i=1}^{n} w_i h_i^k}$$

The value of k is 2.0 for T ≥ 2.5 seconds, 1.0 for T ≤ 0.5 seconds, and shall be linearly interpolated for intermediate values of T. Thus, for $T_{E\text{-}W}$ = 2.11 sec, k was found to be 1.807. Since it is based on the building period, seismic weights, w, and heights, h, of each floor, Eq. 3-12 represents an assumed mode shape that helps capture higher mode response. The values used for calculation of C_{vx} are provided in Table 5.2 and the resulting profile is shown in Figure 5.5. The third and final lateral load profile used was a uniform vertical distribution, scaled such that the sum of the distribution factors equals 1.0. The uniform profile, shown in Figure 5.6, corresponds to rigid-body motion assuming an equal mass distribution throughout the structure and thus is capable of capturing a soft-story mechanism response.

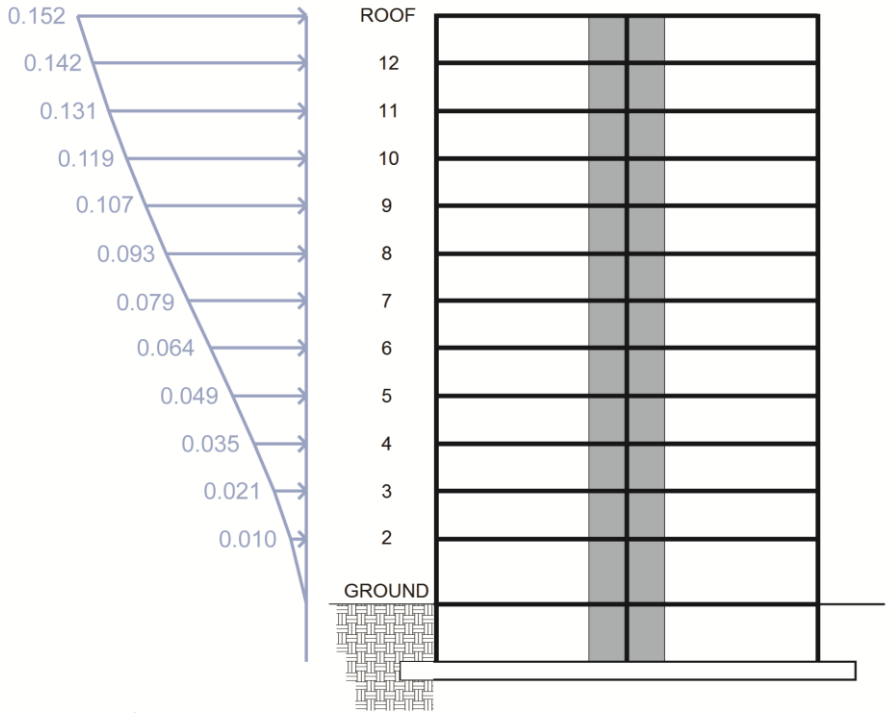

Figure 5.4: Load profile and North-South elevation at wall, first E-W mode

Table 5.2: Values used for calculation of C_{vx}, where k = 1.807

Floor	h_i (ft)	w_i (kips)	h_i^k (ft^k)	$w_i h_i^k$ (k-ft^k)	C_{vx}
Ground	0.0	4059	0	0	**0.000**
Floor 2	18.0	3726	186	691741	**0.004**
Floor 3	30.5	3604	482	1735590	**0.011**
Floor 4	43.0	3604	896	3228861	**0.020**
Floor 5	55.5	3604	1421	5120940	**0.032**
Floor 6	68.0	3604	2051	7392445	**0.046**
Floor 7	80.5	3604	2783	10028694	**0.063**
Floor 8	93.0	3604	3612	13017956	**0.081**
Floor 9	105.5	3604	4537	16350509	**0.102**
Floor 10	118.0	3604	5555	20018089	**0.125**
Floor 11	130.5	3604	6663	24013529	**0.150**
Floor 12	143.0	3604	7861	28330518	**0.177**
Roof	155.5	3327	9147	30431966	**0.190**
				SUM = 160360838	1.000

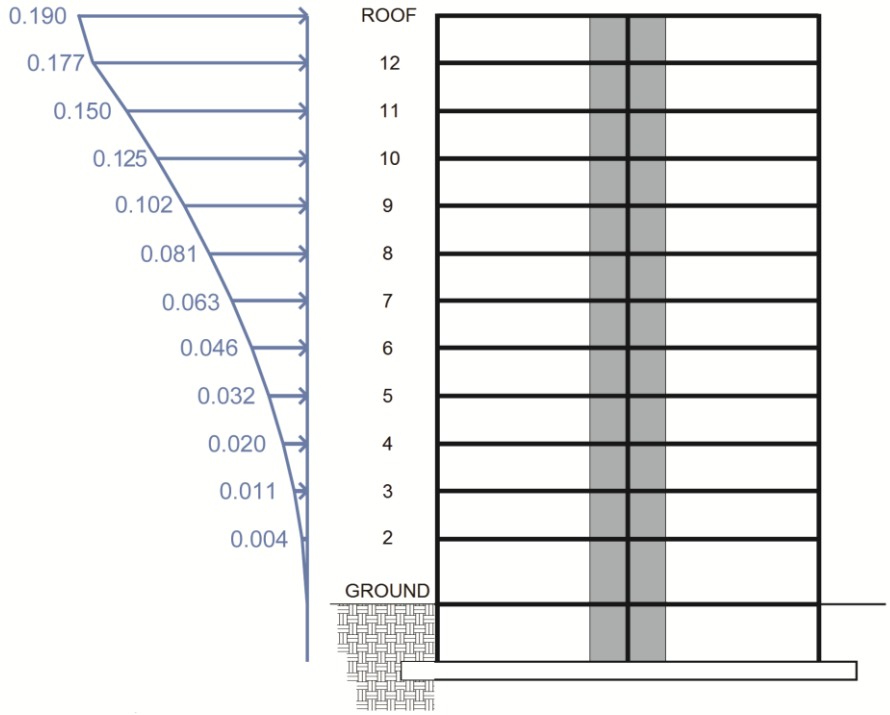

Figure 5.5: Load profile and North-South elevation at wall, FEMA

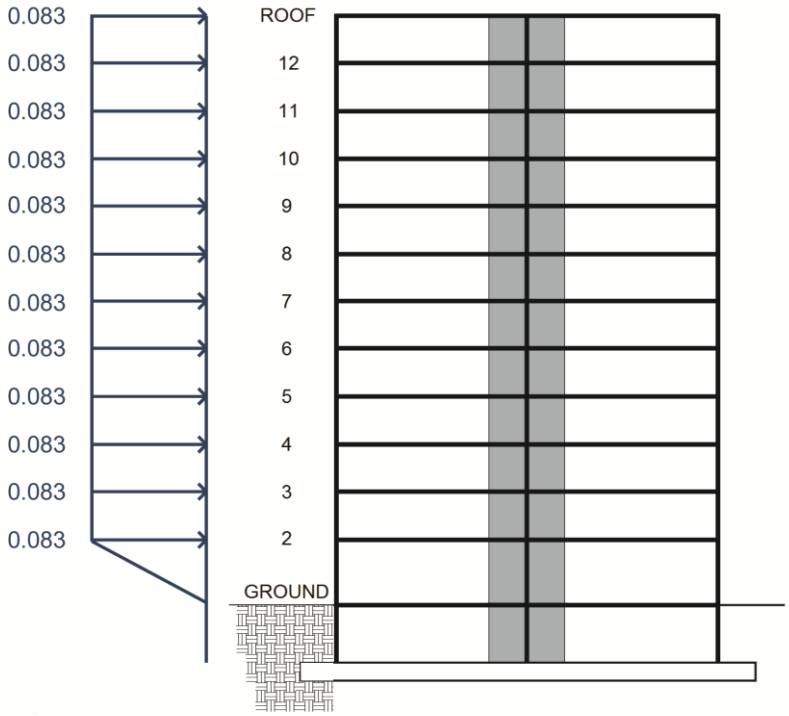

Figure 5.6: Load profile and North-South elevation at wall, uniform

Each lateral load profile was applied at the center of mass to effectively represent earthquake forces. For the asymmetric model, the loads were applied at the center of the structure to be directly compared to the symmetric model. Before the pushover was performed, the dead load was applied as a nonlinear static case so that the weight of the structure would be accounted for. Thus, each static pushover case continued from the state of the structure at the end of the static dead load case. The load application was displacement-controlled, with a target displacement corresponding to a roof drift ratio of about 9%, to allow the base shear force to decrease after the maximum was reached. As such, the structure was pushed until a mechanism formed and the analysis automatically stopped, typically at a displacement much lower than the target. The default nonlinear parameters for solution control were used, except that the maximum total steps allowed for analysis was increased so that the full mechanism could be formed without the analysis stopping prematurely due to total number of steps. The hinge unloading method selected was "apply local redistribution," which is the method that is used for nonlinear direct-integration time history analysis. The plastic hinges were defined to use the isotropic hysteresis type because pushover analyses using hinges defined with the Takeda and pivot hysteresis types would not converge. Additionally, nonlinear geometry P-Delta effects were not included because it prevented the analyses from converging due to a negative slope in the base shear-displacement curve. Since the P-Delta effects were expected to be minimal, it was acceptable to not account for them.

5.2.2 Pushover Results and Discussion

For each pushover analysis performed based on the three profiles previously discussed, the base shear vs. lateral roof drift ratio curve was obtained in the direction of the walls. The total base shear, V_b, was normalized by the effective seismic weight of the first mode, $W_{e,1}$ = 32,930 kips. The comparisons of the three pushover profile results for the symmetric and asymmetric models are shown in Figure 5.7 and Figure 5.8, respectively. Figure 5.9 presents the symmetric model and asymmetric model pushover results in the same plot for direct comparison.

As is commonly observed in pushover analyses, the uniform lateral load profile resulted in the largest base shear forces and the lowest ultimate roof drift ratio, with the highest initial stiffness. In contrast, the code-based FEMA profile had the lowest initial stiffness, smallest base shear forces, and largest ultimate RDR. Thus, the first mode shape profile was bounded by the FEMA profile on the lower end and by the uniform profile on the upper end. However, the first mode shape profile results are much closer in magnitude to the FEMA profile than the uniform profile. While these basic trends are the same for both the symmetric and asymmetric models, the magnitudes and shapes vary. The base shear magnitude of the asymmetric model is lower than the symmetric model for all profiles. Additionally, the ultimate roof drift ratios attained for the asymmetric model do not vary as much and are significantly lower than the symmetric RDRs. For the symmetric model, base shear vs. roof drift ratio curves can be approximated by a tri-linear relationship, if desired. On the other hand, the asymmetric model shows much smoother, rounded curves that do not clearly define the distinct changes from initial stiffness to post-yield stiffness to plateau region as seen in the symmetric curves.

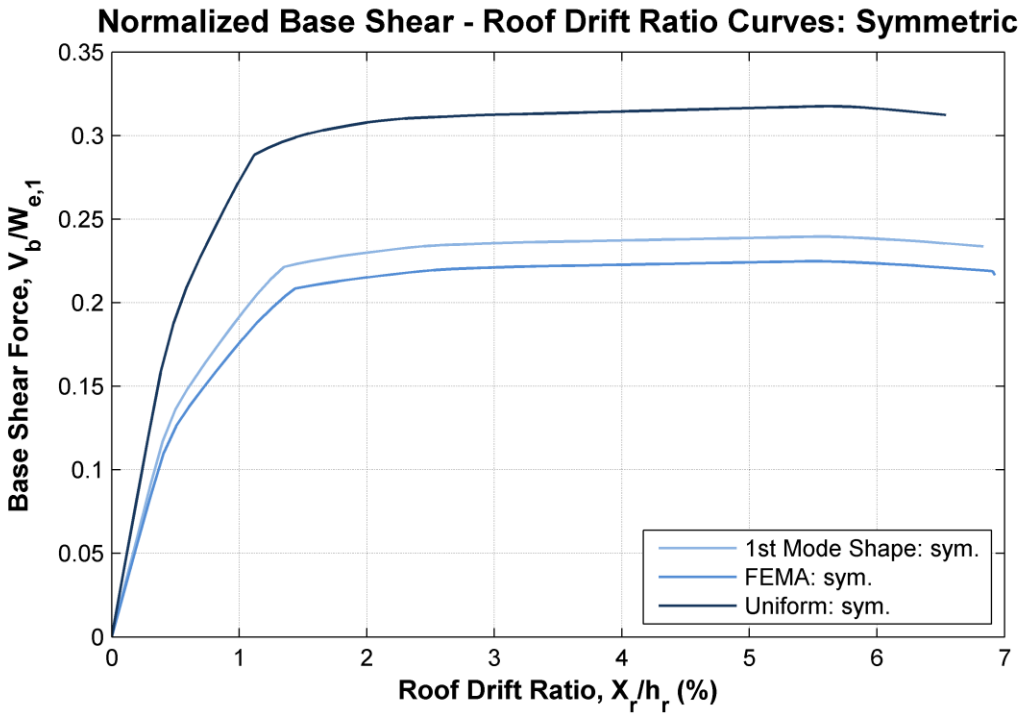

Figure 5.7: Normalized base shear vs. roof drift ratio comparison for symmetric model

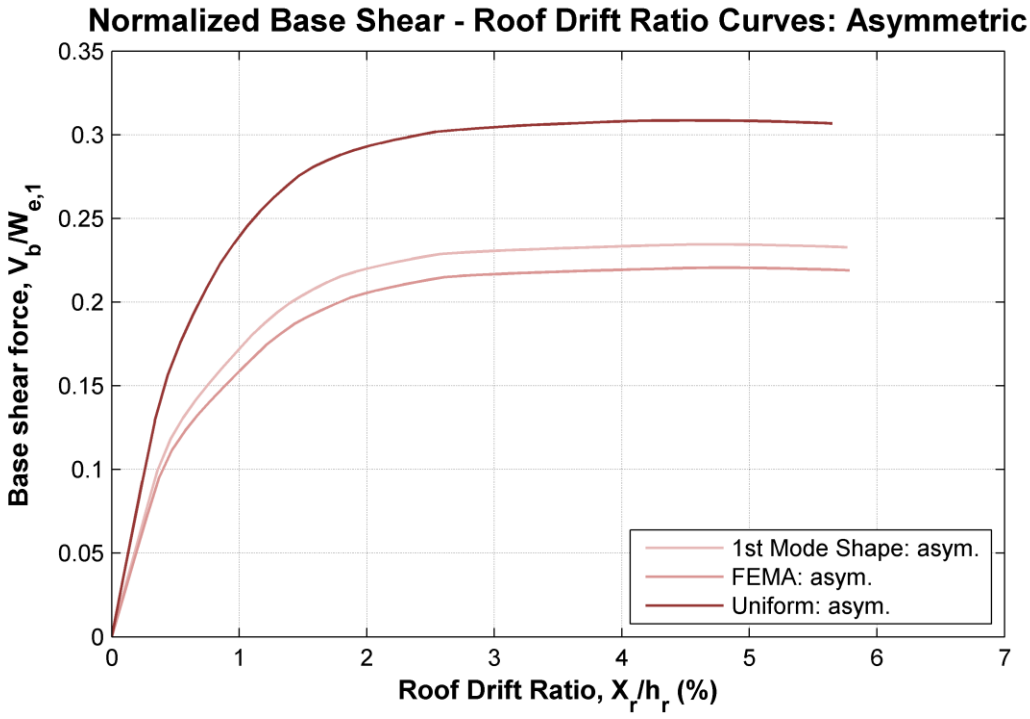

Figure 5.8: Normalized base shear vs. roof drift ratio comparison for asymmetric model

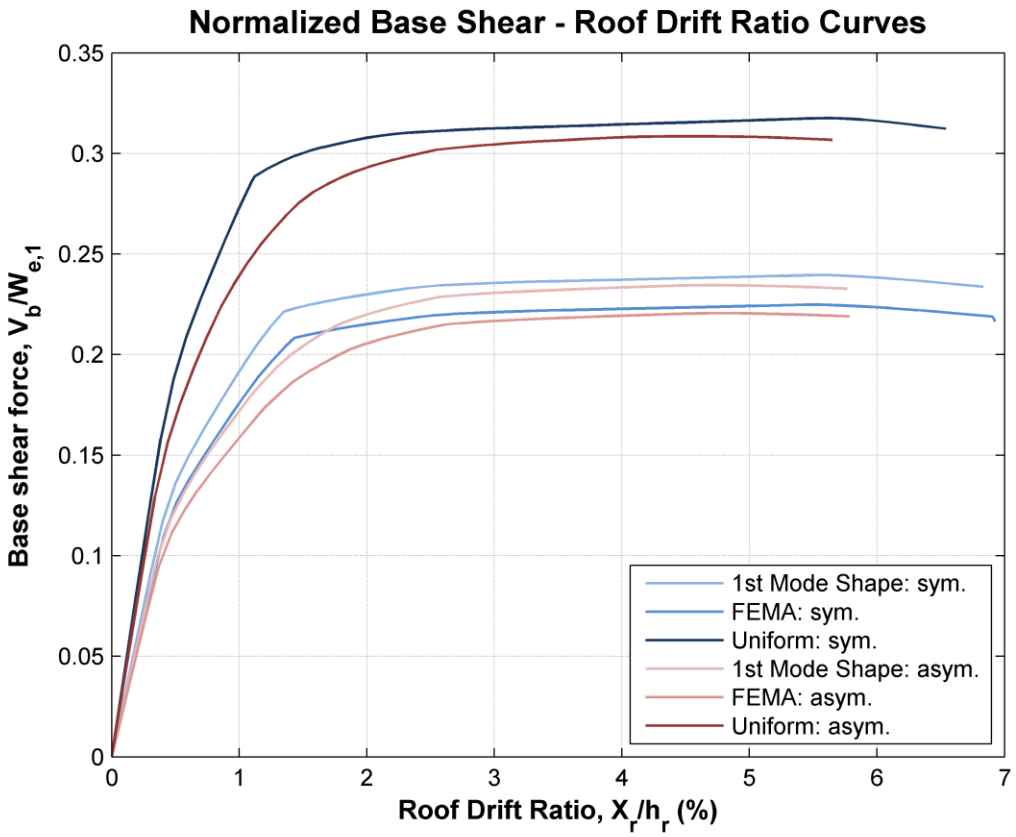

Figure 5.9: Comparison of symmetric model and asymmetric model normalized base shear vs. roof drift ratio results

In terms of expected behavior during a seismic event, the FEMA profile may underestimate the base shear, but has slightly more conservative ultimate roof drift ratio values. The uniform load profile, however, could greatly overestimate the base shear response and underestimate the ultimate roof drift ratio. As such, the first mode shape profile was used to more directly compare the structural response of the symmetric and asymmetric models. To do so, the point on the base shear vs. roof drift ratio curve where the first beam, wall, and column yielded and failed is shown in Figure 5.10. To supplement the figure, Table 5.3 gives the locations and member sections where these hinge states formed. The first yield was measured as Point B on the hinge moment-rotation curve: reference yield for beam and wall sections, and first yield for the columns.

Failure of each member type corresponds to Point E, or the Siv or Civ strain-limit state of the section.

From the comparison plot, it can be seen that the first yield and first failure of each type of member occurred at a larger roof drift ratio for the symmetric model than for the asymmetric model, except for the first beam yields which occurred at almost the same RDR. As such, the displacement ductility capacity of the system is much larger for the symmetric model. For the symmetric model, the first beams that yielded were BM1 sections at mid-height of the building and on Gridlines 2 and 7 of the floor plan at the end of the beams connected to the columns on Gridline C. For the asymmetric model, almost the same floors experienced the first beam yield, but the largest demand occurred only on the beams on Gridline 2 due to the larger stiffness concentrated at the southern half of the floor plan. Similarly, the first beams that failed in the symmetric model were spread symmetrically throughout the structure, mainly the exterior BM1 sections on Gridlines 1 and 8. However, for the asymmetric model, failure first occurred in one beam furthest away from the shear walls: BM1 on Floor 4 of Gridline 1 at Gridline D. While all corner columns and the interior columns on Gridlines 2 and 7 were the first to hinge and fail at the ground level of Gridline B for the symmetric model, the first columns to yield in the asymmetric model were the corner COL1 sections at ground level on Gridline 1, furthest from the walls. However, the first column to fail in the asymmetric model was COL3 on Gridline 2 because it had a larger axial load demand and was less ductile than COL1. The first walls to yield and fail were the two center walls of the symmetric model. However, for the asymmetric model, the wall on Gridline 4 yielded first and none of the walls failed before a mechanism formed in the columns and beams along Gridlines 1, 2 and 3.

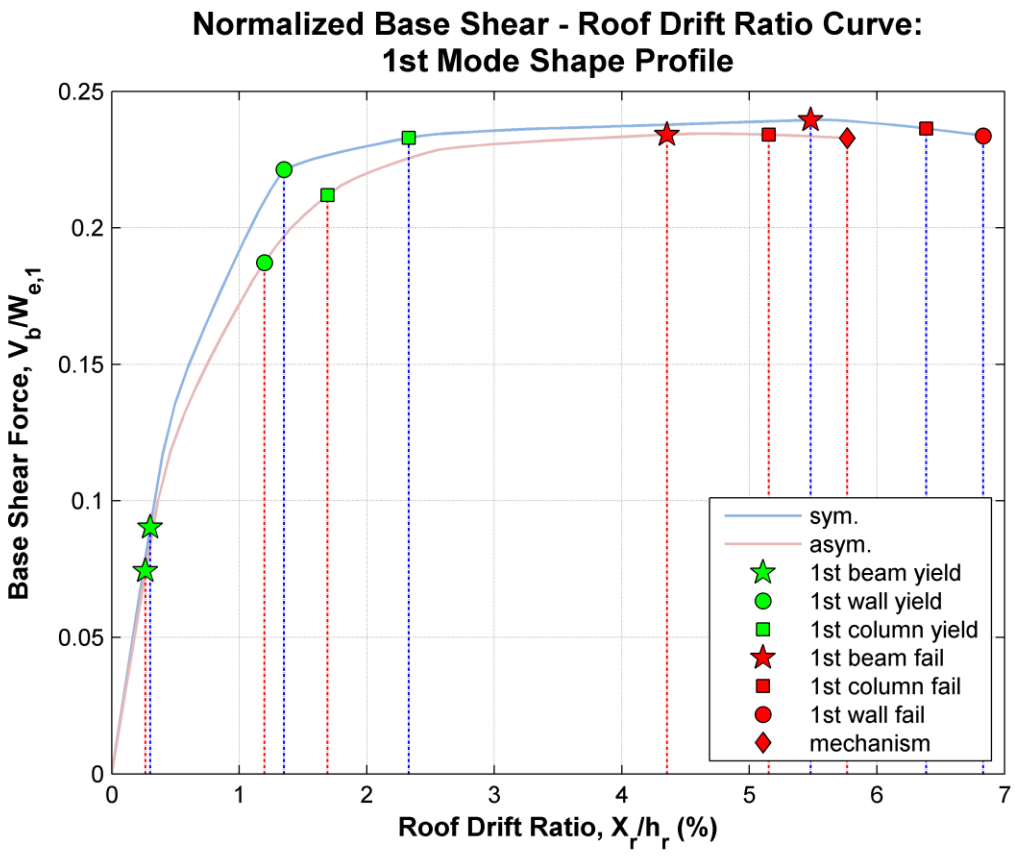

Figure 5.10: Normalized base shear vs. roof drift ratio for first mode shape profile with comparison of monitored hinge states

Table 5.3: Gridline (GL) locations and member sections where monitored hinge states occurred

1st Mode Profile	First Yield		First Fail	
	Symmetric	Asymmetric	Symmetric	Asymmetric
Beams	Floors 5 and 6: BM1 on GL 2 and 7 at GL C	Floors 4 and 5: BM1 on GL 2 at GL C	Many throughout the structure at same time	Floor 4: BM1 on GL 1 at GL D
Columns	COL3 on GL 2 and 7 at GL B; All COL1 (corners)	COL1 on GL 1 at GL A and D	COL3 on GL 2 and 7 at GL B	COL3 on GL 2 at GL B
Walls	WALL45 on GL 4 and 5	WALL45 on GL 4	WALL45 on GL 4 and 5	None

Screenshots of the roof and Gridline 1 elevation of the SAP2000 models at the end of the first mode shape pushover are provided in Figure 5.11 and Figure 5.12, respectively. Red dots represent the failure of a hinge and green, yellow, and orange dots represent the progression of hinges as they approach failure. The magnitudes of the displacements are not to scale when comparing the symmetric and asymmetric figures, so only the hinge formation and shape of the responses can be commented on here. It can clearly be seen that the asymmetric model experiences torsional behavior, with the displacements at Gridline 1 (bottom of roof view figure) being larger than those at Gridline 8 (top of roof view figure). As indicated by the color hinges, the symmetric model forms a mechanism symmetrically on both South and North ends of the model (top and bottom of roof view figure). The asymmetric model, however, has more concentrated hinging away from the walls on Gridline 1, where the displacements are largest.

The elevation screenshots show that all beams on Gridline 1 failed at the end of the first mode shape pushover of the symmetric model, whereas only about the lower two-thirds of the asymmetric model beams hinged. Additionally, the exterior columns of the symmetric model did not fail, but the corner columns on Gridline 1 of the asymmetric model did fail. Thus, the symmetric model formed the desired strong-column weak-beam mechanism, with a linear displacement profile up the height of the structure, displaying pure first mode response. The asymmetric model, however, did not form the true strong-column weak-beam mechanism and the shape of the lateral displacement profile curves slightly. As a result, torsional effects decreased the displacement ductility capacity of the members furthest from the walls due to increased demands at one side of the structure.

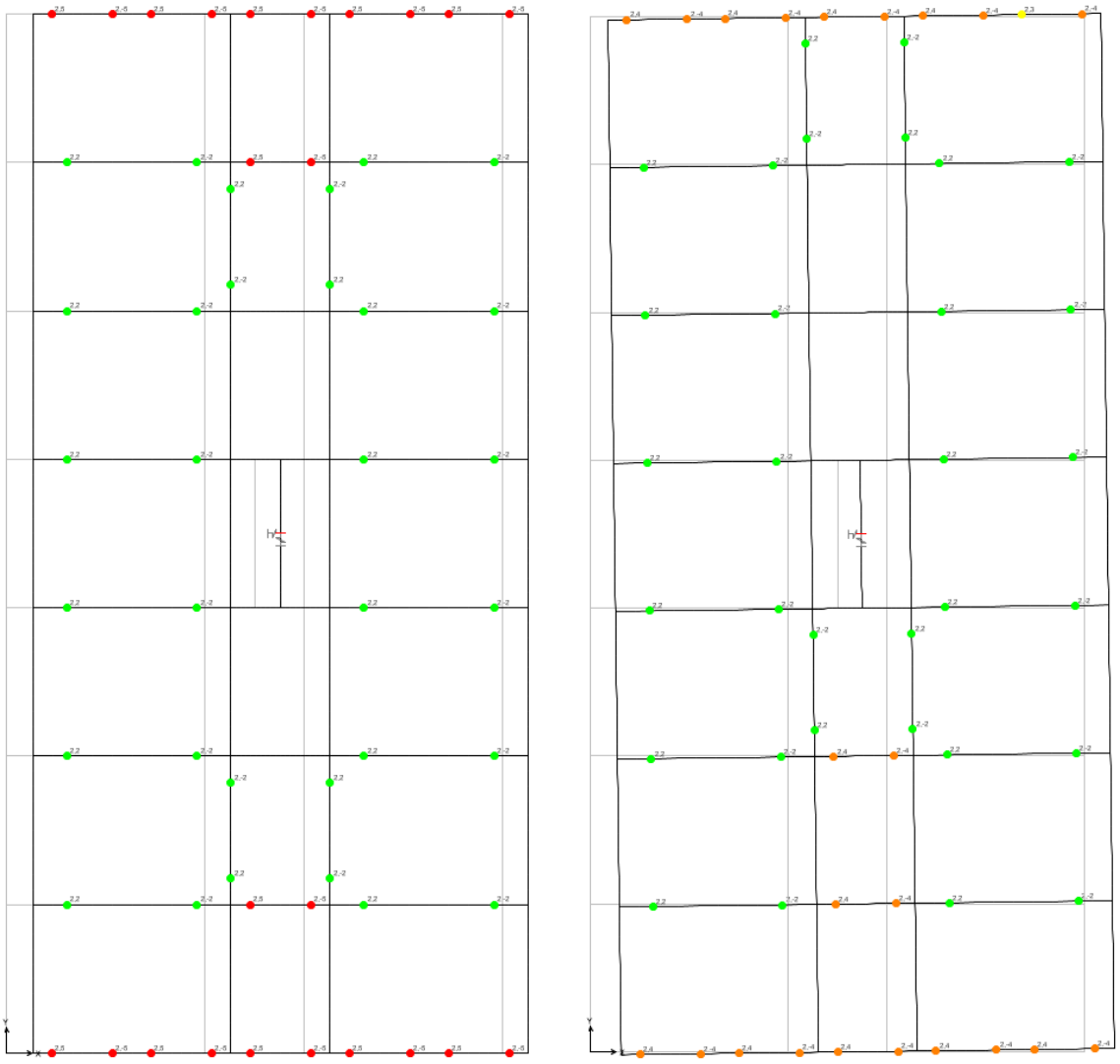

(a) **(b)**

Figure 5.11: Comparison of roof view at end of first mode shape pushover for symmetric (a) and asymmetric (b) models

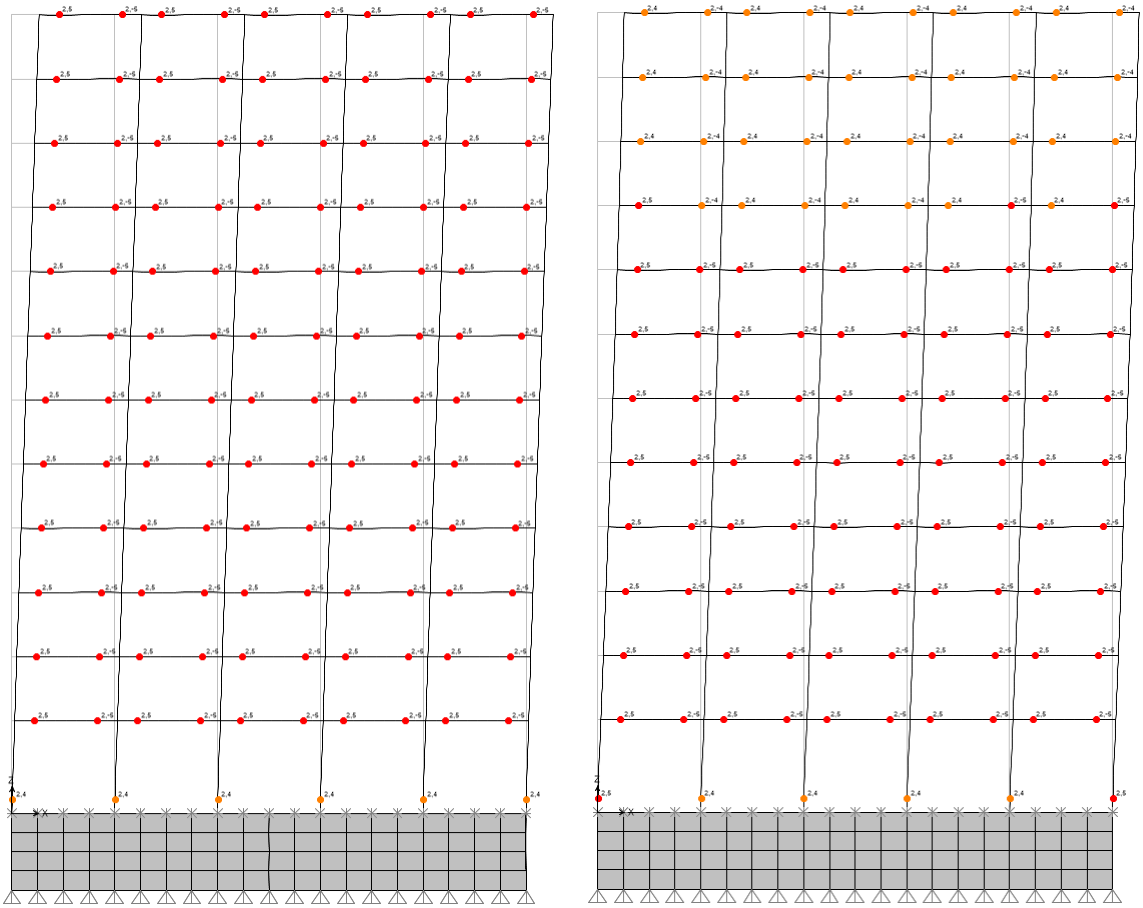

(a) **(b)**

Figure 5.12: Elevation view of Gridline 1 (North end of structure) at the end of first mode pushover for symmetric (a) and asymmetric (b) models

5.3 SAP2000 Nonlinear Time History Analyses and Results

Since ETABS does not account for plastic hinges in dynamic time history analysis, SAP2000 is used to perform another time history analysis that accounts for both material and geometric nonlinearity. The direct-integration time-history analysis method that SAP2000 utilizes to account for plastic hinges takes much more computational effort and time to perform than the FNA method. To reduce the nonlinear dynamic analysis time so that it was feasible to perform, the seven ground motion records needed to be

shortened. In this section, the ground motion studies used to cut the ground acceleration records while still preserving the ground motion characteristics are presented. Additionally, the SAP2000 nonlinear time history analysis parameters used are discussed along with the results of the analyses.

5.3.1 Ground Motion Studies

To reduce the total run-time of the nonlinear time history analysis, the original unscaled suite of seven ground motion pairs were cut to shorter lengths. Studies were done to determine the portion of record that preserved the characteristics of each component (fault normal and fault parallel) of ground motion. The two studies performed were an Arias intensity study and a study of response spectra.

The Arias intensity, I_A, is a calculated measure typically used to find the strong motion duration, which is known to capture most of the energy, of a record. The strong motion duration is defined as the time interval between 5% and 95% of the Arias intensity [11]. The Arias intensity is defined as follows, in units of displacement over time: $I_A = \frac{\pi}{2g}\int_0^{t_d}[a(t)]^2 dt$, where the integral is evaluated over the entire duration of the record, t_d, and $a(t)$ is the ground acceleration time history. Here, the Arias intensity was used to capture the start of the motion and 98% of I_A.

The second study performed on the unscaled ground motion components was based on spectral accelerations and inelastic spectral displacements with 5% damping. The 5% damped spectral accelerations and inelastic spectral displacements were computed based on 10% cumulative increments of the records, such that the first 10%, 20%, 30%, and so on up to 100% of the record lengths were analyzed and compared. In calculating the response spectra, the explicit Newmark integration method was employed

to determine acceleration values for each period, T, of analysis. The inelastic spectral displacements were based on an inelastic response coefficient, R, of 2. A value of R = 2 was used because typically for tall structures, it is found through pushover analysis that displacement ductility demands can be as low as about 2% and the inelastic response coefficient represents ductility for structures with normal occupancy (importance factor of 1.0). Additionally, the Clough hysteretic rule without hardening, shown in Figure 5.13, was used to capture loading and unloading behavior typical of concrete. As shown for this hysteresis, there is a change of stiffness upon yielding, reverse loading, and crossing the x-axis. Additionally, reloading is oriented initially to the yield point and, after the first time, to the point of maximum amplitude. Plots representing the Arias intensity and response spectra studies for each of the ground motion component pairs are presented, along with the uncut record time histories, in Figure 5.14 through Figure 5.20. A summary of the ground motion record study results and the chosen start and stop times of the final records to be used for the time history analyses are presented in Table 5.4.

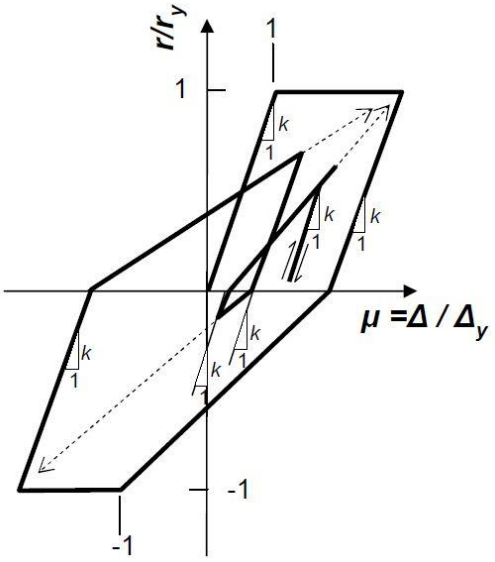

Figure 5.13: Clough hysteretic rule (Figure courtesy of UCSD Professor J. Restrepo, Seismic Design tutorial notes)

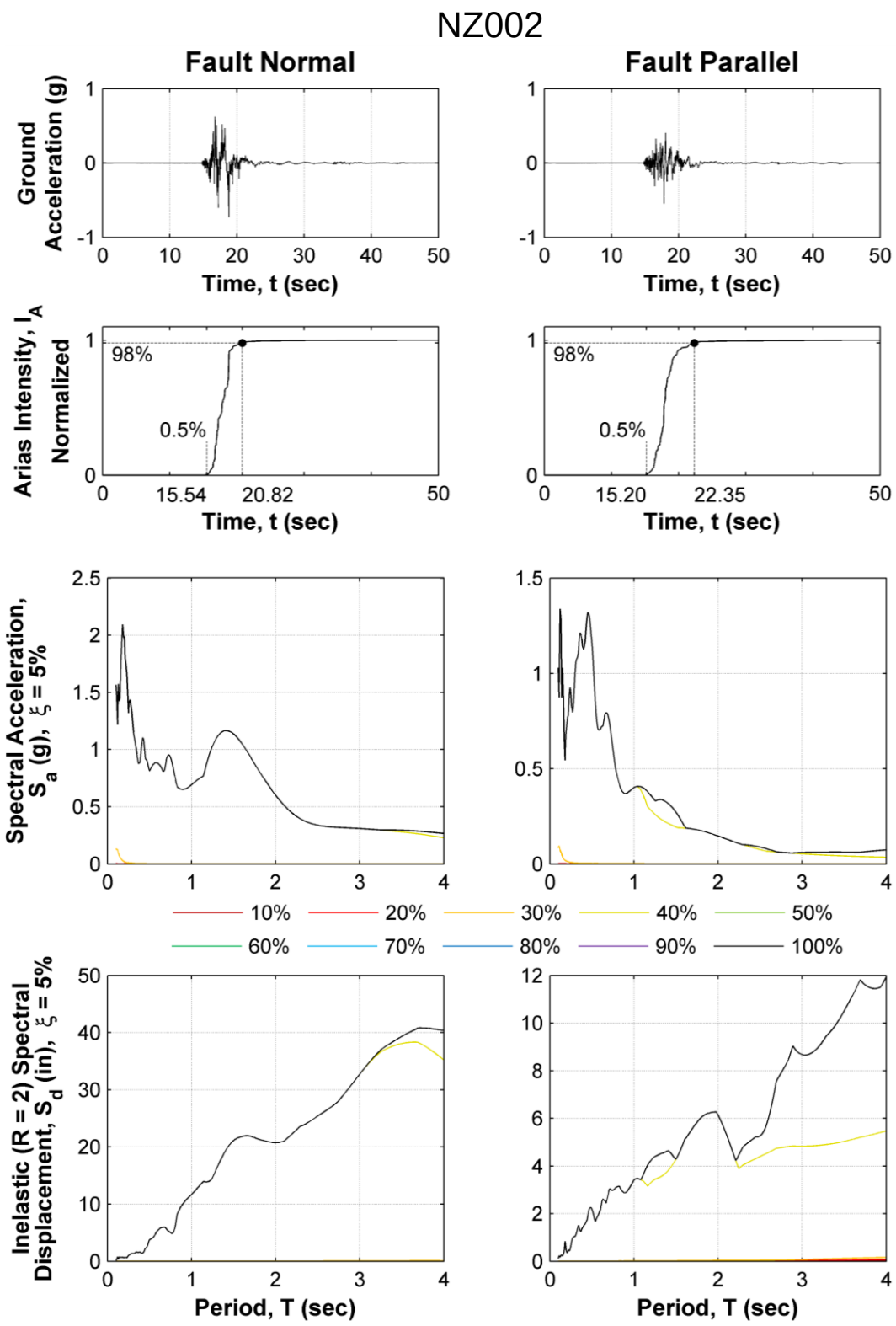

Figure 5.14: Study of original NZ002 ground motion records

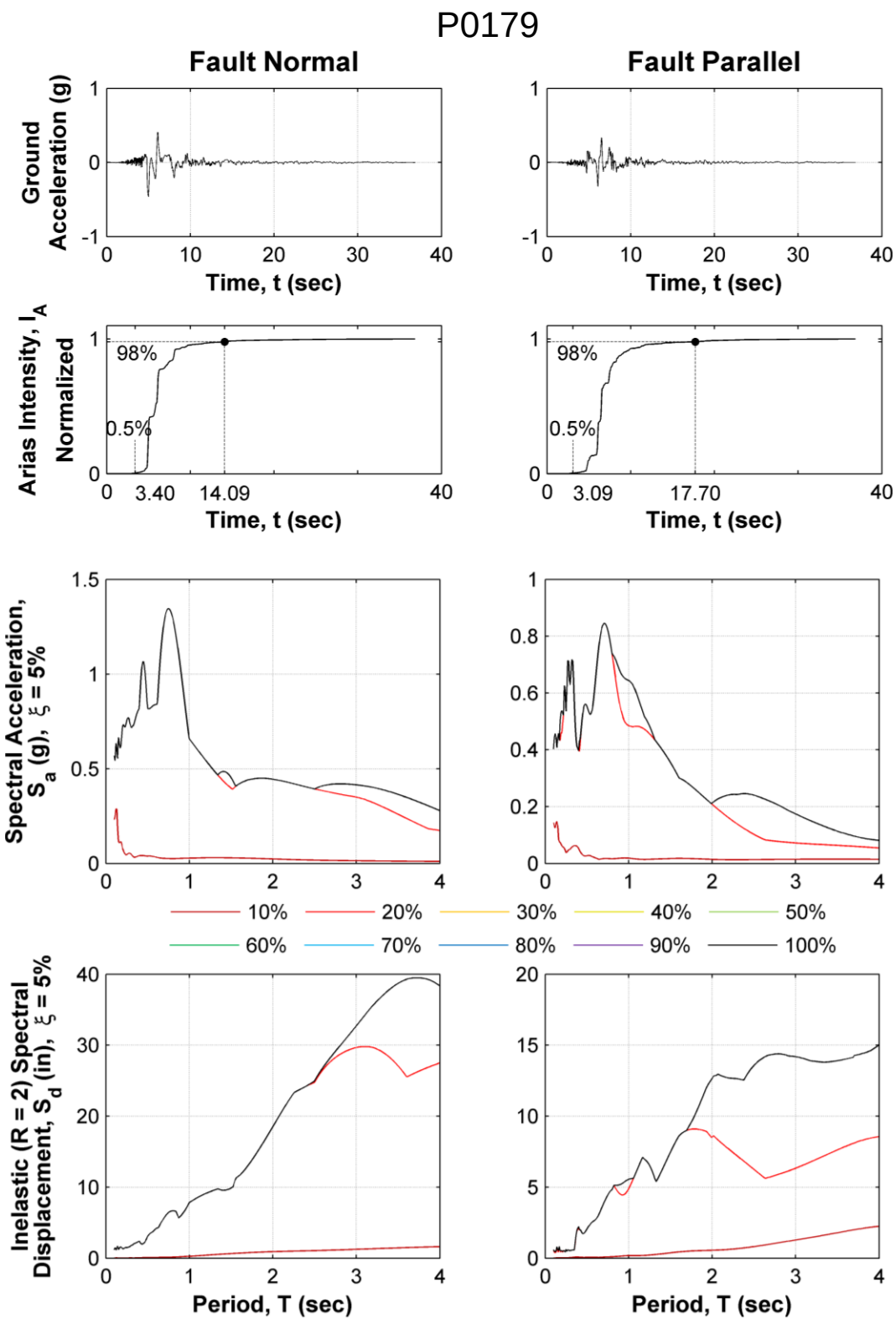

Figure 5.15: Study of original P0179 ground motion records

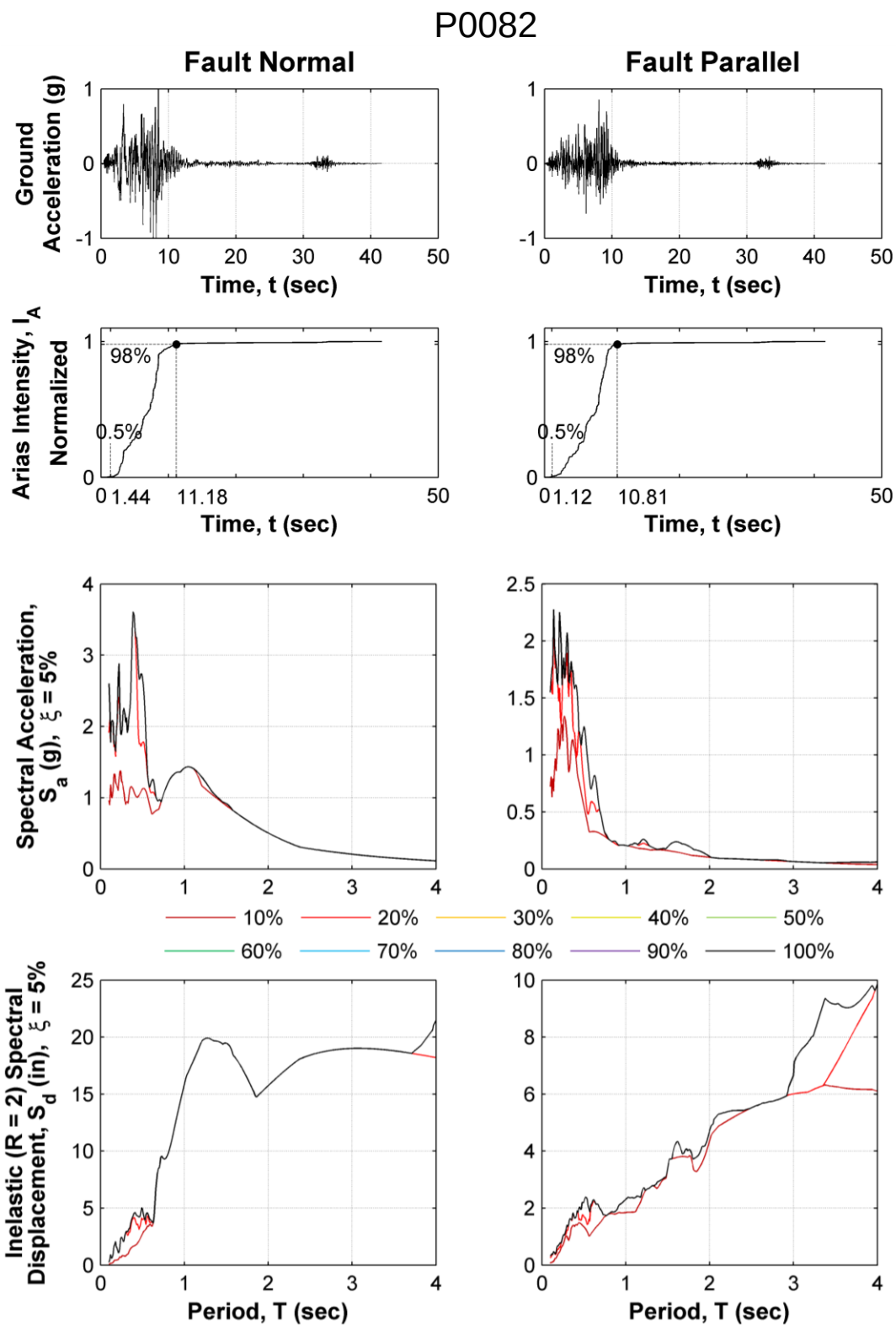

Figure 5.16: Study of original P0082 ground motion records

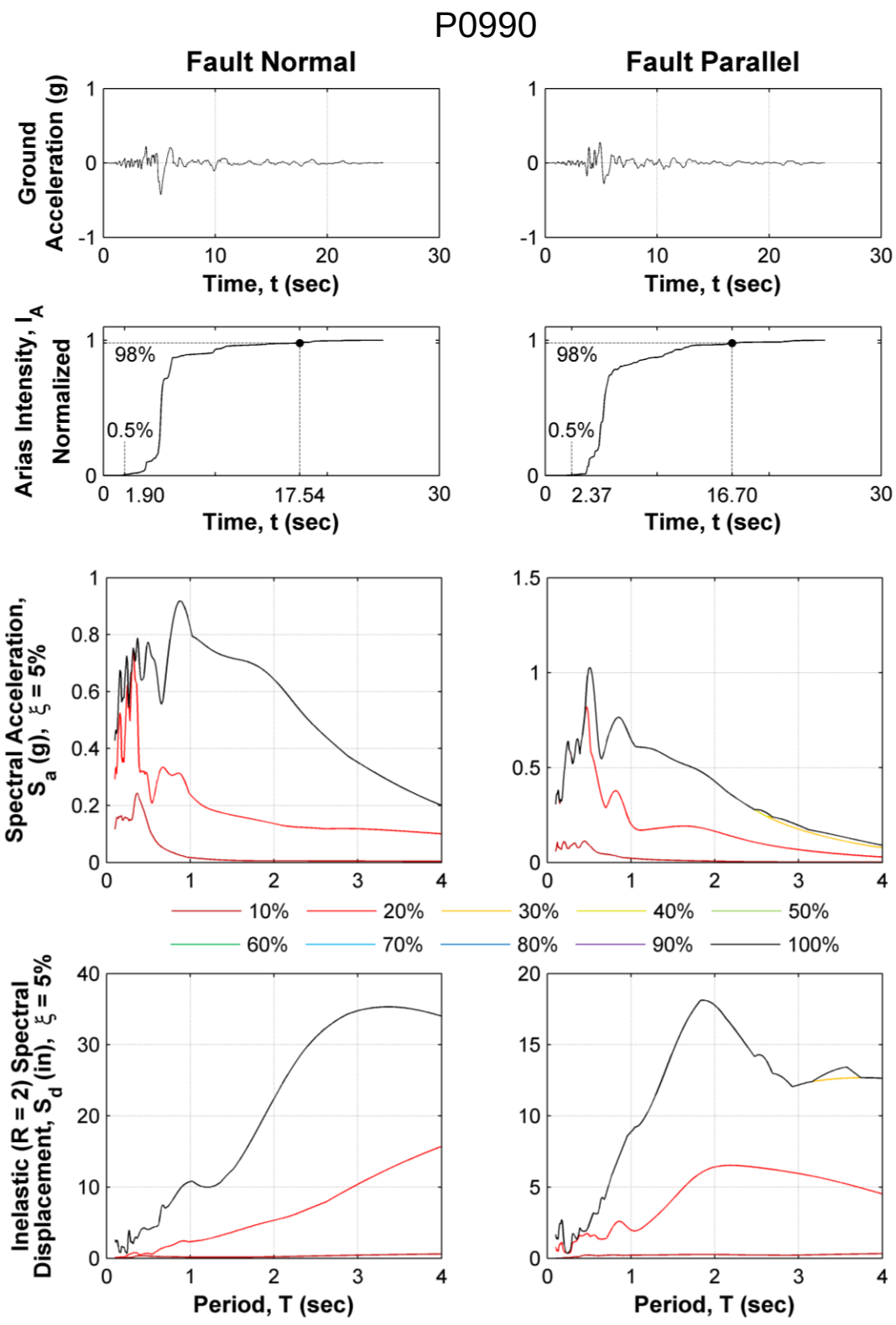

Figure 5.17: Study of original P0990 ground motion records

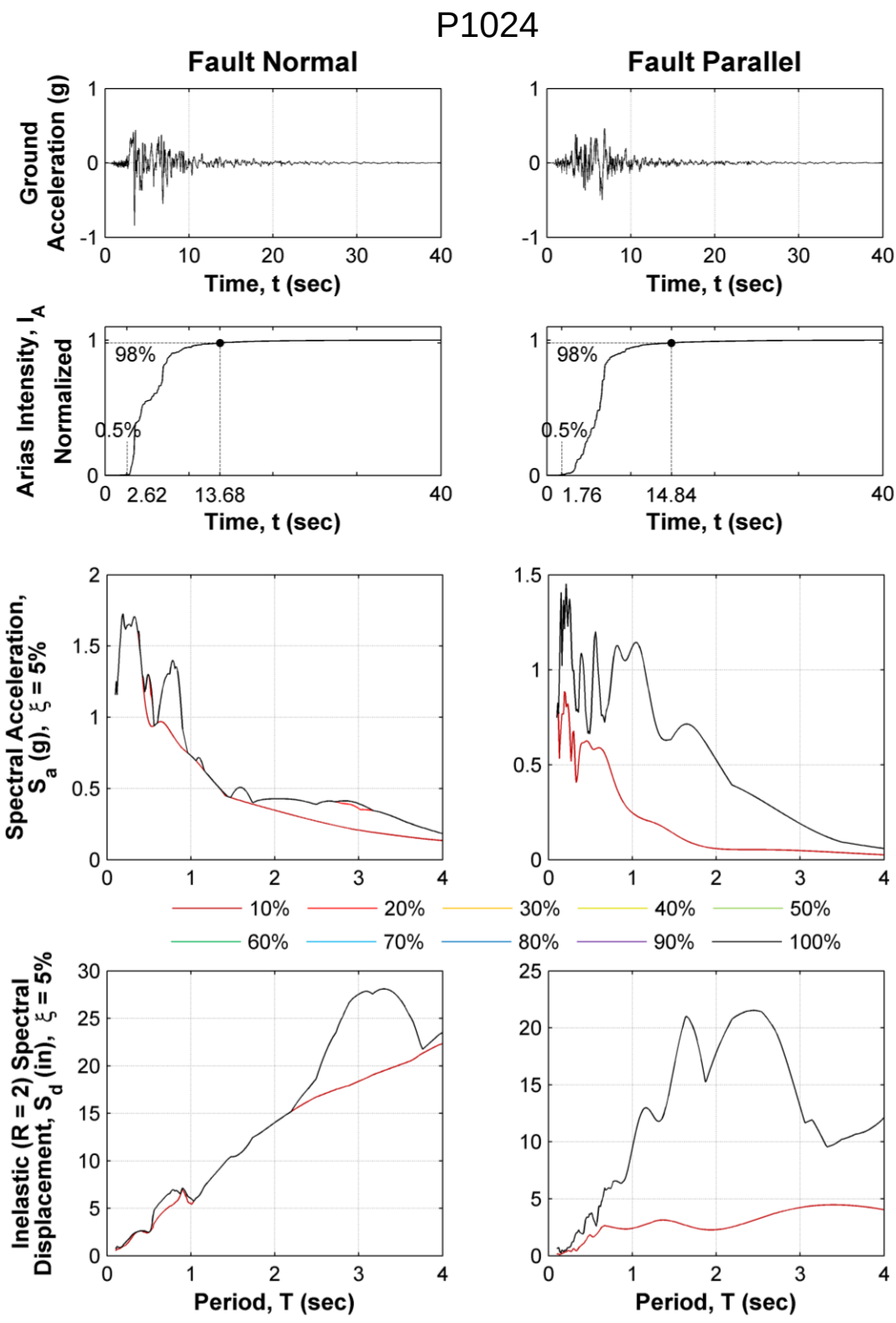

Figure 5.18: Study of original P1024 ground motion records

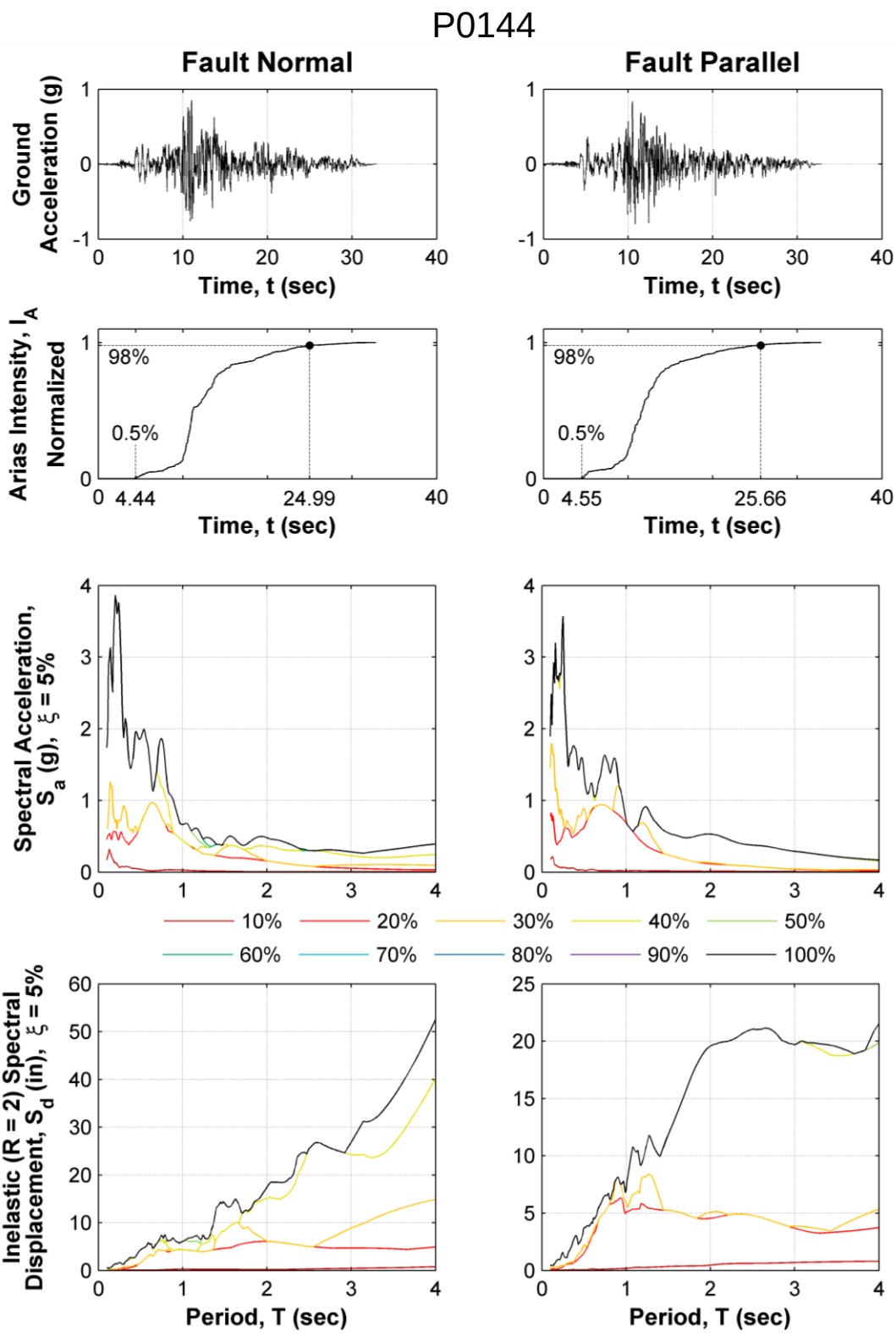

Figure 5.19: Study of original P0144 ground motion records

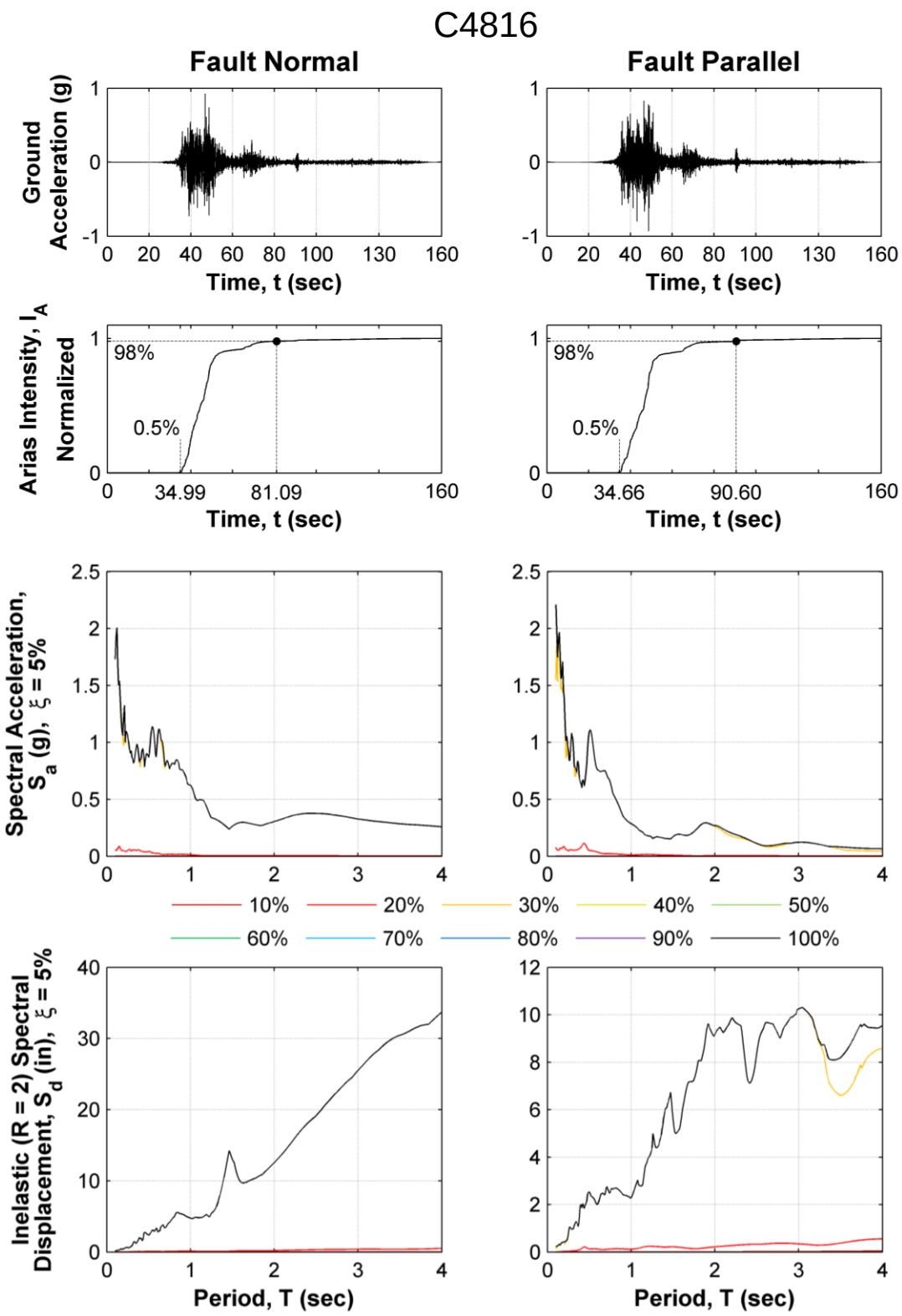

Figure 5.20: Study of original C4816 ground motion records

Table 5.4: Summary of ground motion record studies and chosen new record start and stop times (units: seconds)

Record		Original Record			Arias Intensity			Response Spectra			New Record		
		t_{start}	t_{stop}	Duration	t_{start}	t_{stop}	Duration	t_{start}	t_{stop}	Duration	t_{start}	t_{stop}	Duration
NZ002	FN	0.00	49.94	49.94	14.54	20.82	6.28	9.99	24.97	14.98	10.0	26.0	16.0
	FP				14.20	22.35	8.15	9.99	24.97	14.98			
P0179	FN	0.00	36.82	36.82	2.40	14.09	11.69	0.00	11.05	11.05	0.0	20.0	20.0
	FP				2.09	17.70	15.61	0.00	11.05	11.05			
P0082	FN	0.00	41.64	41.64	0.44	11.18	10.74	0.00	12.49	12.49	0.0	15.0	15.0
	FP				0.12	10.81	10.69	0.00	12.49	12.49			
P0990	FN	0.00	24.99	24.99	0.90	17.54	16.64	0.00	7.50	7.50	0.0	20.0	20.0
	FP				1.37	16.70	15.33	0.00	10.00	10.00			
P1024	FN	0.00	40.00	40.00	1.62	13.68	12.06	0.00	12.00	12.00	0.0	15.0	15.0
	FP				0.76	14.84	14.08	0.00	8.00	8.00			
P0144	FN	0.00	32.84	32.84	3.44	24.99	21.55	0.00	22.99	22.99	0.0	30.0	30.0
	FP				3.55	25.66	22.11	0.00	19.70	19.70			
C4816	FN	0.00	160.00	160.00	33.99	81.09	47.10	16.00	64.00	48.00	20.0	80.0	60.0
	FP				33.66	90.60	56.94	16.00	64.00	48.00			

As shown in Table 5.4, the start and stop times and corresponding duration of each ground motion component record are defined for the original record, the Arias intensity study, and the response spectra study. For the Arias intensity, the start of the ground motion is taken as the time at 0.5% of the Arias intensity minus one second, or $t_{start,I_A} = t(I_A = 0.5\%) - 1\ sec$. The stop time is defined as the time at which the Arias intensity reached 98%: $t_{stop,I_A} = t(I_A = 98\%)$. For the response spectra, the start time was typically taken as the original record start time of 0 seconds. However, for the NZ002 and C4816 records, the response spectra values were essentially zero for the first 10% of the records, so the start times for those records were chosen to be the 10% mark. The response spectra stop time for each record was determined as the first cumulative time interval that converged with the spectral values of the 100% record.

The new record start and stop times were then chosen, at the discretion of the author of this thesis, based on a combination of the Arias intensity and response spectra start and stop times. Although some of the start and stop times from the studies were different for the fault normal and fault parallel components of a given ground motion, the new record components had to be the same length. Thus, both components were accounted for when determining the appropriate start and stop times. For the cut records that started later than the original records, the records were shifted so that they started at an analysis time equal to zero seconds. A summary of the final unscaled acceleration time histories used in SAP2000 is presented in Figure 5.21.

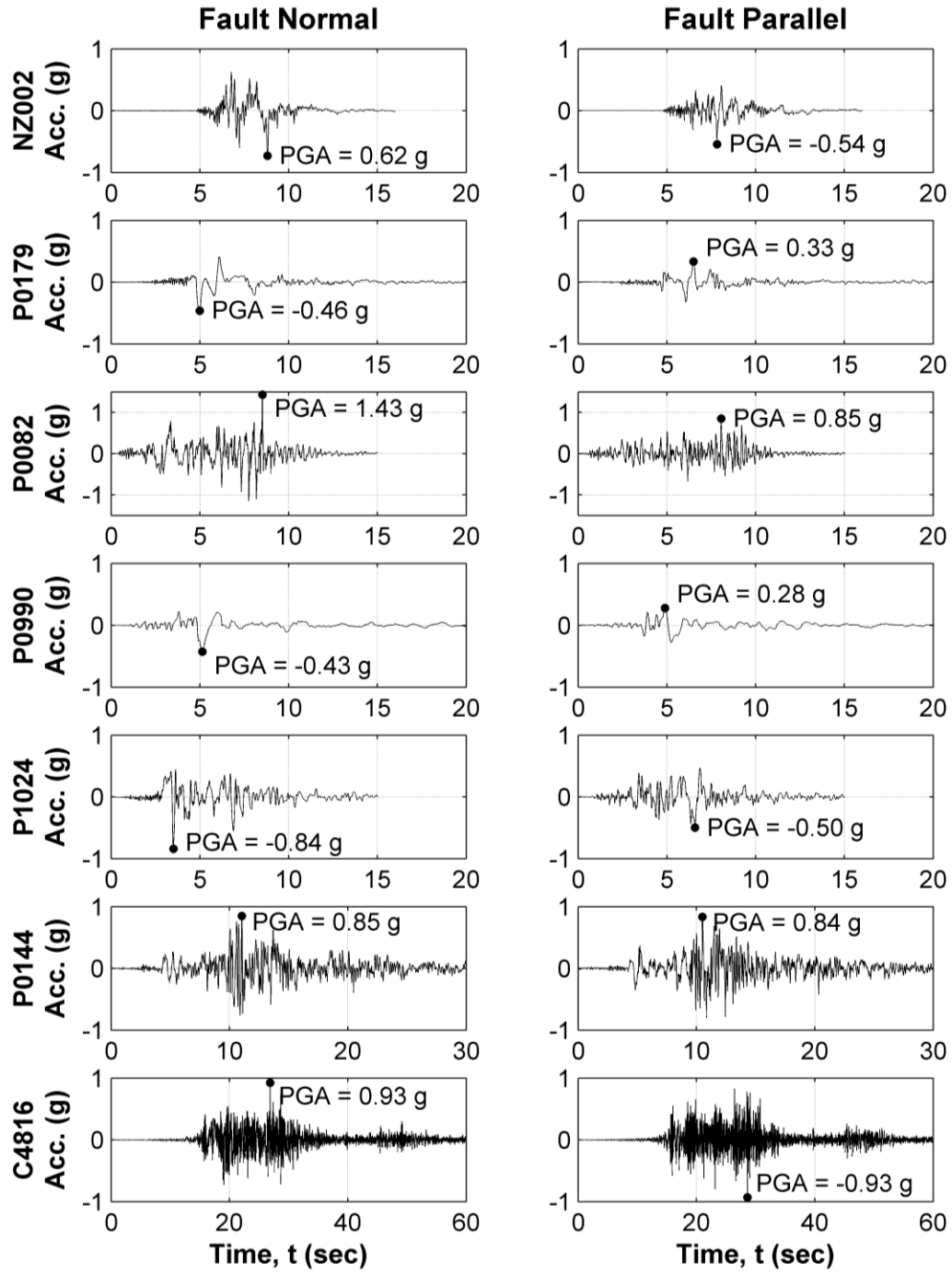

Figure 5.21: Acceleration time histories for all ground motion records (unscaled and cut)

5.3.2 Analysis Parameters

Similar to the time history analysis performed in ETABS, 14 independent nonlinear time history cases were created in SAP2000 to account for the DBE and MCE level scaling of each pair of ground motion. As before, the appropriately scaled fault normal acceleration records were applied in the direction of the walls (E-W, or global X-direction of the model) and fault parallel accelerations were applied in the direction of the frames (N-S, or global Y-direction). Each case was defined as a nonlinear direct-integration time history that started from the state of the structure at the end of a nonlinear static dead load case, as was done with the pushover analyses, to account for the weight of the structure. Nonlinear geometric P-Delta effects were included. Rayleigh proportional damping was assigned as 2% of critical in the 1^{st} and 10^{th} modes.

The time integration method used was the recommended Hilber-Hughes-Taylor method, with $\gamma = 0.5$, $\beta = 0.25$, and $\alpha = 0$, was used and is essentially the same as the Newmark Beta integration method. For the nonlinear solution control parameters, the maximum substep size was set to 0.01 seconds. Since this substep size has a strong correlation to the amount of time the analysis takes to run, the largest time step deemed reasonable was used. A sensitivity analysis was performed for one of the ground motion records, and although a maximum substep size of 0.005 seconds gave slightly more accurate results, the almost doubled analysis time was not worth the small improvement in accuracy. Another parameter a user can input to control analysis time is the minimum substep size. The SAP2000 program starts the analysis with the maximum substep size and automatically decreases it if the analysis has trouble converging, with the minimum substep size as a lower limit. Thus, if the analysis cannot converge at the assigned

minimum substep size the analysis will terminate. When trying to keep the analysis time as short as possible, a minimum substep size of 0.0025 was tried, but the NZ002 case would still not converge after the first large peak in acceleration. In order for the analyses to converge, the minimum substep size was ultimately set to zero for all time history cases, resulting in a longer total analysis time but complete and converged analyses. For the rest of the nonlinear solution control parameters, including the number of iterations per step allowed and the iteration convergence tolerance, the SAP2000 default values were sufficient. The output time step size used for recording data was the same as used in the ETABS THA (Table 5.1).

To account for nonlinear concrete hysteretic behavior, the pivot hysteresis type was assigned to all hinges. The default properties were used except that β_1 and β_2 were set to 0.85, which was chosen to be slightly higher than the default 0.7 to increase energy dissipation. It should be noted that the Takeda hysteresis type was originally assigned to the hinges, but the time-history analyses would not converge after a large peak in ground motion acceleration. Thus, the pivot method was found to be more stable and convergence was not an issue. It should also be noted that although the isotropic hysteresis was used for the static pushover analyses because the Takeda and pivot hysteresis types would not converge, the hinge behavior for the nonlinear time history analysis was able to accommodate more complex hysteresis types because the hinges were not loaded to failure.

5.3.3 Results and Discussion

As was done with the ETABS THA, to evaluate the response of the symmetric and asymmetric structural models under seismic loading, the peak relative displacements over the height of the structure and the peak interstory drift ratio envelopes were computed from the displacement time histories at the corner 1-D (Gridline 1 and Gridline D intersection). These envelopes are found in both the direction of the walls and the frames for the design basis earthquake level and maximum considered earthquake level. The geometric mean of all ground motions was computed and is shown in each envelope plot. Additionally, the displacements and resulting PRD and IDR envelopes were found at the center of the asymmetric model and compared to the results found at corner 1-D. Residual drifts and displacement values are not found, since several seconds of zero acceleration would need to be added to the end of the ground motions to allow for free vibration of the structure and thus would increase the computational time, which is not practical or necessary for the goals of this thesis.

To further compare the results, the total system overturning moment in the direction of the walls, $M_{O,E\text{-}W}$, was determined for a single ground motion record pair at the DBE level. The ground motion chosen to be examined is NZ002 because the peak relative displacement and interstory drift ratio envelope results in the direction of the walls was closest to the geometric mean of all seven ground motions. The total system overturning moment was found by the summation over all floors of the product of the i^{th} floor X-direction acceleration, the i^{th} floor weight, and the distance from the ground level to the i^{th} floor. For both the symmetric and asymmetric models, the floor accelerations were measured at the center of the building, which was about the same as the average

accelerations of each floor. The system overturning moments were normalized by the seismic weight, W, of the structure times the roof height, h_r, measured from the ground.

A comparison of the envelopes for the symmetric and asymmetric models, both measured at corner 1-D, is shown in Figure 5.22 for the DBE level and Figure 5.23 for the MCE level. A bar plot comparison of the maximum roof drift ratio and maximum IDR, using the geometric mean, is provided in Figure 5.24, while the roof drift ratio time history, normalized system overturning moment time history, and the normalized overturning moment - RDR hysteresis are shown in Figure 5.25. A discussion of the symmetric vs. asymmetric results is provided at the end of these four figures.

The comparison of the envelopes measured at corner 1-D and the building center for the asymmetric model is shown in Figure 5.26 for the DBE level and Figure 5.27 for the MCE level. A bar plot comparison of the maximum roof drift ratio and maximum IDR, using the geometric mean, is provided in Figure 5.28, while the roof drift ratio time history, normalized system overturning moment time history, and the normalized overturning moment - RDR hysteresis are shown in Figure 5.29. A discussion of the asymmetric model corner vs. center results is provided at the end of these four figures.

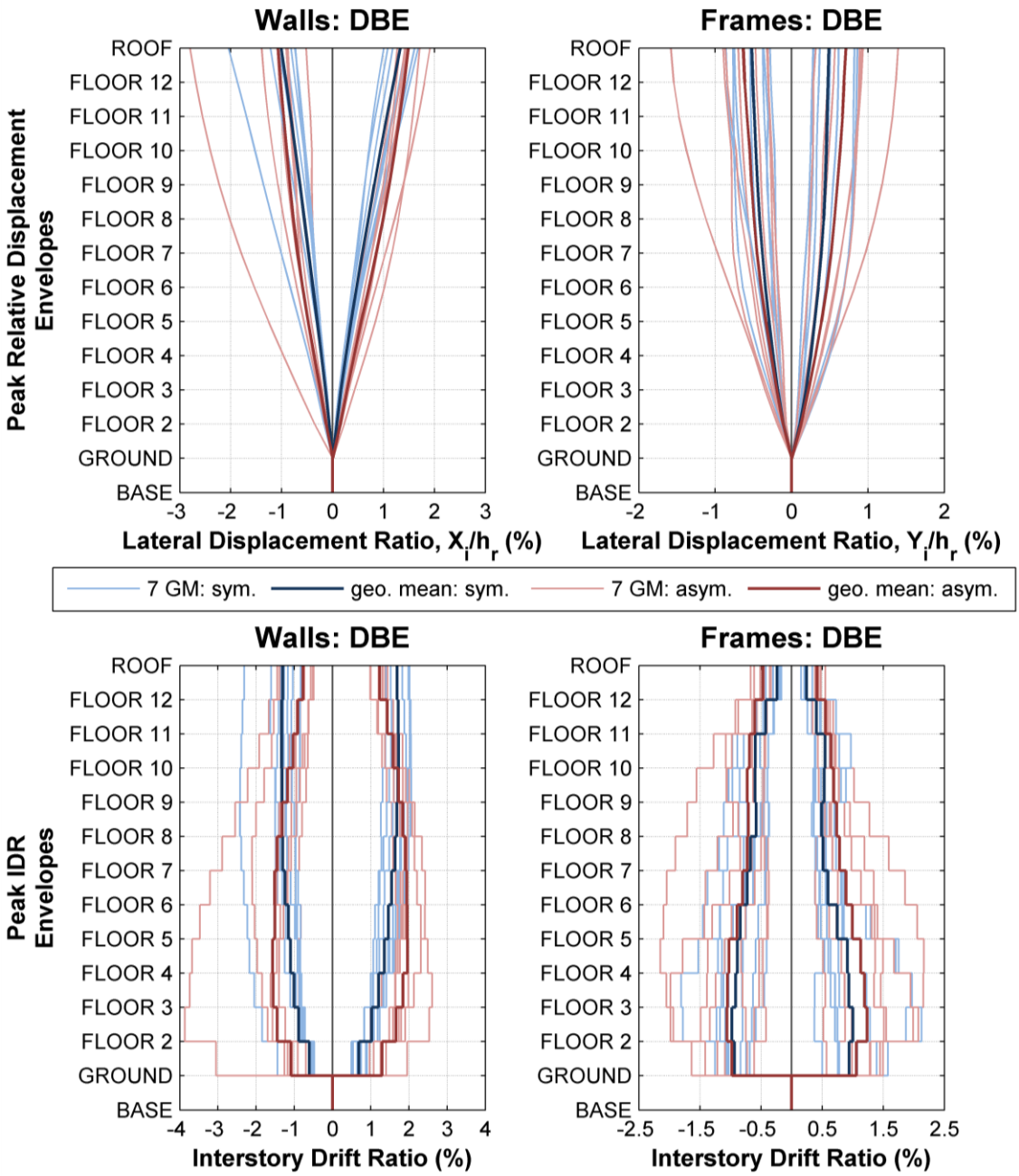

Figure 5.22: Envelopes for symmetric and asymmetric cases at DBE level

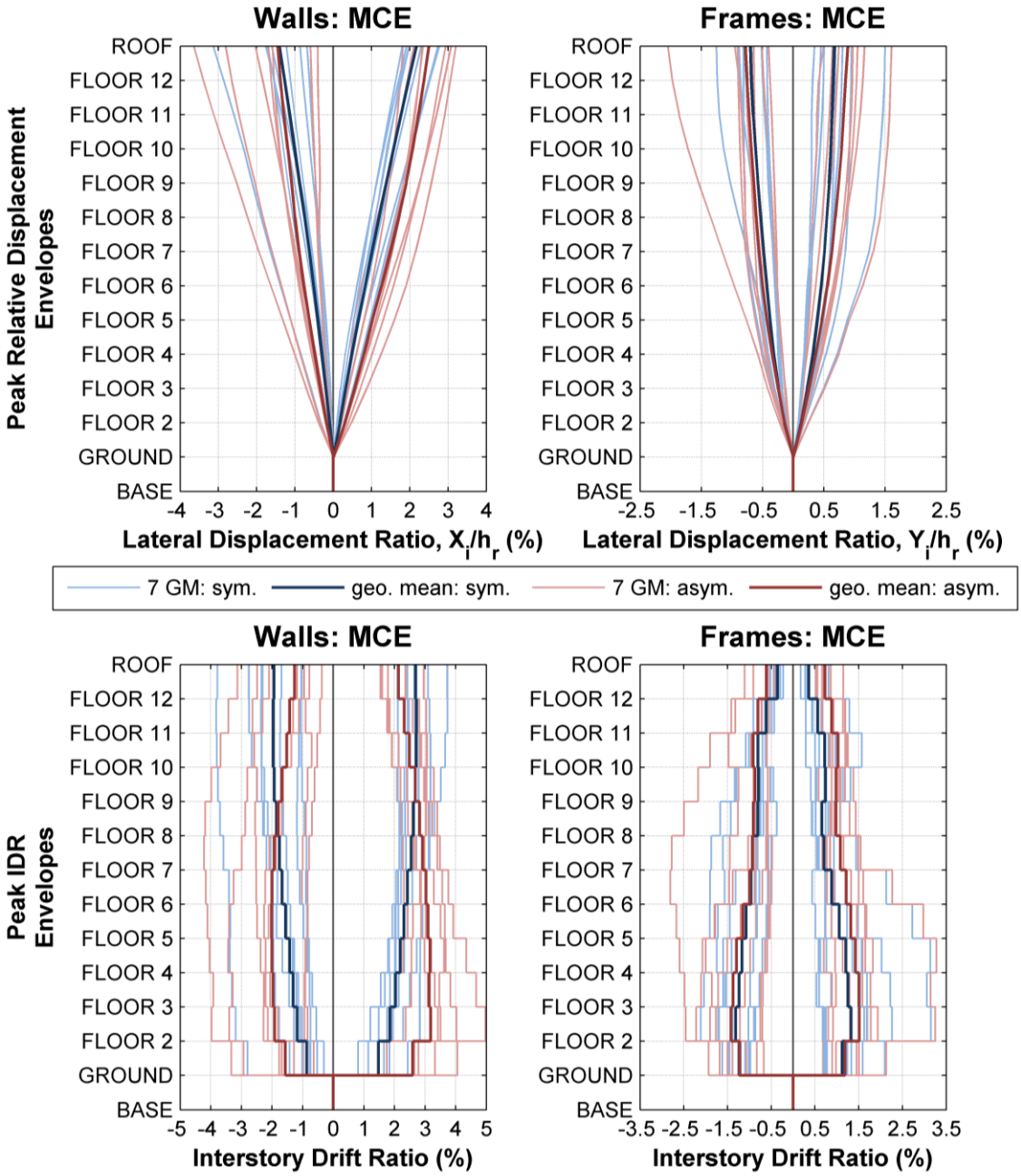

Figure 5.23: Envelopes for symmetric and asymmetric cases at MCE level

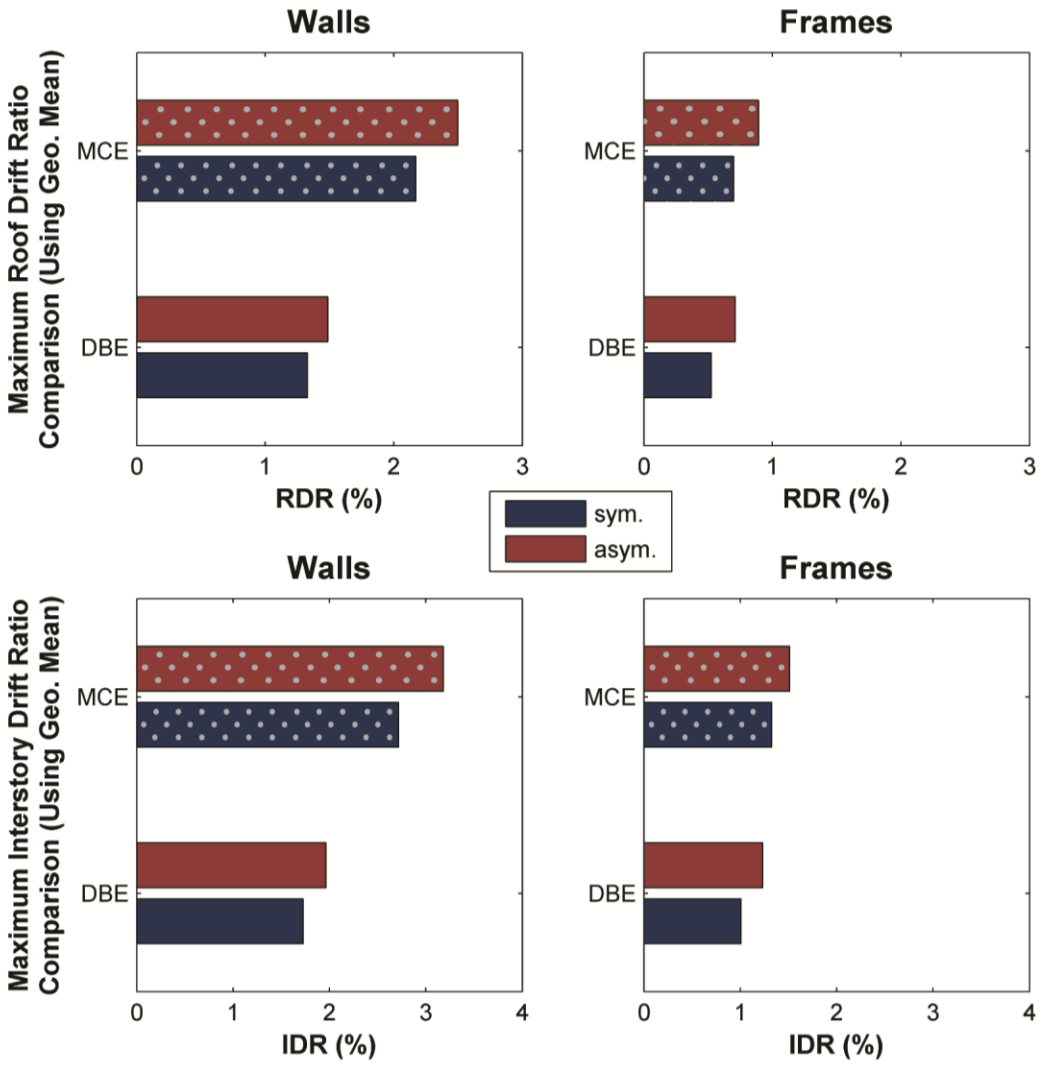

Figure 5.24: Comparison of symmetric and asymmetric model nonlinear THA results

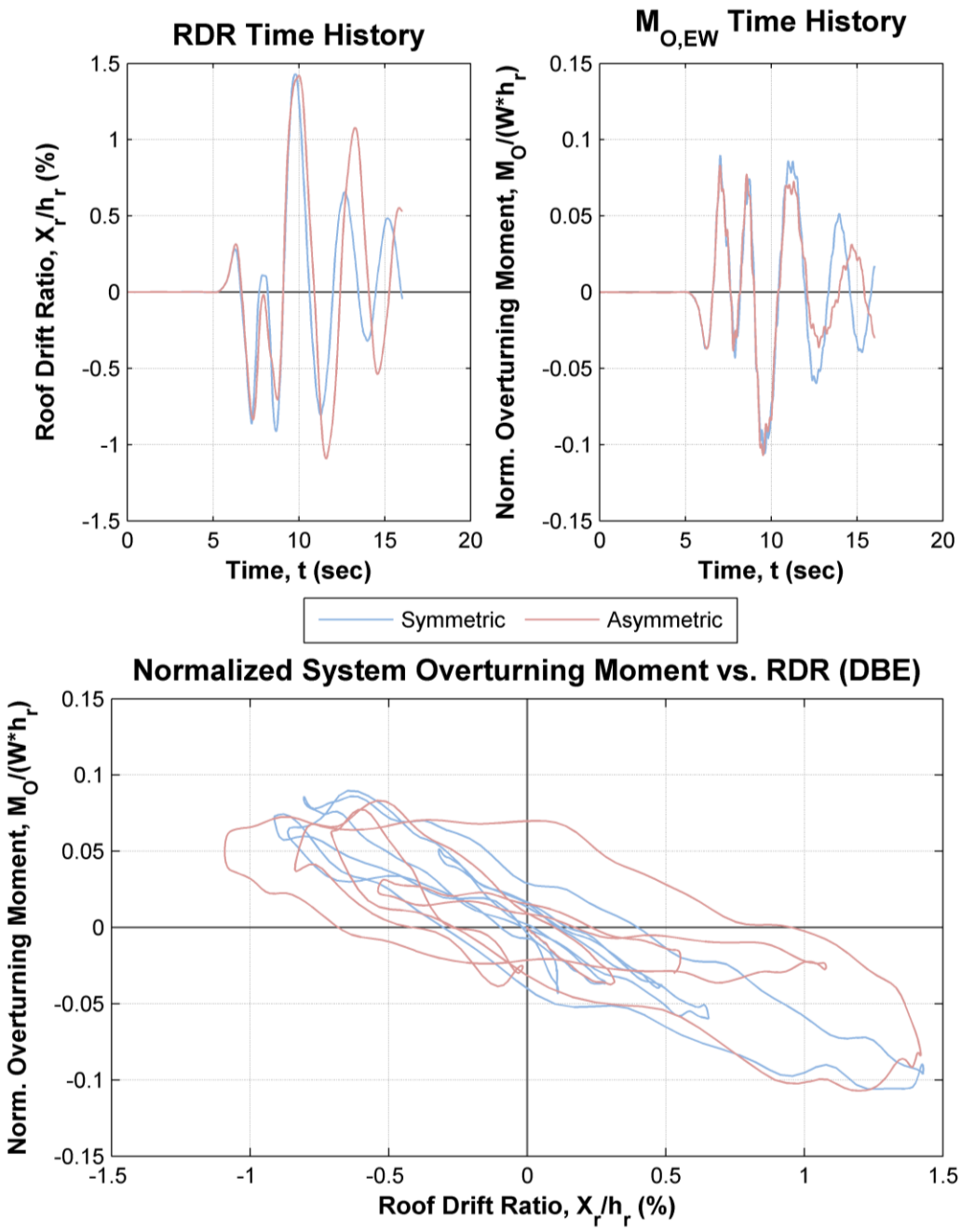

Figure 5.25: Roof drift ratio and normalized system overturning moment comparison of symmetric and asymmetric model for NZ002 at DBE level

As was the case for the essentially linear ETABS THA results, the peak relative displacement envelopes for the asymmetric model reach a larger magnitude than those of the symmetric model in both the direction of the walls and the direction of the frames. Due to the nonlinear behavior, the PRD envelope is not symmetric for the wall direction under the DBE level ground motions, and the asymmetry of the envelopes is even further pronounced at the MCE level because the hinges are pushed further into the nonlinear range. For the frame direction, the PRD envelopes are nearly symmetric at the DBE level, meaning the frames have minimal inelastic response. However, the envelopes are less symmetric for the MCE level, again because the larger demand of the ground motions causes increased nonlinear response. For the frame direction, the asymmetric model shows more asymmetry in the envelopes than the symmetric model, showing that the effect of nonlinearity in the frame direction is amplified with torsional response. As observed in the ETABS THA, the shapes of the symmetric model response envelopes are typical and expected for shear wall and frame structures. Again, the asymmetric model PRD envelopes in the wall direction are more curved than the symmetric model because the influence of the frames where the results are measured, at the corner furthest from the shear walls, is more pronounced. For the frame direction, the PRD envelopes mostly resemble the first North-South mode shape for the DBE level, but for the MCE level, the shape becomes distorted.

Like the PRD envelopes, the peak IDR envelopes are less symmetric in the wall direction than in the frame direction, with the nonlinear effects being amplified at the MCE level. Additionally, the IDR envelopes are more asymmetric for the asymmetric model than the symmetric model for both levels of ground motion. The shape of the IDR

envelopes in the direction of the walls for the asymmetric model shows how torsion causes the IDRs at the lower half of the building to be the largest. However, unlike the ETABS results, the IDRs toward the roof and toward the ground level are fairly similar in magnitude because higher mode effects are more apparent when nonlinear hinges form. This effect of higher modes is more pronounced in the IDR envelopes of the frame direction, which tend to bottle-neck between Floors 8 and 9. Higher mode effects are also more apparent in the SAP2000 analysis results because, due to the assigning of Rayleigh proportional damping in the first and tenth modes, the effective damping ratio on the second through ninth modes is less than 2% (see Figure 7.33 in appendix). Thus, modes 2 through 9 have a greater impact on the structure's response than when 2% damping is assigned to all modes.

From the bar plot comparison of the symmetric and asymmetric model responses, it is clear that both the maximum roof drift ratio and maximum interstory drift ratio responses are much larger in the direction of the walls than the frames. This is consistent with the more demanding fault normal accelerations than the fault parallel accelerations and is expected of the results. It can also be seen from the bar plot comparison that the difference in magnitude between the DBE level and MCE level responses is more pronounced in the wall direction than the frame direction, for both symmetric and asymmetric models. Additionally, the asymmetric model experienced larger maximum responses than the symmetric model. The largest difference between the symmetric and asymmetric response magnitudes occurred at the DBE level for the frame direction, where the asymmetric model showed an increase in RDR magnitude of about 36% and the IDR magnitude increased by about 22%. While the magnitudes in the frame direction

changed the most, the shapes of the PRD and IDR envelopes were altered more for the asymmetric model. For the DBE level in the direction of the walls, the difference between the maximum RDR and maximum IDR responses for the symmetric and asymmetric models changed the least out of the responses. In particular, the wall-direction RDR increased by 12% and the IDR increased by 13% when the walls were placed asymmetrically. At the MCE level, the RDR magnitude increased by 15% and IDR increased by 17% in the wall direction. Thus, the more nonlinear the structure behaves, the more impact torsional response has on the RDR and IDR.

The roof drift ratio and normalized overturning moment time histories for the NZ002 ground motion show how moving a shear wall to create an asymmetric floor plan causes the period of the responses to elongate slightly after the peak response is reached. As seen from the previous results, the roof drift ratio it typically larger for the asymmetric model than the symmetric model. However, the average accelerations achieved, and thus the resulting system overturning moments, are lower for the asymmetric model. This complies with what is commonly observed with nonlinear systems: increased nonlinearity typically leads to larger displacements and lower accelerations because the structure is softened by damage and the period increases. Since the asymmetric model exhibits more evident nonlinear behavior than the symmetric model, more energy is dissipated, as shown by the larger area of the overturning moment vs. roof drift ratio hysteretic plot.

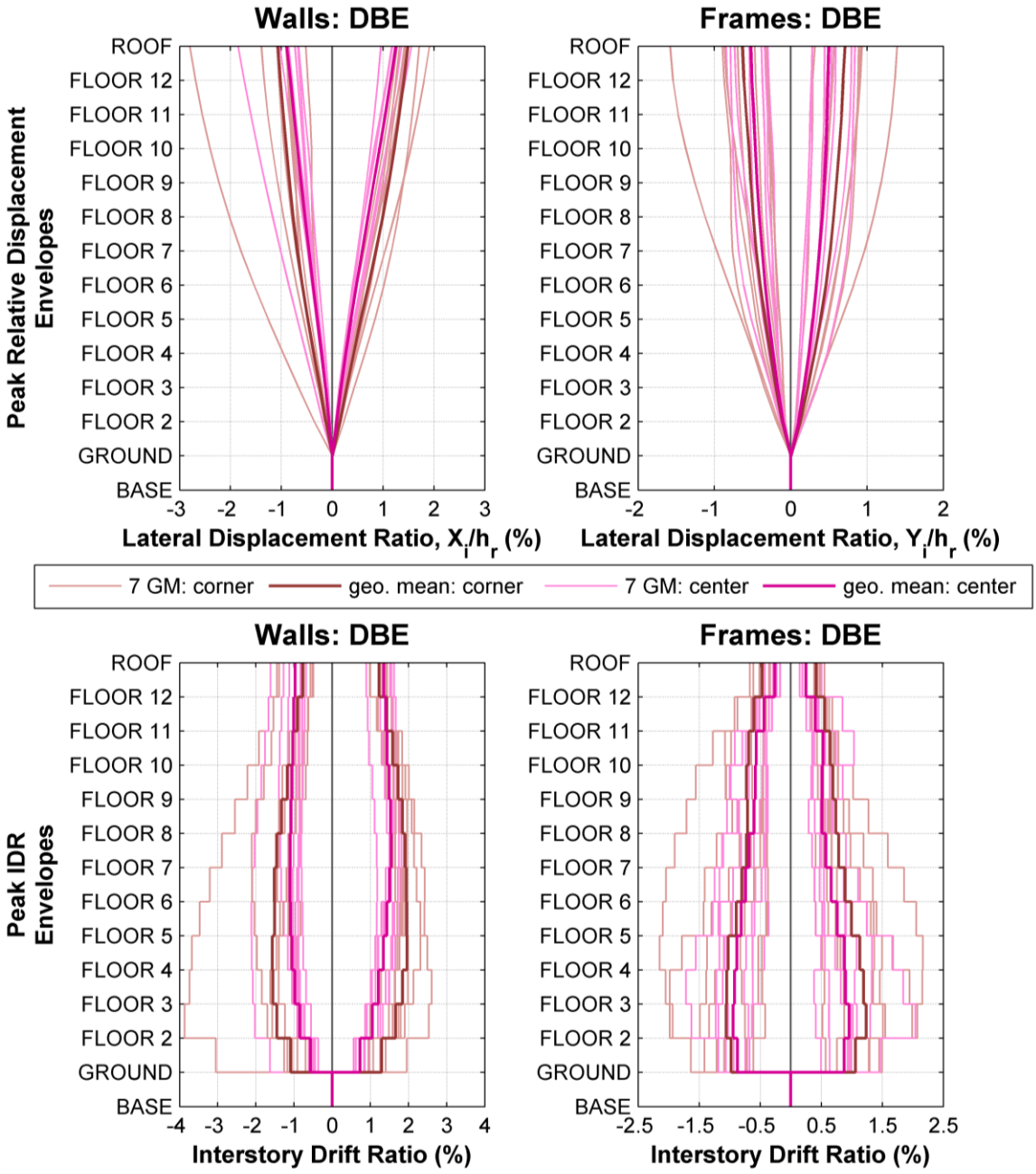

Figure 5.26: Envelopes for asymmetric model measured at corner and center for DBE level

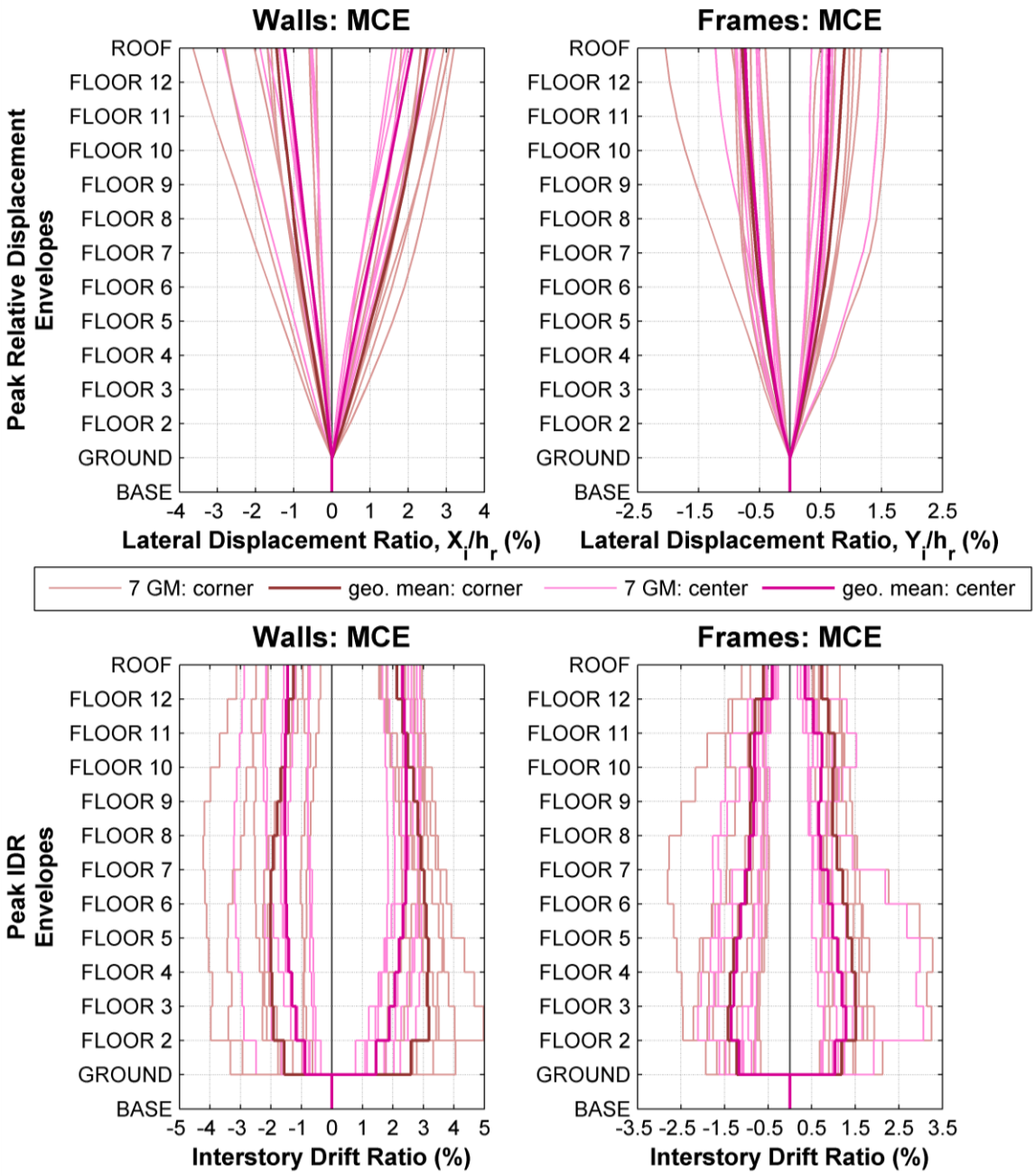

Figure 5.27: Envelopes for asymmetric model measured at corner and center for MCE level

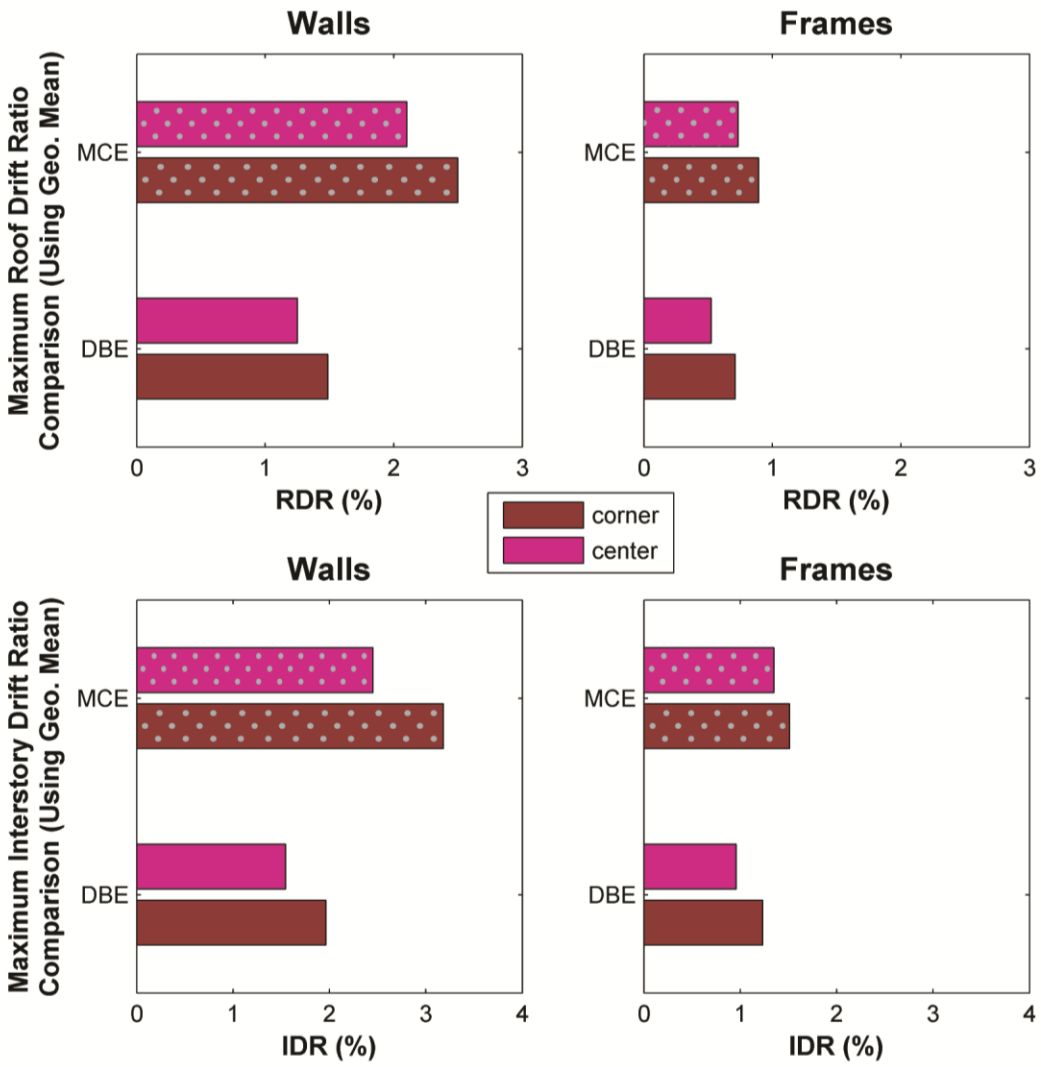

Figure 5.28: Comparison of nonlinear THA results measured at the corner and the center of asymmetric model

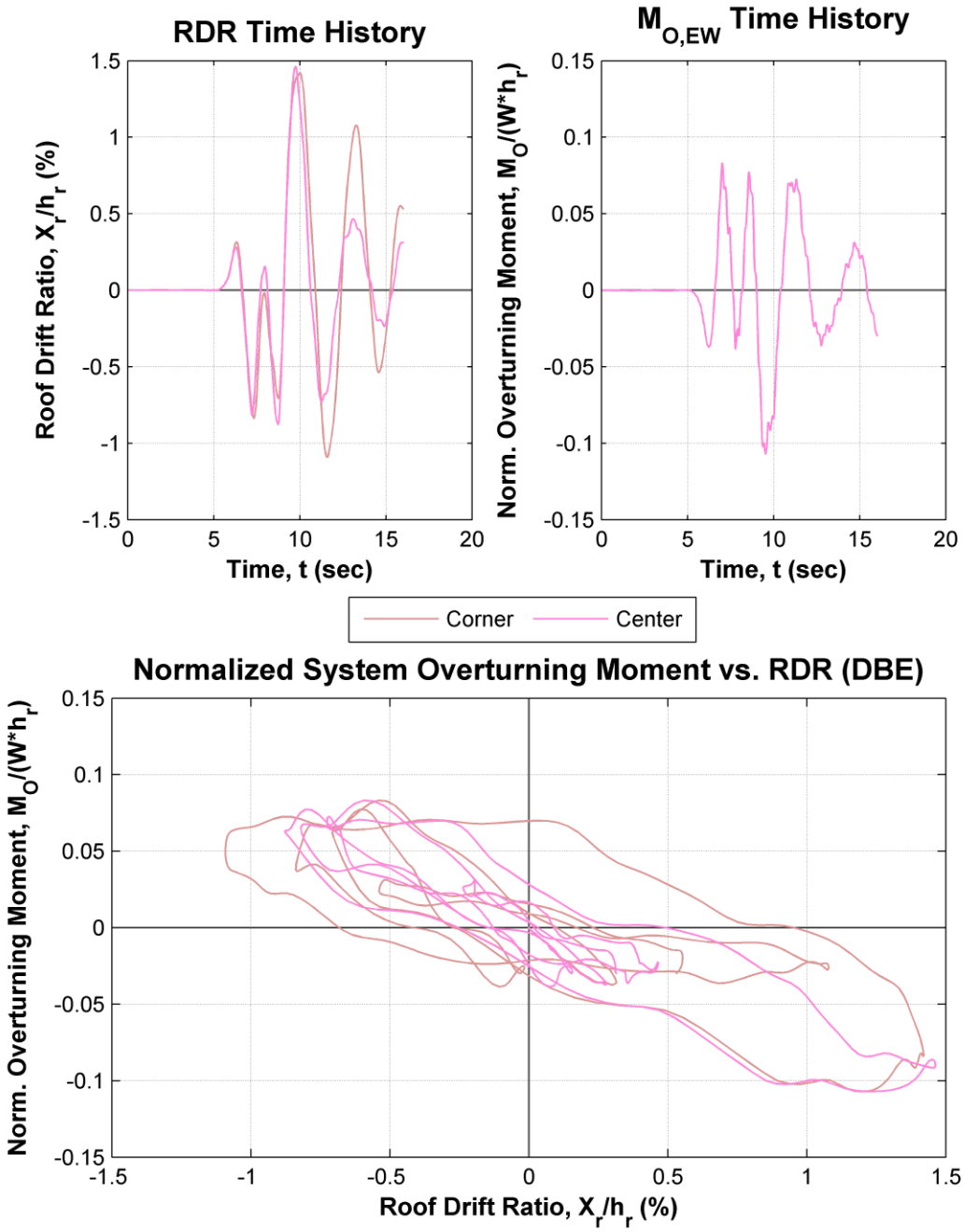

Figure 5.29: Roof drift ratio and normalized system overturning moment comparison of corner and center measurements of asymmetric model for NZ002 at DBE level

As observed when comparing the symmetric and asymmetric models, the peak relative displacement and peak interstory drift ratio envelopes measured at the corner and center of the asymmetric model are more symmetric in the direction of the frames than the direction of the walls. Both sets of envelopes become more asymmetric when the structure is subjected to the larger MCE level accelerations because it experiences more nonlinear damage. The magnitudes of the response envelopes measured at the center of the asymmetric building are typically less than those measured at the corner furthest from the walls. As such, the general response of the center of the asymmetric model is actually quite similar to the symmetric model response, especially in the direction of the frames. In the direction of the walls, however, the PRD envelopes for the center measurements are more similar in shape to the asymmetric corner measurement response because torsion influences the entire structure. For the peak IDR envelopes in the wall direction, the response measured at the center does show a slight increase in IDRs at the mid-height of the structure, but the IDRs are still smallest at the first story above the ground. As before, higher mode effects are apparent in the bottle-neck shape of the frame direction IDR envelopes measured from both the center and the corner. As a general conclusion, the characteristics of torsional response are simply less pronounced when measured at the center than when measured at the corner.

The bar plot comparison of maximum roof drift ratio and maximum interstory drift ratio using the geometric mean also shows that the responses are larger for the corner of the asymmetric model than the center. The difference in magnitudes of the IDR response is greater for the wall direction than the frame direction, and is amplified for the MCE level. As seen with the comparison of the symmetric and asymmetric models, the

greatest change in the magnitudes measured at the center and corner occurred at the DBE level in the frame direction for the RDR response, which was again about 36%. However, it is observed that the maximum IDR achieved at MCE level for the wall direction also has a large difference between responses, with an increase of about 30% at the corner as compared to the center. In the frame direction, the MCE level responses measured at the corner and the center are actually more similar than the DBE level responses. This results from the more nonlinear MCE level response causing torsional effects to be more apparent at the center of the structure than they are at the DBE level.

When comparing the roof drift ratio time history response of NZ002 at DBE level, the corner of the structure shows larger magnitudes than the center of the structure after the peak response is achieved. The elongation of response period for the asymmetric model compared to the symmetric model is not exhibited by the difference in measurements of the corner versus center response of the asymmetric model since rigid diaphragms were used. There is no difference in total system overturning moment because the average floor accelerations used in each case were measured at the building center. Thus, the hysteretic overturning moment-RDR behavior measured at the corner is very similar to that measured at the center, with slightly larger energy dissipation demands at the corner of the structure.

6 CONCLUSIONS AND RECOMMENDATIONS

6.1 Summary of Results

The purpose of performing modal analyses in this thesis, in addition to obtaining the structure's dynamic characteristics, was to check that the modeling techniques used in ETABS and SAP2000 were representative of a reinforced concrete frame-wall structure. Upon comparison of the modal characteristics of the preliminary ETABS models, it was found that modeling the shear walls using frame elements instead of area shell elements is a technique that yields very similar modal properties and can be used with confidence. Similarly, it was found through modal analysis that the SAP2000 model without slabs was fairly similar to the ETABS model with slabs when T-beam sections were modeled instead of the slab. Lastly, modal analysis of the symmetric and asymmetric SAP2000 models showed the torsional dominance in the modes of the asymmetric model, where the symmetric model had regular modes that are typical of frame-wall structures.

The results of the essentially linear ETABS time history analysis showed that the asymmetric model experienced larger peak relative displacement and peak interstory drift ratio demands at the edge of the structure furthest from the walls than those of the symmetric structure at the same location. This was a result of torsion and the larger contribution of the frames along Gridlines 1, 2, and 3 to the overall response. The asymmetry increased maximum roof drift ratio by 21% in the wall direction and 53% in the frame direction. The maximum interstory drift ratio increased by about 35% in both directions when walls are asymmetrically placed. Overall, the effects of torsion on the

asymmetric model were magnified in the direction of the walls for both the DBE and MCE level demands.

The base shear-roof drift ratio results of the SAP2000 pushover analyses showed that the asymmetric model had, overall, lower ductility capacity than the symmetric model, since beam yielding occurred at similar points but failure of each type of member occurred at much lower roof drift ratios and lower base shear values than those of the symmetric model. The ground motion studies provided a systematic way to cut the acceleration records to feasible lengths for nonlinear analysis while still preserving the motion characteristics. Using the cut records, the nonlinear time history analyses performed in SAP2000 resulted in a several different conclusions. First, moving a wall to create an asymmetric floor plan resulted in peak relative displacements and peak interstory drift ratio responses that exhibited torsional effects, which increased when the structure was subjected to higher demands. These torsional effects include larger peak interstory drift ratios towards the lower half of the structure, as opposed to the upper half for the symmetric model, in the direction of the walls. Additionally, the asymmetric model experienced larger displacement response quantities and smaller total system overturning moment.

In terms of nonlinear response, both symmetric and asymmetric model results showed asymmetric envelopes, which increased with an increase in demand, and the influence of higher mode effects on the interstory drift ratio response. After comparing the responses measured at the corner and the center of the asymmetric model, it was clear that torsional effects were amplified toward the exterior of the structure, furthest from the walls. Also, the response at the center of the asymmetric building was quite similar to the

symmetric building response, but still showed torsional effects, which were increased in the direction of the frames. Overall, the more nonlinear the structure behaved, the more influence torsion had on the response of the model with asymmetrically placed lateral force resisting shear walls.

6.2 Relevant Limitations of Research and Recommendations

Since ETABS is intended mainly for designing structures, the analysis options are fairly limited, whereas SAP2000 has more detailed modeling parameters. The versions of ETABS Nonlinear used in this thesis had several limitations that are particularly influential on modeling nonlinear reinforced concrete structures. The first major limitation encountered is that to model material nonlinearity, either link elements must be defined and added to the model as independent elements, or frame elements must be used for all members so that plastic hinges can be defined. Thus, the area shell elements that have more advanced stress distribution could not be used. Additionally, transverse steel reinforcing in beams and columns and all reinforcing in walls could not be directly modeled, so confined versus unconfined concrete could not be accounted for within the modeled elements. As a result, the default hinge properties could not be accurately used. However, the SAP2000 Ultimate version is capable of modeling fiber shear wall sections that account for confinement and all reinforcing can be modeled directly. Since the ETABS symmetric model was used as the base for the SAP2000 models, the effort to remodel the walls using a different type of analysis was not made and not required for the purposes of this thesis.

Due to the many limitations of ETABS Nonlinear discussed, the author of this thesis suggests that a different analysis platform be used for analysis of nonlinear

reinforced concrete structures, such as PERFORM3D, a Computers and Structures, Inc. structural analysis program that has more advanced nonlinear features, including the option to use fiber section analysis instead of lumped plasticity analysis. For future research related to the analyses performed in this thesis, the effect that torsion, through asymmetric lateral force-resisting system placement, has on floor absolute accelerations and residual drifts could be investigated.

7 APPENDIX

7.1 Moment-Curvature Relationships

The values used to normalize the moment-curvature relationships are the seismic weight measured from the ground to the roof, W = 47,152 kips and the height from the ground to the roof, h_r = 1866 inches. The strain-limit state strain values used for the moment-curvature linearization of all sections are presented in Table 7.1.

Table 7.1: Strain-limit state strain values used for all sections

Strain-Limit State	BM1, BM3, BM4	BM2	BM5	COL1	COL2 (all)	COL3	WALL36 and WALL45
Civ, ε_{ccu}	-0.009922	-0.009427	-0.008188	-0.022806	-0.022806	-0.022806	-0.045137
Siii, ε_s -ε_{ccu}	0.045000	0.064539	0.045000	0.055674	0.060630	0.064539	0.071631
Siv, ε_s -ε_{ccu}	0.066667	0.092719	0.066667	0.080898	0.087507	0.092719	0.102175

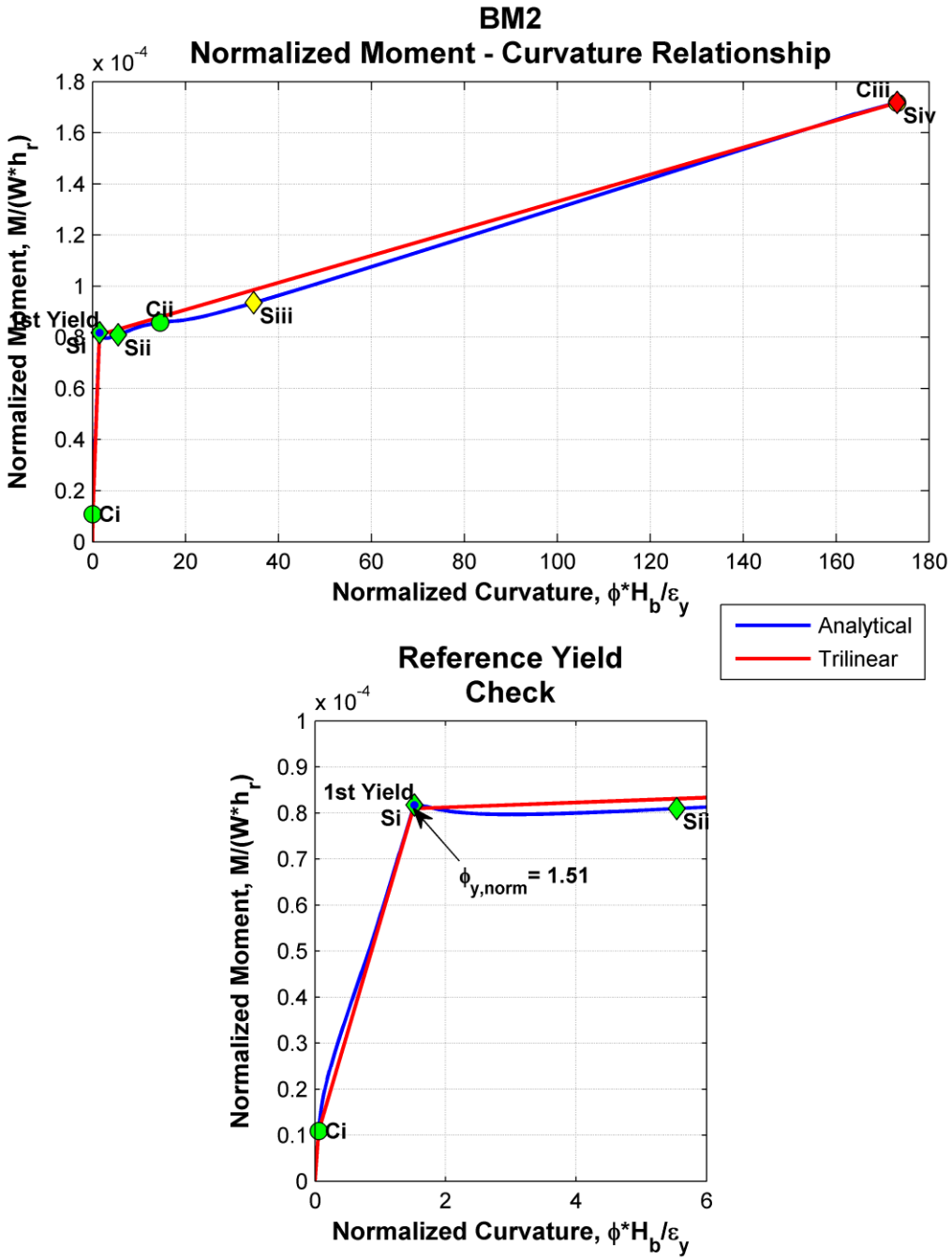

Figure 7.1: Normalized moment-curvature relationship, tri-linear idealization, and reference yield check for BM2

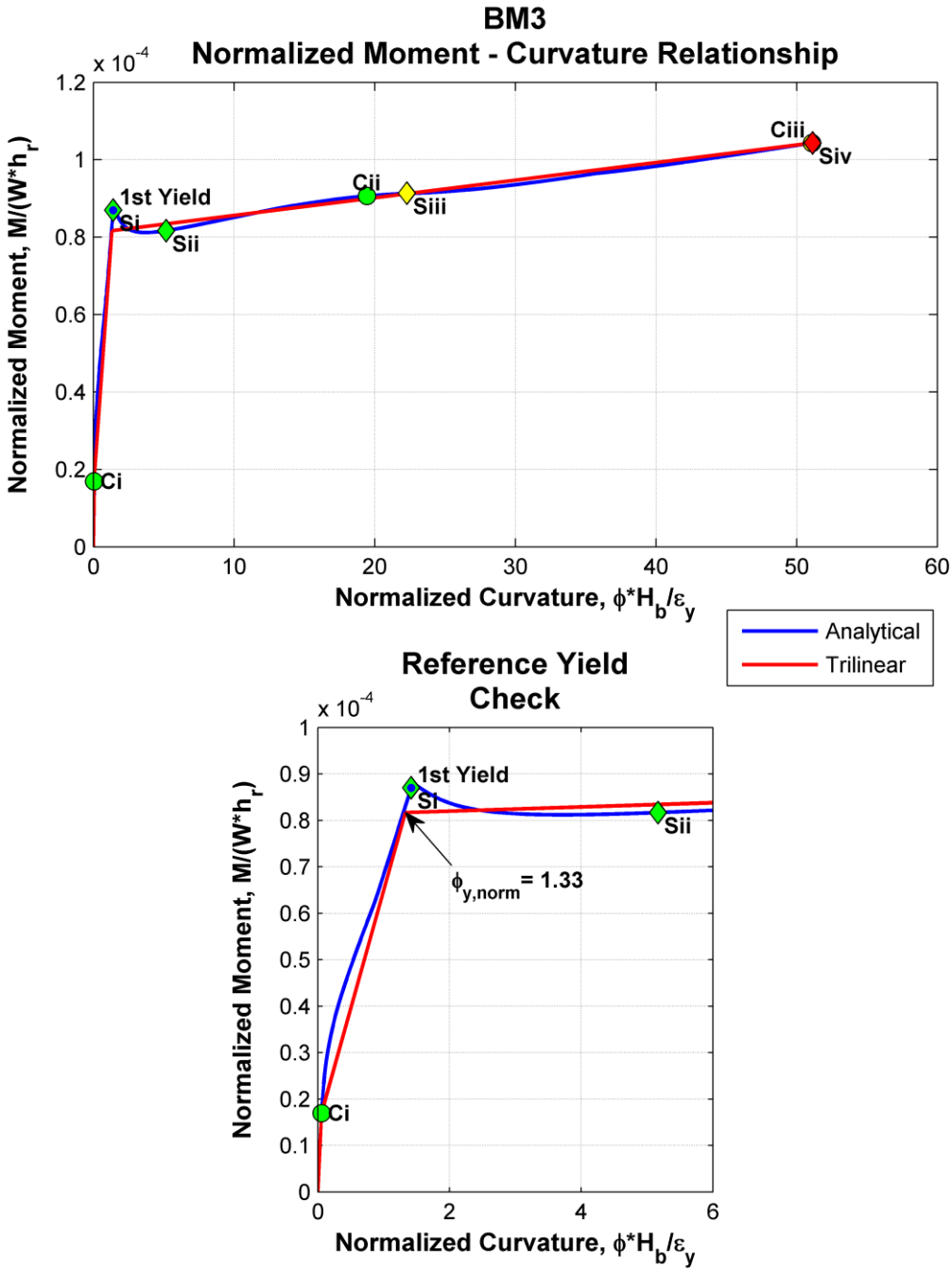

Figure 7.2: Normalized moment-curvature relationship, tri-linear idealization, and reference yield check for BM3

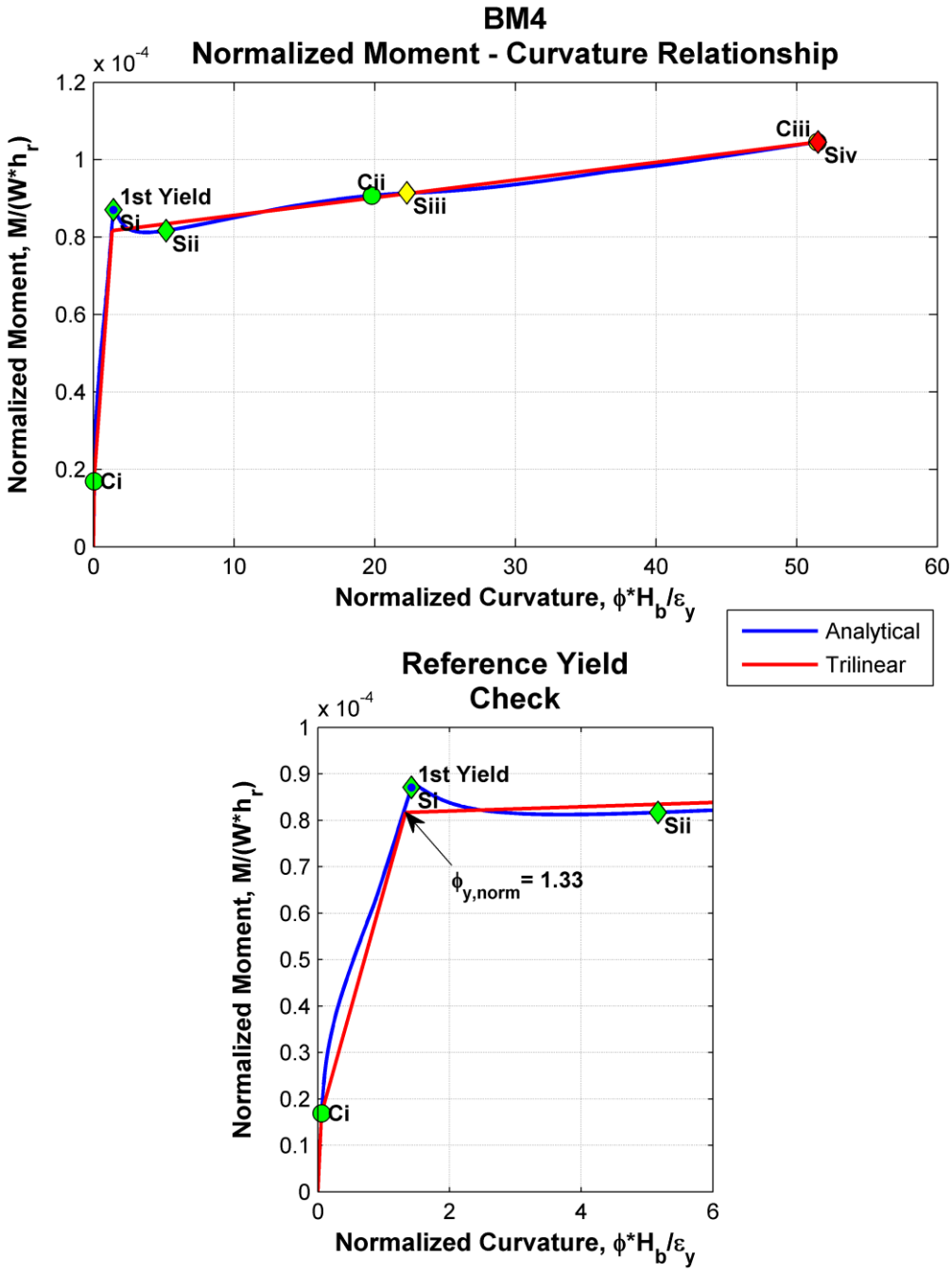

Figure 7.3: Normalized moment-curvature relationship, tri-linear idealization, and reference yield check for BM4

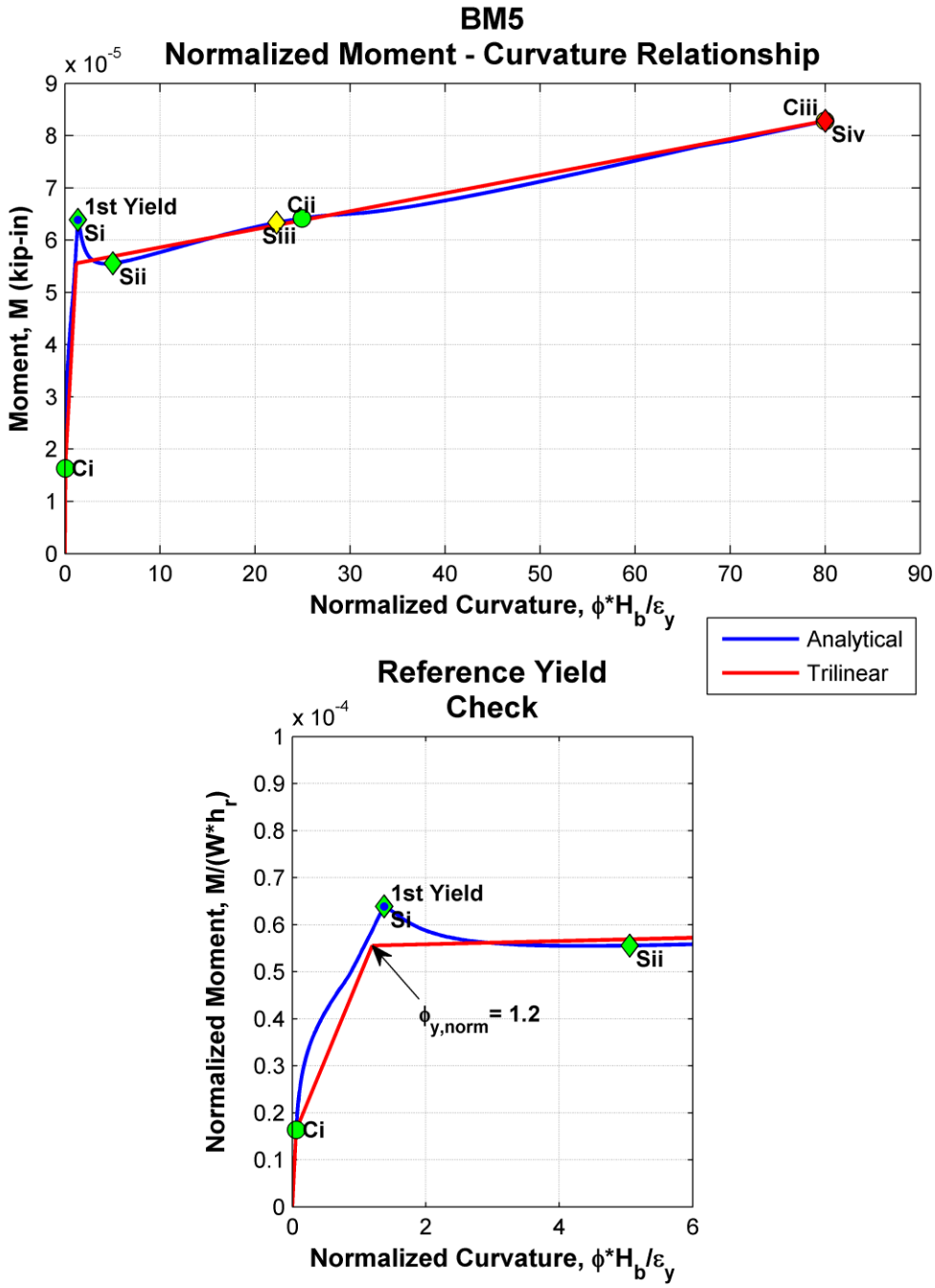

Figure 7.4: Normalized moment-curvature relationship, tri-linear idealization, and reference yield check for BM5

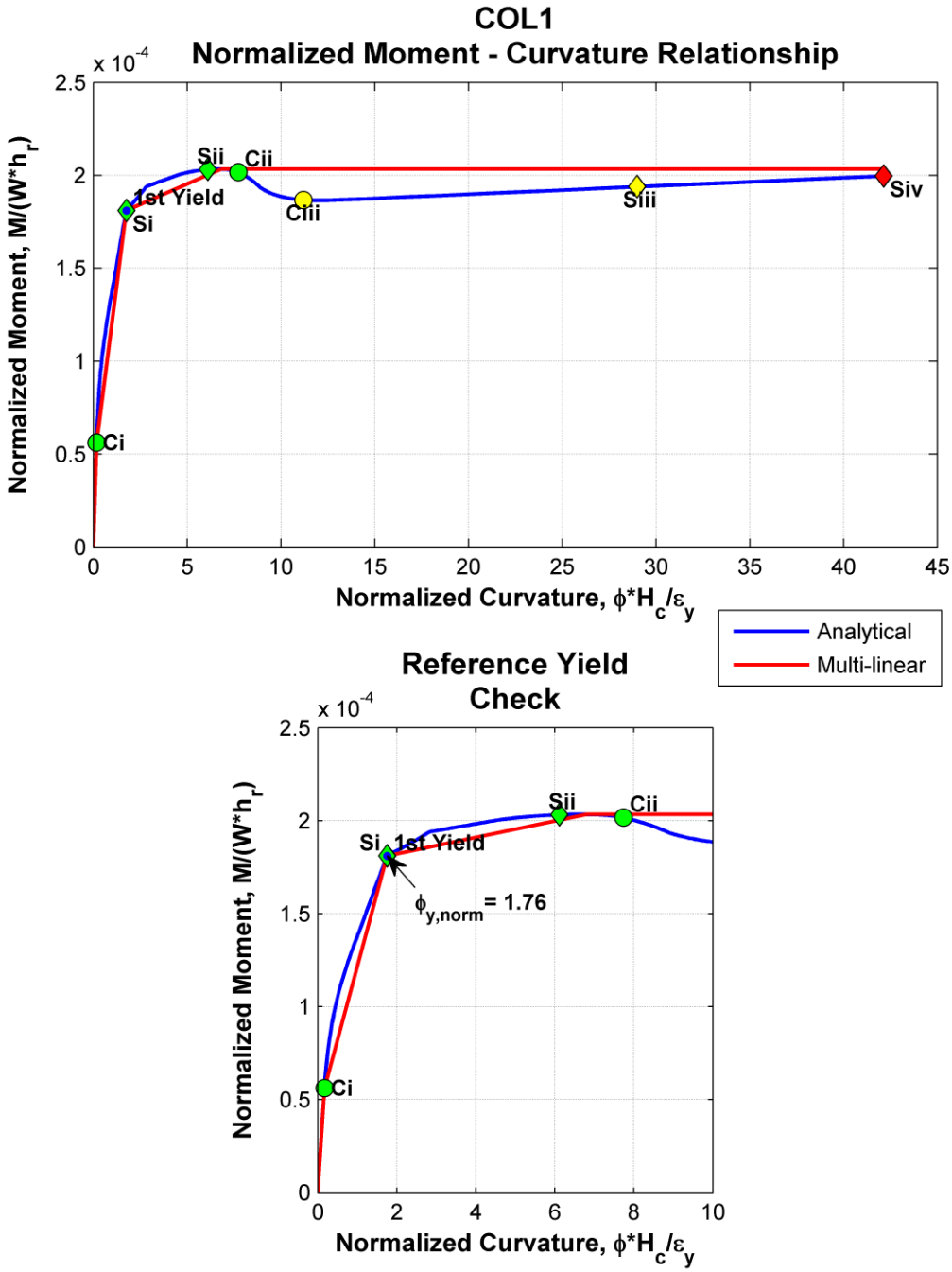

Figure 7.5: Normalized moment-curvature relationship, multi-linear idealization, and reference yield check for COL1

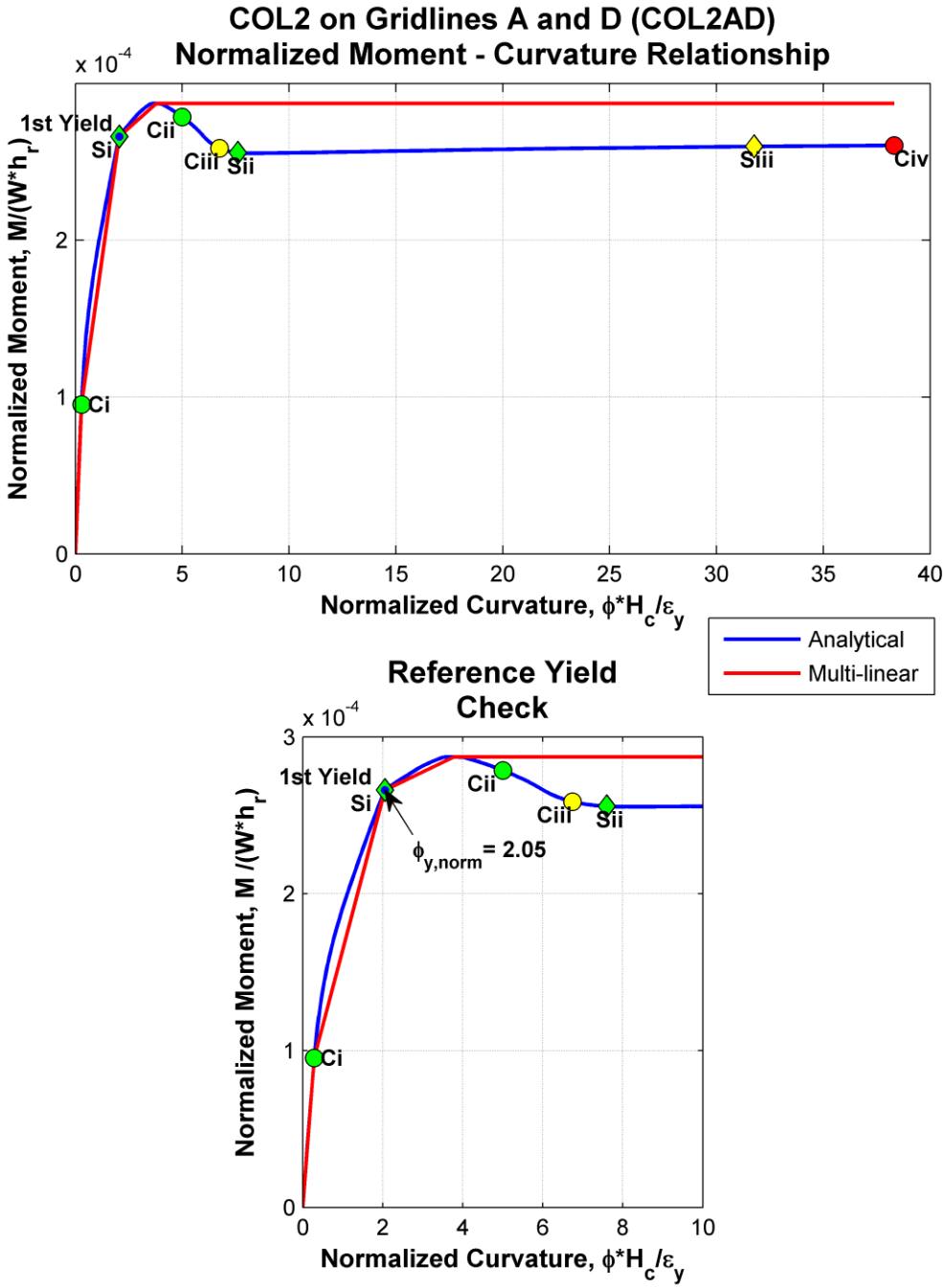

Figure 7.6: Normalized moment-curvature relationship, multi-linear idealization, and reference yield check for COL2AD

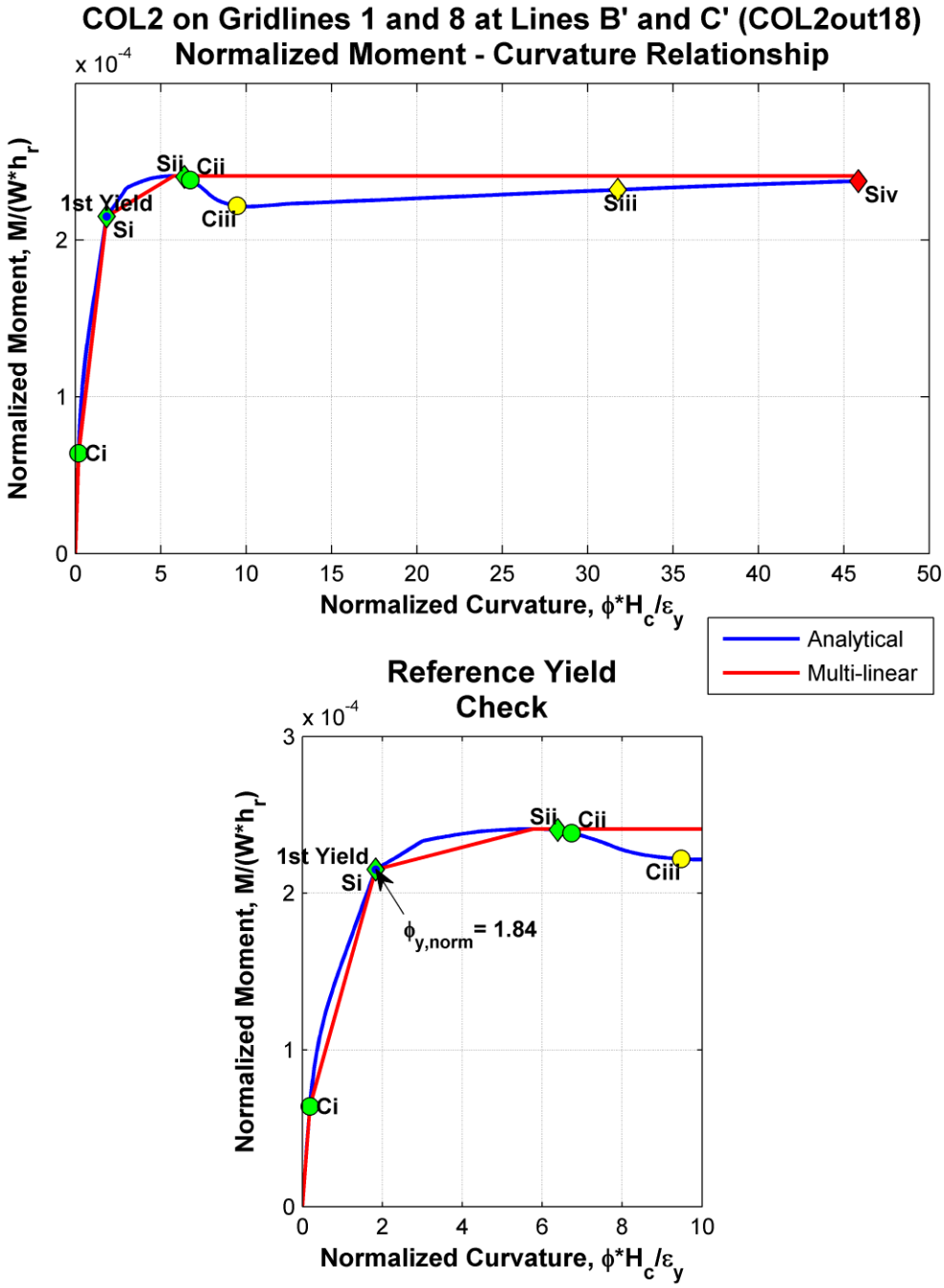

Figure 7.7: Normalized moment-curvature relationship, multi-linear idealization, and reference yield check for COL2out18

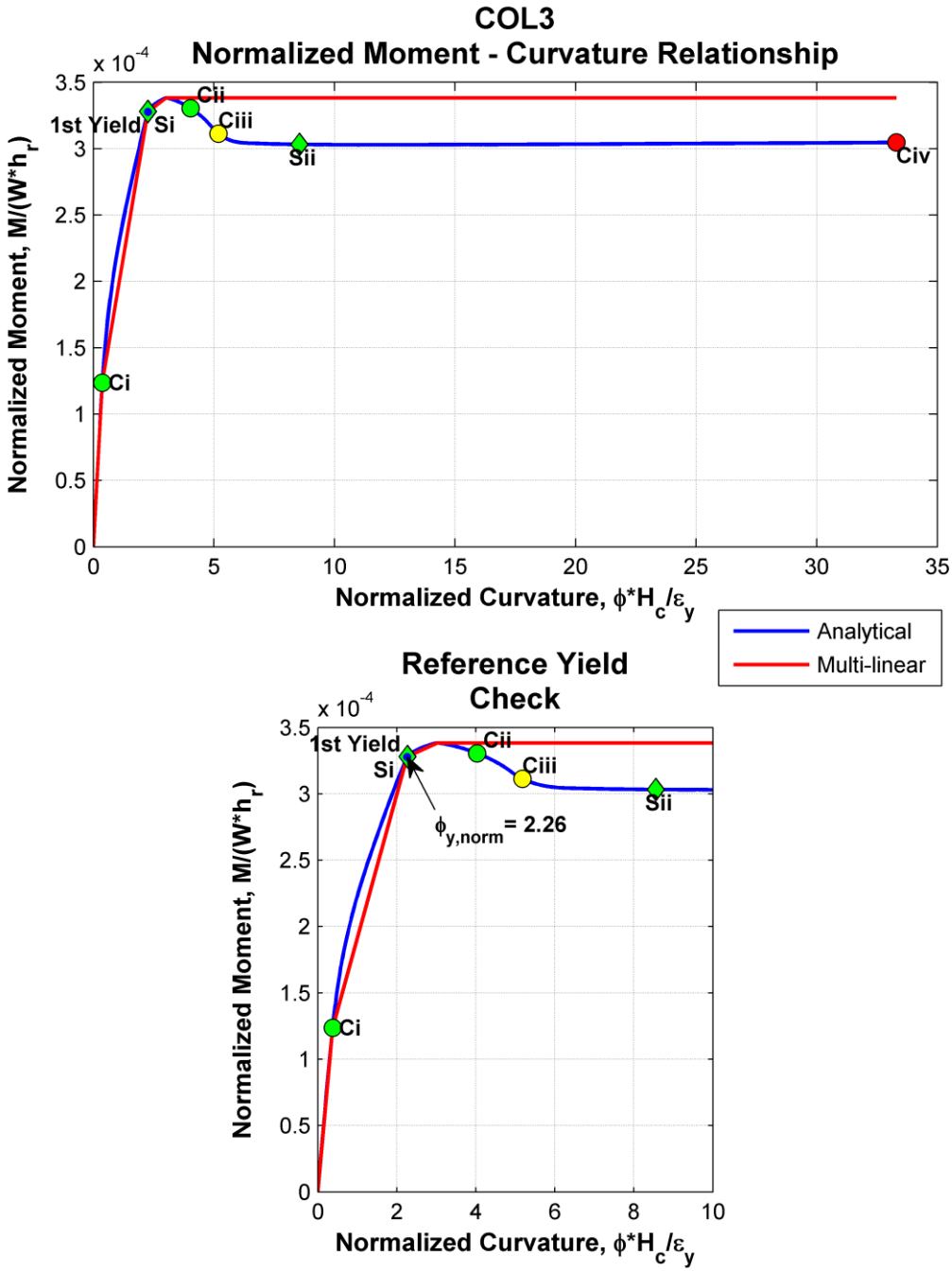

Figure 7.8: Normalized moment-curvature relationship, multi-linear idealization, and reference yield check for COL3

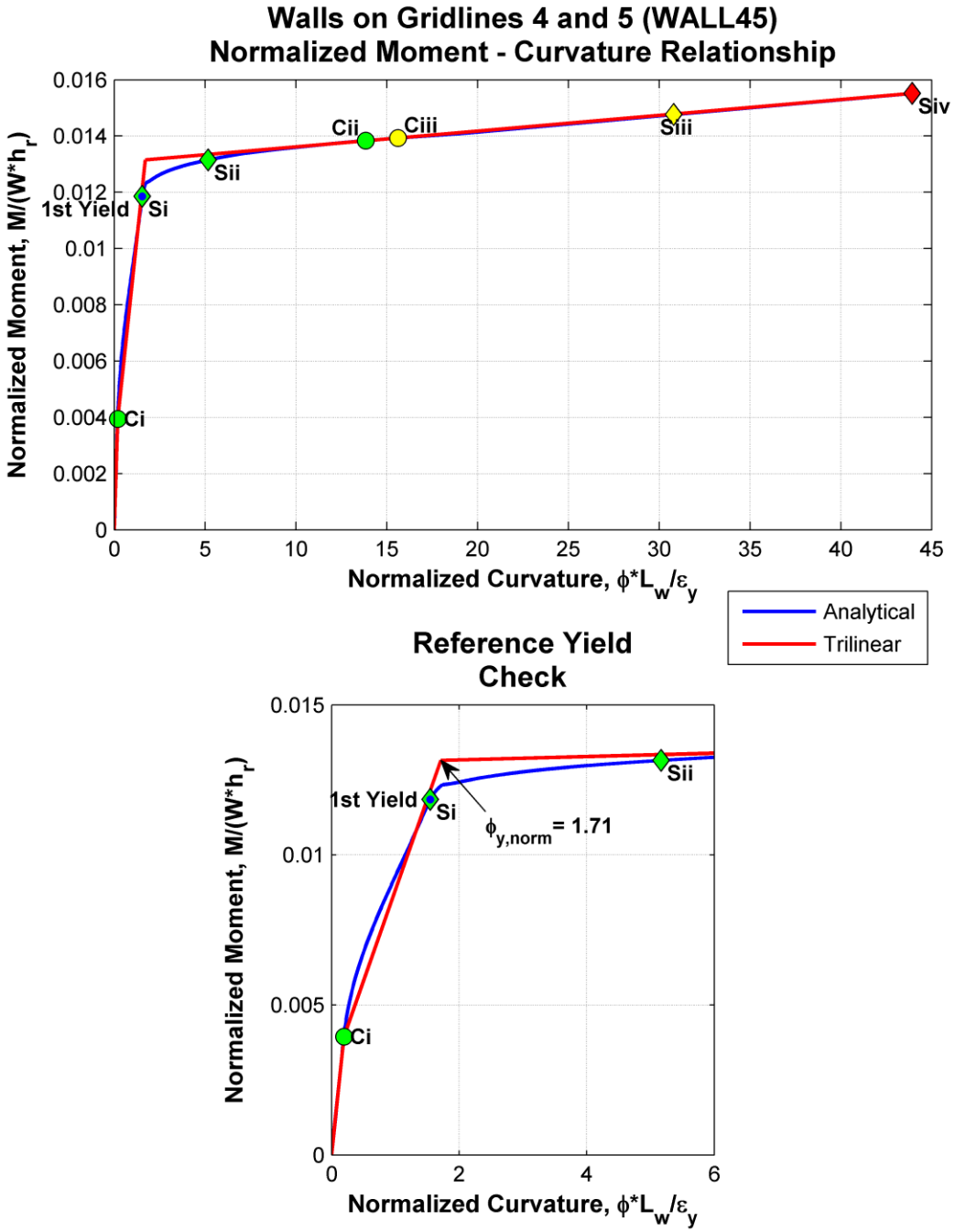

Figure 7.9: Normalized moment-curvature relationship, tri-linear idealization, and reference yield check for WALL45

7.2 Moment-Rotation Relationships

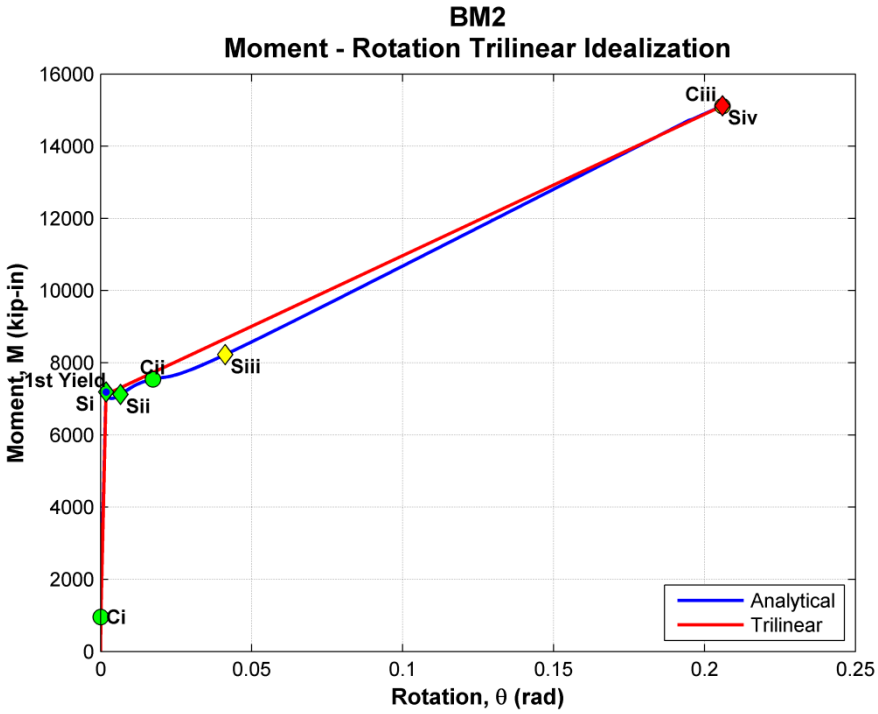

Figure 7.10: Moment-rotation relationship with tri-linear idealization for BM2

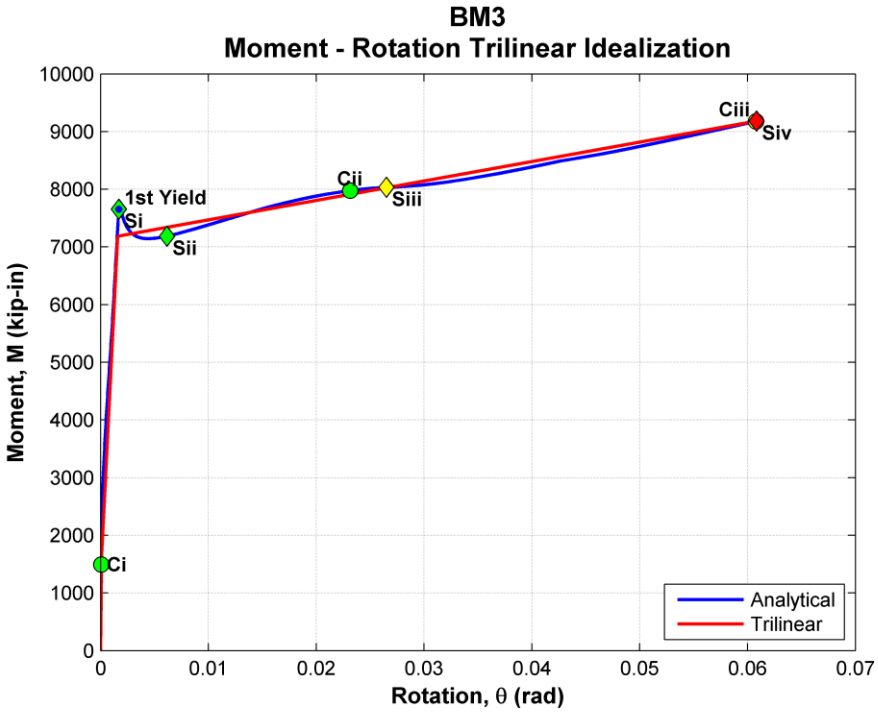

Figure 7.11: Moment-rotation relationship with tri-linear idealization for BM3

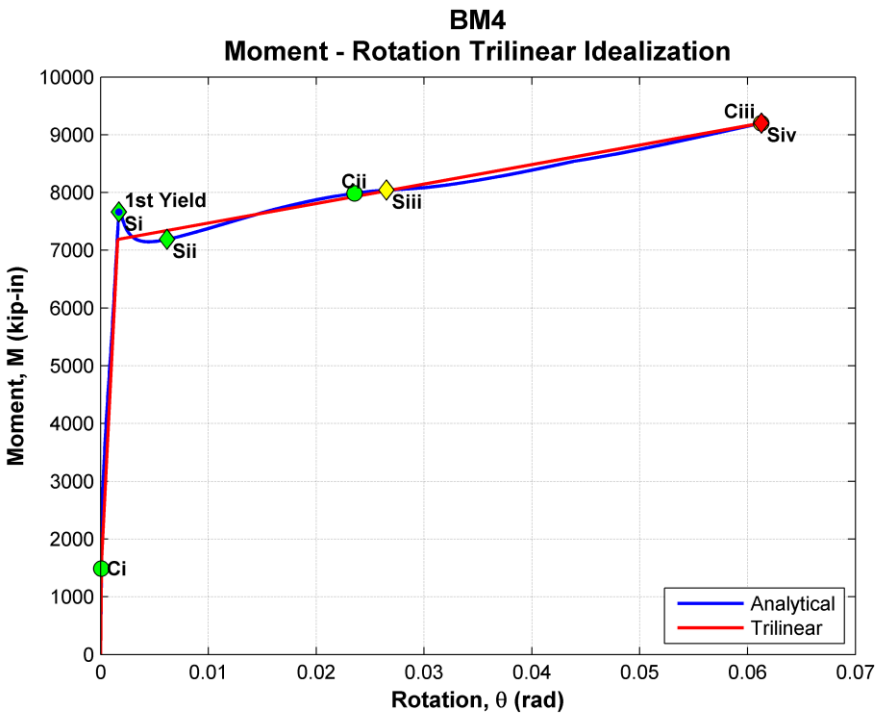

Figure 7.12: Moment-rotation relationship with tri-linear idealization for BM4

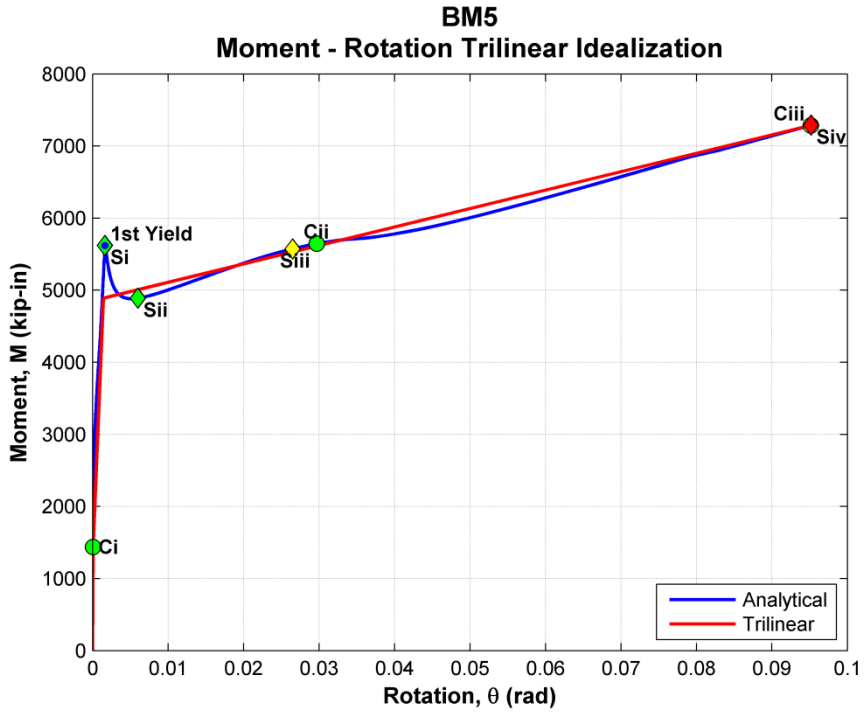

Figure 7.13: Moment-rotation relationship with tri-linear idealization for BM5

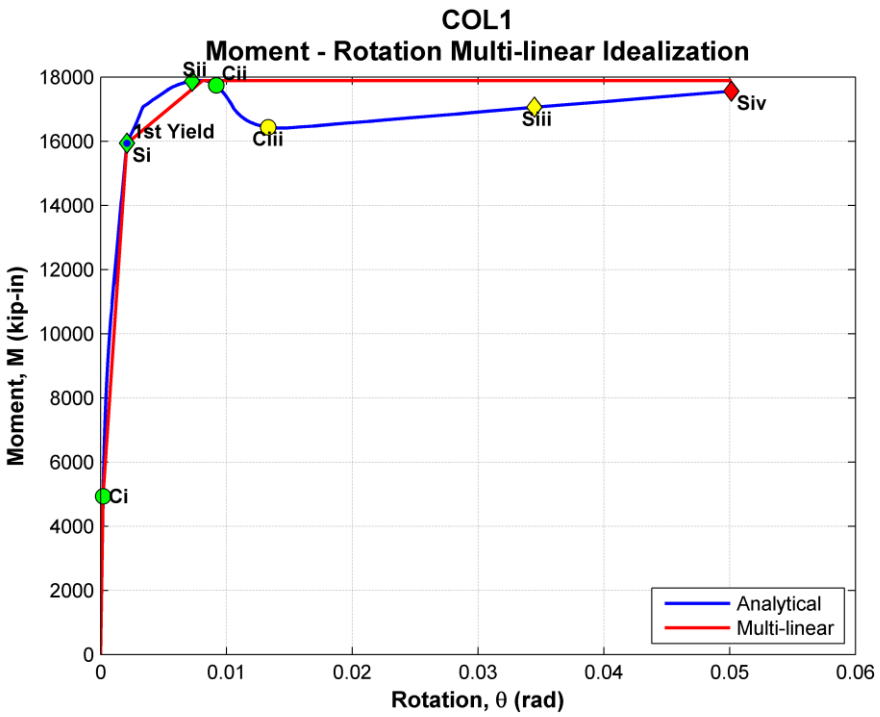

Figure 7.14: Moment-rotation relationship with multi-linear idealization for COL1

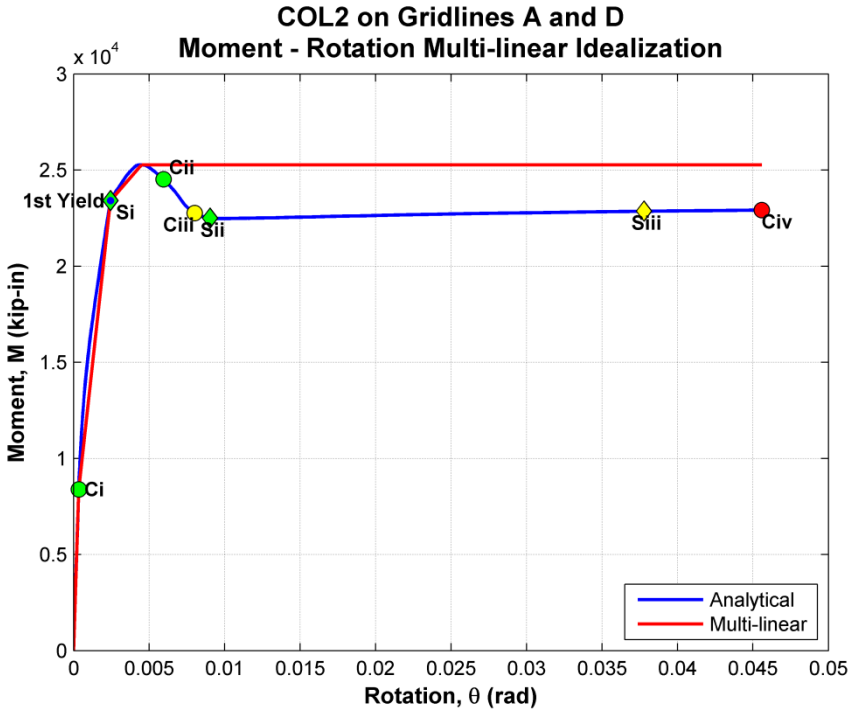

Figure 7.15: Moment-rotation relationship with multi-linear idealization for COL2AD

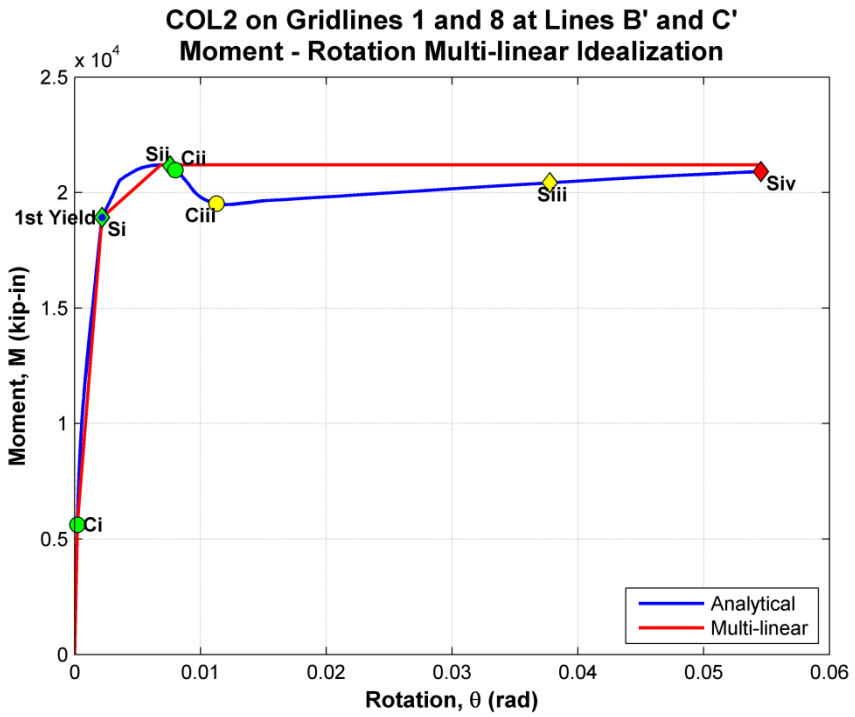

Figure 7.16: Moment-rotation relationship with multi-linear idealization for COL2out18

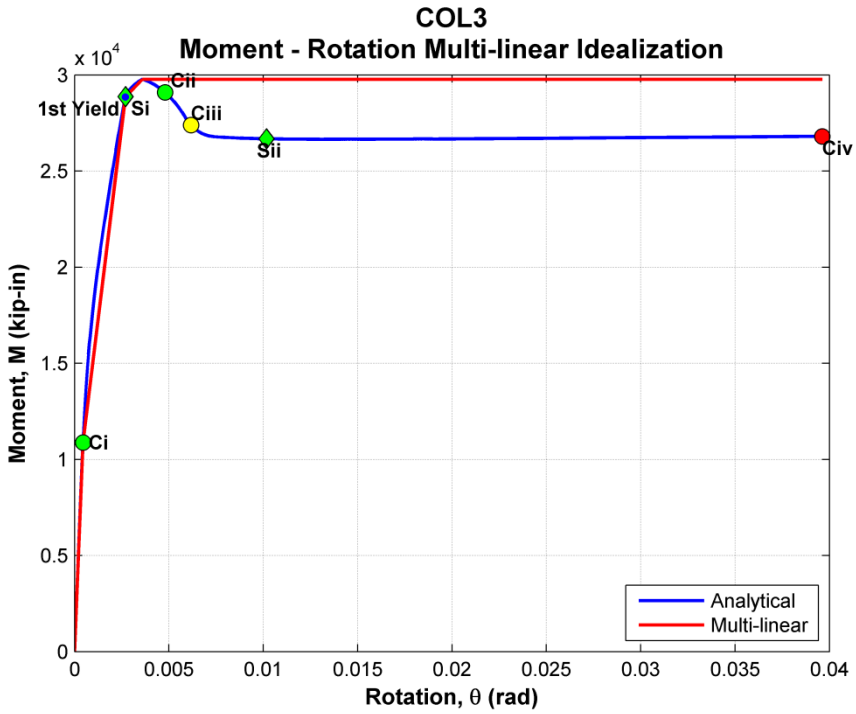

Figure 7.17: Moment-rotation relationship with multi-linear idealization for COL3

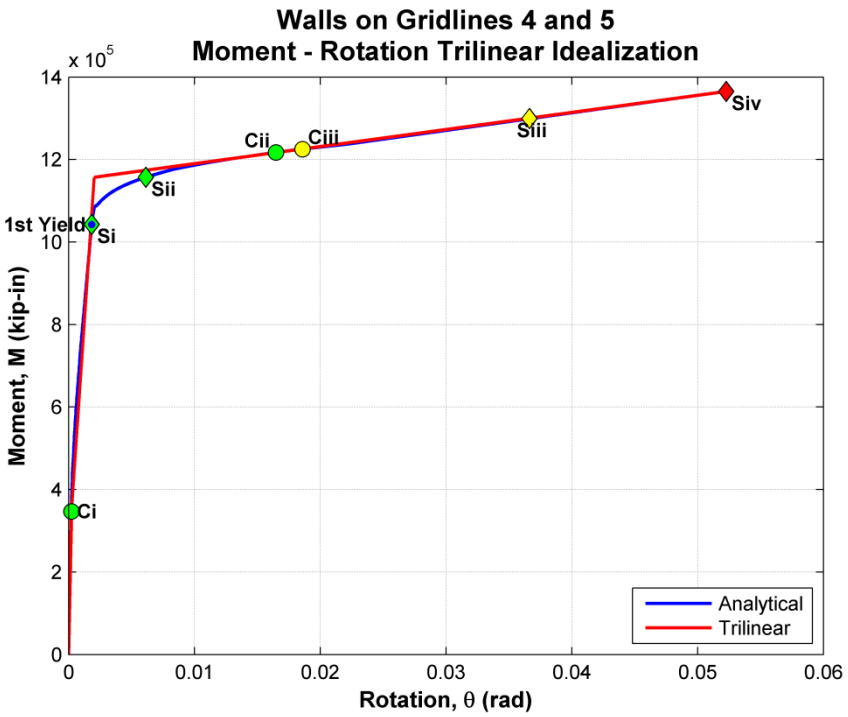

Figure 7.18: Moment-rotation relationship with tri-linear idealization for WALL45

7.3 ETABS THA Results

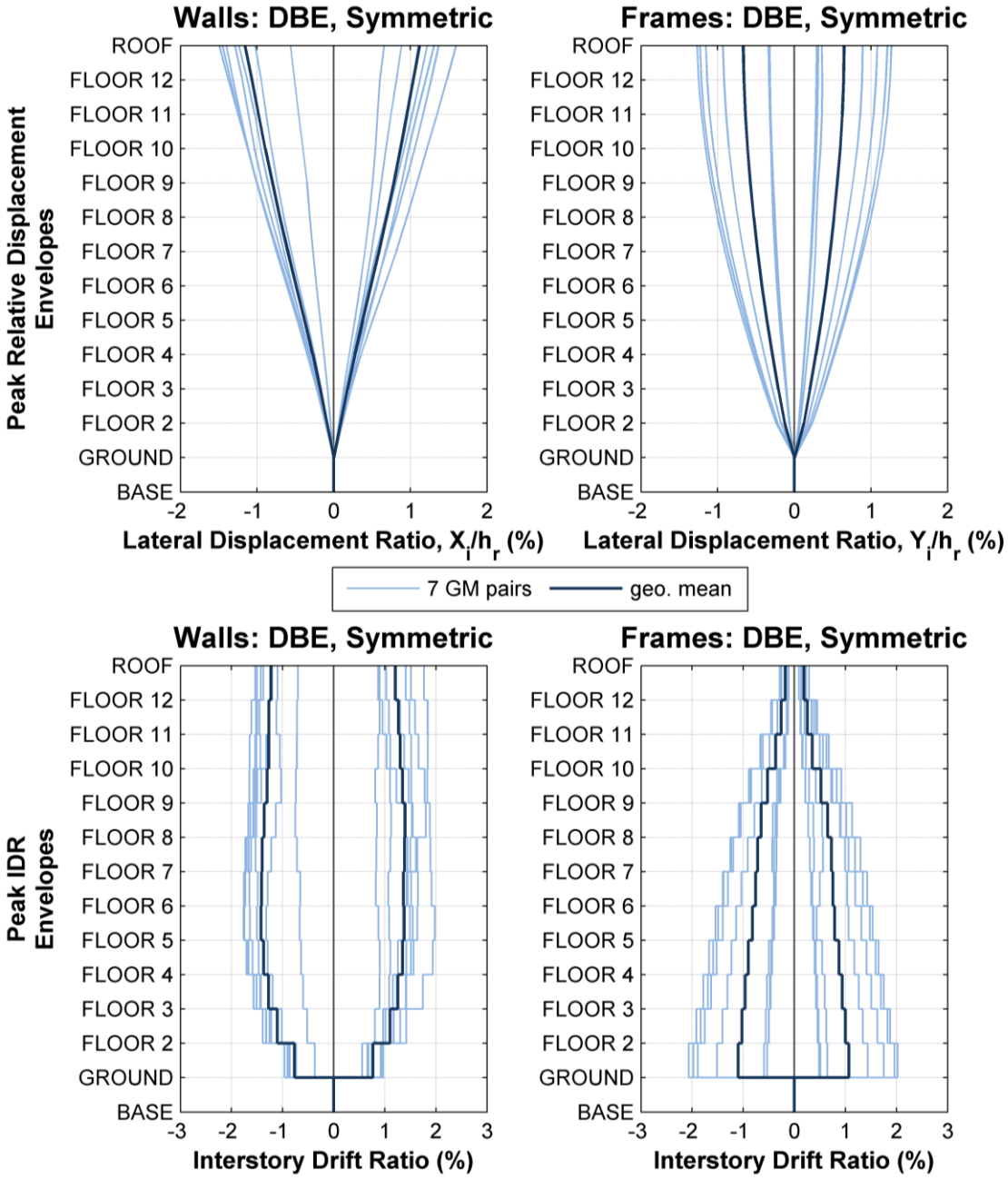

Figure 7.19: Envelopes for symmetric ETABS model at DBE level

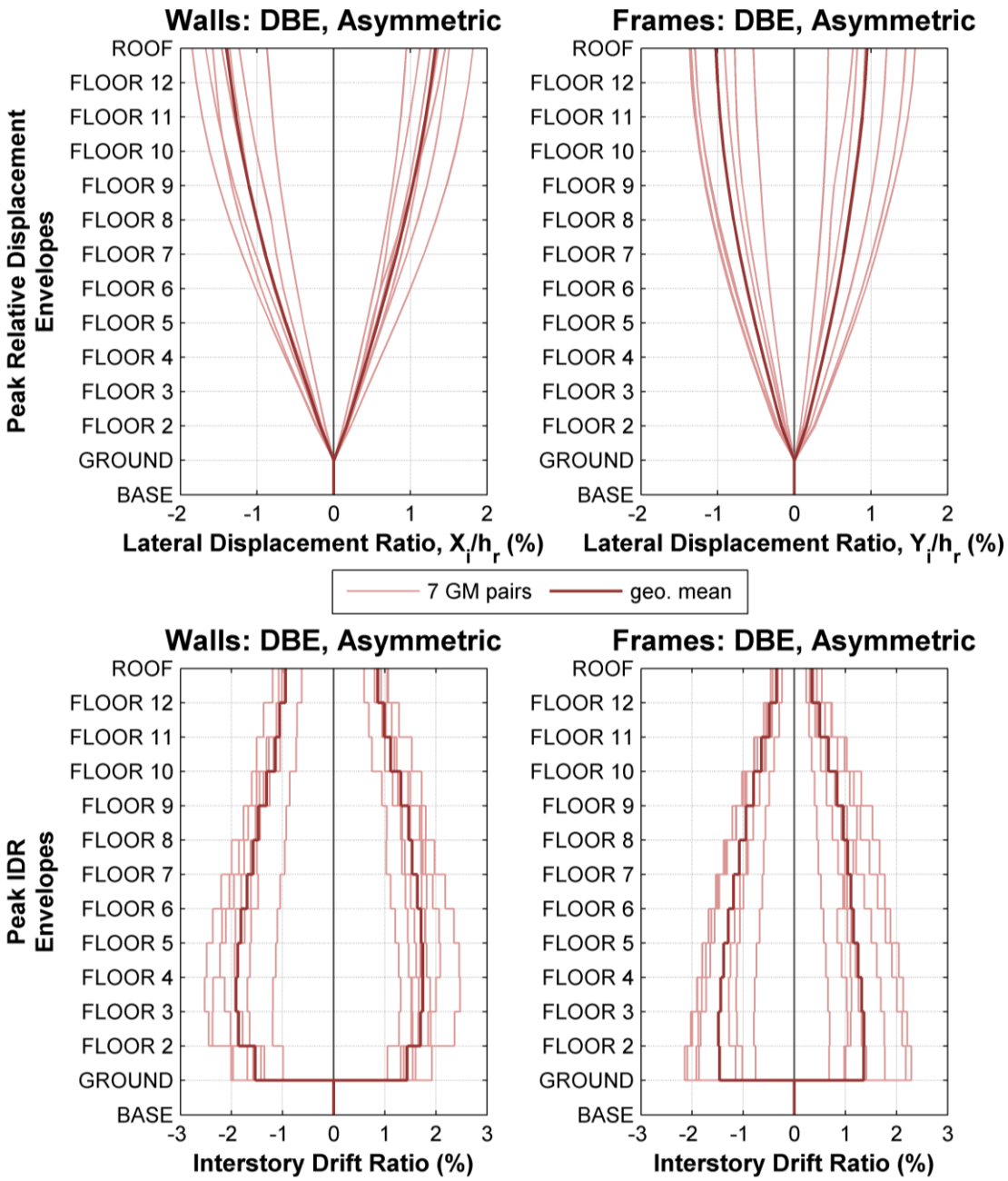

Figure 7.20: Envelopes for asymmetric ETABS model at DBE level

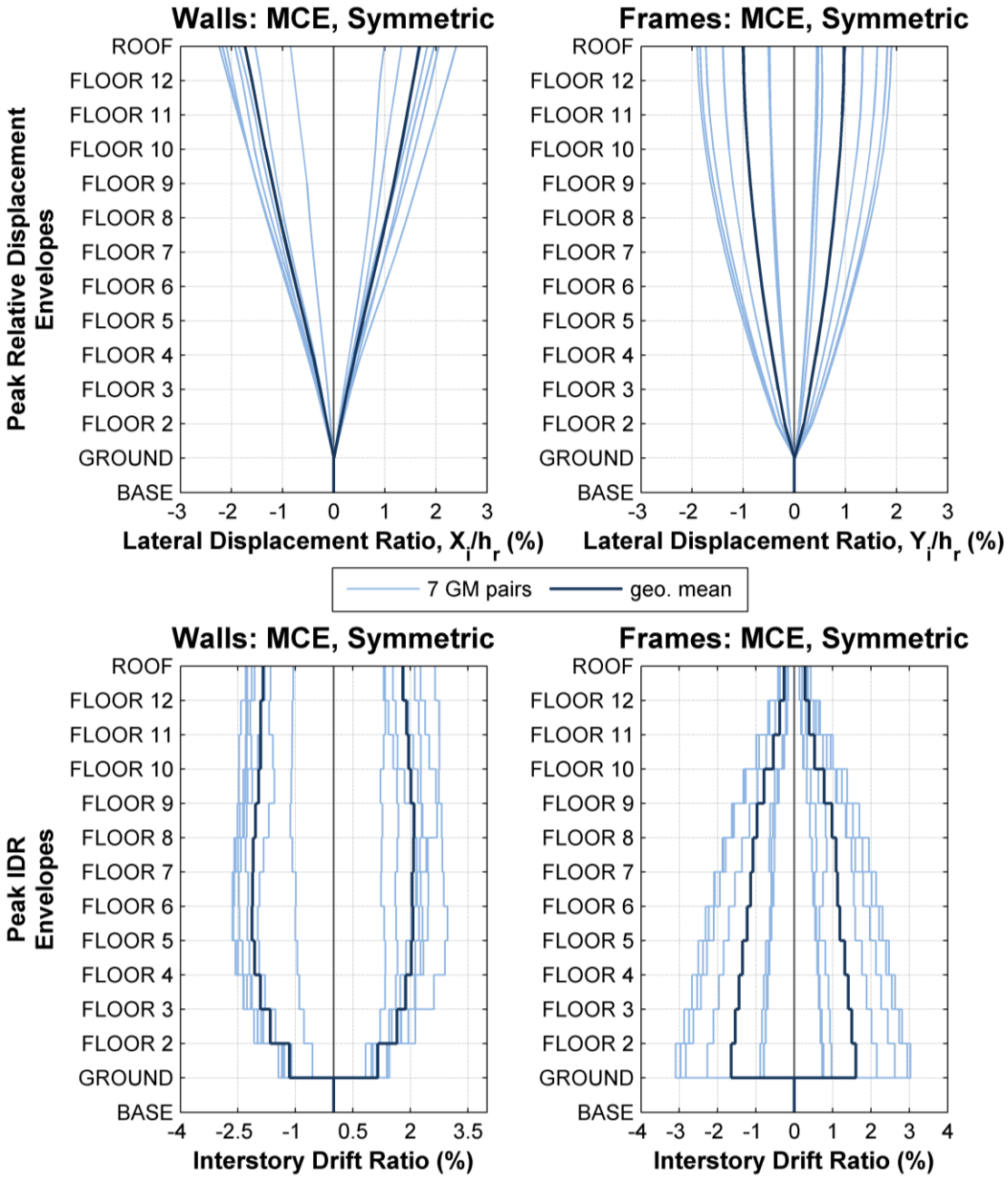

Figure 7.21: Envelopes for symmetric ETABS model at MCE level

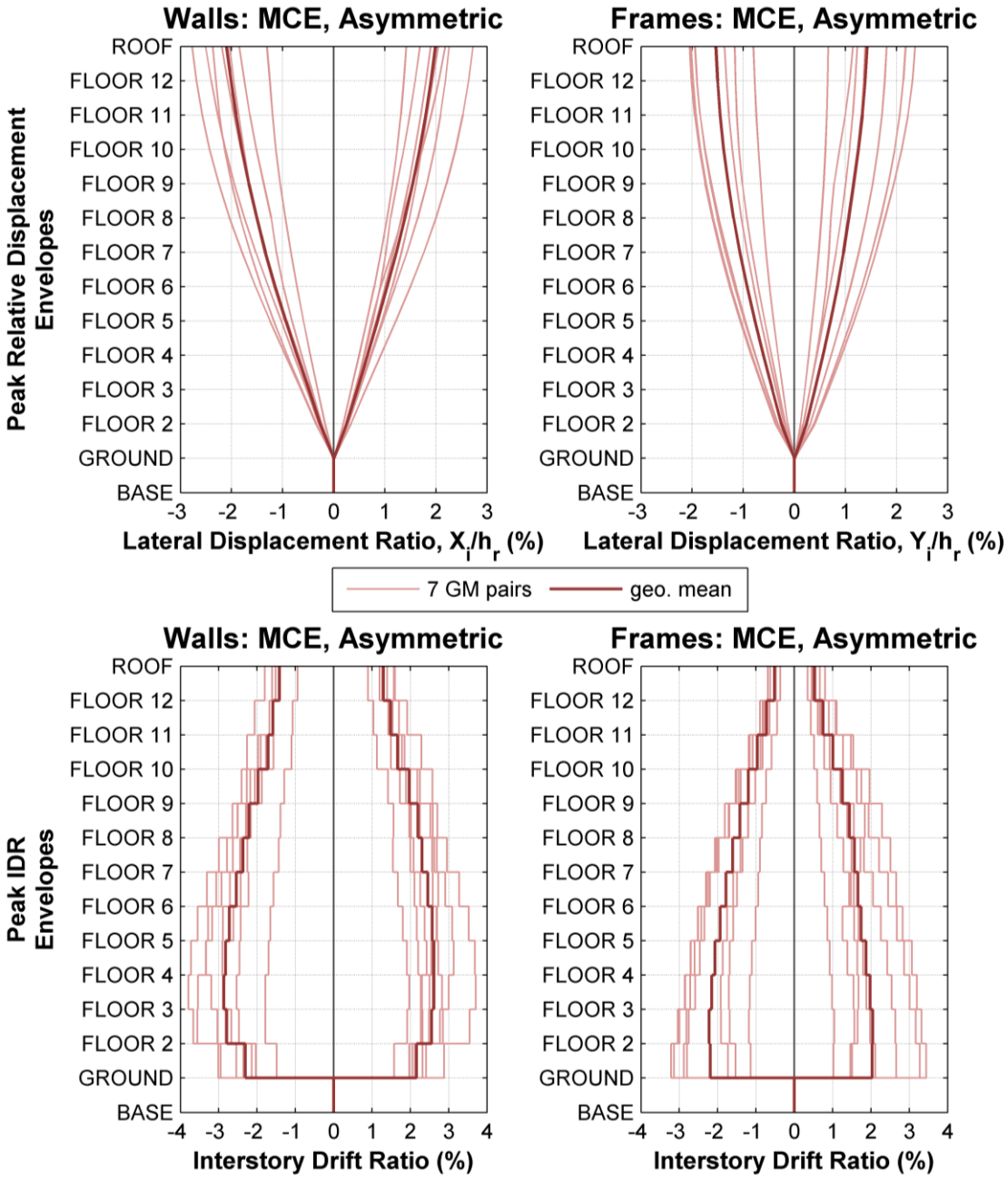

Figure 7.22: Envelopes for asymmetric ETABS model at MCE level

7.4 SAP2000 Nonlinear Static Analysis (Pushover) Screenshots

Screenshots taken of SAP2000 model for the first yield and first fail of beams, columns, and shear walls of the first mode shape pushover profile, as described by Table 5.3, are presented below.

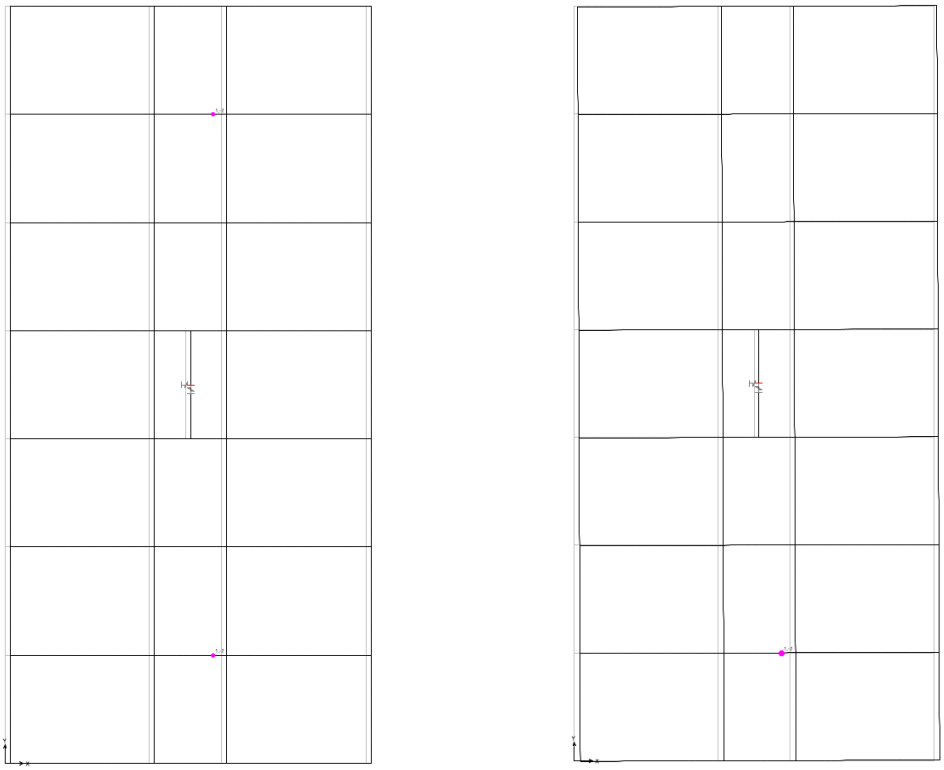

(a) **(b)**

Figure 7.23: Floor 5 at first beam yield of (a) symmetric and (b) asymmetric models

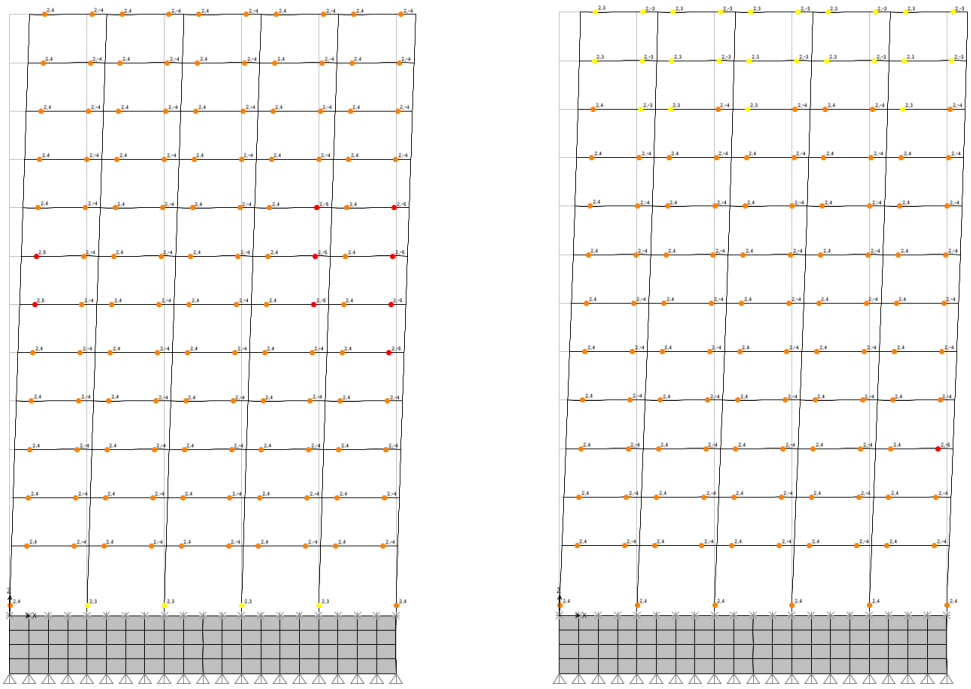

(a) **(b)**

Figure 7.24: Gridline 1 at first beam fail for (a) symmetric and (b) asymmetric models

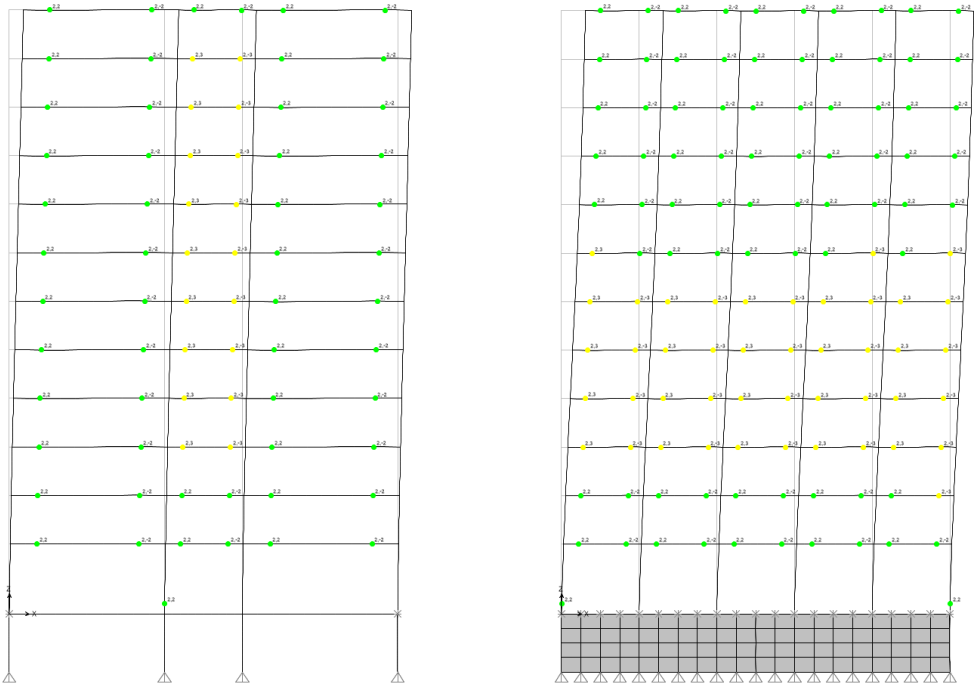

(a) **(b)**

Figure 7.25: (a) Gridlines 2 and 7 at first column yield of symmetric model and (b) Gridline 1 at first column yield of asymmetric model

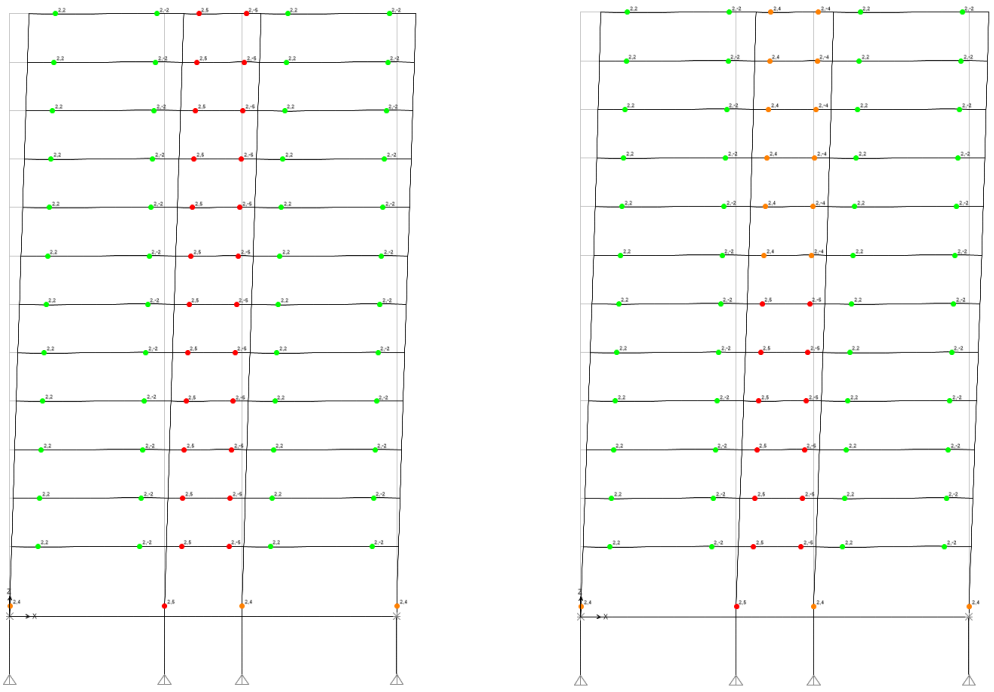

(a) **(b)**

Figure 7.26: Gridline 2 at first column fail for (a) symmetric and (b) asymmetric models

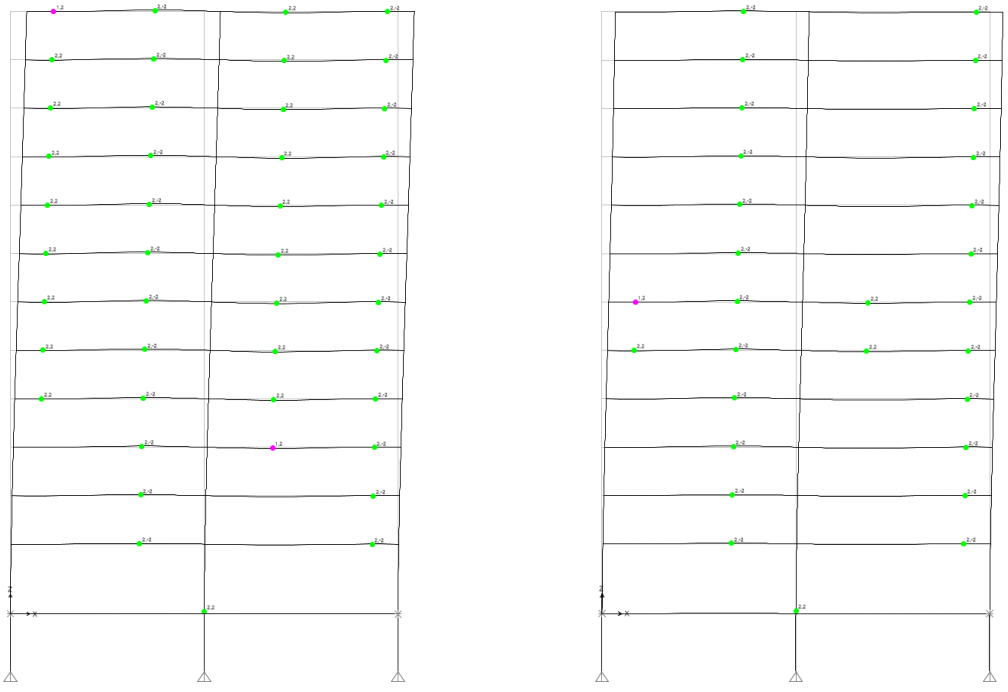

(a) **(b)**

Figure 7.27: Gridline 4 at first wall yield for (a) symmetric and (b) asymmetric models

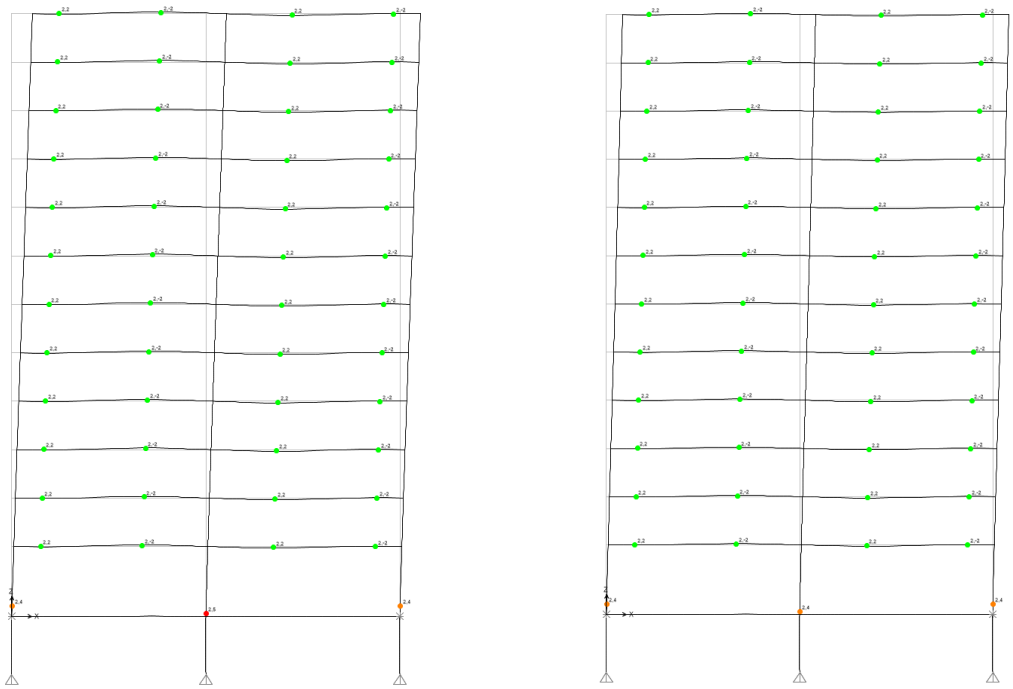

(a) **(b)**

Figure 7.28: Gridline 4 at (a) first wall fail for symmetric model and (b) asymmetric model (no walls failed)

7.5 SAP2000 Nonlinear THA Results

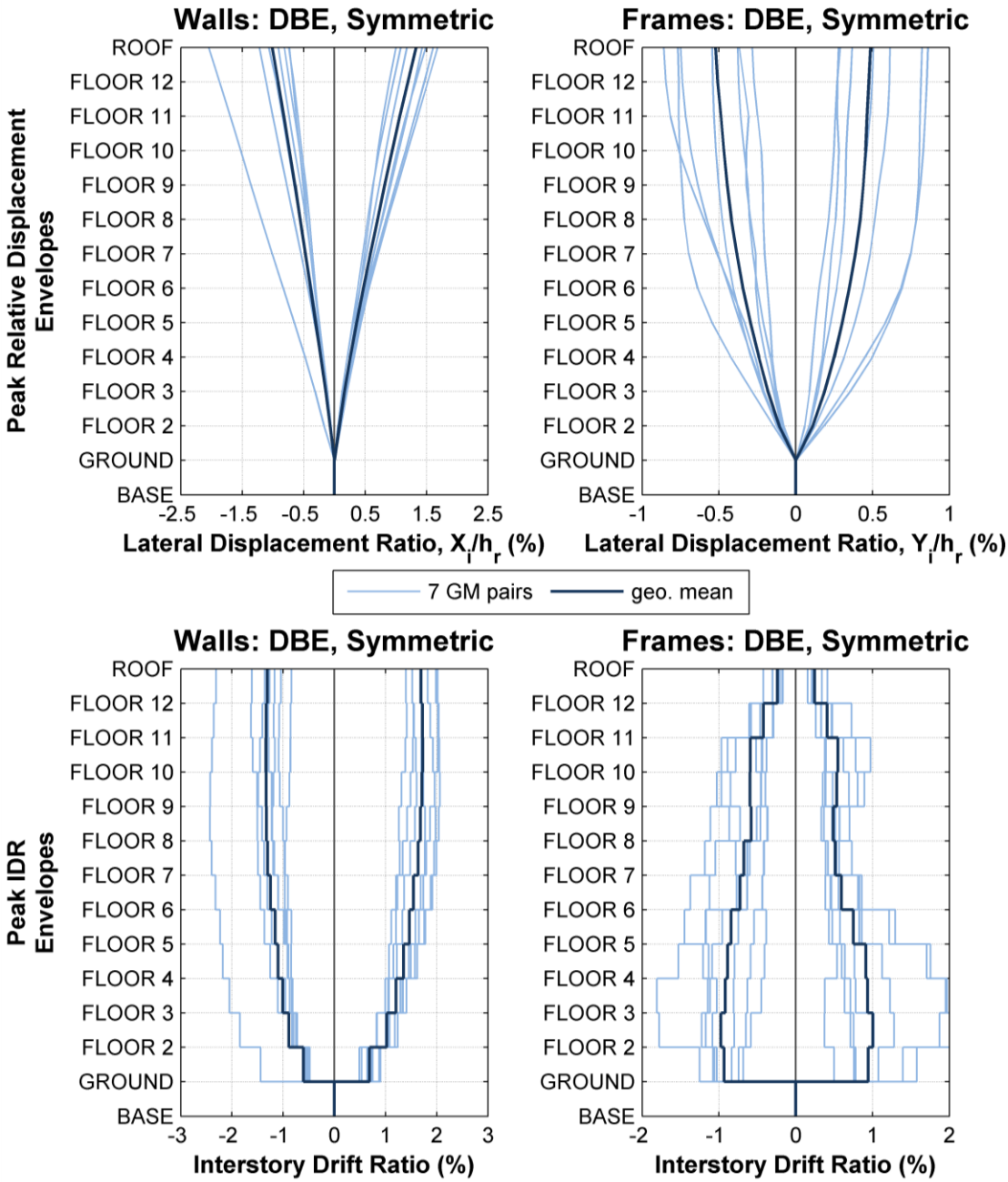

Figure 7.29: Envelopes for symmetric SAP2000 model at DBE level

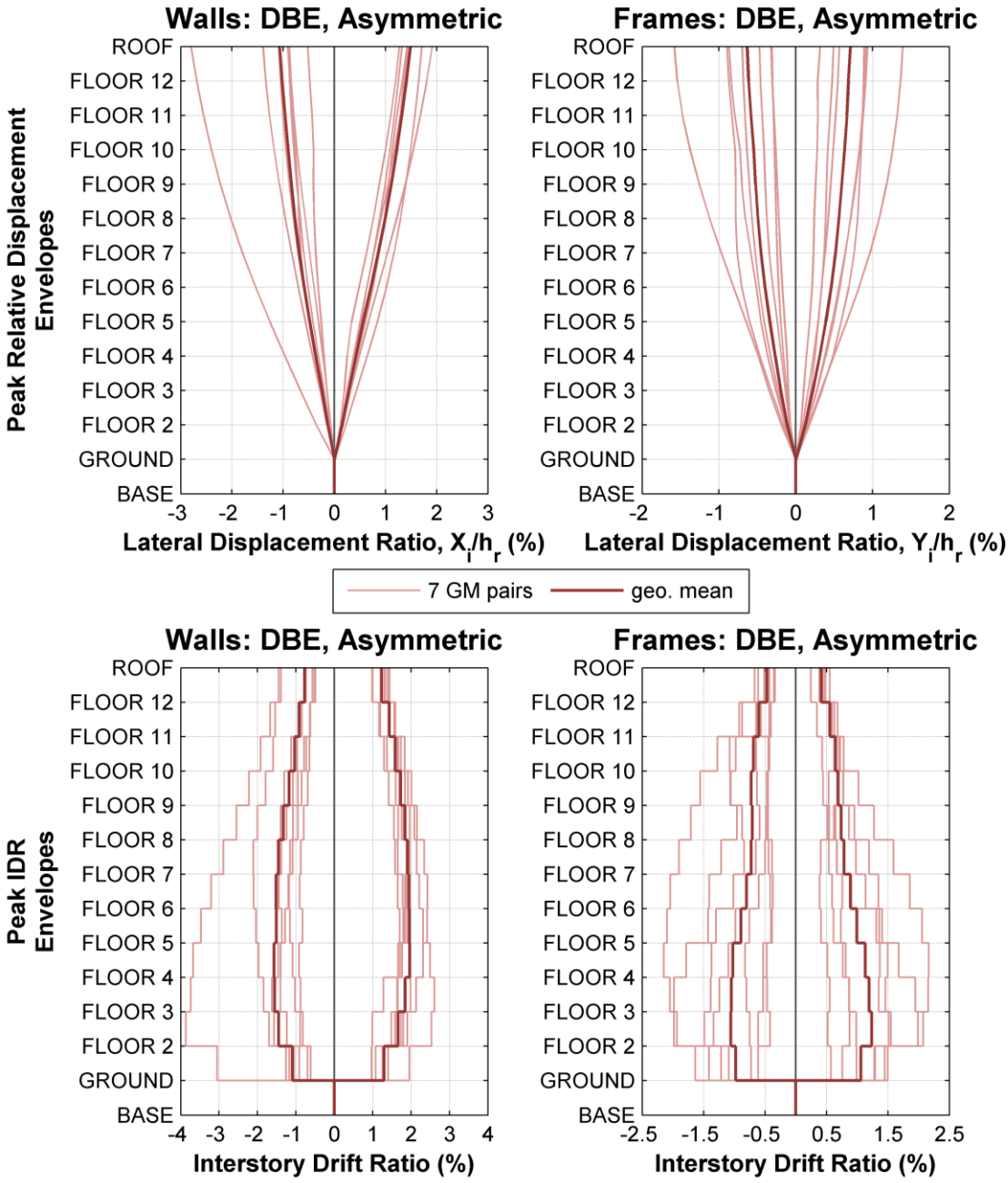

Figure 7.30: Envelopes for asymmetric SAP2000 model at DBE level

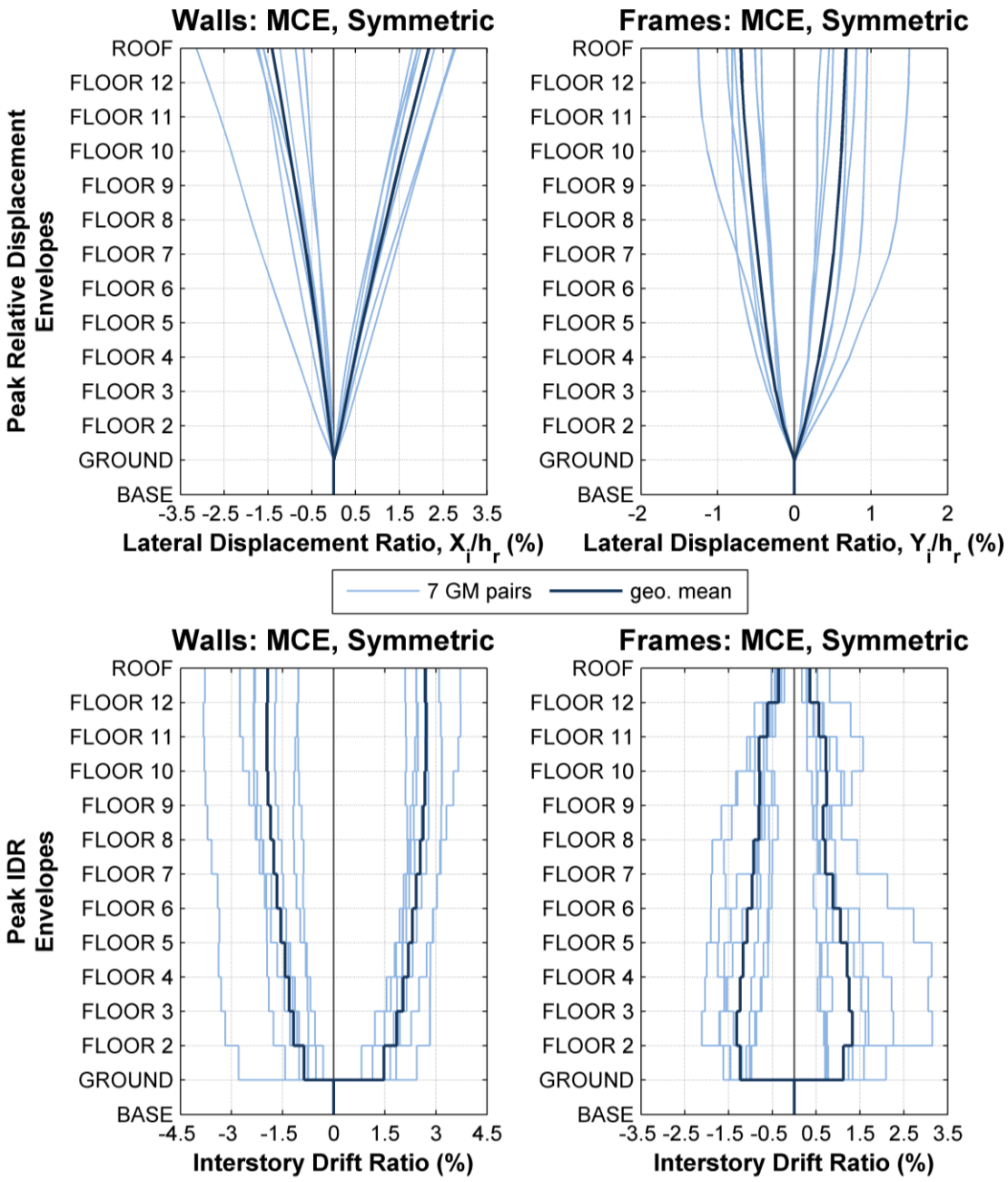

Figure 7.31: Envelopes for symmetric model case at MCE level

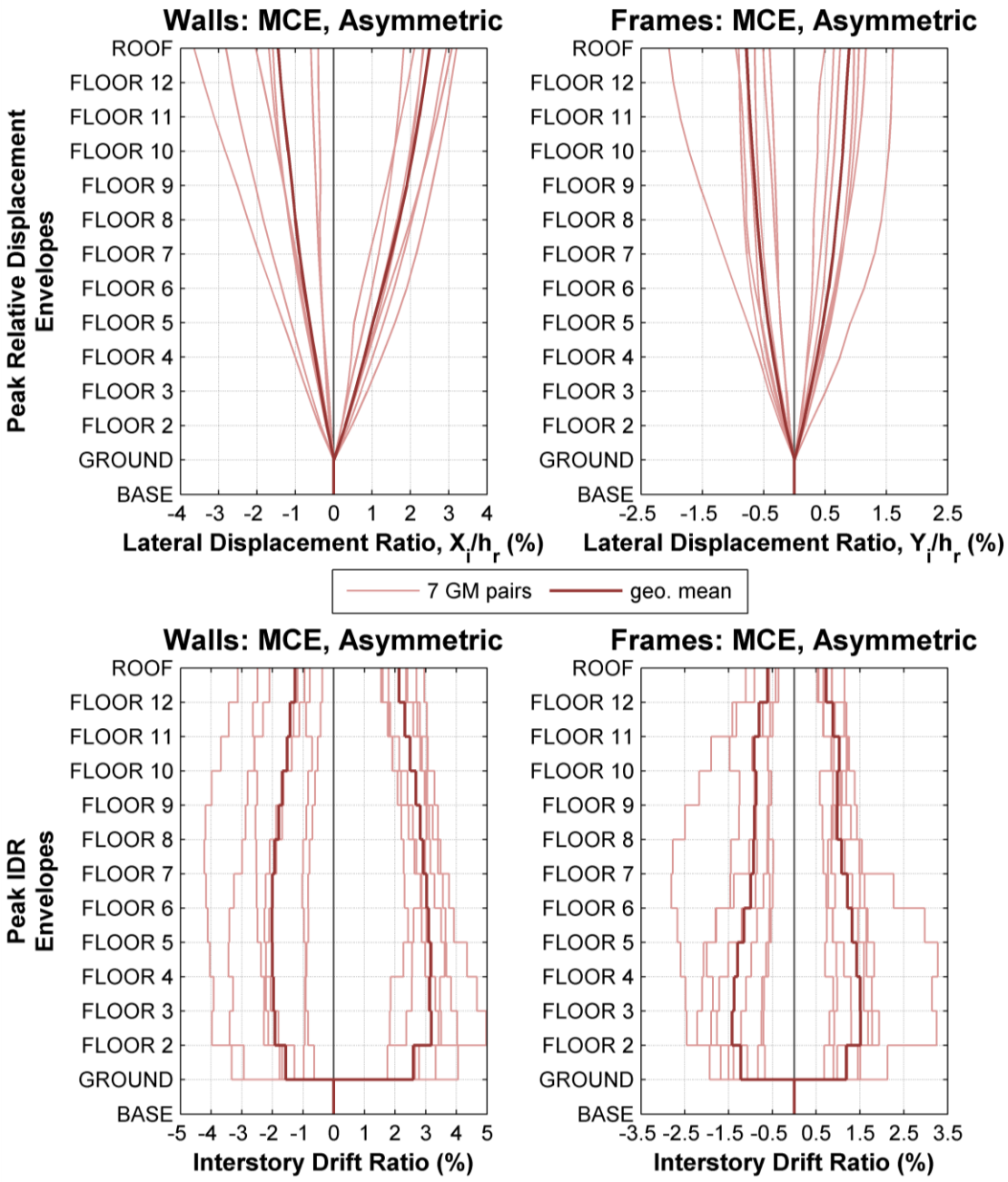

Figure 7.32: Envelopes for asymmetric SAP2000 model at MCE level

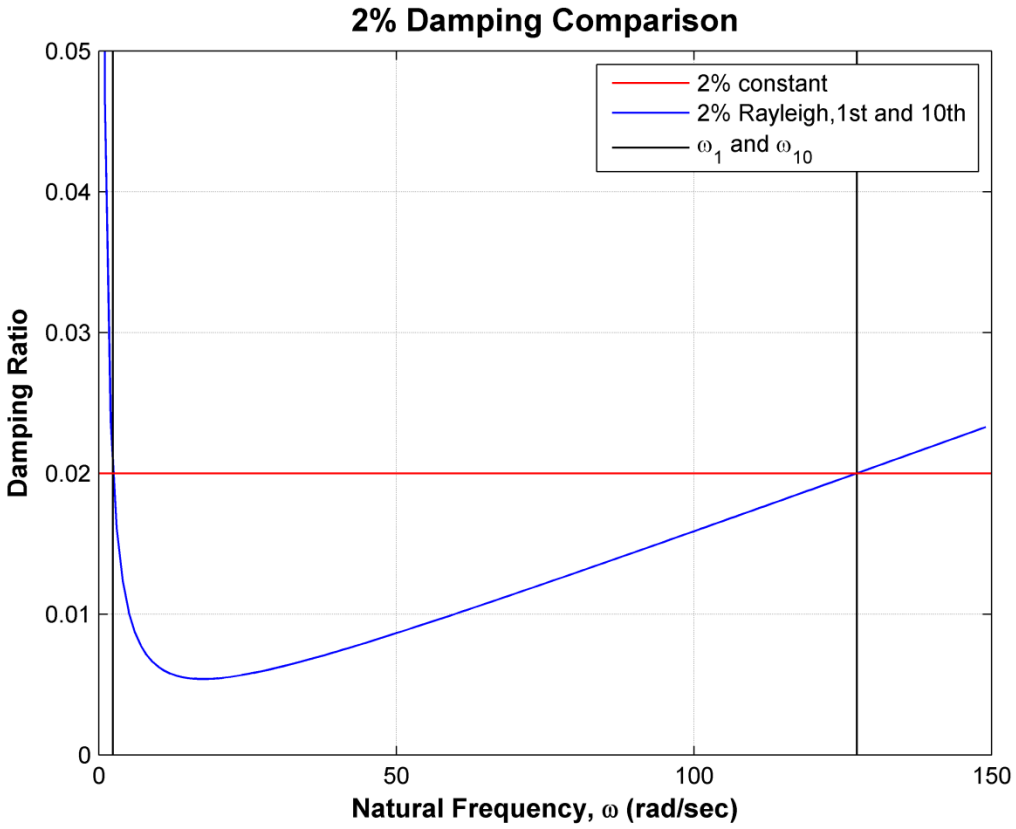

Figure 7.33: Comparison of 2% constant damping and 2% Rayleigh damping

7.6 SAP2000 Model Nonlinear THA Comparison to OpenSees

In addition to his SAP2000 model, Barbosa created a nonlinear fiber-section model of the same NEHRP 13-story building structure in OpenSees that includes the slabs and uses expected material properties. In the model, the beam sections were altered to have slightly more reinforcing than was specified in the design document and the shear walls are modeled as a combination of frame and truss elements. For a detailed description of the OpenSees model parameters, refer to Barbosa's Ph.D. dissertation. Arpit Nema, a Ph.D. student at UCSD, performed nonlinear time history analyses on the OpenSees model using the original suite of seven ground motions and the same DBE and

MCE scale factors used in this thesis. While there are several fundamental differences in how the structure is modeled and the different analysis capabilities of OpenSees and SAP2000, a comparison of the nonlinear time history analyses was performed and is provided in the following figures. It should be clear that the ground motion records used for the SAP2000 analysis were the cut records and the records used for the OpenSees analysis were the full, uncut records.

The results were not as similar as was expected or desired in the direction of the walls, with a 100% difference in maximum RDRs achieved at the MCE level. However, since the frame direction demands were more elastic, the difference in modeling of nonlinear behavior was less apparent and the results were reasonably close despite the different modeling techniques. It was found that the SAP2000 model experienced larger RDR and maximum IDR demands than the OpenSees model. Also shown by the significantly lower peak normalized system overturning moment, the accelerations of the SAP2000 model were lower. However, before and after the peak in response of the OpenSees model, the correlation between the normalized system overturning moments is decent. Thus, the SAP2000 model seemed to be pushed further into the nonlinear range. Additionally, since cracked model properties were used for the SAP2000 model, the initial period of the structure was longer than the OpenSees model, which did not use cracked section properties because the model determines the “cracked” period after the vertical dead load is applied. All sections in the OpenSees model directly account for confined and unconfined regions of concrete throughout the analysis, where the moment-curvature relationships input in the SAP2000 model were linearized idealizations with different hysteretic behavior than what is used in OpenSees.

It was thus determined that the differences between the model properties, including different reinforcing layout and areas, mostly in the beam sections, had a large impact on the difference in nonlinear response. The model behavior is thus nearly incomparable because the SAP2000 model was based on the representative sections of the original design document, and not based directly on the OpenSees code. To be able to more directly compare the difference in programs, the SAP2000 model should be rebuilt with all beam and column sections exactly representing the reinforcing specified in the OpenSees model. However, the wall sections would still need to be modeled as frame elements if plastic hinges are used in SAP2000. More effort should also be focused on tailoring the hysteretic behavior of each plastic hinge to the OpenSees hysteretic behavior. To perform each of these adjustments and better match the models, it would take several weeks to months of trial-and-error, which is the reason why it was not attempted with this thesis. Additionally, the aim of this thesis was ultimately to compare the nonlinear response of a structure with a symmetric floor plan to that of structure with an asymmetric floor plan, so to create matching SAP2000 and OpenSees models could be the scope of a future thesis.

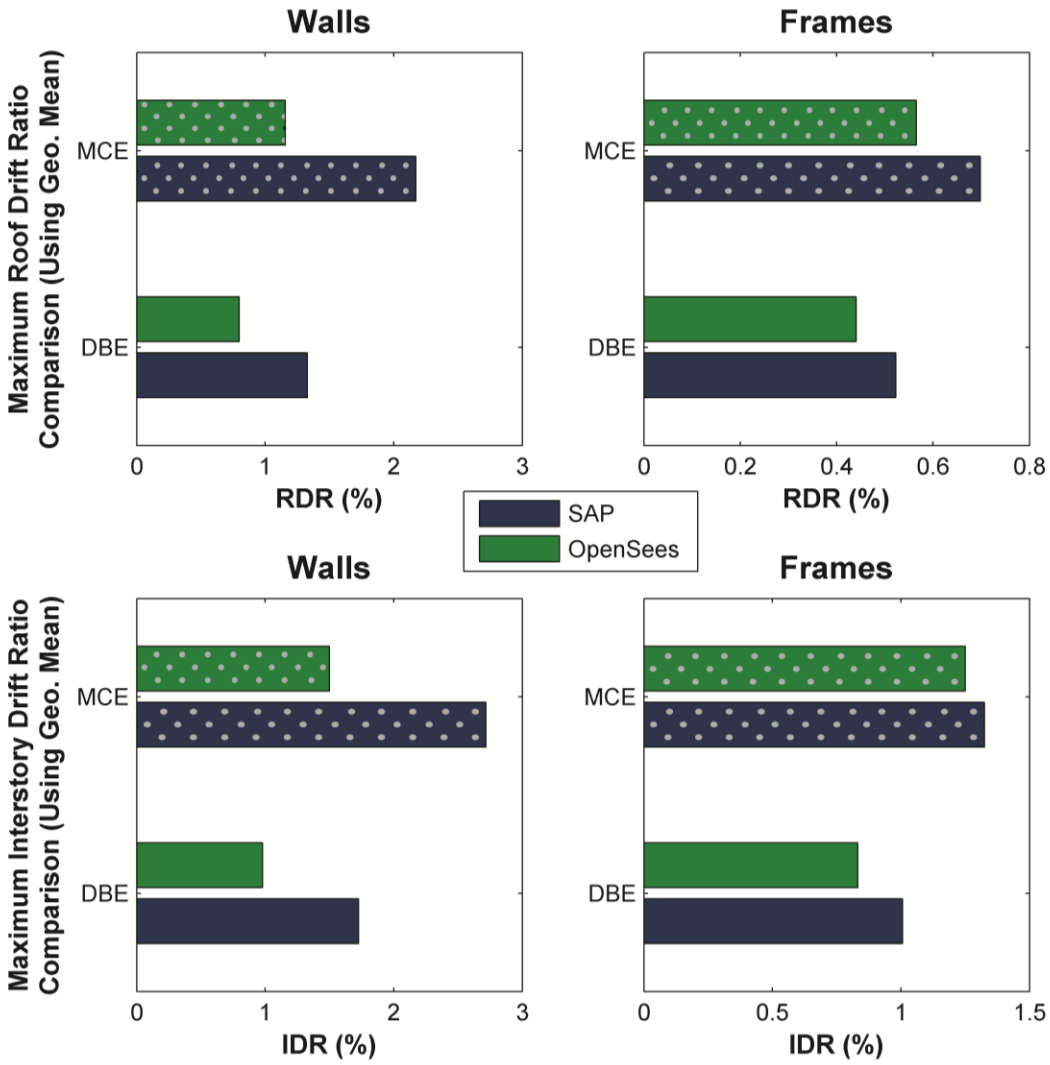

Figure 7.34: Comparison between SAP2000 and OpenSees nonlinear THA results

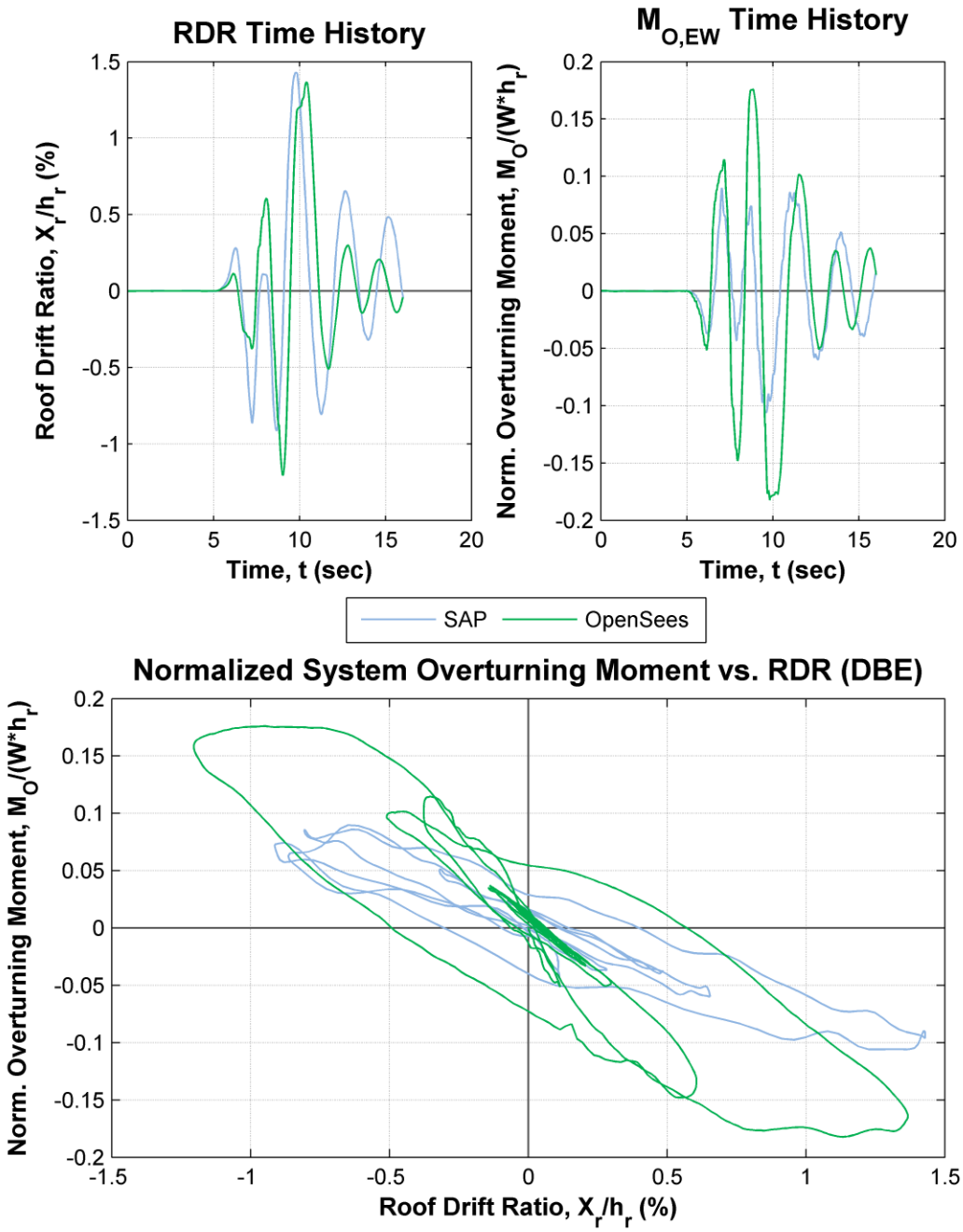

Figure 7.35: Roof drift ratio and system overturning moment comparison of SAP and OpenSees for NZ002 at DBE level

REFERENCES

[1] FEMA 451, "NEHRP Recommended Provisions for Seismic Regulations for New Buildings and Other Structures: Design Examples," Federal Emergency Management Agency, 2006.

[2] NEHRP 2000, "NEHRP Recommended Provisions for Seismic Regulations for New Buildings and Other Structures," Federal Emergency Management Agency and Building Seismic Safety Council, 2001.

[3] A. R. Barbosa, "Simplified Vector-Valued Probabilistic Seismic Hazard Analysis and Probabilistic Seismic Demand Analysis: Application to the 13-Story NEHRP Reinforced Concrete Frame-Wall Building Design Example," PhD Dissertation, Department of Structural Engineering, University of California, San Diego, 2011.

[4] FEMA 450, "NEHRP Recommended Provisions for Seismic Regulation for New Buildings and Other Structures," Federal Emergency Management Agency, 2003.

[5] ASCE 7-05, Minimum Design Loads for Buildings and Other Structures, American Society of Civil Engineers, 2006.

[6] ACI Committee 318, Building Code Requirements for Structural Concrete (ACI 318-08) and Commentary, American Concrete Institute, 2008.

[7] Computers and Structures, Inc., *CSI Analysis Reference Manual for SAP2000, ETABS, and SAFE*, 2005.

[8] O. Kalny and M. Abell, "CSi Technical Knowledge Base," 23 March 2010. [Online]. Available: https://wiki.csiamerica.com/display/kb/Section+Designer. [Accessed 20 February 2014].

[9] O. Kalny and M. Abell, "CSi Technical Knowledge Base," Computers and Structures, Inc., 2 August 2012. [Online]. Available: https://wiki.csiberkeley.com/wiki-staging/x/pZUa. [Accessed February 2014].

[10] M. J. N. Priestley, *Myths and fallacies in earthquake engineering, revisited*, 2003.

[11] A. Arias, *A measure of earthquake intensity*, R. Hansen, Ed., Cambridge, MA: The M.I.T. Press, 1970, pp. 438-483.